This is to certify that the

dissertation entitled

Advanced Electron Paramagnetic Resonance Studies of Biologically Relevant Radicals

presented by

Vladimir Bouchev

has been accepted towards fulfillment
of the requirements for

Ph.D. degree in Chemistry

Major professor

Date 4/29/99

ADVANCED ELECTRON PARAMAGNETIC RESONANCE STUDIES OF BIOLOGICALLY RELEVANT RADICALS

By

Vladimir Bouchev

A DISSERTATION

Submitted to
Michigan State University
in partial fulfillment of the requirements
for the degree of

DOCTOR OF PHILOSOPHY

Department of Chemistry

1999

ABSTRACT

ADVANCED ELECTRON PARAMAGNETIC RESONANCE STUDIES OF BIOLOGICALLY RELEVANT RADICALS

By

Vladimir Bouchev

Electron-Nuclear Double Resonance (ENDOR) and Electron Spin Echo Envelope Modulation (ESEEM) spectroscopies have both established themselves as indispensable methods for measuring small hyperfine couplings. Their application proved to be especially appropriate to paramagnetic species in biologically important disordered systems where the electron-nuclear hyperfine couplings are masked by inhomogeneous broadening of the Electron Paramagnetic Resonance (EPR) lineshape.

This work presents an application of ENDOR and ESEEM methods in combination with isotopic substitution and numerical simulations of experimental data to the study of paramagnetic reaction intermediates emerging during the Pyruvate:Ferredoxin Oxidoreductase (PFOR) catalyzed oxidative decarboxylation of pyruvate. A number of hyperfine coupling parameters were determined and related to a substrate-derived transient radical. The radical intermediate is found to be in close proximity to the thiamin pyrophosphate (TPP) prosthetic group of the enzyme. Two models, the model of a σ–type radical and that of a π–type radical, were considered to account for the observed

couplings. The results of this study help understanding the mechanism of the PFOR reaction.

A two-dimensional variant of ESEEM, the Hyperfine Sublevel Correlation Spectroscopy (HYSCORE) has emerged as a powerful extension of the conventional, one-dimensional ESEEM. In HYSCORE, frequencies that originate from the same hyperfine coupling give rise to cross peaks in the spectra, thus summarizing the lineshape information of many 1D ESEEM data sets in cross-peak contours. This leads to simplification of the assignment of the peaks. However, the HYSCORE of nuclei with spin $I > 1/2$, for which ESEEM techniques demonstrate inherently high sensitivity has not been fully explored. In this work, the HYSCORE echo modulation function for an $S = 1/2$, $I = 1$ spin system was derived using density matrix formalism. Its applicability to the interpretation of the HYSCORE data for ^{2}H-labeled tyrosyl radical has been demonstrated through simulations. The simulations show that the 2D ESEEM function adequately describes the experimental correlation patterns and reproduces, to a good approximation, the τ-suppression-effect modulated lineshapes of the observed HYSCORE cross peaks.

Acknowledgment

I am deeply indebted to my advisor, John McCracken, for teaching me EPR. I would like to thank him for his guidance, help and support during my years at MSU.

I would like to express my thanks to Dr. Andrew Ichimura for his valuable help and collaboration in performing numerous ENDOR experiments. I have benefited greatly from the enlightening discussions with Dr. Marilena DiValentini on pulsed EPR.

I wish to thank the members of the Dr. McCracken and Dr. Babcock groups who more or less directly contributed to this work. Special thanks to Dr. György Filep for being a great friend and colleague.

I am grateful to my wife, Hristina, for her love, care and understanding.

TABLE OF CONTENTS

LIST OF TABLES....vii

LIST OF FIGURES....viii

LIST OF ABBREVIATIONS....xxi

INTRODUCTION....1

Chapter I:
Basic Principles of the Electron Magnetic Resonance Spectroscopy....3

I.1. Introduction....3

I.2. Continuous-Wave Electron Paramagnetic Resonance....5
I.2.1. The Zeeman interaction....5
I.2.2. The hyperfine interaction....9
I.2.3. The nuclear quadrupole interaction....24

I.3. Principles of Electron Nuclear Double Resonance (ENDOR) Spectroscopy....28
I.3.1. Energy levels and resonance conditions....28
I.3.2. Level populations and ENDOR effect....34
I.3.3. Factors influencing ENDOR signal intensity....39
I.3.4. ENDOR lineshapes....41

I.4. Principles of the Electron Spin Echo Envelope Modulation (ESEEM) Spectroscopy....47
I.4.1. Pulses of microwave radiation and their effects....49
I.4.2. Two-pulse electron spin echo....54
I.4.3. Three-pulse electron spin echo (stimulated echo)....56
I.4.4. Four-pulse electron spin echo....61
I.4.5. Origin of ESEEM....63
I.4.6. Density matrix description of ESEEM....73

References....93

Chapter II:
CW-EPR, ENDOR and ESEEM Studies of Pyruvate:Ferredoxin Oxidoreductase (PFOR) Reaction Intermediates....96

II.1. Introduction.....96
II.1.1. 2-Keto oxidoreductases.....97
II.1.2. Mechanism of the oxidative decarboxylation of pyruvate by PFOR.....103

II.2. Application of Advanced EPR Methods to the Study of *Clostridium thermoaceticum* PFOR Reaction Intermediates.....111
II.2.1. Experimental.....111
II.2.2. Results.....112
II.2.3. Discussion.....151
II.2.4. Conclusion.....180

References.....181

Chapter III:
Hyperfine Sublevel Correlation Spectroscopy (HYSCORE) of S = 1/2, I = 1 Spin Systems.....184

III.1. Introduction.....184

III.2. Principles of HYSCORE.....189

III.3. HYSCORE Modulation Function for an S = 1/2, I = 1 Spin System.....207

III.4. Application of HYSCORE to the Study of a Tyrosyl Radical Model System.....217
III.4.1. Introduction.....217
III.4.2. EPR spectroscopic studies of tyrosyl radicals.....218
III.4.3. HYSCORE of 3, 5 ^{2}H-labeled tyrosyl radical model system.....222
III.4.4. τ-suppression effect in HYSCORE.....228
III.4.5. Simulations of the HYSCORE experimental data for 3, 5 ^{2}H-labeled tyrosyl radical.....236

III.5. Conclusion.....253

References.....254

LIST OF TABLES

Table II-1 Hyperfine coupling constants from ^{1}H ENDOR of *Clostridium Thermoaceticum* PFOR reaction intermediates.....122

Table III-1 Hyperfine tensors of tyrosyl radicals.....221

LIST OF FIGURES

Figure I-1 Energy levels of a spin system consisting of one unpaired electron (S = 1/2) and one magnetic nucleus with I = 1/2 as a function of an externally imposed magnetic field.....8

Figure I-2 Interaction of magnetic dipoles μ_e and μ_n arising from an electron spin and a nuclear spin, respectively. The dipoles are aligned with the external magnetic field and are separated by a distance r. Angle θ is between the inter-dipole vector **r** and the applied field $\mathbf{B}_0$.....13

Figure I-3 Valence bond structures for the C_α-H fragment. The two possible electron spin configurations in the s bonding orbital are shown for a spin in the $2p_\pi$ orbital of the carbon atom. (a) Spins parallel in the s bonding orbital and the $2p_\pi$ orbital of carbon. (b) Corresponding spins antiparallel.....17

Figure I-4 Model used for calculation of the dipole-dipole magnetic coupling or unpaired p_π electron density on C_α carbon atom with the nucleus of a hydrogen atom. The spin density is concentrated equally at effective centers of the p_π orbital lobes on either side of C_α. r_p is the distance from the effective coupling centers to C_α nucleus. r_{CH} is the internuclear distance of C and H.....19

Figure I-5 (a) Hyperconjugation in ethyl radical. The admixture of the two exemplary valence bond structures can account for the significant isotropic hyperfine coupling for β hydrogens in aliphatic radicals. (b) Coordinate system for β coupling of hydrogens.....20

Figure I-6 Quadrupolar nuclei (a) oblate, (b) prolate. An oblate quadrupolar nucleus in (c) a uniform electric field, (d) an effective field gradient.....25

Figure I-7 Energy-level diagram in a high magnetic field for the interaction of one unpaired electron (S = 1/2) with an I = 1/2 nucleus (e. g. a proton), detailing the electron Zeeman, nuclear Zeeman, and hyperfine splittings. The case of $g_n > 0$, $A_{iso} > 0$, $|A_{iso}/2| < \nu_n$ is

represented. The four energy levels on the right (1 to 4) are labeled by $|M_S, M_I>$. The heavy arrows indicate the induced EPR and NMR transitions; the broken arrows the various relaxation rates.....30

Figure I-8 ENDOR spectra for (a) $|A_{iso}/2| < \nu_n$ and (b) $|A_{iso}/2| > \nu_n$. The solid lines represent the spectrum observed when the high field EPR transition is monitored and the dashed lines give the spectrum observed when the low field EPR line is monitored.....32

Figure I-9 Energy-level diagram of a hyperfine-coupled spin system in a high magnetic field, consisting of one unpaired electron (S = 1/2) and three equivalent nuclei (I = 1/2).....33

Figure I-10 Population diagram for transient ENDOR with S = 1/2, I = 1/2, $g_n > 0$, $A_{iso} > 0$. (a) unsaturated EPR transition, (b) saturated EPR transition, (c) transient ENDOR effect, (d) final steady state.....36

Figure I-11 Energy-level diagram for S = 1/2, I = 1/2 spin system showing EPR and ENDOR transitions in the absence (a) and presence (b) of quadrupole coupling.....44

Figure I-12 ENDOR lineshapes (absorption: top, first derivative: bottom) resulting from an axially symmetric hyperfine tensor with (a) zero trace (purely dipolar hyperfine interaction) and (b) $A_{iso} \neq 0$. The bottom parts illustrate the procedure for determining $A_{||}$ and $A_{\perp}$.....45

Figure I-13 Inhomogeneously broadened EPR lineshape (total linewidth 10 to 10000 Gauss). (a) $\mathbf{B}_{0,avg}$ is the mean value of the resonant magnetic field. $\mathbf{B}_0$ is the linewidth of the portion of the spectrum excited by a microwave pulse. (b) The individual spin packets (linewidth of the order of 10^{-3} Gauss) have magnetization components precessing independently of each other at frequencies ω_i, ω_0, ω_j.....48

Figure I-14 (a) A microwave pulse is a burst of monochromatic microwave radiation of duration t_p. (b) The frequency spectrum of a pulse gives the spectral density of the field at the sample.....50

Figure I-15 Decomposition of a linearly polarized oscillating magnetic field, $\mathbf{B}_X(t)$, into two counter-rotating circularly-polarized components, B_r and B_l.....51

Figure I-16 Two-pulse electron spin echo sequence and an exemplary two-pulse ESEEM time-domain data set collected for the $Ni(III)(CN)_4(H_2O)_2^-$ complex in a 50 % v/v water/ethylene glycol glass.....55

Figure I-17 Vector diagram illustrating the formation of the two-pulse electron spin echo. (a) two-pulse electron spin echo sequence; (b) at thermal equilibrium the magnetization **M** is aligned with the external magnetic field $\mathbf{B}_0$; (c) the first ($\pi/2$) pulse has torqued **M** onto the XY plane of the rotating frame; (d) **M** is a superposition of spin packets that dephase due to the differences in their precession frequencies; (e) the second pulse rotates the spin packets about the X axis through angle π. The direction of precession of each spin packet is conserved. (f) the individual spin packets refocus along Y to reform **M**, thus generating an echo.....57

Figure I-18 Vector diagram illustrating the formation of the three-pulse electron spin echo. (a) three-pulse electron spin echo sequence; (b), (c) same events as in Figure I-17; (d) the second $\pi/2$ pulse converts the transversal magnetization into a longitudinal one; (e) the magnetization components precess about Z; (f), (g) the third $\pi/2$ pulse rotates the surviving magnetization components (directed along Z) onto the XY plane; (h) the spin packets refocus along Y to reform **M**, thus generating a stimulated echo.....59

Figure I-19 Vector diagram illustrating the formation of the four-pulse electron spin echo. (a) after the second $\pi/2$ pulse the magnetization δM_Z associated with a particular spin packet is brought along the Z axis; (b) the π pulse inverts δM_Z; (c) the fourth ($\pi/2$) pulse rotates δM_Z onto the XY plane; (d) spin packets start precess about Z; (e) during a time period τ after the last pulse various spin packets attain the position shown, which creates the echo along the -Y axis.....62

Figure I-20 Energy-level diagram for an S = 1/2, I = 1/2 spin system described by the Hamiltonian of Equation [I-54].....64

Figure I-21 Vector model showing the interference between electron spin packets that result from transition "branching" in a two-pulse ESEEM experiment. The upper left insert represents the energy-level diagram of Figure I-20, while the upper right insert shows the spin packets across the inhomogeneous line. (a) after the first pulse spin packet *A* precesses in the XY plane at frequency $\omega_A < \omega_0$ acquiring phase $(\omega_A - \omega_0)\tau$ during time τ; (b) the second pulse flips spin packet *A* about X and induces its branching into two portions that precess at frequencies $\omega_A < \omega_0$ and $\omega_C > \omega_0$; (c) spin packet *A* is refocused along Y contributing fully to the spin echo, while spin packet *C* is refocused at an angle $\theta = (\omega_A - \omega_C)\tau$ with respect to Y, giving a contribution to the echo weighted by $\cos(\theta)$.....66

Figure I-22 Energy levels of a spin system and transitions involved in the generation of electron spin echo signals. The resonance field at frequency ω is able to induce transitions in all intervals $\omega_{\alpha,i} - \omega_{\beta,j}$.....77

Figure I-23 Various electron spin echo pulse sequences. Each sequence consists of successive periods of nutation and free precession. (a) two-pulse sequence, $\pi/2 - \tau - \pi - \tau$; (b) three-pulse sequence, $\pi/2 - \tau - \pi/2 - T - \pi/2 - \tau$; (c) four-pulse sequence, $\pi/2 - \tau - \pi/2 - t_1 - \pi - t_2 - \pi/2 - \tau$.....78

Figure I-24 Simulations of (a) powder ENDOR spectrum and (b) a three-pulse ESEEM spectrum for an S = 1/2, I = 1/2 spin system. Parameters: g = 2.004, $g_n = 2.261$ (^{31}P), $A_{||} = 7.0$ MHz, $A_{\perp} = 2.4$ MHz, $B_0 = 3200$ G; $\tau = 200$ ns; dead-time, 240 ns.....91

Figure II-1 First derivative EPR spectra of PFOR from *Hm. Halobium*.....99

Figure II-2 Four subunit catalytic model of 2-keto acid oxidoreductases.....101

Figure II-3 Thiamin pyrophosphate prostetic group of PFOR.....104

Figure II-4 Mechanism of the PFOR catalyzed reaction. Steps: (1) pyruvate

binding; (2) formation of hydroxyethylidene-TPP intermediate; (3) formation of HE-TPP radical and reduction of cluster A; (4) CoA binding and reduction of cluster B; (5) formation of acetyl-CoA and regeneration of TPP anion; (6) reduction of external electron acceptors.....106

Figure II-5 First derivative EPR spectra of *Clostridium Thermoaceticum* PFOR incubated with (a) sodium dithionite, (b) pyruvate and CoA, (c) CoA, or (d) pyruvate. EPR parameters: spectral width, 2000 G; field center, 3400 G; modulation frequency, 100 kHz; modulation amplitude, 10 G; temperature, 10 K; microwave power, 2 mW; microwave frequency, 9.447 GHz.....107

Figure II-6 First derivative EPR spectra of *Clostridium Thermoaceticum* PFOR incubated with (a) pyruvate, and (b) CD_3-labeled pyruvate. EPR parameters: spectral width, 100 G; field center, 3360 G; modulation frequency, 100 kHz; modulation amplitude, 0.5 G; temperature, 10 K; microwave power, 2 mW; microwave frequency, 9.446 GHz.....109

Figure II-7 First derivative EPR spectra of PFOR with pyruvate, (a), ^2H_3C-pyruvate, (b), 3-methyl-2-oxobutyrate, (c), and 2-oxobutyrate, (d). Experimental parameters: field center, 3376 G; field sweep width, 1000 G; modulation frequency, 100 kHz; modulation amplitude, 5.0 G; time constant, 10 ms; microwave power, 0.1 mW; microwave frequency, 9.468 GHz; temperature, 4 K.....113

Figure II-8 First derivative EPR spectra of PFOR reacted with pyruvate. Experimental parameters: field center , 3377.2 G; field sweep width, 100 G; modulation frequency, 100 kHz; modulation amplitude, 1.0 G; time constant, 10 ms; microwave power, 0.05 mW; microwave frequency, 9.482 GHz; temperature: 9.1 K, (a), and 60 K, (b).....115

Figure II-9 First derivative EPR spectra of PFOR reacted with pyruvate, (a), ^{13}C-2 labeled pyruvate, (b), and ^{13}C-3 labeled pyruvate, (c). Experimental parameters: field center, 3377 G; field sweep width, 1000 G; modulation frequency, 100 kHz; modulation amplitude, 10.0 G; time constant, 10 ms; microwave power, 0.05 mW; microwave frequency, 9.481 GHz; temperature, 9.0 K.....116

Figure II-10 First derivative EPR spectra of PFOR reacted with pyruvate, (a), ^{13}C-2 labeled pyruvate, (b), and ^{13}C-3 labeled pyruvate, (c). Experimental parameters: field center, 3377.2 G; field sweep width, 100 G; modulation frequency, 100 kHz; modulation amplitude, 1.0 G; time constant, 10 ms; microwave power, 0.05 mW; 2.0 microwave frequency, 9.481 GHz; temperature, 60.0 K.....119

Figure II-11 ENDOR spectrum of PFOR/pyruvate. Experimental parameters: static magnetic field, 3349 G; microwave frequency, 9.400 GHz; microwave power, 10 mW; rf sweep width, 5.5 MHz; rf fm modulation depth, 100 kHz; rf power, 220 W; time constant, 10 ms; temperature, 60 K.....121

Figure II-12 ENDOR spectrum of PFOR/pyruvate. Experimental parameters: static magnetic field, 3349 G; microwave frequency, 9.400 GHz; microwave power, 10 mW; rf sweep width, 5 MHz; rf fm modulation depth, 100 kHz; rf power, 220 W; time constant, 10 ms; temperature, 60 K. 300 scans were averaged.....123

Figure II-13 ENDOR spectrum of PFOR/pyruvate. Experimental parameters: static magnetic field, 3349 G; microwave frequency, 9.400 GHz; microwave power, 20 mW; rf sweep width, 27 MHz; rf fm modulation depth, 280 kHz; rf power, 220 W; time constant, 10 ms; temperature: 4K, (a), 77K, (b), 200K, (c).....125

Figure II-14 ENDOR spectrum of PFOR/pyruvate. Experimental parameters: static magnetic field, 3322 G;microwave frequency, 9.400 GHz; microwave power, 1 mW; rf sweep width, 27 MHz; rf fm modulation depth, 280 kHz; rf power, 220 W; time constant, 10 ms; temperature: 4K.....127

Figure II-15 ENDOR spectrum of PFOR/$^{2}H_3$C-pyruvate. Experimental parameters: static magnetic field, 3349 G; microwave frequency, 9.400 GHz; microwave power, 5 mW; rf sweep width, 27 MHz; rf fm modulation depth, 100 kHz; rf power, 220 W; time constant, 10 ms; temperature, 60 K.....128

Figure II-16 Solid line: ENDOR spectrum of PFOR/$^{2}H_3$C-pyruvate. Experimental parameters: static magnetic field, 3349 G; microwave

frequency, 9.400 GHz; microwave power, 5 mW; rf sweep width, 6 MHz; rf fm modulation depth, 100 kHz; rf power, 220 W; time constant, 10 ms; temperature, 60 K.....129

Figure II-17 ENDOR spectrum of PFOR reacted with ^{13}C-3 labeled pyruvate, (a), and ^{13}C-2 labeled pyruvate, (b). Experimental parameters: static magnetic field, 3348.5 G; microwave frequency, 9.396 GHz; microwave power, 1 mW; rf sweep width, 35 MHz; rf fm modulation depth, 158.5 kHz; rf power, 220 W; time constant, 41 ms; temperature, 60 K.....130

Figure II-18 ENDOR spectrum of PFOR/3-methyl-2-oxobutyrate, (a). Experimental parameters: static magnetic field, 3349 G; microwave frequency, 9.410 GHz; microwave power, 2 mW; rf sweep width, 27 MHz; rf fm modulation depth, 100 kHz; rf power, 220 W; time constant, 10 ms; temperature, 60 K. ENDOR spectrum of PFOR/2-oxobutyrate, (b). Experimental parameters: static magnetic field, 3349 G; microwave frequency, 9.410 GHz; microwave power, 2 mW; rf sweep width, 27 MHz; rf fm modulation depth, 100 kHz; rf power, 220 W; time constant, 10 ms; temperature, 60 K.....134

Figure II-19 ESE-EPR spectra of PFOR/pyruvate. Experimental parameters: magnetic field sweep width, 900 G; microwave frequency, 9.600 GHz; pulse duration, 17 ns; τ value, 205 ns; T value, 600 ns; temperature, 4.2 K; pulse sequence repetition rate: 1 Hz, (a), and 40 Hz, (b).....137

Figure II-20 Stimulated time domain ESEEM data for PFOR/pyruvate, (a). Experimental parameters: magnetic field strength, 3429 G; microwave frequency, 9.600 GHz; pulse duration, 17 ns; pulse sequence repetition rate, 10 Hz; τ value, 205 ns; initial T value, 100 ns; sample temperature, 4.2 K; number of data points, 1024; number of events averaged for each data point, 14; number of scans, 2. Corresponding frequency domain spectrum obtained by Fourier transformation of the time domain data, (b).....138

Figure II-21 Stimulated ESEEM spectra of PFOR/pyruvate. Experimental parameters: magnetic field strength, 3429 G; microwave frequency, 9.600 GHz; pulse duration, 17 ns; pulse sequence repetition rate, 40 Hz; initial T value, 100 ns; sample temperature, 4.2 K; number of data points, 1024; number of events averaged for each data point, 34;

number of scans, 2; τ value: 205 ns, (a); 240 ns, (b); 275 ns, (c); 340 ns, (d); 480 ns, (e).....142

Figure II-22 Stimulated ESEEM spectra of PFOR/pyruvate. Experimental parameters: magnetic field strength, 3553 G; microwave frequency, 9.600 GHz; pulse duration, 17 ns; pulse sequence repetition rate, 40 Hz; initial T value, 100 ns; sample temperature, 4.2 K; number of data points, 1024; number of events averaged for each data point, 12; number of scans, 2; τ value: 203 ns, (a); 240 ns, (b); 340 ns, (c); 480 ns, (d).....144

Figure II-23 Stimulated ESEEM spectra of PFOR/pyruvate. Experimental parameters: magnetic field strength, 3429 G; microwave frequency, 9.600 GHz; pulse duration, 17 ns; initial T value, 100 ns; τ value, 203 ns; sample temperature, 4.2 K; number of data points, 1024; number of events averaged for each data point, 12; pulse sequence repetition rate: 1 Hz, (a), and 40 Hz, (b).....146

Figure II-24 Stimulated ESEEM data for PFOR/$^{2}H_3C$-pyruvate. (a) Time-domain data; (b) The corresponding frequency-domain data obtained by Fourier transformation of trace (a). Experimental parameters: magnetic field strength, 3429 G; microwave frequency, 9.600 GHz; pulse duration, 17 ns; initial T value, 100 ns; pulse sequence repetition rate, 10 Hz; sample temperature, 4.2 K; number of data points, 1024; number of events averaged for each data point, 14; number of scans averaged, 2; τ value, 203 ns, (b), and 444 ns, (c).....148

Figure II-25 Fourier transform of the time-domain ratio of the two data sets shown in Figure I-20 and Figure I-24 (a).....152

Figure II-26 Stimulated ESEEM spectrum of PFOR/3-methyl-2-oxobutyrate, (a). Experimental parameters: magnetic field strength, 3429 G; microwave frequency, 9.600 GHz; pulse duration, 17 ns; initial T value, 100 ns; τ value, 205 ns; pulse sequence repetition rate, 40 Hz; sample temperature, 4.2 K; number of data points, 1024; number of events averaged for each data point, 34; number of scans averaged, 4. Stimulated ESEEM spectrum of PFOR/2-oxobutyrate, (b). Experimental parameters: magnetic field strength, 3435 G; microwave frequency, 9.600 GHz; pulse duration, 17 ns; initial T value, 100 ns; τ value, 205 ns; pulse sequence repetition rate, 10

Hz; sample temperature, 4.2 K; number of data points, 1024; number of events averaged for each data point, 34; number of scans averaged, 4.....153

Figure II-27 Simulated ^1H ENDOR spectra for PFOR paramagnetic reaction intermediate. Each simulation data set is plotted using dotted lines and shown in comparison with the experimental spectrum (solid line). Simulation parameters: g = 5.5856012, B = 3349 G; (a) $A_{xx}^{(1)} = A_{yy}^{(1)} = 11.95$ MHz, $A_{zz}^{(1)} = 16.90$ MHz, $A_{xx}^{(2)} = A_{yy}^{(2)} = 14.66$ MHz, $A_{zz}^{(2)} = 19.10$ MHz, number of θ increments in the range 0° - 90°, 80, Gaussian linewidth, 0.40 MHz; (b) $A_{xx}^{(1)} = A_{yy}^{(1)} = 11.95$ MHz, $A_{zz}^{(1)} = 19.10$ MHz, $A_{xx}^{(2)} = A_{yy}^{(2)} = 14.66$ MHz, $A_{zz}^{(2)} = 16.90$ MHz, number of θ increments in the range 0° - 90°, 80, Gaussian linewidth, 0.40 MHz; (c) $A_{xx} = 11.65$ MHz, $A_{yy} = 15.50$ MHz, $A_{zz} = 19.10$ MHz, number of θ increments in the range 0° - 90°, 40, number of φ increments in the range 0° - 90°, 40, Gaussian linewidth, 0.30 MHz.....157

Figure II-28 Simulated ^2H ENDOR spectra for PFOR paramagnetic reaction intermediate. Each simulation data set is plotted using dotted lines and shown in comparison with the experimental spectrum (solid line). Simulation parameters: g = 0.85739, B = 3349 G; (**a**) $A_{xx}^{(1)} = A_{yy}^{(1)} = 1.80$ MHz, $A_{zz}^{(1)} = 2.60$ MHz, $e^2qQ^{(1)} = 0.05$ MHz, $A_{xx}^{(2)} = A_{yy}^{(2)} = 2.2$ MHz, $A_{zz}^{(2)} = 2.965$ MHz, $e^2qQ^{(2)} = 0.04$ MHz, $\eta^{(1)} = \eta^{(2)} = 0.1$, number of θ increments in the range 0° - 90°, 40, number of φ increments in the range 0° - 90°, 40, Gaussian linewidth, 0.092 MHz; (**b**) $A_{xx}^{(1)} = A_{yy}^{(1)} = 1.83$ MHz, $A_{zz}^{(1)} = 2.93$ MHz, $A_{xx}^{(2)} = A_{yy}^{(2)} = 2.25$ MHz, $A_{zz}^{(2)} = 2.47$ MHz, $e^2qQ^{(1)} = e^2qQ^{(2)} = 0.05$ MHz, $\eta^{(1)} = \eta^{(2)} = 0.1$, number of θ increments in the range 0° - 90°, 40, number of φ increments in the range 0° - 90°, 40, Gaussian linewidth, 0.0925 MHz; (**c**) $A_{xx} = 1.74$ MHz, $A_{yy} = 2.30$ MHz, $A_{zz} = 2.934$ MHz, $e^2qQ = 0.05$, $\eta = 0.1$, number of θ increments in the range 0° - 90°, 40, number of φ increments in the range 0° - 90°, 40, Gaussian linewidth, 0.085 MHz.....162

Figure II-29 Hydroxyethyl thiamin pyrophosphate radical (HE-TPP).....168

Figure II-30 Resonance structures for HE-TPP radical.....169

Figure II-31 Simulated ^{14}N ESEEM frequency domain spectrum. Simulation parameters: nuclear Larmor frequency, ν_I = 1.05 MHz; $A_\perp$ = 1.36 MHz, $A_{||}$ = 2.36 MHz; e^2qQ = 1.9 MHz, η = 0.74; number of θ increments in the range 0-90°, 60, number of φ increments in the range 0-90°, 40; τ = 205 ns.....173

Figure II-32 Simulated ^{31}P ENDOR spectra for PFOR paramagnetic reaction intermediate. Each simulation data set is plotted using dotted lines and shown in comparison with the experimental spectrum (solid line). Simulation parameters: g = 2.2633, B = 3345 G; (**a**) A_{iso} = 0.53 MHz, T = 0 MHz, number of θ increments in the range 0° - 90°, 80, Gaussian linewidth, 0.09 MHz; (**b**) A_{iso} = 0 MHz, T = 0.59 MHz, number of θ increments in the range 0° - 90°, 80, Gaussian linewidth, 0.08 MHz; (**c**) A_{iso} = 6.15 MHz, T = 5.725 MHz, number of θ increments in the range 0° - 90°, 160, Gaussian linewidth, 0.09 MHz; (**d**) A_{iso} = 0.53 MHz, T = 0.12 MHz, number of θ increments in the range 0° - 90°, 80, Gaussian linewidth, 0.07 MHz.....176

Figure II-33 A constrained conformation of the HE-TPP radical. All valence bond lengths and valence angles are set to their equilibrium values in the optimal conformation. P^2 - O distance is fixed at 2.5 Å. Optimization of the molecular geometry has been performed by adjusting dihedral angles.....179

Figure III-1 Sequence of events during a four-pulse ESEEM experiment. The amplitude of the four-pulse echo is measured as a function of t_1 and t_2.....185

Figure III-2 (a) An exemplary 2D time-domain data matrix, with only 33 of all the 128 t_1-slices shown. (b) 3D representation of the HYSCORE frequency-domain magnitude spectrum obtained by 2D Fast Fourier Transformation of the time-domain data matrix and taking the absolute value of the resulting complex matrix. (c) Contour plot of the above spectrum.....186

Figu

Figu

Figu

Figu

Figur

Figur

Figur

Figur

Figur

Figure III-3 Schematic HYSCORE 2D spectrum for an S = 1/2, I = 1/2 spin system. Solid squares: peaks observed for ideal pulses. Open squares: diagonal peaks that are observed only for non-ideal pulses that cause partial excitation.....191

Figure III-4 HYSCORE absolute value spectrum of irradiated (a) succinic acid and (b) malonic acid after Fourier transformation with respect to t_1 and t_2.....198

Figure III-5 Schematic HYSCORE contour plots of cross peaks arising from an S = 1/2, I = 1/2 spin system considered at the level of first-order perturbation theory. (a) $\omega_I > A_{||}/2$; (b) $\omega_I < A_{\perp}/2$.....201

Figure III-6 Simulated HYSCORE contour plots arising from an S = 1/2, I = 1/2 spin system with an axially symmetric hyperfine tensor. Parameters: ν_I = 3 MHz; (a) $A_{||}$ = 3.6 MHz, $A_{\perp}$ = 1.2 MHz; (b) $A_{||}$ = 5.2 MHz, $A_{\perp}$ = 0.4 MHz.....204

Figure III-7 Simulated HYSCORE contour plots arising from an S = 1/2, I = 1/2 spin system with a rhombic hyperfine tensor. Parameters: ν_I = 3 MHz, A_{xx} = - 0.04 MHz, A_{yy} = 1.64 MHz, A_{zz} = 4.40 MHz.....206

Figure III-8 Spin-density distribution in the tyrosine neutral radical.....219

Figure III-9 (a) Time-domain HYSCORE data (128×128 data points) from 3,5 ^{2}H-tyrosyl, with τ = 200 ns; (b) the corresponding HYSCORE frequency-domain contour plot. B_0 = 3129 G, ν = 8.910 GHz.....223

Figure III-10 Definition of the position of the external magnetic field vector, $\mathbf{B}_0$, in the principal axis system of a hyperfine tensor with rhombic symmetry.....224

Figure III-11 (a) HYSCORE contour plot of 3,5 ^{2}H-tyrosyl (same as Figure

III-9b); (b) the corresponding frequency-domain simulation using the following parameters: nuclear Larmor frequency, ν_I = 2.1 MHz; A_{xx} = - 3.82 MHz, A_{yy} = - 2.98 MHz, A_{zz} = -1.0 MHz; tau-value, τ = 200 ns.....226

Figure III-12 Calculated suppression effect as a function of A_{zz} ($0 < A_{zz} < 6\omega_I$) and $\omega_I\tau$ assuming $\omega = |\omega_I \pm A_{zz}/2|$. Dark (light) shading corresponds to weak (strong) suppression effect. The sum of the suppression function over $\omega_I\tau$ results in an amplitude function with only two suppression holes at $\omega = 0$ and $\omega = 2\omega_I$ (top).....230

Figure III-13 HYSCORE contour plot of 3,5 ^{2}H-tyrosyl radical taken at various values of τ: (a) 200 ns; (b) 300 ns; (c) 400 ns; (d) 500 ns; (e) 600 ns...232

Figure III-14 Simulated HYSCORE spectra of 3,5 ^{2}H-tyrosyl radical. (a) A 3D plot of the time-domain simulated data (128×128 points). (b) The corresponding 3D frequency-domain magnitude spectrum obtained by 2D Fourier transformation of the time-domain data in (a). (c) Contour plot of the frequency spectrum. Parameters: nuclear Larmor frequency, ν_I = 2.1 MHz; A_{xx} = - 2.3 MHz, A_{yy} = - 3.1 MHz, A_{zz} = -0.9 MHz; η = 0.1; e^2qQ = 0.22 MHz; λ = 0.7 μsec^{-1}; tau-value, τ = 200 ns; number of θ increments over the interval 0-90°, 30; maximum number of φ increments over the interval 0-90°, 30.....238

Figure III-15 Frequency-domain contour plots for the 3,5 ^{2}H-tyrosyl radical HYSCORE time-domain simulations performed with the C program "mims4" using the following parameters: nuclear Larmor frequency, ν_I = 2.1 MHz; A_{xx} = - 2.3 MHz, A_{yy} = - 3.1 MHz, A_{zz} = -0.9 MHz; η = 0.1; e^2qQ = 0.22 MHz; λ = 0.7 μsec^{-1}; number of time-domain data points, 128×128; number of θ increments over the interval 0-90°, 30; maximum number of φ increments over the interval 0-90°, 30; tau-value, τ = 150 ns (a), 200 ns (b), 300 ns (c), 400 ns (d), 500 ns (e), 600 ns (f).....243

Figure III-16 Frequency-domain contour plots for the 3,5 ^{2}H-tyrosyl radical HYSCORE time-domain simulations performed with the C program

"mims4" using the following parameters: nuclear Larmor frequency, ν_I = 2.1 MHz; A_{xx} = - 2.3 MHz, A_{yy} = - 3.1 MHz, A_{zz} = -0.9 MHz; number of time-domain data points, 128×128; number of θ increments over the interval 0-90°, 30; maximum number of φ increments over the interval 0-90°, 30; λ = 0.7 μsec^{-1}; tau-value, τ = 200 ns; η = 0.1; e^2qQ = 0, (a), e^2qQ = 0.3 MHz, (b).....250

LIST OF ABBREVIATIONS

Ac	-	Acetyl
C	-	The C programming language
CoA	-	Coenzyme A
CODH/ACS	-	CO dehydrogenase/acetyl-coenzyme A synthase
CW	-	Continuous-wave
1D	-	One-dimensional
2D	-	Two-dimensional
3D	-	Three-dimensional
ENDOR	-	Electron-nuclear double resonance
EPR	-	Electron paramagnetic resonance
ESE	-	Electron spin echo
ESEEM	-	Electron spin-echo envelope modulation
ESR	-	Electron spin resonance
Fd		Ferredoxin
fm	-	Frequency modulation
FORTRAN	-	Formula translator (programming language)
FT	-	Fourier transform
GO	-	Galactose oxidase
HE-TPP	-	Hydroxyethyl-thiamin pyrophosphate
HFI	-	Hyperfine interaction
HYSCORE	-	Hyperfine sublevel correlation spectroscopy
MATLAB	-	Matrix laboratory (programming and visualization software package)
MW	-	Microwave
NAD	-	Nicotinamide adenine dinucleotide
NMR	-	Nuclear magnetic resonance
NQI	-	Nuclear quadrupole interaction
PDC	-	Pyruvate decarboxylase
PDH	-	Pyruvate dehydrogenase
PFOR	-	Pyruvate:Ferredoxin Oxidoreductase
PGHS	-	Prostaglandine H synthase
PS II	-	Photosystem II
rf	-	Radio frequency
RNR	-	Ribonucleotide reductase
TPP	-	Thiamin pyrophosphate

INTRODUCTION

Electron paramagnetic resonance spectroscopy (EPR) has established itself as the most informative method for the investigation of molecules with unpaired electrons. However, for paramagnetic species stabilized in disordered solid matrices such as polycrystals, glasses, frozen solutions, biological and polymeric matrices, the resolution of the traditional, continuous-wave (CW) EPR is reduced due to inhomogeneous broadening of the EPR lineshape, which can mask the details of the EPR spectra. Both electron-nuclear double resonance spectroscopy (ENDOR) and electron spin echo envelope modulation spectroscopy (ESEEM) have proven especially suitable for resolving small electron-nuclear hyperfine interactions in samples of randomly oriented paramagnetic species.

Chapter I of this Dissertation covers the basic principles of EPR spectroscopy. It emphasizes the main characteristics, advantages and drawbacks of the continuous-wave, double resonance, and time-domain EPR methods. In principle, ENDOR and ESEEM offer identical information on hyperfine interactions. However, the two techniques are considered complementary to each other since they show different degree of applicability towards various systems. Thus, ESEEM is more useful for measuring weaker hyperfine couplings of nuclei with small magnetic moments, whereas ENDOR experiments on such systems are typically difficult to perform.

Chapter II presents a CW-EPR, ENDOR, and ESEEM study of pyruvate: ferredoxin oxidoreductase (PFOR) paramagnetic reaction intermediates. These EPR techniques are used in combination with isotopic substitutions to characterize the

magnetic and structural properties of the trapped transient intermediates. Determination of the electronic and nuclear structures of paramagnetic reaction intermediates provides insight into the molecular mechanisms of the enzyme catalyzed reaction.

Chapter III first gives an introduction to a relatively recent two-dimensional (2D) version of ESEEM, the hyperfine sublevel correlation spectroscopy (HYSCORE). In HYSCORE frequencies that originate from the same hyperfine coupling give rise to cross peaks in the spectra, simplifying peak assignments and summarizing the lineshape information of many 1D ESEEM data sets in cross-peak contours. The HYSCORE modulation function for a spin system consisting of an unpaired electron (spin S = 1/2) coupled to a nucleus of spin I = 1 is derived using the density matrix formalism. The function is applied to interpret through simulations experimental HYSCORE data for a deuterium-labeled tyrosyl radical model system.

Chapter I

Basic Principles of the Electron Magnetic Resonance Spectroscopy

I.1. Introduction

Since its discovery by Zavoisky in 1945,[1] Electron Paramagnetic Resonance (EPR) spectroscopy has undergone rapid development. It has established itself as the most versatile method for the investigation of molecules with unpaired electrons. Apart from the highly sensitive detection of paramagnetic species, information on the electron spin state, electronic and spatial structure, and internal dynamics can be obtained from the EPR studies. A great diversity of systems, which range from single crystals containing unpaired electrons to complex biological and polymeric matrices, has proven amenable to study by EPR spectroscopy. However, as the field of application of the conventional EPR spectroscopy has broadened, the limitations of the spectral interpretations have become increasingly apparent. For instance, EPR linewidth changes may occur over the range of rotational correlation times from approximately 1 ns to 1 μs. Hence, EPR is less applicable at regions of much slower or faster molecular motions. Another limitation is associated with significantly overlapped EPR spectra due to the presence of multiple radical species. For paramagnetic species stabilized in disordered solid matrices (polycrystals, glasses, frozen solutions) the resolution of EPR is strongly reduced, owing to inhomogeneous EPR line broadening. However, obtaining information on weak magnetic interaction is necessary to solve structural problems, especially in the

studies of biologically relevant paramagnetic species that are effectively immobilized in proteins. To overcome these limitations various modifications of the method have been developed. Multiple resonance methods, in which the sample is irradiated simultaneously with more than one resonant field, offer the possibility of improving the spectral resolution by introducing additional selection rules. In the electron-nuclear double resonance (ENDOR) technique nuclear magnetic resonance (NMR) quanta are detected in the microwave range (quantum transformation) resulting in a sensitivity enhanced by several orders of magnitude over conventional NMR spectroscopy of radicals. An alternative approach to the traditional CW-EPR experiment is the pulsed EPR spectroscopy, which is primarily based on the electron spin echo (ESE) phenomenon. ESE is a time-domain method, in which the time evolution of the spin system is recorded directly. The electron spin echo envelope modulation (ESEEM) technique of pulsed EPR spectroscopy has emerged as a powerful method for the measurement of electron-nuclear hyperfine couplings that are masked by inhomogeneous broadening of the EPR lineshape.

The numerous theoretical and experimental methods of EPR and their applications are extensively covered in a number of books and reviews.[2-16] In this chapter only a short overview of the basic principles of EPR will be given. The discussion will be confined to organic radical states in accordance with the goal of this Dissertation. Section I.2 gives an overview on the fundamentals of EPR and the types of magnetic interactions of a paramagnetic system. Section I.3 outlines the ENDOR experiment and the resulting ENDOR spectra. Section I.4 describes briefly the electron spin echo phenomenon and introduces the basic ESEEM experiment by means of a semiclassical description as well as a density matrix formalism.

I.2. Continuous-Wave Electron Paramagnetic Resonance

The basic electron spin resonance experiment involves the application of a microwave oscillating magnetic field to invert the electron magnetic moment, along with its associated spin, in an imposed external magnetic field. Molecules or atoms that have unpaired electrons possess electron spin angular momentum, which results in a permanent magnetic dipole moment, μ_e, given by

$$\mu_e = - g_e \mu_B \mathbf{S} \qquad [I\text{-}1]$$

where g_e is the "g-factor", equal to 2.0023 for a completely free electron, μ_B is the Bohr magneton ($\mu_B = e \hbar / (2 m_e c)$, where e is the electron electrical charge, m_e is the electron mass, and c is the speed of light), and **S** is the spin angular momentum of the molecule or atom due to its unpaired electrons. For a species with a single unpaired electron, S = 1/2. According to the classical electrodynamics, a torque $\mu_e \times \mathbf{B}_0$ will be exerted on the spin in the presence of an external magnetic field $\mathbf{B}_0$. It causes the spin to have preferred orientation in the field, precessing around the magnetic field axis at the classical Larmor frequency $\omega_0 = g_e \mu_B |\mathbf{B}_0|$. The energy of this interaction is $E = - \mu_e \cdot \mathbf{B}_0$.

I.2.1. The Zeeman interaction

The quantum mechanical approach to the electron motion is more relevant than the classical theory. For a quantum mechanical system the interaction energy with the

external magnetic field is quantized. There will be (2 S + 1) states associated with different energies and spin orientations. For example, an S = 1/2 species placed in an external magnetic field will have two possible energy configurations and two possible orientations of the electron spin - antiparallel and parallel to the external magnetic field. The quantization of the electron spin angular momentum in an external magnetic field is described by the Zeeman Hamiltonian given by

$$\mathcal{H}_{e,Zeeman} = g_e \mu_B \mathbf{B}_0 \cdot \mathbf{S}. \qquad [I\text{-}2]$$

A number of other interactions between the unpaired electrons and their environment may exist. These include the interaction of the unpaired electrons with magnetic nuclei, the interaction among the unpaired electrons, and the coupling between the spin and orbital motion of the unpaired electron. The spin-orbit coupling is described by the Hamiltonian $\mathcal{H}_{s\text{-}o} = - \lambda \mathbf{L} \cdot \mathbf{S}$, where $\mathbf{L}$ is the orbital angular momentum and λ is the spin-orbit constant for a particular shell in a particular atom. Normally a vector coupling approach is used to compound the spin and orbital angular momenta into a resultant moment. This corresponds to combining $\mathcal{H}_{e,Zeeman}$ and $\mathcal{H}_{s\text{-}o}$ and introducing an effective spin. As a result, the effects of spin-orbit coupling are incorporated into a g-tensor. The combined Hamiltonian is given by

$$\mathcal{H}_{e,Zeeman} = \mu_B \mathbf{B}_0 \cdot \mathbf{g} \cdot \mathbf{S}, \qquad [I\text{-}3]$$

where **g** is, in general, anisotropic and different from g_e for a free electron. However, for randomly oriented organic free radicals such as those that are subject of this study the g-tensor is isotropic and the deviations from g_e are small, usually by less than 1%. With a scalar g and an external magnetic field along the z axis ($\mathbf{B}_0 = [0, 0, B_0]$) the Zeeman Hamiltonian reduces to $\mathcal{H}_{e,Zeeman} = g\,\mu_B\,B_0\,S_z$. The two eigenstates of this Hamiltonian in the case of a S = 1/2 system are characterized by the magnetic quantum number M_S having values of -1/2 (state $|\beta>$) and +1/2 (state $|\alpha>$). Physically, the two states correspond to different alignment of the magnetic moment with respect to the external magnetic field. The magnetization is parallel to the field direction in state $|\alpha>$, and antiparallel with respect to the field in state $|\beta>$. The two eigenvalues are given by

$$E_\alpha = g\,\mu_B\,B_0/2, \qquad \text{[I-4a]}$$

$$E_\beta = -\,g\,\mu_B\,B_0/2, \qquad \text{[I-4b]}$$

the energy splitting between the two levels being $\Delta E = g\,\mu_B\,B_0$, Figure I-1. EPR transitions between the two energy states are induced by applying a uniform, linearly polarized microwave radiation to the sample and the change in the power of the microwave radiation returning from the sample to the detector is measured. At resonance, the splitting between the energy levels equals the energy of the incident microwave radiation:

$$g\,\mu_B\,B_0 = \hbar\,\omega_0. \qquad \text{[I-5]}$$

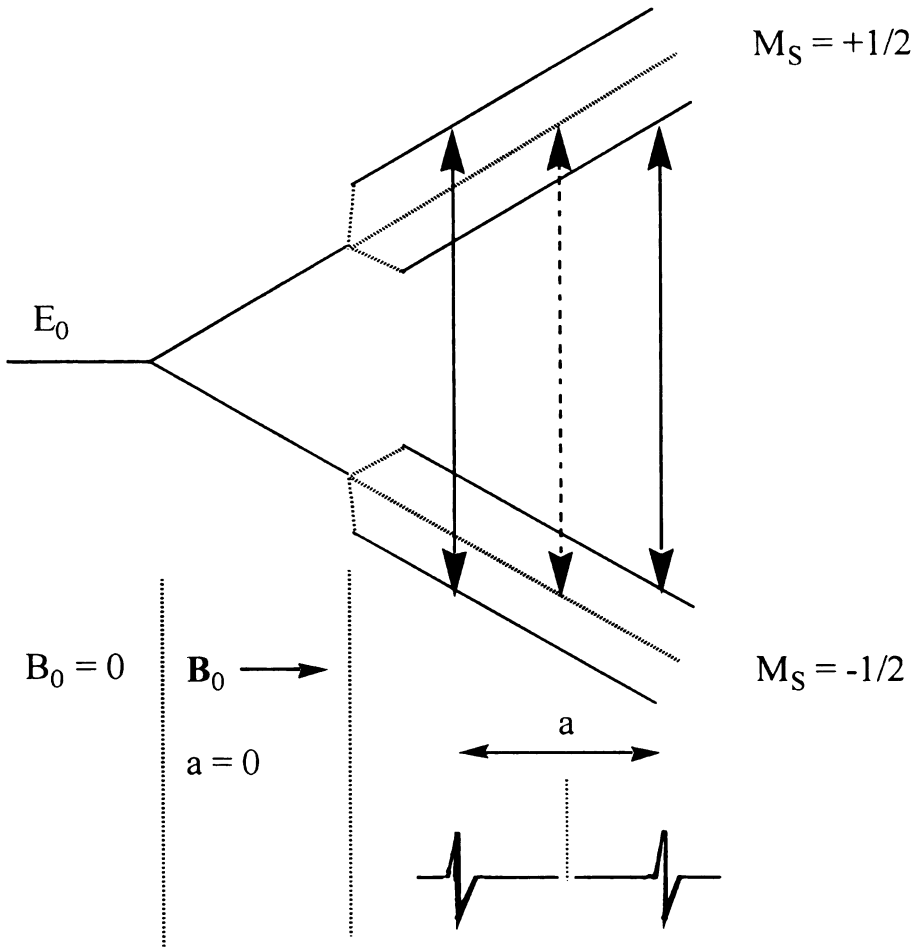

Figure I-1: Energy levels of a spin system consisting of one unpaired electron (S = 1/2) and one magnetic nucleus with I = 1/2 as a function of an externally imposed magnetic field. When hyperfine interaction (cf. Section I.2.2.) is present (characterized by the isotropic hyperfine constant *a*), each of the two energy levels is split into two sublevels, which results in two EPR lines separated by *a*.

In an EPR experiment, the sample is irradiated at a fixed microwave frequency, while the magnetic field is swept to adjust the energy level splitting to the energy of the electromagnetic quantum. For paramagnetic species with g = 2.0 and with microwave frequency 9. GHz, the resonance occurs at field strength

$$B_0 = \hbar \omega_0/(g \mu_B) = 3215 \text{ G.} \qquad [I\text{-}6]$$

When the sample is in thermal equilibrium with its environment in the EPR spectrometer, the number of the α spins, N_α, relative to the number of the β spins, N_β, is given by the Boltzmann factor,

$$N_\alpha/N_\beta = \exp[-\Delta E/(k_B T)], \qquad [I\text{-}7]$$

where k_B is the Boltzmann's constant and T is the sample temperature. At 298 K this ratio equals 0.9986; i. e., for every 10000 molecules in state $|\beta>$ there will be 9986 molecules in state $|\alpha>$. Because of this population difference net absorption of microwave power will be detected. The ratio decreases with decreasing the temperature. For example, it becomes 0.8976 at 4 K meaning that the resolution is expected to improve upon lowering the temperature from 298 K to 4 K.

I.2.2. The hyperfine interaction

An important feature of the EPR spectra is their hyperfine structure. It arises from the magnetic interaction between the electron spin and the magnetic dipole moments of

surrounding nuclei. A nucleus with an uneven number of protons or an uneven number of neutrons has spin I, associated with a magnetic moment $\mu_n = \gamma \mathbf{I}$, where γ is the magnetogyric ratio for the isotope. (By analogy with the electron magnetic moment, the nuclear magnetic moment is expressed sometimes as $\mu_n = g_n \mu_{B,n} \mathbf{I}$, where g_n is the nuclear g factor and $\mu_{B,n}$ is the nuclear Bohr magneton.) Subsequently, a magnetic nucleus located in the vicinity of the unpaired electron generates a local magnetic field, B_{local}, that can add to or subtract from the applied external field. Thus, the total field the electron experiences is $B = B_0 + B_{local}$, and the EPR condition is

$$g \mu_B (B_0 + B_{local}) = \hbar \omega_0. \qquad [I\text{-}8]$$

It is evident that the value of the external field necessary to achieve resonance will depend on B_{local}. The nuclear spin is quantized in the total magnetic field composed of the external field $\mathbf{B}_0$ and the field due to the electron, yielding (2 I + 1) distinct nuclear spin states. (Figure I-1 shows the situation for I = 1/2). Each of the (2I + 1) nuclear spin states will generate a different B_{local} magnetic field. Consequently, there will be (2I + 1) different B_0 values which will satisfy the EPR condition resulting in (2 I + 1) lines in the EPR spectrum. These lines will have equal intensity as the nuclear spin states are almost equally populated. For example, the hyperfine interaction of the electron with a single ^1H nucleus (I = 1/2) results in two EPR lines because half of the paramagnetic species will have their proton spin aligned with the external field (magnetic quantum number $M_I = +1/2$) while the other half will have spin antiparallel to the external magnetic field

(magnetic quantum number $M_I = - 1/2$). Therefore, half of the paramagnets in the sample ($M_I = + 1/2$) will resonate at applied field strength

$$B_0 = \hbar \omega_0/(g \mu_B) - a/2, \qquad \text{[I-8a]}$$

while the other half ($M_I = - 1/2$) will resonate when

$$B_0 = \hbar \omega_0/(g \mu_B) + a/2. \qquad \text{[I-8b]}$$

In the above expressions a is the hyperfine coupling constant. It should be noted that these resonance conditions are valid only when $a << \hbar \omega_0/(g \mu_B)$, since they do not account for the nuclear Zeeman interaction.

From the physical point of view the origin of the hyperfine interaction in the hydrogen atom is the non-zero 1s electron density at the nucleus. In general, the electrons in s-orbitals have a non-zero probability density at the nucleus and can give rise to hyperfine interaction. This hyperfine interaction is *isotropic* because of the spherical symmetry of s-orbitals. Fermi has shown that the energy of the isotropic hyperfine interaction (also referred to as an instance of Fermi contact interaction) is given by

$$\mathcal{H}_{iso} = - (2/3) \mu_0 |\psi(0)|^2 \mu_{e,z} \mu_{n,z}, \qquad \text{[I-9]}$$

where μ_0 is the permeability of vacuum and $|\psi(0)|^2$ is the electron probability distribution over a spherical volume. Using the operator relations between the magnetic moment and the spin angular momentum (cf. Equation I-1), one obtains the result

$$\mathcal{H}_{iso} = A_{iso}\, S_z\, I_z, \qquad \text{[I-10]}$$

where A_{iso} is the isotropic hyperfine coupling constant given by

$$A_{iso} = (2/3)\, \mu_0\, g\, \mu_B\, \gamma\, |\psi(0)|^2. \qquad \text{[I-11]}$$

In more general form (used with an arbitrary external field $\mathbf{B}_0$),

$$\mathcal{H}_{iso} = A_{iso}\, \mathbf{S}\cdot\mathbf{I} \ . \qquad \text{[I-12]}$$

A_{iso} is the hyperfine coupling constant expressed in frequency units (i. e., A_{iso}/h). It is related to the constant a, given in magnetic-field units, as $a = A_{iso}/(g\, \mu_B)$.

Electron-nuclear magnetic interaction can also be due to magnetic interaction between the magnetic dipoles of the electron and the nearby nucleus. This interaction arises when the electron resides on a orbital with orbital quantum number $l > 0$, which has non-spherical symmetry. Since the electron probability distribution is zero at the nucleus no Fermi contact interaction is possible. Hence, this hyperfine interaction is

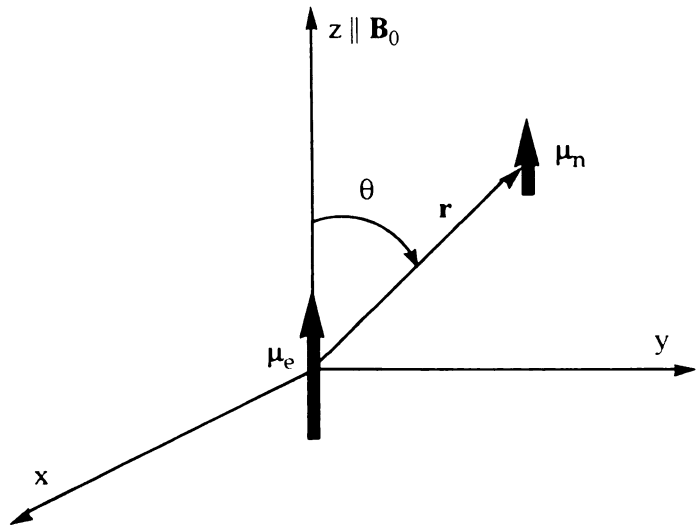

Figure I-2: Interaction of magnetic dipoles μ_e and μ_n arising from an electron spin and a nuclear spin, respectively. The dipoles are aligned with the external magnetic field and are separated by a distance r. Angle θ is between the inter-dipole vector **r** and the applied field $\mathbf{B}_0$.

anisotropic, Figure I-2. According to the electromagnetic theory, the magnetic field at the nucleus due to the electron dipole moment μ_e at distance r is

$$\mathbf{B}_e = - (\mu_0 / 4\pi) \nabla(\mu_e \cdot \mathbf{r}) / r^3 = (\mu_0 / 4\pi) \{ - \mu_e / r^3 + 3 (\mu_e \cdot \mathbf{r}) \mathbf{r} / r^5 \}. \qquad [I\text{-}13]$$

The energy of the nuclear magnetic dipole in this field is

$$\mathcal{H}_{aniso} = - \mu_n \cdot \mathbf{B}_e = - (\mu_0 / 4\pi) \{ - (\mu_e \cdot \mu_n) / r^3 + 3 (\mu_e \cdot \mathbf{r}) (\mu_n \cdot \mathbf{r}) / r^5 \}. \qquad [I\text{-}14]$$

By replacing the magnetic moments with the appropriate operators one can obtain the following expression for $\mathcal{H}_{aniso}$:

$$\mathcal{H}_{aniso} = - (\mu_0 / 4\pi) g \mu_B \gamma \{(\mathbf{I} \cdot \mathbf{S}) / r^3 + 3 (\mathbf{S} \cdot \mathbf{r}) (\mathbf{I} \cdot \mathbf{r}) / r^5\}. \qquad [I\text{-}15]$$

After expanding the vectors and averaging over the electron spatial variables, the above spin Hamiltonian can be rewritten in a matrix form:

$$\mathcal{H}_{aniso} = - (\mu_0/4\pi) g \mu_B \gamma \times$$

$$\begin{bmatrix} S_x & S_y & S_z \end{bmatrix} \begin{bmatrix} \left\langle r^2 - 3x^2/r^5 \right\rangle & \left\langle -3\,x\,y/r^5 \right\rangle & \left\langle -3\,x\,z/r^5 \right\rangle \\ \left\langle -3\,x\,y/r^5 \right\rangle & \left\langle r^2 - 3y^2/r^5 \right\rangle & \left\langle -3\,y\,z/r^5 \right\rangle \\ \left\langle -3\,x\,z/r^5 \right\rangle & \left\langle -3\,y\,z/r^5 \right\rangle & \left\langle r^2 - 3z^2/r^5 \right\rangle \end{bmatrix} \begin{bmatrix} I_x \\ I_y \\ I_z \end{bmatrix} =$$

$$= \mathbf{S}^t \cdot \mathbf{T} \cdot \mathbf{I}. \qquad [I\text{-}16]$$

(The angular brackets in the above expression imply that integration over the electron space distribution has been performed.) The matrix **T** is symmetric about its diagonal and traceless. The isotropic and anisotropic hyperfine coupling can be combined to yield one matrix, **A**,

$$\mathbf{A} = A_{iso} \mathbf{1} + \mathbf{T}, \qquad [I\text{-}17]$$

whose trace is $Tr\{\mathbf{A}\} = 3\ A_{iso}$. In liquids of low viscosity the anisotropic component of the hyperfine interaction is time-averaged to zero. However, in more rigid systems such as crystals, it may be the dominant component of the hyperfine interaction. When the crystal is rotated (i. e., the unit vector $\mathbf{n}$ along $\mathbf{B}_0$ is changed) the value of $\mathbf{n}^t \cdot \mathbf{A} \cdot \mathbf{n}$ changes. Since $\mathbf{A}$ is symmetrical it can always be cast into diagonal form by a suitable choice of axes. Single crystal EPR measurements yield $\mathbf{A}$ which can then be separated into its two components. The anisotropic portion of the hyperfine interaction provides geometric information and is related to the symmetry of the paramagnetic species. The isotropic part reports on the unpaired electron spin density and is related to the nature of the molecular wavefunctions.

The observed isotropic nuclear magnetic couplings arise from unpaired spin density in atomic orbitals centered on the coupling nucleus. If the isotropic hyperfine coupling comes from a particular atomic orbital of the coupling atom in the radical, the unpaired spin density of that atomic orbital can be obtained from the ratio of the measured coupling parameter to that for the corresponding orbital for the free atom. This is the case of hydrogen hyperfine coupling in σ-type organic radicals, in which the unpaired electron is primarily located in the σ orbital that would normally form a chemical bond. The σ orbitals have in principle a considerable s-atomic orbital component. The extensive s-unpaired spin density at the hydrogen gives rise to hyperfine coupling constants of large magnitudes (150 - 400 MHz) and positive sign. For instance, the measured isotropic proton hyperfine constant in the formyl radical, H·CO, is 384 MHz,[17] which, together with the experimental value of 1420 MHz for the coupling in the hydrogen atom, yields a unpaired electron spin population in the hydrogen 1s orbital

equal to 0.27. This value implies that the resonance structure [H·+:CO] corresponding to an excited state has a significant contribution to the overall electronic structure of the radical. The participation of this structure produces a positive spin density on the 1s orbital of the hydrogen atom by direct transfer of the unpaired electron. It should be noted that along with its large isotropic component the hyperfine interaction in σ-type radicals may also exhibit a large anisotropy.

There exist indirect coupling mechanisms that result in significant isotropic hyperfine coupling of the unpaired electron located in particular molecular orbital with nuclei situated in the node of the orbital, where the isotropic hyperfine coupling should be identically zero. Isotropic hyperfine coupling can originate from the phenomenon of *spin polarization of covalent chemical bonds*. For example, the proton coupling in a $C_\alpha H$ fragment of a π -type free organic radical, in which the unpaired electron occupies a π molecular orbital (constructed as a linear combination of carbon $2p_z$ atomic orbitals), has a large isotropic component. This evidences the presence of some induced unpaired electron density on the proton. According to Hund's rule for an atom, the state of highest spin multiplicity has the lowest energy. This is due to the favorable exchange interaction between two electrons with parallel spins located in different orbitals of the same atom. Thus, because of the exchange interaction, an α spin unpaired electron located in the $2p_z$ orbital of C_α will constrain the C_α electron participating in the σ bond to an α spin state, Figure I-3. Consequently, the generated positive spin density at the carbon will induce negative electron spin density (i. e., excess of β spin over α spin) at the proton (relative to the p_π spin density on C_α) since the electrons participating in a covalent bond must be of opposite spin. The negative spin density induced on the proton gives rise to negative

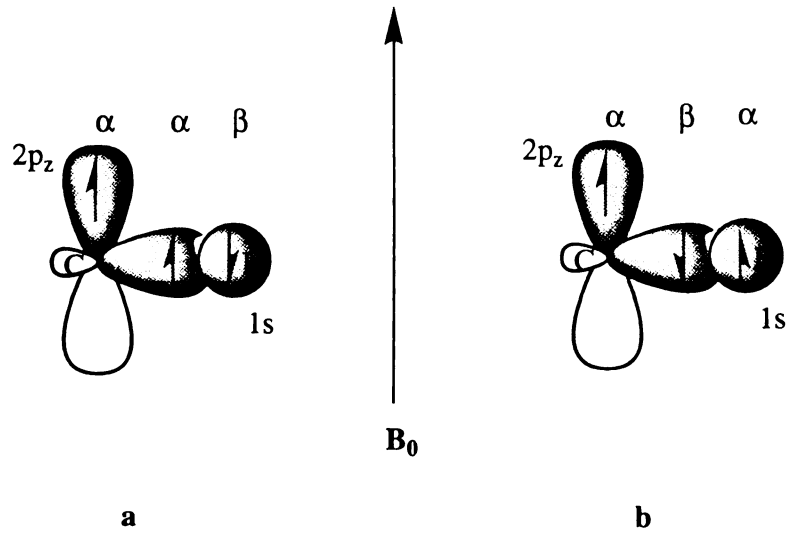

Figure I-3: Valence bond structures for the C_α-H fragment. The two possible electron spin configurations in the s bonding orbital are shown for a spin in the $2p_\pi$ orbital of the carbon atom. (a) Spins parallel in the s bonding orbital and the $2p_\pi$ orbital of carbon. (b) Corresponding spins antiparallel.

hyperfine coupling constants for α protons. For planar conjugated organic radicals, there exists a linear correspondence between the isotropic proton hyperfine parameter A_{iso}^H and the unpaired π electron population $\rho_\pi^{C\alpha}$ of the adjacent carbon $2p_z$ orbital that contributes to the π system. It is given by the well known McConnell relation:[18]

$$A_{iso}^{H} = Q^{\alpha}_{CH}\, \rho_{\pi}^{C\alpha}\,, \qquad [I\text{-}18]$$

where Q^{α}_{CH}, $Q^{\alpha}_{CH} < 0$, is an experimentally obtained proportionality constant. This relation holds remarkably well for a wide range of neutral π radicals and is applicable to nuclei other than protons.

The anisotropic component of the proton hyperfine coupling for an $C_{\alpha}H$ fragment is of magnitude comparable to the isotropic component. It is due to the dipole-dipole interaction of the proton magnetic moment with ρ_{π}^{C} spin density on the α carbon. The principal elements of the hyperfine tensor **A** are commonly found to be along the axis of a coordinate system defined, as shown in Figure I-4, by the p_{π} orbital (i. .e. the $2p_z$ orbital of C_{α}) as the x axis, the $C_{\alpha}H$ bond as the z axis, and the $\mathbf{z} \times \mathbf{x}$ cross product as the y axis.

Another effective model for the hyperfine coupling mechanism is *hyperconjugation*. It can account for the EPR observed splittings from protons in the alkyl groups of alkyl-substituted π-type radicals. Hyperconjugation can occur when two fragments of a molecule interact provided there is a compatibility in the symmetry properties and energies of their wavefunctions. For example, the admixture of valence bond structures as those shown in Figure I-5 (a) for the ethyl radical equalizes the magnetic couplings of all five hydrogens. Both the molecular-orbital theory and the valence bond theory predict that the spin density on the β hydrogens is positive as opposed to that on the α hydrogens. Similarly to α proton hyperfine coupling, the isotropic β proton coupling is proportional to the π spin density on the α carbon to which

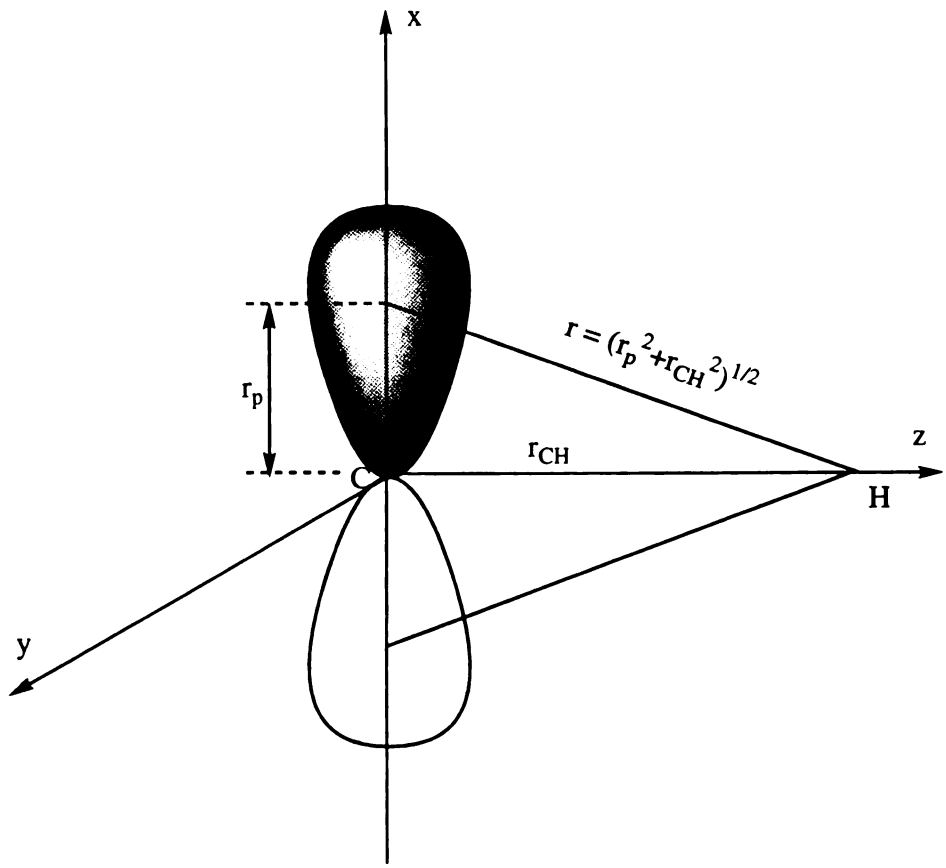

Figure I-4: Model used for calculation of the dipole-dipole magnetic coupling or unpaired p_π electron density on C_α carbon atom with the nucleus of a hydrogen atom. The spin density is concentrated equally at effective centers of the p_π orbital lobes on either side of C_α. r_p is the distance from the effective coupling centers to C_α nucleus. r_{CH} is the internuclear distance of C and H.

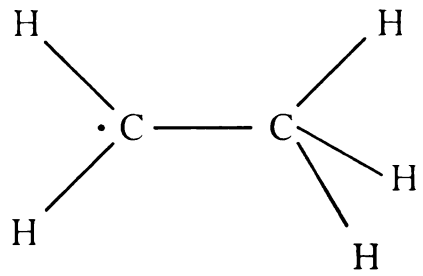

1

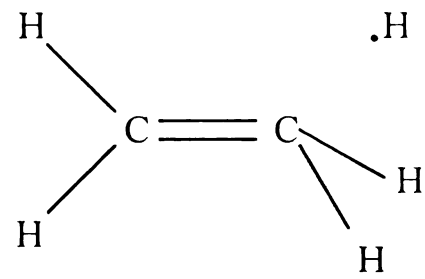

2

a

Figure I-5: (a) Hyperconjugation in ethyl radical. The admixture of the two exemplary valence bond structures can account for the significant isotropic hyperfine coupling for β hydrogens in aliphatic radicals. (b) Coordinate system for β coupling of hydrogens.

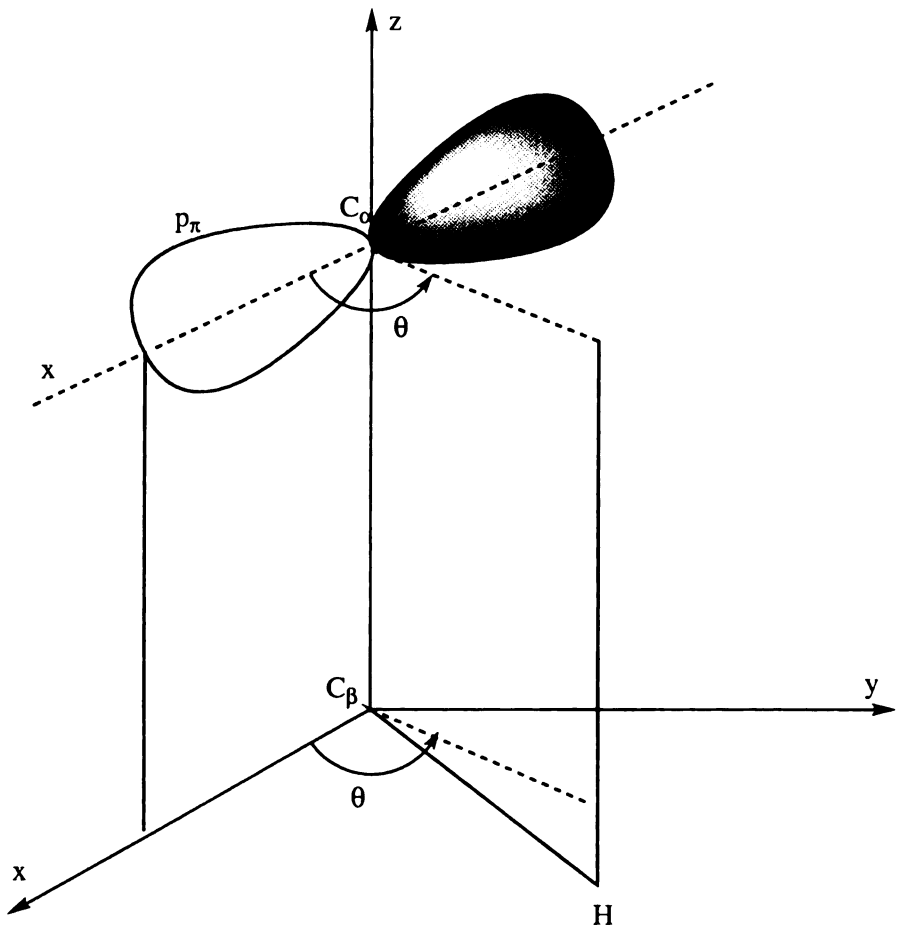

b

Figure I-5 (b)

the magnetically coupled proton is attached:[19]

$$A_{iso}^{H\beta} = Q^{\beta}_{CH}(\theta)\, \rho_{\pi}^{C\alpha} . \qquad [I\text{-}19]$$

In this case, however, the magnitude of the coupling will depend on the orientation of the $C_\beta H$ bond with respect to the $2p_\pi$ orbital of the C_α carbon atom where the unpaired electron is located. This orientation is given by the dihedral angle θ between the plane defined by atoms C_α, C_β, and H, and the plane containing the both the $2p_z$ orbital of the C_α carbon and the $C_\alpha C_\beta$ bond, Figure I-5 (b). The function $Q^{\beta}_{CH}(\theta)$ has the form

$$Q^{\beta}_{CH}(\theta) = Q^{\beta}_{0} + Q^{\beta}_{2} \cos^2(\theta) , \qquad [I\text{-}20]$$

where $Q^{\beta}_{0} << Q^{\beta}_{2}$. The typical values reported in the literature are 8-9 MHz for (Q^{β}_{0} $\rho_{\pi}^{C\alpha}$) and 122-125 MHz for (Q^{β}_{2} $\rho_{\pi}^{C\alpha}$).[5] The orientationally independent term in the above expression has been viewed as arising either from torsional oscillations around the $C_\alpha C_\beta$ bond or from direct or consecutive spin polarization involving both $C_\alpha C_\beta$ and $C_\beta H$ bonds. The second term is associated with hyperconjugation.

If there is free internal rotation about the $C_\alpha C_\beta$ bond then the isotropic hyperfine coupling is orientationally averaged. Since $\langle\cos^2\theta\rangle = 1/2$, $Q^{\beta}_{CH,rot} = Q^{\beta}_{0} + 1/2\, Q^{\beta}_{2}$, and

$$A_{iso}^{H\beta} = Q^{\beta}_{CH,rot}\, \rho_{\pi}^{C\alpha} \cong 1/2\, Q_2^{\beta} \rho_{\pi}^{C\alpha} \qquad [I\text{-}21]$$

The last equation is used to derive experimental values for Q^{β}_{CH} by measuring the β methyl proton couplings from spectra of radicals in solutions. For alkyl radicals $Q^{\beta}_{CH,rot}$ = 164 MHz.[5)]

Superimposed on the isotropic β proton coupling in π-type radicals is a much smaller (ca. 10% of the value of the isotropic component) anisotropic component arising primarily from the direct magnetic dipole-dipole interaction of the β protons with the π spin density of C_{α} atom. To a great extent, the anisotropic coupling tensor for β protons has axial symmetry. From the principal values of the dipolar hyperfine tensor, the dipolar field generated by the unpaired electron spin density on C_{α} can be obtained and the C_{α}-H distance can be calculated in the dipolar approximation:

$$(A_{\parallel} - A_{\perp}) / 3 = T = \rho_{\pi}^{C\alpha}\, g\, \mu_B\, g_n\, \mu_{B,n}/r^3 . \qquad [I\text{-}22]$$

The hyperconjugation model of hyperfine coupling of β protons can be extended to γ protons. Unlike the β proton splittings that are generally about the same magnitude (or even larger) as the splittings for an α proton replacing the substituent to C_{α}, the hyperfine couplings arising from γ protons are up to two orders of magnitude smaller. For example, the γ proton isotropic hyperfine coupling constant in the acetoxyl radical ($CH_3COO\cdot$) equals 4.8 MHz.[20)]

I.2.3. The nuclear quadrupole interaction

Nuclei with nuclear spin $I \geq 1$ can have a non-spherical charge distribution resulting in a quadrupole moment that is collinear with the magnetic moment, Figure I-6. The quadrupole moment can interact with an inhomogeneous electric field adopting a preferred orientation in the field. The electric field gradient is determined by the electronic structure of the paramagnetic species, reflecting non-uniformities in the surrounding electron density. Hence, measuring the quadrupole parameters can yield structural information. The nuclear spin (through its associated magnetic moment) is quantized along the axis of the effective magnetic field generated by the spectrometer and the nearby unpaired electrons. The effect of this magnetic interaction is modified by the quadrupole interaction since the quadrupole moment acts to orient the nucleus in the direction of the largest electric field gradient. Consequently, the competition between the effects of the magnetic moment and the quadrupole moment can manifest itself in the result of the EPR experiments. Due to the collinearity of the axes of the nuclear quadrupole moment and the nuclear spin angular momentum, the Hamiltonian for the quadrupole interaction can be expressed in terms of the nuclear spin,

$$\mathcal{H}_{NQI} = K\,[3\,I_z^2 - I^2 + \eta\,(I_x^2 - I_y^2)], \qquad [I\text{-}23]$$

where K is the quadrupole coupling constant, $K = e^2qQ/[4\,h\,I\,(2I\text{-}1)]$, η is the asymmetry parameter defined through the principal values V_{ii} of the electric field gradient tensor, $\eta = |V_{xx} - V_{yy}|/V_{zz}$. The eigenvalues of this Hamiltonian are $E_{\pm} = -K\,(1 \pm \eta)$, $E_0 = 2K$,

which yields the frequencies $\nu_+ = K (3 + \eta)$, $\nu_- = K (3 - \eta)$, $\nu_0 = 2 K \eta$. $\mathcal{H}_{NQI}$ is frequently written as $\mathcal{H}_{NQI} = \mathbf{I}\cdot\mathbf{Q}\cdot\mathbf{I}$, in terms of the traceless tensor **Q** whose elements are $Q_{ij} = V_{ij}\, eQ / [2I (2I - 1)]$, where eQ is the quadrupole moment.

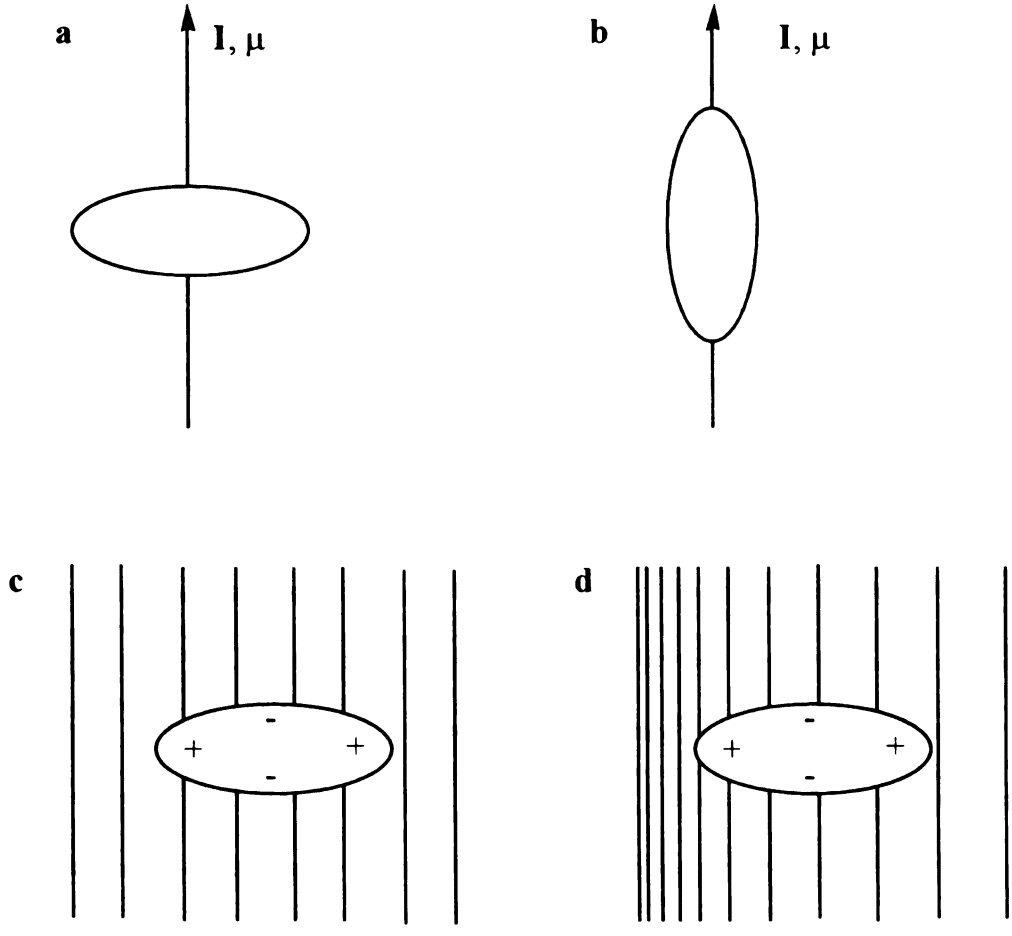

Figure I-6: Quadrupolar nuclei (a) oblate, (b) prolate. An oblate quadrupolar nucleus in (c) a uniform electric field, (d) an effective field gradient.

The nuclear quadrupole frequencies can be directly observed in ESEEM (or ENDOR) under conditions of "exact cancellation". In the case of an S = 1/2, I = 1 system, if the isotropic hyperfine constant equals twice the nuclear Larmor frequency the energy levels in one spin manifold collapse, which results in appearance of pure quadrupole frequencies, ν_+, ν_-, and ν_0.

The general spin hamiltonian which describes the EPR spectra (as well as other magnetic resonance spectra, e. g., ENDOR or ESEEM) is composed of electron Zeeman, nuclear Zeeman, nuclear hyperfine and quadrupolar effects, as well as other interactions not considered above, e. g., electron-electron dipolar and exchange interactions:

$$\mathcal{H} = \mathcal{H}_{e,Zeeman} + \mathcal{H}_{n,Zeeman} + \mathcal{H}_{HFC} + \mathcal{H}_{NQI} + \ldots \qquad [I\text{-}24]$$

In principle, these interactions can all occur simultaneously for a given paramagnetic species. The observed positions and relative intensities of the lines can, in general, be obtained from this Hamiltonian by numerical diagonalization and spectral simulations rather than by finding analytic solutions for energies and transition probabilities. However, analyses for many systems can be obtained using analytical results derived for various limiting cases. These limiting cases are determined by the relative magnitudes of the different interactions and their anisotropies. Thus, for the majority of organic radicals the anisotropy of **g** is not important. Since the nuclear Zeeman energy is always weak compared to the electron Zeeman interaction and typically weaker than the hyperfine term, the nuclear Zeeman term can often be omitted. In many cases, it is possible to treat

the hyperfine interaction as perturbation, provided the magnitude of the electron Zeeman interaction is predominant.

Analysis of the EPR spectra allow extracting the tensor elements for the various interactions, the most precise information being obtained from measurements on single crystals. However, such measurements are only possible for a limited number of substances. The materials of biological interest are normally not found in a single-crystal form and, in most cases, the preparation of single crystals containing biologically important radicals is difficult. The EPR of samples in the form of polycrystals, glasses, powders, or frozen solutions yields "powder" type spectra. These spectra are the sums of the EPR spectra of the individual, randomly oriented paramagnetic species for all possible orientations. Hence, the analysis of the powder spectra is more complex. Moreover, for paramagnetic species stabilized in disordered solid matrices, the resolution of EPR is reduced to a few gauss, owing to inhomogeneous spectral broadening caused by the presence of multiple, small hyperfine couplings. In these cases no hyperfine information is obtainable, if the splittings are narrower than the inhomogeneous spectral width (usually tens to hundreds of gauss).

Various modifications of the EPR spectroscopy have been developed, which allow resolving weak hyperfine couplings in disordered systems of the order of a few Hertz. Two of the most widely used methods are the Electron Nuclear Double Resonance (ENDOR) and the Electron Spin Echo Envelope Modulation (ESEEM) spectroscopy. These techniques not only yield the weak couplings but have the advantage of reducing the number of peaks and decreasing the linewidths associated with the various transitions.

In the following two Sections, the principles of these methods will be introduced and their applicability, advantages and limitations will be briefly discussed.

I.3. Principles of Electron Nuclear Double Resonance (ENDOR) Spectroscopy

Electron Nuclear Double Resonance (ENDOR) spectroscopy is the most widely used technique for measuring weak nuclear hyperfine and quadrupole couplings in disordered systems of paramagnetic species.[10-12,21] ENDOR yields the NMR spectrum of the paramagnetic system by detecting the change in the amplitude of the saturated EPR signal upon sweeping the frequency of an additional radiofrequency field. Because hyperfine couplings on the order of a few kiloHertz can be resolved, ENDOR inherently provides much higher resolution than the conventional EPR spectroscopy. This section presents a phenomenological introduction to ENDOR spectroscopy.

I.3.1. Energy levels and resonance conditions

The spin Hamiltonian describing the interaction of one electron (spin quantum number. S = 1/2) with a number of nuclei each of spin $\mathbf{I}_i$ in an external magnetic field $\mathbf{B}_0$ is composed of electron Zeeman, nuclear Zeeman, hyperfine, and quadrupole interactions (if nuclei of spin I > 1/2 are present):

$$\mathcal{H} = \mu_B \mathbf{B}_0 \cdot \mathbf{g} \cdot \mathbf{S} - \sum_i g_{n,i} \mu_{B,n} \mathbf{B}_0 \cdot \mathbf{I}_i + h \sum_i \mathbf{S} \cdot \mathbf{A}_i \cdot \mathbf{I}_i + h \sum_i \mathbf{I}_i \cdot \mathbf{Q}_i \cdot \mathbf{I}_i \qquad [I\text{-}25]$$

where $\mathbf{g}$, $\mathbf{A}_i$ and $\mathbf{Q}_i$ denote the electronic g, hyperfine, and nuclear quadrupole coupling tensors, respectively, μ_B and $\mu_{B,n}$ are the electronic and nuclear Bohr magnetons, respectively, $g_{n,i}$ is the nuclear g factor for nucleus i, and h is Planck's constant. The eigenfrequencies of this Hamiltonian can be easily obtained in the simple case of a single nucleus of spin I = 1/2 (e. g., a proton) interacting with the electron. In the high-field approximation, in which $\mathbf{S}$ and $\mathbf{I}$ are quantized along the external field $\mathbf{B}_0$, and with the assumption of all interactions being isotropic these are given by

$$E(M_S, M_I)/h = \nu_e M_S - \nu_n M_I + A_{iso} M_S M_I , \qquad [I\text{-}26]$$

where

$$\nu_e = g \mu_B B_0/h, \qquad [I\text{-}27]$$

$$\nu_n = g_n \mu_{B,n} B_0/h, \qquad [I\text{-}28]$$

are the free electron and free nuclear frequencies (related to the Zeeman energies) and M_S and M_I are the electron spin and nuclear spin projections. The corresponding eigenvectors are simple product functions $|M_S, M_I>$. This leads to the energy level diagram shown in Figure I-7. Two EPR transitions, 1<->2 and 3<->4, are obtained by applying the selection rules for electron spin transitions,

$$\Delta M_S = \pm 1, \quad \Delta M_I = 0. \qquad [I\text{-}29]$$

The corresponding resonance frequencies are

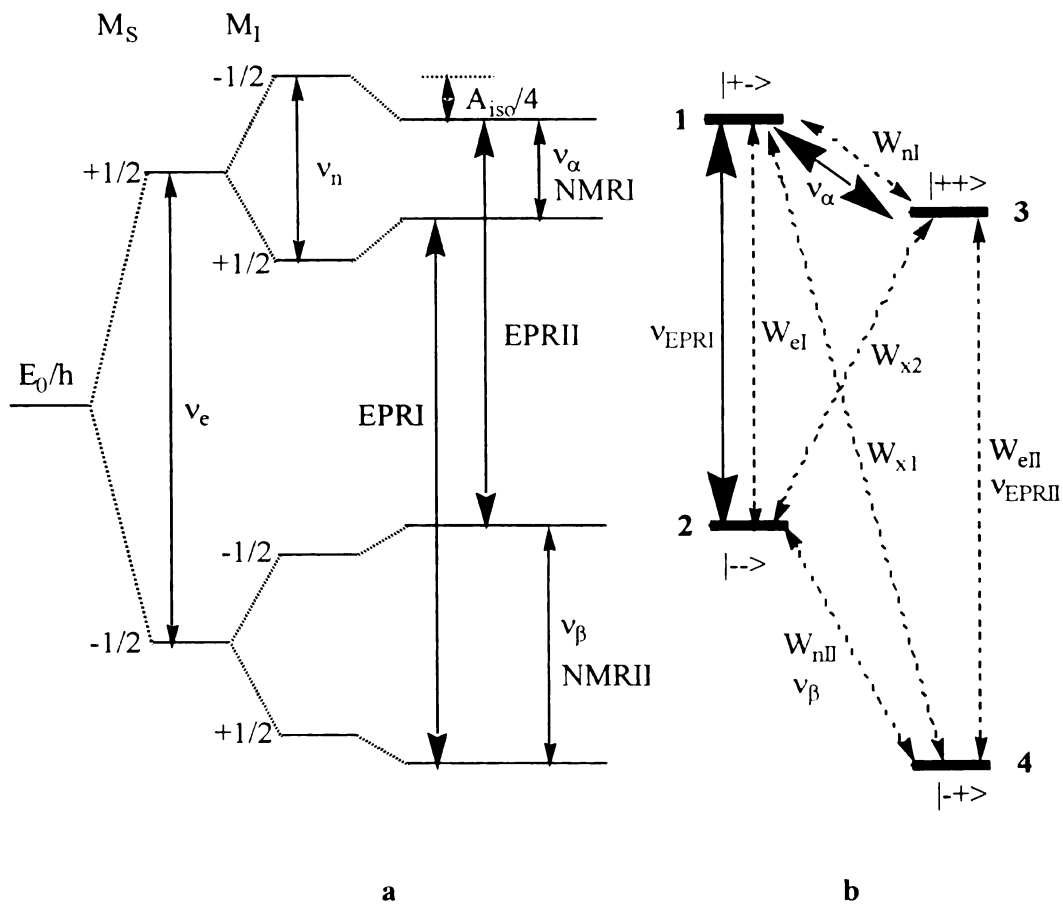

Figure I-7: Energy-level diagram in a high magnetic field for the interaction of one unpaired electron (S = 1/2) with an I = 1/2 nucleus (e. g. a proton), detailing the electron Zeeman, nuclear Zeeman, and hyperfine splittings. The case of $g_n > 0$, $A_{iso} > 0$, $|A_{iso}/2| < \nu_n$ is represented. The four energy levels on the right (1 to 4) are labeled by $|M_S, M_I>$. The heavy arrows indicate the induced EPR and NMR transitions; the broken arrows the various relaxation rates. (After Ref. 12)

$$\nu_{EPR} = \nu_e \pm A_{iso}/2. \qquad [I\text{-}30]$$

The application of the NMR selection rules

$$\Delta M_I = \pm 1, \qquad \Delta M_S = 0, \qquad [I\text{-}31]$$

yields two NMR transitions, 1<->3 and 2<->4, at the frequencies:

$$\nu_{NMR} = |\nu_n \pm A_{iso}/2|. \qquad [I\text{-}32]$$

These NMR transitions are detected in ENDOR via intensity change of a simultaneously irradiated EPR transition.

If $\nu_n > |A_{iso}/2|$, Figure I-8, the two ENDOR lines are equally spaced about the free nuclear frequency ν_n and separated by the hyperfine constant $|A_{iso}|$. If $\nu_n < |A_{iso}/2|$, the lines are centered around $|A_{iso}/2|$ and their separation is $2\nu_n$. For the hypothetical case $\nu_n = |A_{iso}/2|$ only one signal would be detected.

From Equation I-32 it follows that both the hyperfine constants and the free nuclear frequencies are obtainable from an ENDOR experiment. Nuclei can be identified from ν_n using tabulated nuclear g factors. The ENDOR data can be used to assign a certain hyperfine constant to a specific nucleus. The hyperfine constants can also be measured from the EPR spectra. However, the EPR spectra involving contributions from different sets of equivalent protons coupled to the unpaired electron can become too

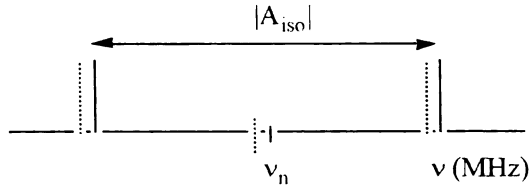

a

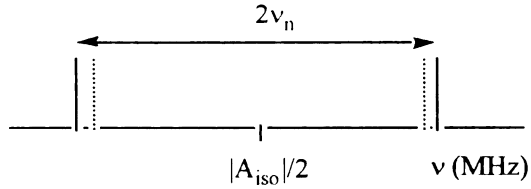

b

Figure I-8: ENDOR spectra for (a) $|A_{iso}/2| < \nu_n$ and (b) $|A_{iso}/2| > \nu_n$. The solid lines represent the spectrum observed when the high field EPR transition is monitored and the dashed lines give the spectrum observed when the low field EPR line is monitored. (After Ref. 2)

complex for an ambiguous interpretation. The resolution enhancement and reduced complexity of the ENDOR spectra is demonstrated in Figure I-9, which represents the energy level diagram for a hyperfine-coupled system consisting of one unpaired electron ($S = 1/2$) and three equivalent nuclei each of spin $I_i = 1/2$, e. g., a group of methyl protons. The four nuclear spin sublevels for each $M_S = +1/2$ and $M_S = -1/2$ correspond to the possible values of the total nuclear spin angular momentum, $I = 3/2, 1/2$, with degeneracies $d(I = 3/2) = 1$ and $d(I = 1/2) = 3$. Owing to the transition-frequency

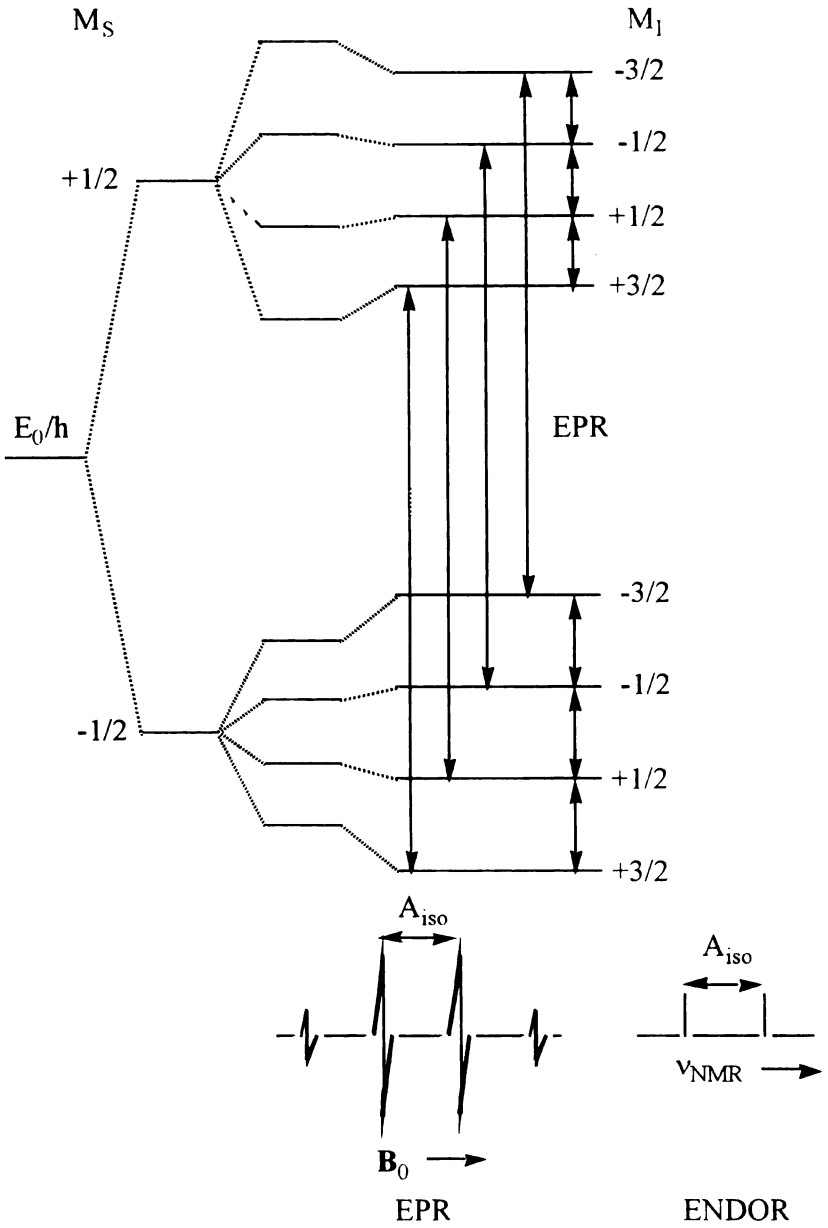

Figure I-9: Energy-level diagram of a hyperfine-coupled spin system in a high magnetic field, consisting of one unpaired electron (S = 1/2) and three equivalent nuclei (I = 1/2).

degeneracies, four EPR transitions are obtained with binomial intensity distribution (1:3:3:1). On the other hand, the ENDOR spectrum exhibits only two signals because of the degeneracy of all NMR transitions within the same M_S state. Addition of nonequivalent nuclei to the system multiplicatively increases the number of signals in the EPR spectrum, whereas the number of ENDOR signals increases additively. Thus, while the spectral density in EPR is given quantitatively by

$$\frac{\prod_{i=1}^{k}(2n_iI_i+1)}{\sum_{i=1}^{k}2|A_i|n_iI_i}. \qquad [I\text{-}33]$$

the ENDOR spectral density is generally much smaller and represented by

$$\frac{2k}{A_{max}}, \qquad [I\text{-}34]$$

where k stands for the total number of sets i of equivalent nuclei, n_i is the number of equivalent nuclei in each group i, each of spin I_i, and A_{max} denotes the largest hyperfine constant.

I.3.2. Level populations and ENDOR effect

To explain how an ENDOR response is generated various relaxation pathways and consequent energy level populations have to be considered. The theory of the

ENDOR mechanisms incorporates the relaxation theory and is rather complex. Here only a qualitative description from an elementary mechanistic point of view will be given. Suppose the four energy levels in Figure I-7 are initially in thermal equilibrium with each other so that their relative populations are given by Boltzmann's law. The population difference between the nuclear spin sublevels ($1\leftrightarrow3$, $2\leftrightarrow4$) is much smaller (ca. 10^{-6}) than that between the electron spin levels ($1\leftrightarrow2$ and $3\leftrightarrow4$) (on the order of 10^{-3} at room temperature and $B_0 \sim 3000$ G), thus the former can be neglected. Since the population difference between electron spin levels is small compared with k_BT at a temperature above a few Kelvin, the electronic Boltzmann factor can be expanded,

$$N(M_S = 1/2)/N(M_S = -1/2) = \exp(- g \mu_B B_0 /(k_BT)) =$$

$$1 - g \mu_B B_0 /(k_BT) = 1 - \varepsilon, \qquad [I\text{-}35]$$

where $\varepsilon = g \mu_B B_0/(k_BT)$. Initially, the upper electron spin level will be $1 - \varepsilon$ as less populated as the lower electron spin level, Figure I-10 (a). In conventional EPR experiments EPR transitions between these electron levels are induced with sufficiently low microwave power to avoid saturation. With no saturation the thermal equilibrium populations are maintained by the electron spin-lattice relaxation interactions. In this case the electron spin-lattice relaxation (characteristic time T_{1e}) will cause the hot spins to return from the upper electron spin level at a higher rate than the rate of induced absorption. However, if a strong microwave field is applied to drive an EPR transition between the electron spin levels, e. g., between levels 3 and 4, so that the induced

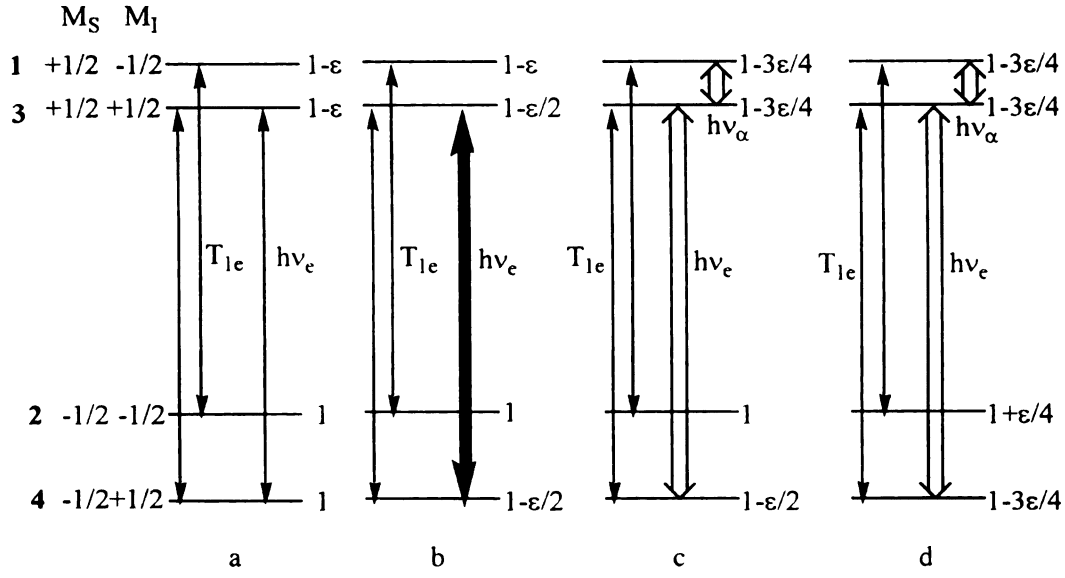

Figure I-10: Population diagram for transient ENDOR with S = 1/2, I = 1/2, $g_n > 0$, $A_{iso} > 0$. (a) unsaturated EPR transition, (b) saturated EPR transition, (c) transient ENDOR effect, (d) final steady state. (After Ref. 11)

transition rate competes successfully with the electron spin-lattice relaxation, these levels will become equally populated as shown in Figure I-10 (b). The EPR signal will fade away as the population difference goes to zero. The population difference between the electron spin levels can be restored and the EPR line desaturated by additionally pumping either 1↔3 or 2↔4 NMR transition using a strong saturating radiofrequency field, Figure I-10 (c). Both absorption (4↔2) and emission (1↔3), which equalize the populations of the corresponding NMR levels, can be induced by the coherent external radiation field with equal probability. From Figure I-10, it is clear that the maximum

ENDOR effect amounts to 1/4 of the unsaturated EPR intensity. It should be noted that the ENDOR signal is always an absorption signal since it is the increase in the intensity of the saturated EPR transition that is monitored. This detection scheme leads to a ENDOR signal that is about 10^5 times as intense as the signal in a conventional NMR experiment on paramagnetic systems.

The above simplified description of the ENDOR experiment is used in the explanation of the first ENDOR experiment performed by Feher[22] and is relevant to a *transient ENDOR* effect. It ignores the existence of relaxation processes other than the electron spin-lattice relaxation. In fact, in the presence of saturating microwave and radiofrequency fields the three energy levels involved would eventually become equally populated after a short time and the EPR signal would disappear, Figure I-10 (d). To obtain a steady-state change of the EPR signal intensity the effective relaxation time T_{1e}^{eff} must be changed - by providing a parallel relaxation path for the electron spins. Along with the radiationless electron spin-lattice (characteristic rate $W_e = (2T_e)^{-1}$) relaxation, the existence of nuclear spin-lattice (characteristic rate W_n) and cross-relaxation processes due to simultaneous electron and nuclear spin relaxation transitions (characteristic rates W_{x1} and W_{x2}) have to be taken into account. When the EPR transition $1 \leftrightarrow 2$ is partially saturated, Figure I-7 (b), the subsequent change in the EPR signal intensity will depend on the microwave induced transition rate in competition with all other processes that contribute to the effective electron spin relaxation between the two EPR levels. The effective relaxation rate comprises the electron spin-lattice relaxation W_{e1} as well as the bypass process $1 \rightarrow 3 \rightarrow 4 \rightarrow 2$ involving nuclear spin

relaxation W_{n1} (1→3), electron spin relaxation W_{e2} (3→4), and nuclear spin relaxation W_{n2} (4→2). Other bypass processes include the cross-relaxation rates W_{x1} or W_{x2} together with W_n rate(s). The effective relaxation rate between levels 1 and 2 can be enhanced by applying an external radiofrequency field, in resonance with the nuclear transitions, which competes with W_{n1} or W_{n2}. This causes a higher efficiency of the relaxation bypass and leads to desaturation of the EPR transition with a concomitant increase of the EPR signal intensity.

It is evident that the magnitude of the ENDOR effect will depend upon the relative magnitudes of the various relaxation rates, W_e, W_n, W_{x1}, and W_{x2}. If cross relaxation does not play a significant role (i. e., $W_x < W_e, W_n$) then the relaxation rates W_e and W_n have to be of comparable magnitudes in order to avoid a relaxation bottleneck along the bypass route for the electron spin. The above condition is usually satisfied for radicals in solutions as well as for radicals in solids that are not strongly coupled to the vibrational modes of the matrix. Since the rate W_e is inversely proportional to the rotational correlation time τ_R (the time constant for Brownian rotational motion of molecules in solution), whereas W_n is proportional to τ_R, an adjustment of the relaxation rates can be achieved by temperature variation. According to the Debye-Einstein equation the rotational correlation time is determined by the effective molecular volume V_{eff}, the viscosity η, and the temperature T:[12]

$$\tau_R = V_{eff}\,\eta/(k_B\,T). \qquad [I\text{-}36]$$

As the temperature decreases and the viscosity increases, W_e will become smaller while W_n will become larger. Hence, the optimization of the ENDOR experiment can be done by selecting appropriate temperature and solvent viscosity. For example, for protons, where $W_n << W_e$, optimum ENDOR signals in solvents of low viscosity (such as toluene or tetrahydrofuran) are observed near the freezing points of the solvents. For high viscosity solvents the optimum temperature is close to the room temperature.

If W_e and W_n are not of comparable magnitudes the cross-relaxation processes must be effective for a successful ENDOR experiment. This is the case of paramagnetic defects in solids or transition metal ions in crystals, where $W_n << W_x < W_e$ and an alternate relaxation pathway that involves W_x is predominant in generating an ENDOR response.

I.3.3. Factors influencing ENDOR signal intensity

The relaxation properties of the particular nuclei in the different molecular positions are deterministic of the ENDOR signal intensity. Therefore, the information from the intensity distribution in an ENDOR spectrum is not meaningful. Additional effects may obscure any conclusion from ENDOR signal intensities. One of the difficulties in analyzing the intensities comes from fact that the radiofrequency power is not constant over the scanned frequency range. This problem can usually be corrected for in studies of ENDOR line intensities. Another effect is the systematic decrease of the signal intensities in the case of small hyperfine couplings. Signals close to the free nuclear frequency are generally weak even if they are generated by many equivalent nuclei. This originates from the *incomplete hyperfine line separation*. When the hyperfine

separation is of the order of the homogeneous EPR linewidth (given by the inverse of the electron spin-spin relaxation time, $1/T_{2e}$) the saturation of one hyperfine line may lead to partial saturation of other lines, because of the overlap. The result is a reduction of the ENDOR enhancement. The ENDOR signal intensity is also influenced by the so called *hyperfine enhancement effect*. The nuclear spin interacts with an effective oscillating field that is the external radiofrequency field at the nucleus modified by the hyperfine field. As a result, the probability for the NMR transition will be proportional to the hyperfine enhancement factor given (for isotropic solutions) by ν_{ENDOR}/ν_n; i. e., the intensity will be increased with increasing ENDOR detection frequency. Therefore, the high-frequency component of an ENDOR line pair will be more intense than the low-frequency one at the same radiofrequency power. The hyperfine enhancement effect becomes more pronounced as the difference between the two components increases. In solid state ENDOR, the resonance frequency, ν_{ENDOR}, and the hyperfine enhancement factor are governed by different anisotropic hyperfine components. For instance, if the z axis is parallel to the static magnetic field B_0 the ENDOR resonance frequency is determined by the element A_{xx} of the hyperfine tensor, whereas the transition moment is governed by the A_{zz} tensor component. This leads to unexpected intensity patterns of low- and high-frequency lines in the solid state ENDOR spectra.

Since the intensity distribution of an ENDOR spectrum does not reflect the multiplicity, i. e., the number of equivalent nuclei belonging to each set, other techniques are used to determine the number of equivalent nuclei belonging to a particular hyperfine constant. One of the methods uses *specific isotopic labeling*, e. g., selective deuteration. While selective deuteration increases the density of spectral lines in EPR, thus decreasing

the resolution, replacement of a proton by a deuteron removes its contribution to the ENDOR spectrum because the proton and deuteron ENDOR transitions occur in different spectral regions.

I.3.4. ENDOR lineshapes

It is convenient to express the NMR (ENDOR) resonance condition, Equation I-32, in a more general form,

$$\nu_{NMR}\,(M_I, M_I + 1) = |\, -\nu_n + M_S\, A_{iso}|. \qquad [I\text{-}37]$$

In this form, M_S is retained explicitly, which allows assignment of a hyperfine constant to one of the M_S states if the sign of A_{iso} is known. The relation is precise only to first order and holds for nuclei that exhibit small hyperfine constants, e. g., protons in organic π radicals. Second-order effects that lead to line shifting or even splitting have to be considered if large (above 30 MHz for X-band EPR) hyperfine constants are present.

If anisotropic hyperfine effects are present due to orientation dependent electron-dipole-nuclear-dipole interaction, the ENDOR frequencies are given in the strong field approximation by an expression similar to Equation I-37,

$$\nu_{ENDOR}\,(M_I <-> M_{I+1}) = |\, -\nu_n + M_S\, R|, \qquad [I\text{-}38]$$

where

$$R = (A_{z'x'}^2 + A_{z'y'}^2 + A_{z'z'}^2)^{1/2} \qquad [I\text{-}39]$$

is the effective hyperfine coupling for a particular orientation of the magnetic field with respect to the axes of a laboratory coordinate system x'y'z' (usually defined according to the geometry of the radical or the crystal). If **A** is diagonal in the laboratory frame **R** is reduced to $R = A_{z'z'}$. The above formula can be used to obtain all components of the hyperfine tensor **A** by measuring the observed hyperfine splitting R versus the angle of rotation about three mutually perpendicular axes.

In the principal axis system xyz of the hyperfine tensor **A**,

$$R = (A_{xx}^2 l_x^2 + A_{yy}^2 l_y^2 + A_{zz}^2 l_z^2)^{1/2} , \qquad [I\text{-}40]$$

where l_x, l_y, and l_z are the direction cosines of the field $\mathbf{B}_0$ with respect to the axes x, y, and z.

Generally, the diagonal elements of the hyperfine tensor contain the isotropic (Fermi contact) interaction A_{iso} and the traceless dipolar interaction component B_{ii}:

$$B_{ii} = A_{ii} - A_{iso}, \qquad i = x, y, z. \qquad [I\text{-}41]$$

For small anisotropies, $|B_{ii}| << |A_{iso}|$, and R can be approximated as

$$R = A_{iso} + B_{xx} l_x^2 + B_{yy} l_y^2 + B_{zz} l_z^2 . \qquad [I\text{-}42]$$

For the common case of axial symmetry around z

$$B_{xx} = B_{yy} = B_{\perp}, \quad [I\text{-}43a]$$

$$B_{zz} = B_{||}, \text{ and} \quad [I\text{-}43b]$$

$$B_{||} = -2\, B_{\perp}. \quad [I\text{-}43c]$$

These relations result in the following expression for R:

$$R = A_{iso} + B_{||}\,[3\cos^2(\theta) - 1]/2, \quad [I\text{-}44]$$

where θ is the angle between $\mathbf{B}_0$ and the symmetry axis z.

For nuclei with $I > 1/2$, the quadrupole interaction gives rise to additional splittings of the ENDOR signals. In the simple case in which the hyperfine and quadrupole tensors have the same principal axes, $|Q| << |A|$, and the magnetic field is aligned along a principal axis (e. g., the z axis) the resonance condition is given by

$$\nu_{ENDOR}\,(M_I <-> M_{I+1}) = |\, -\nu_n + M_S\, A_{ii} + 3/2\, Q_{ii}\,(2M_I + 1)|. \quad [I\text{-}45]$$

Figure I-11 shows the energy level diagram for a $S = 1/2$, $I = 1$ spin system, e. g., a deuteron coupled to an unpaired electron. It is clear from the diagram that if the quadrupole interaction is negligible, the same two ENDOR transitions are observed for each of the three EPR lines ($\Delta M_S = 0$; $\Delta M_I = 1, 0, -1$). However, with a quadrupole interaction of a significant magnitude two ENDOR lines will be observed for the ΔM_I = -

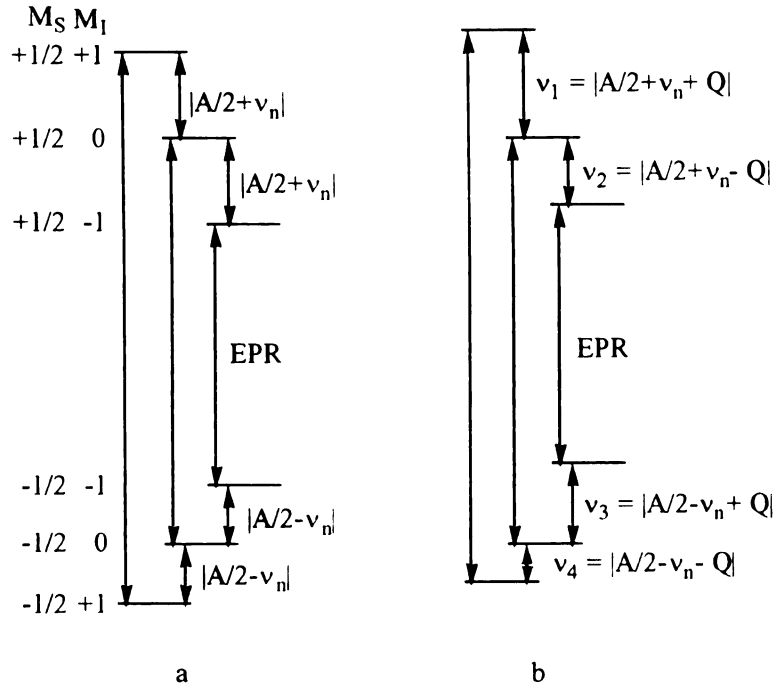

Figure I-11: Energy-level diagram for S = 1/2, I = 1 spin system showing EPR and ENDOR transitions in the absence (a) and presence (b) of quadrupole coupling. (After Ref. 11)

1 EPR transition, two different ENDOR signals will be observed for the $\Delta M_I = 1$ EPR line, and four ENDOR lines are expected for the $\Delta M_I = 0$ EPR line.[11]

In *disordered solids*, such as those studied here, due to averaging the absorptions from different orientations of the paramagnetic species with respect to the external magnetic field, the narrow liquid phase ENDOR lines broaden and may become weak, Figure I-12.[11,23] In the special case when the shape of the EPR spectrum is dominated

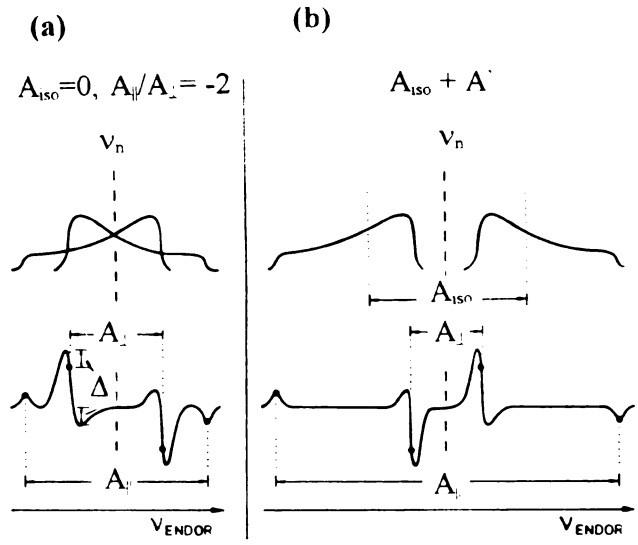

Figure I-12: ENDOR lineshapes (absorption: top, first derivative: bottom) resulting from an axially symmetric hyperfine tensor with (a) zero trace (purely dipolar hyperfine interaction) and (b) $A_{iso} \neq 0$. The bottom parts illustrate the procedure for determining $A_{||}$ and $A_{\perp}$. (From Ref. 12)

by a particular dipolar interaction, e. g., large g anisotropy or pronounced hyperfine anisotropy of one nucleus, single-crystal-type ENDOR spectra can be recorded from powders with randomly oriented paramagnetic species. By using appropriate EPR field settings orientation selection of paramagnetic species can be performed and the hyperfine tensor components of other nuclei can be detected relative to the tensor axes of the dominating interaction. In the absence of a dominating dipolar interaction no orientation selection in an ENDOR experiment is possible and a powder-type spectrum is obtained. The ENDOR absorptions are spread over the range of the hyperfine coupling values with

some buildup of intensity at three values corresponding to those paramagnetic species that have one of their respective principal axes oriented along the magnetic field (i. e., at canonical orientations). If the hyperfine anisotropy pertaining to the nucleus is small, narrower and stronger powder ENDOR signals are obtained. Thus, for an α proton that is bonded directly to the sp^2 hybridized carbon of an organic π radical the anisotropy amounts to about half of A_{iso} and the principal hyperfine tensor values occur near $1/2A_{iso}$, A_{iso}, and $3/2A_{iso}$. On the other hand, β-protons whose hyperfine tensor has approximately axial symmetry with anisotropy amounting to about 10% of A_{iso} exhibit quite strong ENDOR lines in disordered solids.[11]

Another feature in the ENDOR spectra of most solid disordered systems is the *matrix line* occurring at the free nuclear Larmor frequency. It is due to a remote, purely dipolar interaction between an unpaired electron and surrounding magnetic nuclei in the matrix. This interaction is averaged to zero in liquids by the rapid tumbling of the paramagnetic species. Hence, the matrix line can be used to probe the amount of molecular motion as a function of the temperature as well as to compare the amount of molecular motion in different phases and matrices at the same temperature. The appearance of this line also depends on the magnetic nuclei in the local environment of the unpaired spin. For example, if a radical site is located in a protein structure, both protons in the protein structure and the solvent molecules will contribute to a proton matrix line.

I.4. Principles of the Electron Spin Echo Envelope Modulation (ESEEM) Spectroscopy

Electron spin echo envelope modulation (ESEEM) technique of pulsed electron paramagnetic resonance (EPR) is a powerful technique capable of measuring small hyperfine couplings in systems with large inhomogeneously broadened EPR lines.[3-4,13-16,24-26] The inhomogeneity in an EPR line originates from the presence of multiple anisotropic interactions in the paramagnetic powder system. Due to these interactions the electron is subjected to the effect of slightly different local fields which results in that only a small fraction of the electron spins is at resonance at any given time. The superposition of these *spin packets* yields the observed EPR spectrum, Figure I-13. The inhomogeneous broadening of the EPR lineshape masks the details of the EPR spectra and reduces the resolution to a few tens of gauss. The ESEEM spectroscopy circumvents the inhomogeneity problem by directly recording the time evolution of the spin system which allows observation of the individual spin packets. Unlike the continuous wave (CW) EPR, which is a frequency domain spectroscopy, ESEEM is a time domain technique based on the phenomenon of the electron spin echo (ESE). In ESEEM experiments the spin system is probed by high energy resonant microwave pulses of nanosecond-range duration while keeping the static magnetic field constant. The short microwave pulses are able to excite only a small portion of the inhomogeneously broadened EPR spectrum. The paramagnetic sample response to these pulses consists in spontaneous emission of microwave energy, called the *spin echo*. The integrated intensity of the echo is measured as a function of the time separation between some of the pulses.

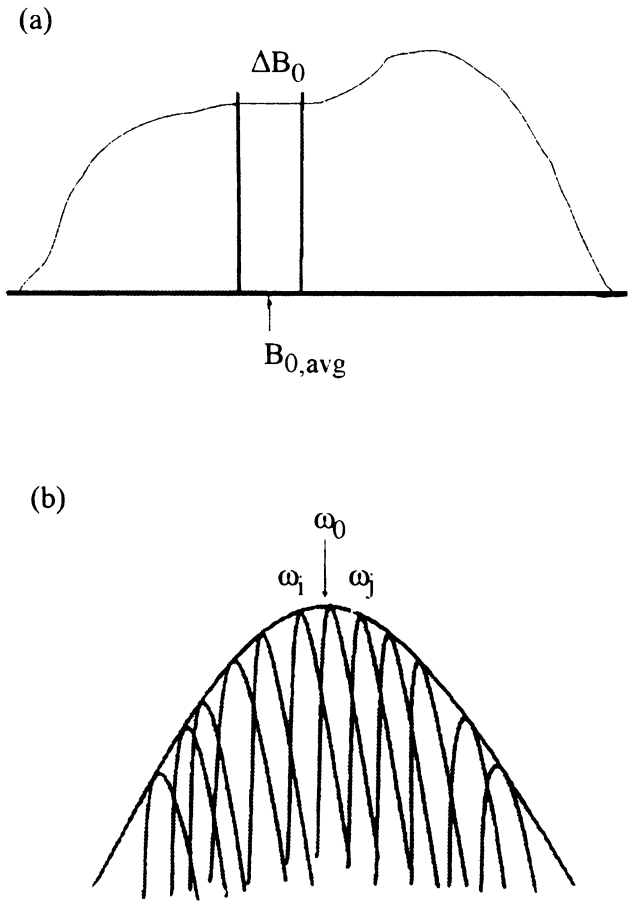

Figure I-13: Inhomogeneously broadened EPR lineshape (total linewidth 10 to 10000 gauss). (a) $\mathbf{B}_{0,avg}$ is the mean value of the resonant magnetic field. $\mathbf{B}_0$ is the linewidth of the portion of the spectrum excited by a microwave pulse. (b) The individual spin packets (linewidth of the order of 10^{-3} gauss) have magnetization components precessing independently of each other at frequencies ω_i, ω_0, ω_j.

The superhyperfine interactions manifest themselves as modulations of the electron spin echo envelope whose periods are related to the nuclear magnetic resonance (NMR) transition frequencies of the sample.

In this Section a semiclassical picture of the different ESEEM variations for an S = 1/2, I = 1/2 spin system will be given, followed by a quantum mechanical description of the ESEEM experiment.

I.4.1. Pulses of microwave radiation and their effects

When a paramagnetic material is placed in a static external magnetic field $\mathbf{B}_0$ along the z axis of a laboratory coordinate system, the magnetic moments associated with the individual spins obtain preferred orientations, precessing around the axis of the external field at angular frequency ω_0. The precession cones are oriented either parallel (spin α) or antiparallel (spin β) with respect to $\mathbf{B}_0$. For electrons the β spin state has lower energy than the α spin state, therefore, higher population (according to Boltzmann's law). Because of the population difference, the superposition of individual magnetic moments results in a total macroscopic magnetization **M**, parallel to $\mathbf{B}_0$. In an ESE experiment a linearly polarized oscillating microwave electromagnetic field, whose magnetic component, $\mathbf{B}_1$, is perpendicular to the static magnetic field $\mathbf{B}_0$ (i. e., along the x axis of the laboratory coordinate system), is applied at frequency ω during the pulses (Figure I-14):

$$\mathbf{B}_x(t) = 2\,\mathbf{B}_1 \cos(\omega t). \qquad [I\text{-}46]$$

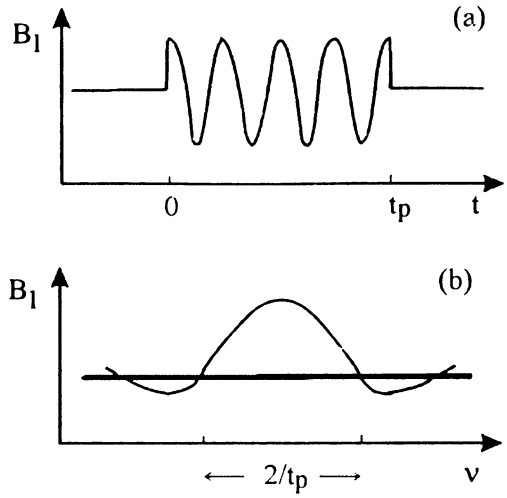

Figure I-14: (a) A microwave pulse is a burst of monochromatic microwave radiation of duration t_p. (b) The frequency spectrum of a pulse gives the spectral density of the field at the sample. (From Ref. 3)

It is most useful to analyze the effect of this linearly polarized oscillating field by decomposing it into two circularly polarized components, $\mathbf{B}_r$ and $\mathbf{B}_l$, that rotate in the plane perpendicular to $\mathbf{B}_0$ in directions opposite to one another (Figure I-15):[3,27]

$$\mathbf{B}_r = B_1 [\mathbf{x} \cos(\omega t) + \mathbf{y} \sin(\omega t)], \qquad [I\text{-}47a]$$

$$\mathbf{B}_l = B_1 [\mathbf{x} \cos(\omega t) - \mathbf{y} \sin(\omega t)]. \qquad [I\text{-}47b]$$

Since one component (e. g., $\mathbf{B}_r$) rotates in the same sense as the precession of the electron spins and the other in the opposite sense, near resonance ($\omega \cong \omega_0$) the counter-rotating component will have little effect on the resonance experiment and will, therefore, be neglected.

The time dependency of $\mathbf{B}_1$ can be eliminated by introducing a coordinate system XYZ, rotating about the axis of the laboratory static field $\mathbf{B}_0$ at angular frequency ω equal to the carrier frequency of the pulse. In the rotating reference frame $\mathbf{B}_1$ will be

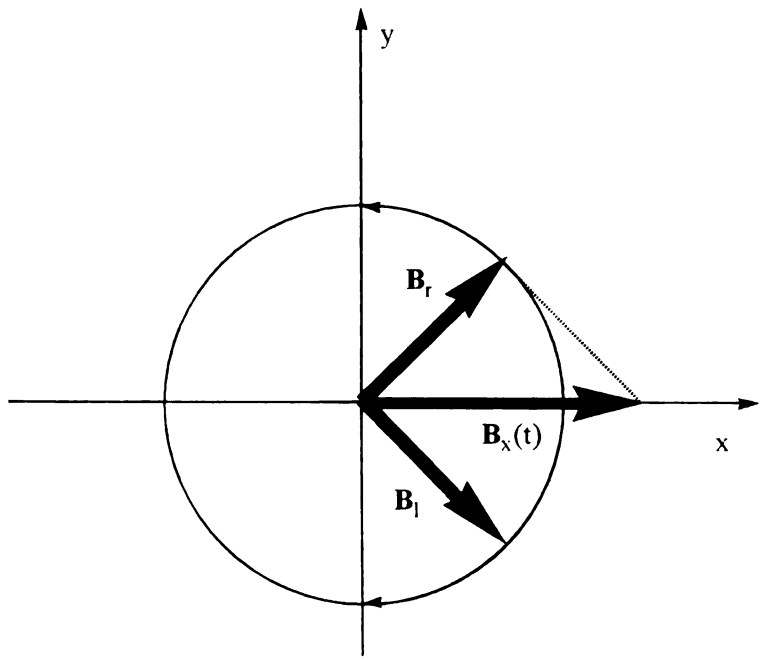

Figure I-15: Decomposition of a linearly polarized oscillating magnetic field, $\mathbf{B}_X(t)$, into two counter-rotating circularly-polarized components, B_r and B_l.

static. Its direction will be taken to define the X axis in the rotating frame, thus $\mathbf{B}_1 = B_1 \mathbf{x}$. Since the axis of rotation coincide with the direction of the laboratory field, $\mathbf{B}_0$ will also be static in the rotating frame, directed along the Z axis. In the absence of $\mathbf{B}_1$ the magnetization in the rotating coordinate system appears to precess about $\mathbf{B}_0$ at a frequency $(\omega_0 - \omega)$ corresponding to a magnetic field of magnitude $(\omega_0 - \omega)/\gamma$ and direction along the Z axis. The combination of the microwave field $\mathbf{B}_1$ and the laboratory field $\mathbf{z}(\omega_0 - \omega)/\gamma$ yields an effective magnetic field

$$\mathbf{B} = B_1 \mathbf{x} + [(\omega_0 - \omega)/\omega_0] B_0 \mathbf{z} . \qquad [I\text{-}48]$$

When the microwave pulse is applied for a period of time t_p the effective magnetic field torques the magnetization **M** in the reference frame as described quantitatively by the fundamental Bloch equation:

$$\frac{d\mathbf{M}}{dt} = \gamma(\mathbf{B} \times \mathbf{M}). \qquad [I\text{-}49]$$

The result is a precession of the magnetization about **B** at a frequency $\gamma\mathbf{B}$. At exact resonance, $\mathbf{B} = \mathbf{B}_1 = B_1 \mathbf{x}$., and the magnetization precesses about $\mathbf{B}_1$ at angular frequency $\omega_1 = \gamma B_1$. The magnetization before and after the microwave field is switched on is obtained by solving the Bloch equations that describe the time dependent behavior

of the magnetization. At time t = 0 when the microwave field is switched on, the solutions are

$$M_Z = M_0 \cos(\omega_1 t) \qquad \text{[I-50a]}$$

$$M_Y = M_0 \sin(\omega_1 t), \qquad \text{[I-50b]}$$

where $\omega_1 = \gamma B_1$ and M_0 is the magnitude of the magnetization at thermal equilibrium (i. e., at time t = 0 when the magnetization has been aligned with the Z axis and microwave field has not been applied yet). These solutions describe a circle in the YZ plane. At the end of the pulse, $t = t_p$, the components of the magnetization are

$$M_Z(t_p) = M_0 \cos(\omega_1 t_p) \qquad \text{[I-51a]}$$

$$M_Y(t_p) = M_0 \sin(\omega_1 t_p). \qquad \text{[I-51b]}$$

If the duration and the power of the microwave pulse are selected such that $\omega_1 t_p = \pi/2$ then

$$M_Z(t_p) = 0,\ M_Y(t_p) = M_0, \qquad \text{[I-52]}$$

indicating that the magnetization has been rotated by $\pi/2$ and lies, with its entire equilibrium value, along the Y axis. Applying a π pulse, for which $\omega_1 t_p = \pi$, yields

$$M_Z(t_p) = - M_0, M_Y (t_p) = 0, \qquad [I\text{-}53]$$

meaning that the magnetization has been wholly aligned along the -Z axis.

In pulsed EPR techniques, short pulses (tens of nanoseconds) are necessary, which make possible neglecting the effects of electron spin relaxation while ensuring a reasonable spectral width. Generation of a $\pi/2$ pulse of duration 10 ns requires a microwave magnetic field equal to about 9 gauss.[3] This represents a large amount of microwave power, which is difficult to achieve. On the other hand, a microwave pulse of finite length can excite only a portion of the inhomogeneously broadened EPR line. The excitation bandwidth is inversely proportional to the pulse duration t_p, $\Delta\nu = 1/t_p$. Hence, a specific flip angle can be achieved by either increasing t_p and simultaneously decreasing B_1 (decreasing the microwave power), thus exciting a wider portion of the EPR line (making the pulse more selective); or vice versa, decreasing t_p and simultaneously increasing B_1, thus making the pulse less selective. However, in the latter case values of t_p and B_1 are subjected to limitations imposed by the technological difficulties associated with fast switching of large microwave powers.

I.4.2. Two-pulse electron spin echo

In the simplest ESE experiment, a two-pulse sequence (denoted as $\pi/2 - \tau - \pi - \tau$) is employed to generate a spin echo, Figure I-16. The duration t_p and the amplitude of the pulses are chosen so that the flip angle $\theta = \omega_1 t_p$ is 90° for the first pulse and 180° for the second pulse. If the time interval between the pulses is τ, the echo is observed at time τ

after the second pulse. The plot of the echo intensity as a function of τ shows an overall decay of the electron spin magnetization (characterized by the phase memory time, T_M or T_2^*) that is modulated by the electron-nuclear hyperfine interactions.

A vector diagram for the two-pulse experiment is depicted in Figure I-17.[26] Following the first pulse, the magnetization is brought into the plane perpendicular to z

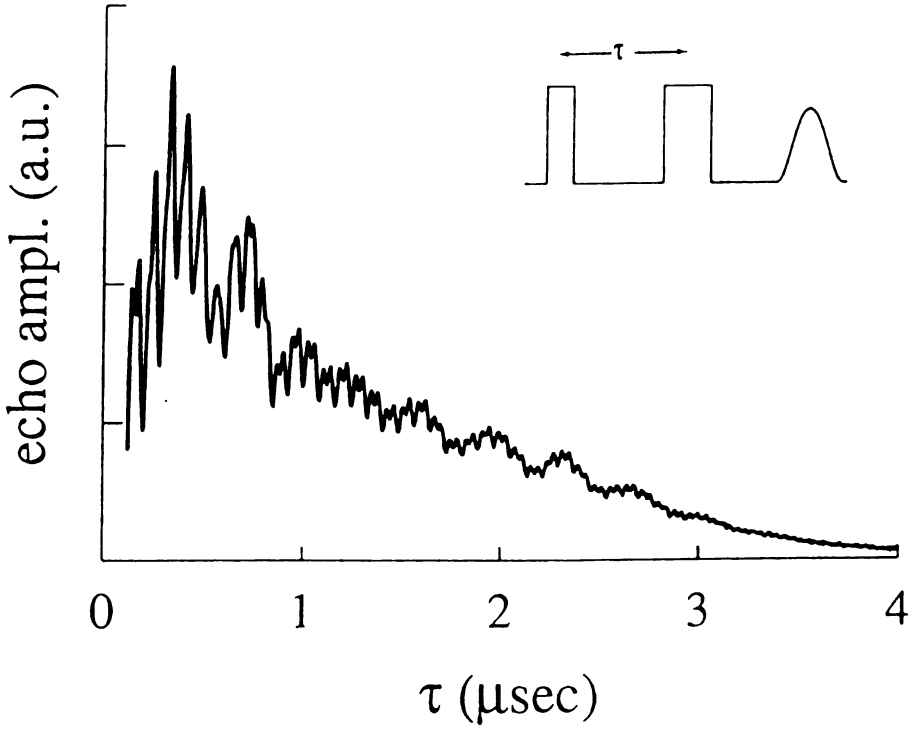

Figure I-16: Two-pulse electron spin echo sequence and an exemplary two-pulse ESEEM time-domain data set collected for the $Ni(III)(CN)_4(H_2O)_2^-$ complex in a 50% v/v water/ethylene glycol glass. (From Ref. 24)

axis. In the laboratory frame the magnetization rotates about z at angular frequency ω_0 but in the rotating frame it appears static, directed along the -Y axis. Because the individual spin packets (i. e., groups of spins that have different local magnetic environments) precess at different frequencies, they will fan out in the transverse plane during the free precession period τ, which results in loss of the macroscopic magnetization. During the time τ spin packets that have precession frequencies larger than ω_0 (e. g., spin packets labeled 2, 3 and 4) will accumulate positive phase angles with respect to the -Y axis while spin packets with an effective local field weaker than $\mathbf{B}_0$ (e. g., spin packets labeled 5, 6, and 7) will develop negative phase angles. Thus, the presence of inhomogeneities in the spin system is essential for the echo phenomenon. The second pulse torques the magnetization of every spin packet about the X axis through an angle of 180°. Since the original angular frequencies and directions of precession of the individual spin packets remain unaltered, the spin packets rephase into a microscopic magnetic moment along the Y axis after time τ following the second pulse. Refocusing of the magnetization results in an emission of microwave radiation by the sample and is called the spin echo.

I.4.3. Three-pulse electron spin echo (stimulated echo)

The three pulse sequence ($\pi/2$ - τ - $\pi/2$ - T - $\pi/2$ - τ) creates a stimulated echo at time τ after the third pulse. Figure I-18 shows the vector diagram for the 3-pulse experiment.[26] The first pulse rotates the magnetization about the X axis so that it becomes aligned along the -Y axis. This is followed by dephasing of the magnetization in

Figure I-17: Vector diagram illustrating the formation of the two-pulse electron spin echo. (a) two-pulse electron spin echo sequence; (b) at thermal equilibrium the magnetization **M** is aligned with the external magnetic field $\mathbf{B}_0$; (c) the first ($\pi/2$) pulse has torqued **M** onto the XY plane of the rotating frame; (d) **M** is a superposition of spin packets that dephase due to the differences in their precession frequencies; (e) the second pulse rotates the spin packets about the X axis through angle π. The direction of precession of each spin packet is conserved. (f) the individual spin packets refocus along Y to reform **M**, thus generating an echo. (After Ref. 26)

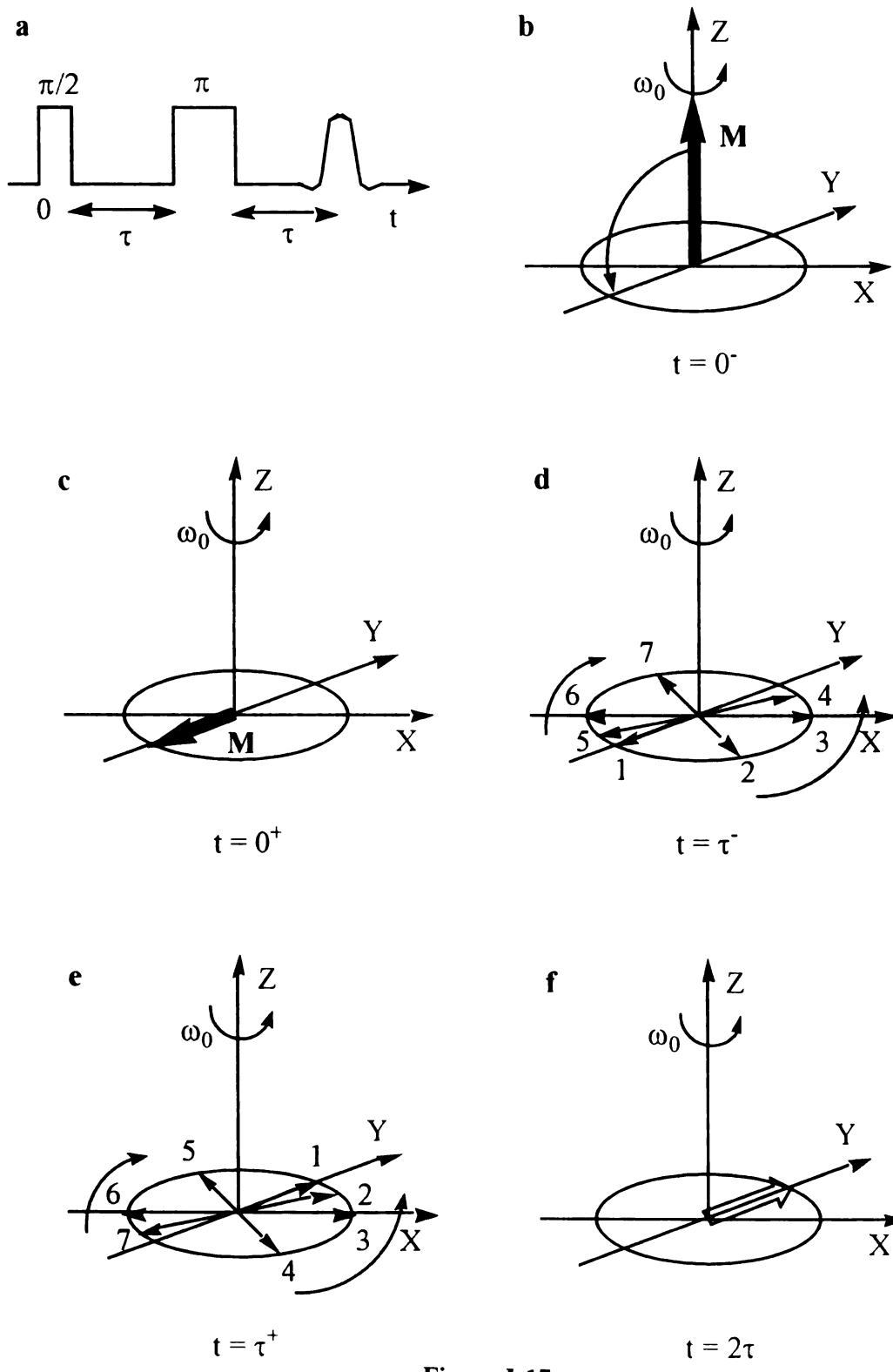
a
π/2
π
0
τ
τ
t
b
Z
ω0
M
Y
X
t = 0-
c
Z
ω0
Y
M
X
t = 0+
d
Z
ω0
Y
7
6
4
5
3
X
1
2
t = τ-
e
Z
ω0
Y
5
1
6
2
7
3
X
4
t = τ+
f
Z
ω0
Y
X
t = 2τ

Figure I-17

Figure I-18: Vector diagram illustrating the formation of the three-pulse electron spin echo. (a) three-pulse electron spin echo sequence; (b), (c) same events as in Figure I-17; (d) the second $\pi/2$ pulse converts the transversal magnetization into a longitudinal one; (e) the magnetization components precess about Z; (f), (g) the third $\pi/2$ pulse rotates the surviving magnetization components (directed along Z) onto the XY plane; (h) the spin packets refocus along Y to reform **M**, thus generating a stimulated echo. (After Ref. 26)

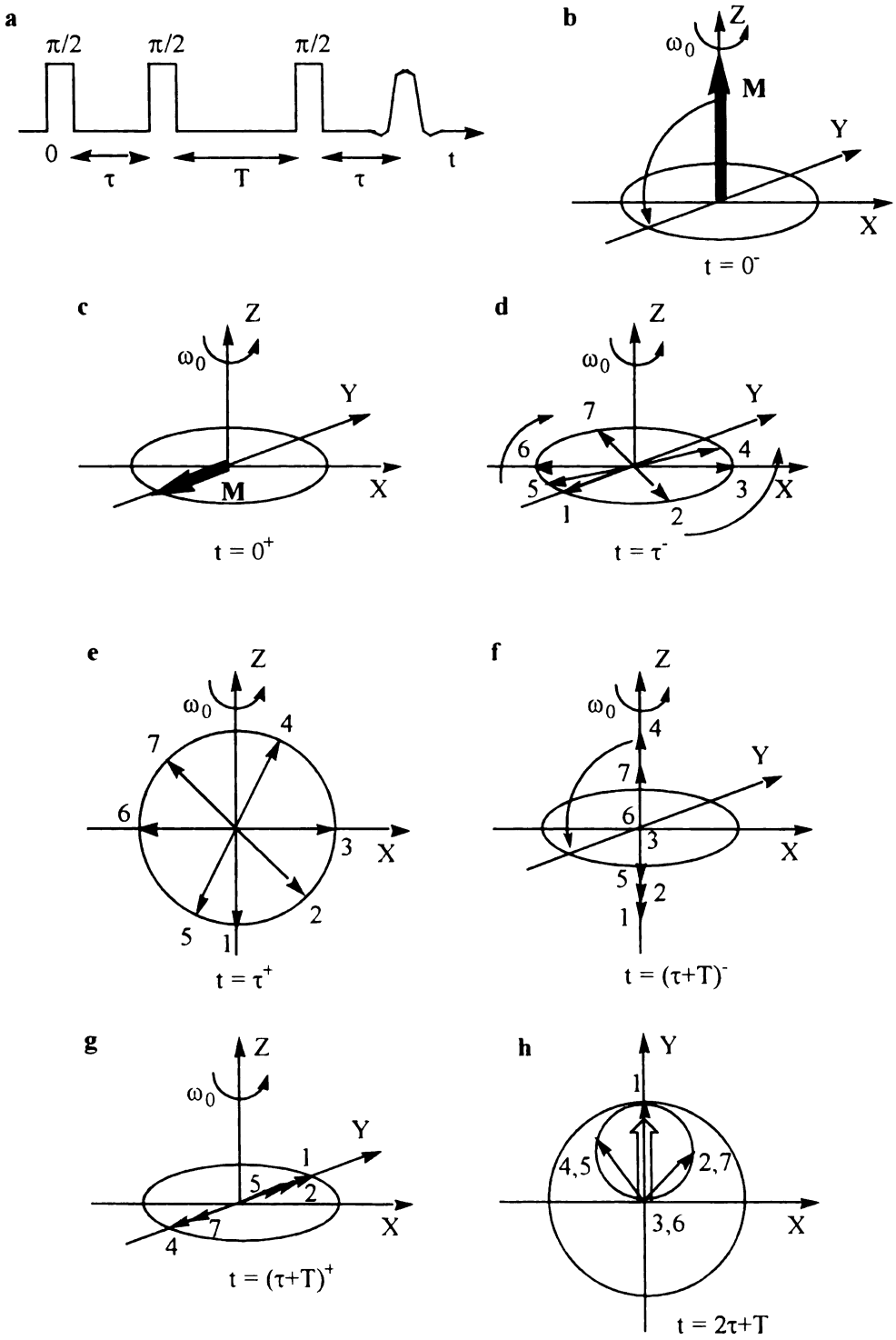
a
π/2
π/2
π/2
0
τ
T
τ
t
b
Z
ω0
M
Y
X
t = 0-
c
Z
ω0
Y
M
X
t = 0+
d
Z
ω0
Y
7
6
4
5
3
X
1
2
t = τ-
e
Z
ω0
4
7
6
3
X
5
1
2
t = τ+
f
Z
ω0
4
Y
7
6
3
X
5
2
1
t = (τ+T)-
g
Z
ω0
Y
1
5
2
X
7
4
t = (τ+T)+
h
Y
1
4,5
2,7
3,6
X
t = 2τ+T

Figure I-18

the transverse plane as described above for the primary echo. The second pulse rotates the Y components of the dephased magnetization by 90° storing them along the -Z axis during the waiting time T. If the free precession period T satisfies the condition $T_{2e} << T < T_{1e}$, where T_{2e} and T_{1e} are the transversal and longitudinal relaxation times of the electron, respectively, the magnetization in the transverse plane will fully decay during the free precession period T and only the longitudinal magnetization M_Z will survive. The third 90° pulse transfers this polarization pattern to magnetization in the XY plane, which, after time τ following the third pulse refocuses along the Y axis, yielding the stimulated echo. It should be noted that owing to the incomplete refocusing of the magnetization vectors, the stimulated echo has a "diffused" magnetization pattern, which reduces the intensity of the echo to about half the intensity of the two pulse echo.[14)]

I.4.4. Four-pulse electron spin echo

The four pulse sequence ($\pi/2 - \tau - \pi/2 - t_1 - \pi - t_2 - \pi/2 - \tau$) utilized in the HYSCORE experiment (cf. Chapter III) is essentially the stimulated echo pulse scheme with an additional π pulse inserted between the second and third $\pi/2$ pulses. This additional pulse inverts the magnetization, while interchanging spin packets that belong to the opposite electronic manifolds. This results in mixing, or correlating, hyperfine frequencies that arise from the same coupling. Consider a spin packet denoted as δM_Z that lies along the -Z axis after the second $\pi/2$ pulse, Figure I-19.[28)] The π (mixing) pulse inverts δM_Z onto the +Z axis. The spin packet is rotated onto the -Y axis by the last $\pi/2$ pulse, where it starts precessing about the Z axis. The different components refocus to

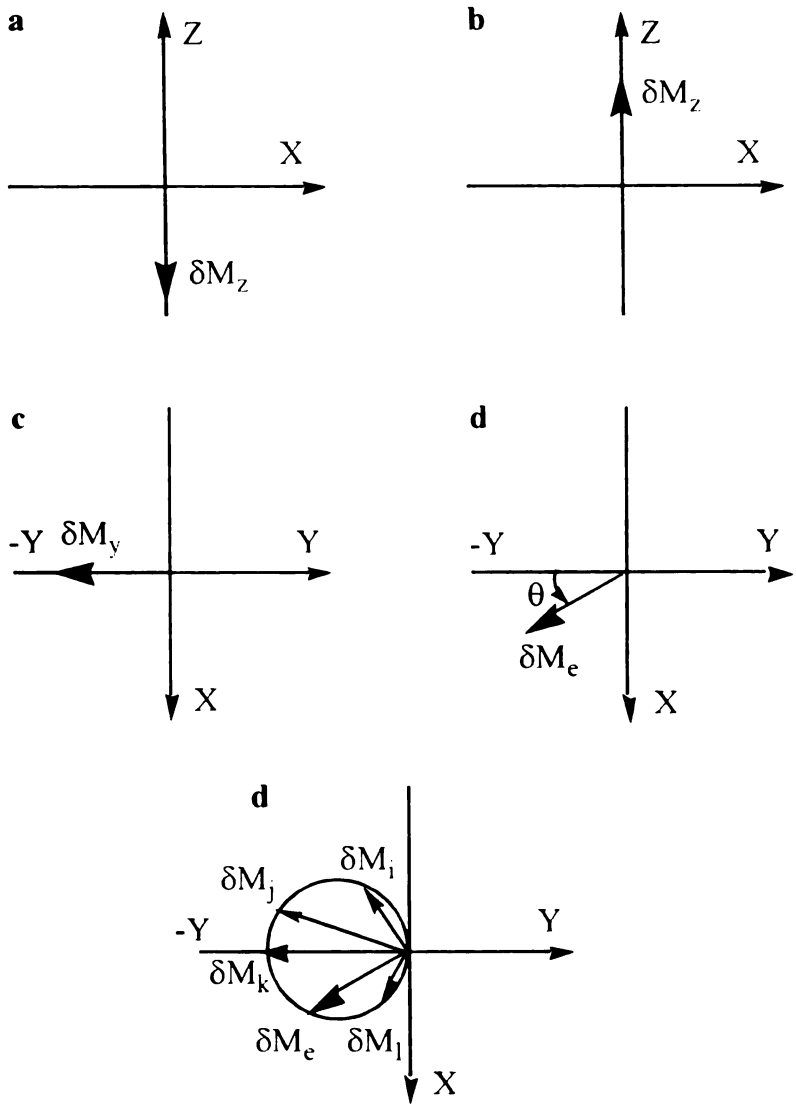

Figure I-19: Vector diagram illustrating the formation of the four-pulse electron spin echo. (a) after the second $\pi/2$ pulse the magnetization δM_Z associated with a particular spin packet is brought along the Z axis; (b) the π pulse inverts δM_Z; (c) the fourth ($\pi/2$) pulse rotates δM_Z onto the XY plane; (d) spin packets start precess about Z; (e) during a time period τ after the last pulse various spin packets attain the position shown, which creates the echo along the -Y axis. (After Ref. 28)

form an echo after a waiting period τ, following the fourth pulse.

1.4.5. Origin of ESEEM

The origin of the modulation phenomenon can be qualitatively understood by introducing a semi-classical description combining the classical vector model of echo formation with the quantum mechanical treatment of a simple anisotropic system consisting of one electron coupled to a spin 1/2 nucleus.[24] The spin Hamiltonian of such system consists of electron Zeeman, nuclear Zeeman, and electron-nuclear hyperfine interaction terms:

$$\mathcal{H} / \hbar = \omega_S S_z + A_{zz} S_z I_z + A_{xz} S_z I_x - \omega_I I_z , \qquad [I\text{-}54]$$

where $A_{zz} = A = A_{||} \cos^2(\theta) + A_{\perp} \sin^2(\theta)$, $A_{xz} = B = (A_{||} - A_{\perp}) \cos(\theta) \sin(\theta)$, $\omega_S = g \mu_B B_0 / \hbar$, and $\omega_I = g_n \mu_{B,n} B_0 / \hbar$. $A_{||}$ and $A_{\perp}$ are the principal values of an axially symmetric hyperfine tensor that can be described in terms of a Fermi contact coupling A_{iso} and a traceless dipole-dipole coupling term, $T = g g_n \mu_B \mu_{B,n}/r^3$, with $A_{||} = A_{iso} + 2T$ and $A_{\perp} = A_{iso} - T$. The angle θ describes the orientation of the principal axes of the hyperfine tensor with respect to the laboratory field $\mathbf{B}_0$. The remaining terms have their usual meaning. Eigenvalues and eigenvectors of the above Hamiltonian can be obtained easily after constructing the Hamiltonian matrix in the uncoupled basis set consisting of electron and nuclear spin product states, $|M_S, M_I\rangle$. The diagonalization can be managed

independently for the two electron spin manifolds since the only term in $\mathcal{H}$ that gives rise to off-diagonal elements is that involving I_x. The results are summarized in the energy level scheme of Figure I-20, where $\omega_S = \omega_0$ and the normalized probability amplitudes for the EPR transitions are given by

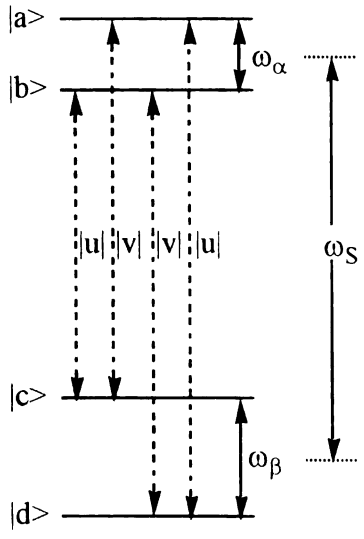

$$|a\rangle = \cos(\eta/2)|{+}{+}\rangle + \sin(\eta/2)|{+}{-}\rangle$$

$$|b\rangle = -\sin(\eta/2)|{+}{+}\rangle + \cos(\eta/2)|{+}{-}\rangle$$

$$|c\rangle = \cos(\xi/2)|{-}{+}\rangle + \sin(\xi/2)|{-}{-}\rangle$$

$$|d\rangle = -\sin(\xi/2)|{+}{+}\rangle + \cos(\xi/2)|{-}{-}\rangle$$

$$\omega_\alpha = [(\omega_I - A/2)^2 + B^2/4]^{1/2}$$

$$\omega_\beta = [(\omega_I + A/2)^2 + B^2/4]^{1/2}$$

Figure I-20: Energy-level diagram for an S = 1/2, I = 1/2 spin system described by the Hamiltonian of Equation [I-54].

$$| u |= 2\frac{< b | S_y | c >}{g\mu_B B_1} = \sin\left[\frac{\eta - \xi}{2}\right] \qquad \text{[I-55a]}$$

$$| v |= 2\frac{< a | S_y | c >}{g\mu_B B_1} = \cos\left[\frac{\eta - \xi}{2}\right] \qquad \text{[I-55b]}$$

The angles η and ξ define the axes of quantization for the α and β spin manifolds, respectively, and are given by $\sin(\eta) = B/2\omega_\alpha$ and $\sin(\xi) = B/2\omega_\beta$. In general, due to the anisotropic nature of the electron-nuclear spin interaction, which mixes the nuclear spin states all four of the possible EPR transitions for the S = 1/2, I = 1/2 spin system are allowed. They can be excited coherently in a pulsed EPR experiment, provided that the microwave pulses have sufficient bandwidth. Thus, the microwave pulse bandwidth places an experimental constraint on the ESEEM experiment. The quantum mechanical effect that is responsible for the nuclear modulation phenomenon is the so called "branching of transitions", i. e., the fact that the microwave pulses can induce transitions that start at one energy level but end at more than one distinct levels. The semi-classical picture illustrating this effect is shown in Figure I-21. The microwave frequency ω_0 is taken to be equal to ω_S of Figure I-20. The four partially allowed transitions are labeled *A*, *B*, *C*, and *D*. The discussion will focus on transitions *A* and *C*. After the application of the first $\pi/2$ pulse, the transverse magnetization that corresponds to transition *A* has fallen behind the frame precession (since $\omega_A < \omega_0$). Thus in the rotating frame, spin packet *A* has acquired a negative phase with respect to the Y axis, $(\omega_A - \omega_0)\tau$, during the free precession period τ. In a two-pulse experiment, the second pulse not only torques the spin

Figure I-21: Vector model showing the interference between electron spin packets that result from transition "branching" in a two-pulse ESEEM experiment. The upper left insert represents the energy-level diagram of Figure I-20, while the upper right insert shows the spin packets across the inhomogeneous line. (a) after the first pulse spin packet *A* precesses in the XY plane at frequency $\omega_A < \omega_0$ acquiring phase $(\omega_A - \omega_0)\tau$ during time τ; (b) the second pulse flips spin packet *A* about X and induces its branching into two portions that precess at frequencies $\omega_A < \omega_0$ and $\omega_C > \omega_0$; (c) spin packet *A* is refocused along Y contributing fully to the spin echo, while spin packet *C* is refocused at an angle $\theta = (\omega_A - \omega_C)\tau$ with respect to Y, giving a contribution to the echo weighted by $\cos(\theta)$.

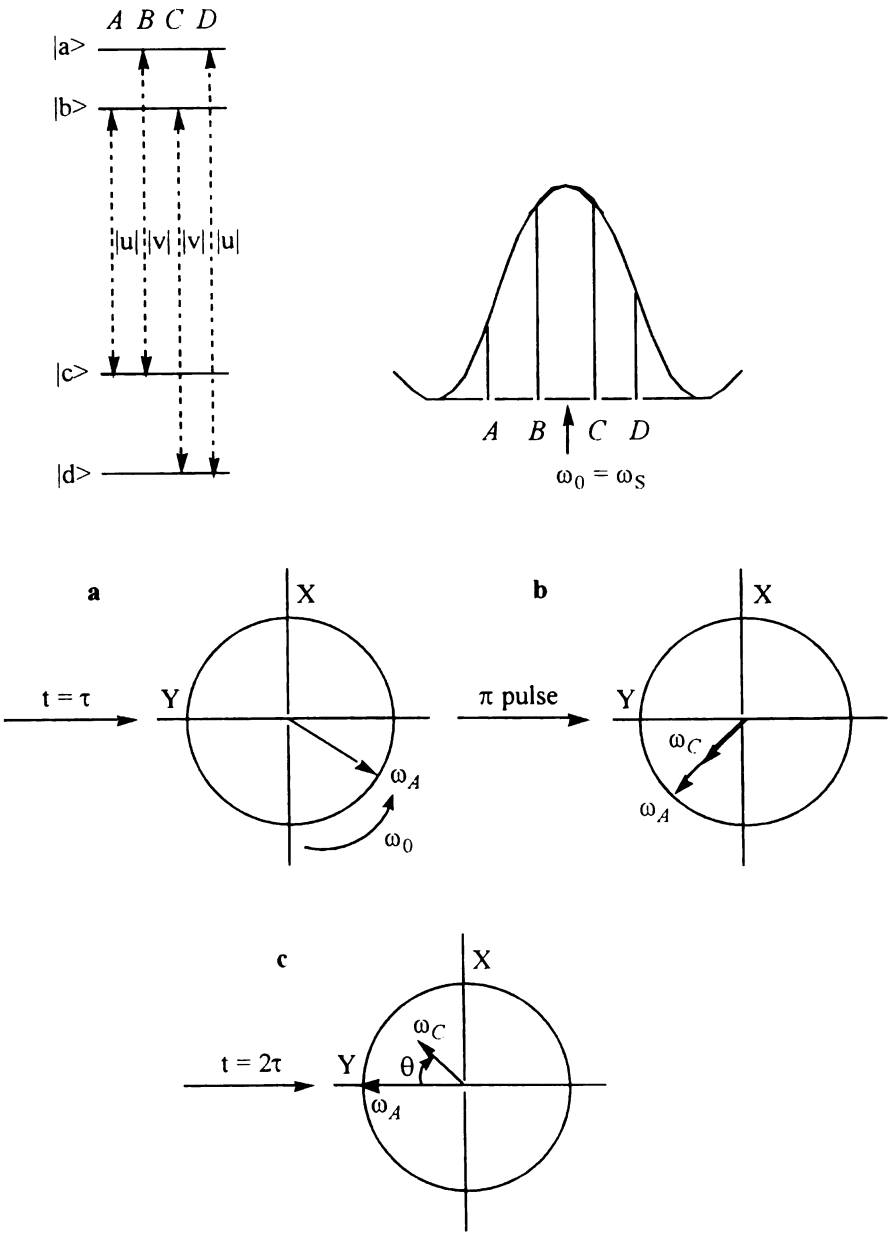
A B C D
|a>
|b>
|u| |v| |v| |u|
|c>
|d>
A B C D
$\omega_0 = \omega_S$
a
X
t = τ
Y
ω_A
ω_0
b
X
π pulse
Y
ω_C
ω_A
c
X
ω_C
t = 2τ
Y
θ
ω_A

Figure I-21

packet A by 180° about X, but since it excites all transitions simultaneously, it will induce "branching" of A into two portions, precessing at ω_A and ω_C. Because the new spin packet C has a precession frequency larger than ω_0, it will precess in the opposite direction from the packet that maintains the ω_A precession frequency. Hence, while the spin packet A refocuses wholly along Y axis after time τ following the second pulse, spin packet C will be at an angle $(\omega_A - \omega_C)\tau$ with respect to Y axis. Both "branched" portions, A and C, will interfere with the echo formation, however to a different extent depending on the projection of the "branched" spin packet onto the Y axis. While packet A contributes fully to the echo, the contribution of C is reduced by $\cos[(\omega_A - \omega_C)\tau] = \cos(\omega_\alpha \tau)$, where ω_α is the NMR frequency in the $|\alpha\rangle$ electron spin manifold (the difference between levels $|a\rangle$ and $|b\rangle$), and weighted by the probability for "branching", k (the fraction of the magnetization split from spin packet A upon the second pulse). It is evident that the maximum contribution of the magnetization vector of the C spin packet is obtained only if $(\omega_A - \omega_C)\tau = 2\pi n$, for n = 0, 1, 2, ... Therefore, the modulation of the echo envelope as a function of τ will be given by

$$E_{mod}(\tau) = 1 - k \cos(\omega_\alpha \tau), \qquad [I\text{-}56]$$

Thus the echo amplitude as a function of τ will be modulated by the frequency ω_α and will depend on the extent of "branching" k (the modulation depth). The same reasoning holds for all other combinations of spin packets formed by branching of transitions. For

instance, the pair of transitions *B* and *D* will result in ω_β being a modulation frequency as well.

The detailed quantum mechanical treatment outlined later shows that for a S = 1/2, I = 1/2 spin system the primary echo is modulated at the fundamental hyperfine frequencies ω_α and ω_β, as well as at their sum and difference combinations, $\omega_\alpha \pm \omega_\beta$,[29,30]

$$E_{mod}(\tau) = 1 - (k/4)\{2 - 2\cos(\omega_\alpha\tau) - 2\cos(\omega_\beta\tau) + \cos[(\omega_\alpha + \omega_\beta)\tau] + \cos[(\omega_\alpha - \omega_\beta)\tau]\}. \quad [I\text{-}57]$$

The modulation depth parameter, k, which is related to the product of the transition probabilities, $|u|^2|v|^2$, for the two different EPR transitions associated with "branching" is given by

$$k = \sin^2(\eta - \xi) = [\omega_I B/(\omega_\alpha\omega_\beta)]^2. \quad [I\text{-}58]$$

The modulation frequencies can be resolved by Fourier transformation of the echo envelope function. It should be pointed out that since the combination frequencies have opposite phase to the fundamental ones (cf. Equation I-57), negative components can also appear in the two-pulse ESEEM spectra. The Fourier transformation is usually preceded by a dead-time reconstruction procedure, according to the algorithm given by Mims,[31] to reduce the lineshape distortions introduced by the spectrometer dead-time (ca. 150 ns).

The experimentally observed ESEEM function can be represented as a product of the quantum mechanically derived modulation function, $E_{mod}(\tau)$, and a decay function, $E_{decay}(\tau)$, that describes the loss of magnetization due to spin relaxation:

$$E(\tau) = E_{decay}(\tau)\, E_{mod}(\tau) \quad [I\text{-}59]$$

$E_{decay}(\tau)$ is usually modeled with exponentials of the type $\exp(-\tau/\tau_0)^n$, where n = 1, 2, or 1/2.[32] In the two-pulse ESEEM, the magnetization decays in the transverse plane, primarily due to the spin-spin relaxation characterized by the (homogeneous) relaxation time, T_2^* (T_M), which is of the order of 1 μs for most systems of interest. The rapid background decay broadens the peaks and reduces the frequency resolution of the two-pulse ESEEM measurement. A further complexity of the ESEEM experiment is added when N nuclei that are coupled to a single paramagnetic center contribute to the modulation pattern. In this case, the modulation function is a product of modulation functions for the individual nuclei,[16,24,33,34]

$$E(\tau) = E_{decay}(\tau)\prod_{i=1}^{N} E_{mod}^{(i)}(\tau) \quad [I\text{-}60]$$

The result of taking the product of functions $E^{(i)}_{mod}(\tau)$, each of which is given by Equation I-57, will contain not only the fundamental ($\Delta M_I = \pm 1$) frequencies and combination frequencies for each nucleus, but also frequencies that are combinations of

the frequencies arising from different nuclei. Therefore, the two-pulse ESEEM data (or the corresponding ESEEM frequency spectrum obtained from Fourier transformation of the time domain data[31] may become very complex even when only a few nuclei contribute to the echo modulation.

The product rule, Equation I-60, is the basis of an approach to analyzing complex ESEEM data. The contributions from various nuclei are sorted out by isotopically substituting one nucleus, then dividing the ESEEM functions for the original (non-labeled) and isotopically substituted sample. Since the modulation function of several nuclei is the product of the modulation functions of the individual nuclei the division of the modulation functions for both samples cancels out all individual nuclei functions, except for the modulation functions of the two isotopic nuclei. For example, the ratio of the ESEEM functions for a sample in which one hydrogen is replaced by deuterium and the ordinary (non-labeled) sample is given by

$$E_{div}(\tau) = E^{D}(\tau)/E^{H}(\tau). \qquad [I\text{-}61]$$

Due to the lack of nuclear quadrupole interaction of H (I = 1/2), $E^{H}(\tau)$ features very small modulation depth compared with $E^{D}(\tau)$, so $E_{div}(\tau)$ to a very good approximation is identical to the deuterium modulation function, and can be analyzed by numerical simulations. Although this rule is strictly correct only for two-pulse single-crystal ESEEM, it has also been found applicable to disordered samples. An application of this approach is outlined in Chapter II.

The problems of the increased complexity and decreased frequency resolution of the two-pulse ESEEM experiment, which complicate the data analysis, are alleviated in the three-pulse ESEEM experiment. In the 3-pulse ESEEM τ is kept constant and the amplitude of the spin echo is measured as a function of T (or, equivalently, $T + \tau$). The explicit form of the three-pulse envelope modulation function in the case of a $S = 1/2$, $I = 1/2$ spin system is[29,30]

$$E_{mod}(\tau, T) = 1 - (k/4)\{[1 - \cos(\omega_\alpha \tau)]\,[1 - \cos(\omega_\beta \tau + \omega_\beta T)] + [1 - \cos(\omega_\beta \tau)]\,[1 - \cos(\omega_\alpha \tau + \omega_\alpha T)]\}. \quad [I\text{-}62]$$

This equation shows that only the fundamental hyperfine frequencies contribute to the modulation, which leads to simpler spectra in the three-pulse ESEEM. Since the background decay for the three pulse sequence is governed by electron spin-lattice relaxation, electron cross relaxation, and nuclear spin-spin relaxation, all of which are characterized by relaxation times much longer than the electron spin-spin relaxation time, the modulations extend over longer periods. This fact results in better resolution in the frequency domain for three-pulse ESEEM spectra than for two-pulse ESEEM spectra. Equation I-62 also shows that because the stimulated ESEEM function depends on τ as a parameter, it is possible to enhance or suppress certain frequencies by varying τ. This effect, known as the τ-suppression effect, is useful in making spectral assignments. It may lead to blind spots in the three-pulse ESEEM spectra, which may yield lineshape distortion in disordered systems[25,30,35]. The product rule for the overall modulation function, when multiple nuclei are coupled to the paramagnetic center, is less complex

than in the case of the two-pulse experiment since the products are taken only between the frequencies belonging to the same electron spin manifold[24,25]

$$E(\tau,T) = \frac{E_{decay}(T)}{2}\left[\prod_{i=1}^{N} E^{(i)}_{mod,\alpha}(\tau,T) + \prod_{j=1}^{N} E^{(j)}_{mod,\beta}(\tau,T)\right] \qquad [I\text{-}63]$$

I.4.6. Density matrix description of ESEEM

The density operator formalism provides a powerful method for calculating the properties of ensembles in statistical mechanics.[36] It has proven especially useful to describe the time evolution of ensembles of spins in magnetic resonance.[3,27,37] Here the derivation of the modulation formula for the two pulse ESEEM experiment will be outlined, following Mims.[29] The same derivation steps are followed in Chapter III, where an expression for the two-dimensional echo envelope modulation effect in a four-pulse spin echo experiment is obtained.

The state of the system described by the vector $|\Psi(t)>$ can be expressed by an expansion in terms of a complete orthonormal set of functions $|\phi_k>$ with coefficients $c_k(t)$

$$|\Psi(t)\rangle = \sum_k c_k(t)|\phi_k\rangle \qquad [I\text{-}64]$$

The density operator, ρ, which describes the projection of one basis set onto another, is given by

$$\rho(t) = |\Psi(t)><\Psi(t)|, \qquad [I\text{-}65]$$

and the corresponding matrix has elements

$$\rho_{ij} = <\phi_i|\rho(t)|\phi_j>. \qquad [I\text{-}66]$$

The expectation value of an macroscopic observable represented by the operator O is obtained in quantum statistics by taking an ensemble average over $<\Psi|O|\Psi>$,

$$\langle O \rangle = \overline{\langle \Psi | O | \Psi \rangle}. \qquad [I\text{-}67]$$

From Equations I-64 - I-67 it follows that

$$<O>(t) = Tr\{\rho(t)\cdot O\}. \qquad [I\text{-}68]$$

This equation makes possible the calculation of the properties of ensembles, provided that the density matrix is known. In an electron spin echo experiment the expectation value of interest is the magnetization which is detected along the Y axis. Since it is proportional to the Y-component of the electron spin, S_Y, the normalized echo amplitude is given by

$$\mathbf{E} = \frac{\mathbf{Tr}\{\rho_E \mathbf{S}_Y\}}{\mathbf{Tr}\{\rho_0 \mathbf{S}_Y\}}, \qquad \text{[I-69]}$$

where ρ_E is the density matrix at the time of echo formation and ρ_0 is the density matrix before the application of the pulse sequence.

The equation of motion for the density matrix can be derived from the time dependent Schrödinger equation, and takes the form

$$\frac{d}{dt}\rho(t) = \frac{i}{\hbar}\left[\rho(t), \mathcal{H}(t)\right], \qquad \text{[I-70]}$$

where $\mathcal{H}(t)$ is the time dependent Hamiltonian of the system. Integration of this differential equation allows determination of the density matrix at time t_f, $\rho(t_f)$, in terms of the density matrix $\rho(t_i)$ at an initial time t_i:

$$\rho(t_f) = \exp[-i\,\mathcal{H}(t_f - t_i)/\hbar]\,\rho(t_i)\,\exp[i\,\mathcal{H}(t_f - t_i)/\hbar]. \qquad \text{[I-71]}$$

Thus, the density matrix ρ_E at the time of appearance of the echo can be obtained from the initial, thermal equilibrium density matrix ρ_0.

The system Hamiltonian consists of a time dependent and a time independent component,

$$\mathcal{H} = \mathcal{H}_0 + \mathcal{H}_1(t). \qquad \text{[I-72]}$$

The Hamiltonian $\mathcal{H}_0$ describes the static interactions such as the electronic Zeeman, nuclear Zeeman, electron-nuclear hyperfine, and nuclear quadrupole interactions

$$\mathcal{H}_0 = \mathcal{H}_{e,Z} + \mathcal{H}_{n,Z} + \mathcal{H}_{HFI} + \mathcal{H}_{NQI} \cdots \quad [I\text{-}73]$$

$\mathcal{H}_1$ is the portion of the total Hamiltonian that describes the interaction of the spin system with the microwave resonance field.

The trace $Tr\{\rho S_Y\}$ is obtained by first taking the sum over the $|\alpha_i>$ and $|\beta_j>$ states of each quantized system, which yields the envelope modulation function, then summing over the systems that make up the inhomogeneously broadened EPR line, which gives the form of the spin echo signal, Figure I-22. These two summations can be carried out independently, if the distribution of values of $\mathcal{H}_0$,

$$\mathcal{H}_{0,k} = \mathcal{H}_{0,av} + \Delta\mathcal{H}_{0,k} , \quad [I\text{-}74]$$

about a mean value, $\mathcal{H}_{0,av}$, is such that the spread in the inhomogeneous shifts, $\Delta\mathcal{H}_{0,k}$, is large compared with the hyperfine interlevel spacings within each of the α and β electron spin manifolds. Another assumption is that $\Delta\mathcal{H}_{0,k}$ only varies the spacing between α and β electron spin manifolds but does not cause an inhomogeneous distribution of the intervals within each manifold.

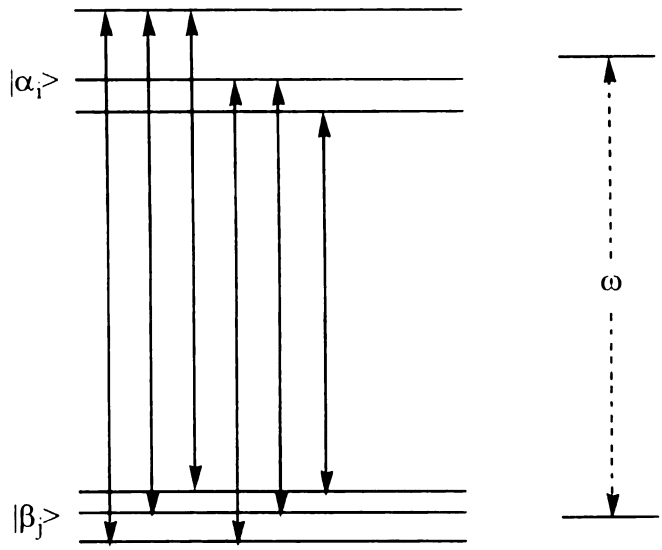

Figure I-22: Energy levels of a spin system and transitions involved in the generation of electron spin echo signals. The resonance field at frequency ω is able to induce transitions in all intervals $\omega_{\alpha,i} - \omega_{\beta,j}$.

To calculate ρ_E the integrated form of the equation of motion, Equation I-71, is applied to the successive periods $(t_f - t_i)$ of nutation and free precession that make up the spin echo sequence, Figure I-23. In the case of a S = 1/2 spin system the calculation can be performed in terms of submatrices for the α and β electron spin manifolds. For the free precession portions of the echo experiment, $\mathcal{H} = \mathcal{H}_0$, i. e., there is no time dependency in the Hamiltonian, and the solutions of Equation I-70 can be obtained in a simple form. In the representation that diagonalizes $\mathcal{H}_0$ the transformation matrices

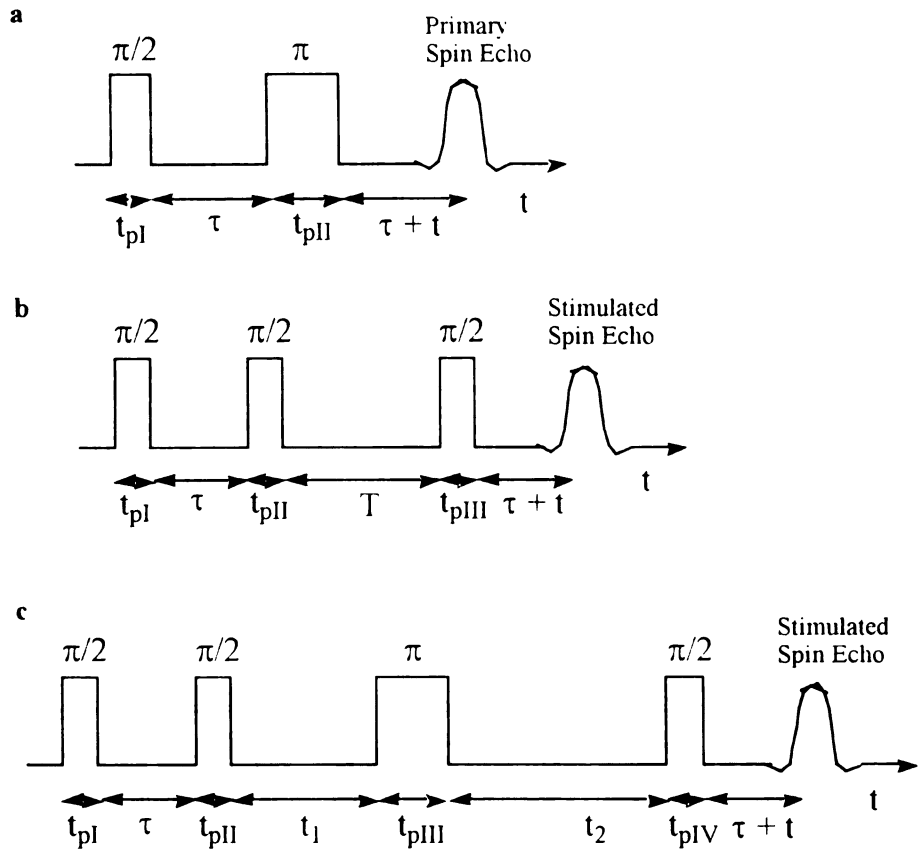

Figure I-23: Various electron spin echo pulse sequences. Each sequence consists of successive periods of nutation and free precession. (a) two-pulse sequence, $\pi/2 - \tau - \pi - \tau$; (b) three-pulse sequence, $\pi/2 - \tau - \pi/2 - T - \pi/2 - \tau$; (c) four-pulse sequence, $\pi/2 - \tau - \pi/2 - t_1 - \pi - t_2 - \pi/2 - \tau$.

$\exp[\pm i\,\mathcal{H}_0(t_f - t_i)/\hbar]$ are diagonal with elements $\exp[i\,\omega_{\alpha_i}(t_f - t_i)/\hbar]$, $\exp[i\,\omega_{\beta_j}(t_f - t_i)/\hbar]$.

Consequently, the transformation results in the off-diagonal elements of ρ being

multiplied by phase factors $\exp[i\,(\omega_{\alpha_i} - \omega_{\beta_j})(t_f - t_i)/\hbar]$, where ω_{α_i} and ω_{β_j} are the nuclear transition frequencies in the α and β electron spin manifolds, respectively.

During the pulses the system evolves under the influence of both $\mathcal{H}_0$ and $\mathcal{H}_1(t)$. The interaction of the spin system with the magnetic component of the oscillating radiation field is given by the time dependent Hamiltonian

$$\mathcal{H}_1(t) = 2\,\mathcal{H}_N \cos(\omega\, t) = \mathcal{H}_N\,[\exp(i\,\omega\, t) + \exp(-i\,\omega\, t)], \qquad [I\text{-}75]$$

where ω is the frequency of the oscillating field and the Hermitian operator $\mathcal{H}_N$ consists of the singled-out time independent factors that connect states from different electron spin manifolds. In the basis consisting of states $|\alpha_i>$, $|\beta_j>$, (i. e., in the $\mathcal{H}_{e,Z} + \mathcal{H}_{n,Z}$ representation) the matrix of this Hamiltonian can be partitioned into four submatrices,

$$\mathcal{H}_1(t) = \begin{array}{c} \begin{matrix} |\alpha_i> & |\beta_j> \end{matrix} \\ \begin{bmatrix} 0 & \mathcal{H}_N \exp(-i\,\omega\, t) \\ \mathcal{H}_N^{+} \exp(i\,\omega\, t) & 0 \end{bmatrix} \end{array}. \qquad [I\text{-}76]$$

The time dependency can be removed from $\mathcal{H}_1$ by the following similarity transformation (which is equivalent to introducing a frame rotating about z at angular frequency ω):

$$\mathcal{H}_1 = \exp(i\,\omega\,\Sigma_z\, t/2)\,\mathcal{H}_1(t)\exp(-i\,\omega\,\Sigma_z\, t/2). \qquad [I\text{-}77]$$

The matrix Σ_z has the meaning of the operator S_z. It is composed (in submatrix form) of identity matrices I of dimension equal to the number of the nuclear spin states (i. e., equal to 2I + 1, where I is the nuclear spin)),

$$\Sigma_z = \begin{bmatrix} I & 0 \\ 0 & -I \end{bmatrix}. \qquad \text{[I-78]}$$

Substitution of Equations I-76 and I-78 into Equation I-77 gives[29]

$$\mathcal{H}_1 = \begin{bmatrix} 0 & < \alpha_i \mid \mathcal{H}_N \mid \beta_j > \\ < \beta_j \mid \mathcal{H}_N^{+} \mid \alpha_i > & 0 \end{bmatrix}. \qquad \text{[I-79]}$$

After applying analogous transformations to $\mathcal{H}_0$ and ρ the whole problem is restated in the rotating frame of reference.

The appropriate rotation operators (propagators) for the nutation period p (of duration $t_{N,p}$) and the free precession period l (of duration t_l) are then expressed as

$$R_{N,p} = \exp[i\,(\mathcal{H}_0 + \mathcal{H}_1)t_{N,p}/\hbar], \qquad \text{[I-80]}$$

$$R_{t,l} = \exp[i\,\mathcal{H}_0\,t_l/\hbar]. \qquad \text{[I-81]}$$

Consecutively, the evolution of the density matrix can be cast in the form

$$\rho_E = R^{-1} \rho_0 R, \qquad [I\text{-}82]$$

where the general operator R is composed of products of $R_{N,p}$ and $R_{t,l}$ for the different nutation and free precession periods of the spin echo sequence. Since $\mathcal{H}_0$ and $\mathcal{H}_1$ are Hermitian and $R_{N,p}$ and $R_{t,l}$ unitary operators ($R^{-1} = R^+$), ρ_E can be written out as

$$\rho_E = R^+ \rho_0 R. \qquad [I\text{-}83]$$

The initial density matrix ρ_0 describes the spin system at thermal equilibrium in an applied static field $\mathbf{B}_0$. It is diagonal in the representation which diagonalizes S_z, with elements given by the Boltzmann populations ρ_{ii}^0. With the assumption that the initial Boltzmann populations of all sublevels in a given electron spin manifold are the same, ρ_0 can be written out using the submatrices $\rho_\alpha^0 = aI$, $\rho_\beta^0 = bI$ as

$$\rho_0 = \begin{bmatrix} \rho_\alpha^0 & 0 \\ 0 & \rho_\beta^0 \end{bmatrix} = \begin{bmatrix} aI & 0 \\ 0 & bI \end{bmatrix}. \qquad [I\text{-}84]$$

The rotation operators can also be written in terms of submatrices for the α and β electron spin states. Thus, the free precession operator, which contains only the static ($\mathcal{H}_0$) Hamiltonian is

$$R_{t,l} = \begin{bmatrix} P_{t,l} & 0 \\ 0 & Q_{t,l} \end{bmatrix}, \qquad \text{[I-85]}$$

while the nutation operator is expressed as

$$R_{N,p} = \begin{bmatrix} T_{N,p} & U_{N,p} \\ V_{N,p} & W_{N,p} \end{bmatrix}. \qquad \text{[I-86]}$$

The diagonal matrices P and Q for the free precession have elements

$$(P_{jj})_{t,l} = \exp[\, i\, (\, \omega_{\alpha j} - \omega/2\,)t_l\,], \qquad \text{[I-87a]}$$

$$(Q_{jj})_{t,l} = \exp[\, i\, (\, \omega_{\beta j} + \omega/2\,)t_l\,]. \qquad \text{[I-87b]}$$

P and Q are influenced by the inhomogeneous broadening term, $\Delta\mathcal{H}_{0,k}$, as they are related to the static Hamiltonian $\mathcal{H}_0$. In the $\mathcal{H}_{e,Z} + \mathcal{H}_{n,Z}$ representation $\Delta\mathcal{H}_{0,k}$ is given by the diagonal matrix

$$\mathcal{H}_{0,k} = \frac{\hbar\Delta\omega_k}{2}\begin{bmatrix} I & 0 \\ 0 & -I \end{bmatrix}. \qquad \text{[I-88]}$$

Hence, the nuclear sublevel shifts $\Delta\omega_k$ generated by the inhomogeneous broadening term appear as part of the NMR frequencies $\omega_{\alpha j}$, $\omega_{\beta j}$. As a result, scalar factors of the type $\exp(\pm\Delta\omega_k)$ are introduced into P and Q and, subsequently, into ρ_E and the modulation

function E. When accumulated over the inhomogeneously broadened line, these phase factors give rise to free induction signals that appear immediately after a pulse and last for a relatively short time. However, they do not contribute to the modulation of the electron spin echo. It is therefore permissible to keep only those matrix product terms in the trace $Tr\{\rho_E S_Y\}$, in which the scalar factors cancel out upon carrying out the multiplication of the rotation matrices.[29)]

A major simplifying assumption in the Mims approach to deriving the echo modulation function is that $\mathcal{H}_0 << \mathcal{H}_1$, which is analogous to the common assumption that the excitation bandwidth $\gamma\mathcal{H}_1$ is much larger than the EPR linewidth. It should be noted, however, that the condition $\mathcal{H}_0 << \mathcal{H}_1$ is not always satisfied since some of the matrix elements in $\mathcal{H}_1$ may be small due to the partially forbidden nature of the transitions concerned. With this assumption, however, it is relatively simple to obtain the nutation matrices $R_{N,p}$, or, equivalently, T, U, V, and W. Since $\mathcal{H}_0 << \mathcal{H}_1$, $R_{N,p} = \exp(i \mathcal{H}_1 t_{N,p}/\hbar)$, and the inhomogeneous broadening term $\Delta\mathcal{H}_{0,k}$ does not appear in the nutation matrices.

It is convenient to carry out the nutation matrix manipulations in the representation in which $\mathcal{H}_0$ is diagonal (the "interaction representation").[29)] In a basis of vectors $|M_S, M_I>$, where M_S, M_I are the electron and nuclear magnetic quantum numbers (i. e., in the representation of the combined electronic Zeeman and nuclear Zeeman interactions) the Hamiltonian $\mathcal{H}_0$ is block diagonal. The unitary transformation that completely diagonalizes $\mathcal{H}_0$ is represented in submatrix form as

$$\mathcal{H}_0^D = \begin{bmatrix} M_\alpha^+ & 0 \\ 0 & M_\beta^+ \end{bmatrix} \mathcal{H}_0 \begin{bmatrix} M_\alpha & 0 \\ 0 & M_\beta \end{bmatrix}, \qquad \text{[I-89]}$$

where M_α and M_β are unitary matrices of dimension $(2I + 1)$, which describe the state mixing caused by the hyperfine interaction in the α and β electron spin manifolds. Thus, M_α and M_β are the matrices diagonalizing the blocks of the block-diagonal Hamiltonian.

In the interaction representation $\mathcal{H}_1$ and S_Y take the form

$$\mathcal{H}_1 = \frac{\hbar \omega_N}{2} \begin{bmatrix} 0 & M \\ M^+ & 0 \end{bmatrix}, \qquad \text{[I-90]}$$

$$S_Y = \frac{i}{2} \begin{bmatrix} 0 & -M \\ M^+ & 0 \end{bmatrix}, \qquad \text{[I-91]}$$

where $M = M_\alpha^+ M_\beta$ is also a unitary matrix. The above form for H_1, along with the assumption $\mathcal{H}_0 << \mathcal{H}_1$, leads to major simplification in the nutation matrices. The operator $R_{N,p} = \exp(i\,\mathcal{H}_1 t_{N,p}/\hbar)$ can be expanded to yield

$$R_{N,p} = \begin{bmatrix} I & 0 \\ 0 & I \end{bmatrix} \cos(\omega_N t_{N,p}/2) + i \begin{bmatrix} 0 & M \\ M^+ & 0 \end{bmatrix} \sin(\omega_N t_{N,p}/2). \qquad \text{[I-92]}$$

The submatrices T, U, V, and W then take the form

$$T_{N,p} = W_{N,p} = I \cos(\omega_N t_{N,p}/2) , \qquad [I\text{-}93a]$$

$$U_{N,p} = i M \sin(\omega_N t_{N,p}/2) , \qquad [I\text{-}93b]$$

$$V_{N,p} = i M^{+} \sin(\omega_N t_{N,p}/2) . \qquad [I\text{-}93c]$$

Thus, given a specific spin system Hamiltonian, $\mathcal{H}_0$, the echo amplitude can be obtained with the above free precession and nutation matrices for any particular spin echo sequence.

For a *two pulse sequence* ρ_E at time $2\tau + t$, where t is a variable time after a waiting period τ following the last pulse, is evaluated according to

$$\rho_E = R_{\tau+t}^{+} R_{N,II}^{+} R_{\tau}^{+} R_{N,I}^{+} \rho_0 R_{N,I} R_{\tau} R_{N,II} R_{\tau+t}, \qquad [I\text{-}94]$$

with

$$R_{N,I} = \begin{bmatrix} T_I & U_I \\ V_I & W_I \end{bmatrix}, \qquad [I\text{-}95a]$$

$$R_{N,II} = \begin{bmatrix} T_{II} & U_{II} \\ V_{II} & W_{II} \end{bmatrix}, \qquad [I\text{-}95b]$$

$$R_{\tau} = \begin{bmatrix} P_{\tau} & 0 \\ 0 & Q_{\tau} \end{bmatrix}, \qquad [I\text{-}96a]$$

$$R_{\tau+t} = \begin{bmatrix} P_{\tau+t} & 0 \\ 0 & Q_{\tau+t} \end{bmatrix}, \qquad \text{[I-96b]}$$

and ρ_0 defined by Equation I-84. The evaluation of $Tr\{\rho_E S_Y\}$ by multiplying matrices given by Equations I-84, I-91, I-95, and I-96 results in a sum of sixteen product terms. However, the phase factors associated with inhomogeneous broadening cancel out in only four of them. The phase factor cancellation constraint requires that, for a term to be retained in the sum, each occurrence of a matrix P in the product must be accompanied by the presence of either a corresponding matrix Q or the adjoint of P, P^+; *and*, conversely, each occurrence of a matrix Q must have a corresponding occurrence of an appropriate matrix P or the matrix Q^+. For example, the term

$$Q_{\tau+t}{}^+ W_{II}{}^+ Q_\tau{}^+ U_I{}^+ \rho_\alpha{}^0 T_I P_\tau T_{II} P_{\tau+t} M,$$

which appears in the expression for the trace will lead to accumulation of positive phase factors from the matrices $Q_{\tau+t}{}^+$, $Q_\tau{}^+$, P_τ, and $P_{\tau+t}$, and should be excluded from the sum. On the other hand, in the term

$$Q_{\tau+t}{}^+ U_{II}{}^+ P_\tau{}^+ T_I{}^+ \rho_\alpha{}^0 U_I Q_\tau V_{II} P_{\tau+t} M,$$

the positive phase factors introduced by $Q_{\tau+t}{}^+$ and $P_{\tau+t}$ are eliminated by the negative factors introduced by $P_\tau{}^+$ and Q_τ. It is evident that exact cancellation of the phase factors

occurs when $t \cong 0$, i. e., the maximum of the echo signal is observed when the two pulses and the echo are equally spaced. Therefore, t will be set to zero in the subsequent considerations.

After elimination of the unwanted terms, the expression for the trace $Tr\{\rho_E S_Y\}$,

$$\begin{aligned} Tr\{\rho_E S_Y\} = i/2\, Tr\{ &- Q_{\tau+t}^{+}\, U_{II}^{+}\, P_{\tau}^{+}\, T_{I}^{+}\, \rho_{\alpha}^{0}\, U_I\, Q_{\tau}\, V_{II}\, P_{\tau+t}\, M \\ &+ P_{\tau+t}^{+}\, V_{II}^{+}\, Q_{\tau}^{+}\, U_{I}^{+}\, \rho_{\alpha}^{0}\, T_I\, P_{\tau}\, U_{II}\, Q_{\tau+t}\, M^{+} \\ &- Q_{\tau+t}^{+}\, U_{II}^{+}\, P_{\tau}^{+}\, V_{I}^{+}\, \rho_{\beta}^{0}\, W_I\, Q_{\tau}\, V_{II}\, P_{\tau+t}\, M \\ &+ P_{\tau+t}^{+}\, V_{II}^{+}\, Q_{\tau}^{+}\, W_{I}^{+}\, \rho_{\beta}^{0}\, V_I\, P_{\tau}\, U_{II}\, Q_{\tau+t}\, M^{+}\}. \end{aligned} \qquad [I\text{-}97]$$

contains both product terms and their Hermitian conjugates. Combining each term with its Hermitian conjugate and substituting matrices ρ_{α}^{0}, ρ_{β}^{0}, T, U, V, and W according to Equations I-84 and I-93 one obtains the general expression for the (unnormalized) two-pulse echo modulation function:

$$\begin{aligned} E(\tau) = (1/2)\,(a - b)\, \sin(\omega_N t_{pI})\, \sin^2(\omega_N t_{pII}/2) \times \\ Tr\{ Q_{\tau+t}^{+}\, M^{+}\, P_{\tau}^{+}\, M\, Q_{\tau}\, M^{+}\, P_{\tau+t}\, M \\ - Q_{\tau+t}^{+}\, M^{+}\, P_{\tau}^{+}\, M\, Q_{\tau}\, M^{+}\, P_{\tau+t}\, M \}. \end{aligned} \qquad [I\text{-}98]$$

The normalization factor $Tr\{\rho_0\, S_Y\}$ for the envelope modulation function is given by the echo amplitude at $\tau \rightarrow 0$ and can be found by setting all free precession matrices P and Q

equal to the identity matrix I. Under these conditions the trace becomes $\mathrm{Tr}\{I\}$, which equals the number of hyperfine levels (i. e., 2I + 1, where I is the nuclear spin) in each electron spin manifold. The normalized two-pulse echo modulation function is then

$$E_n(\tau) = \mathrm{Tr}\{ Q_{\tau+t}^{+} M^{+} P_{\tau}^{+} M Q_{\tau} M^{+} P_{\tau+t} M$$
$$- Q_{\tau+t}^{+} M^{+} P_{\tau}^{+} M Q_{\tau} M^{+} P_{\tau+t} M\} / \mathrm{Tr}\{I\}. \qquad \text{[I-99]}$$

For a four-level electron-nuclear system, Figure I-17, described by the Hamiltonian given by Equation I-54, the unitary transformation matrix M has a simple form:

$$M = \begin{bmatrix} v & u \\ -u^{*} & v^{*} \end{bmatrix}, \qquad \text{[I-100]}$$

and the normalized echo modulation function takes the form

$$E_n(\tau) = |v|^4 + |u|^4 + |v|^2|u|^2 \{2\cos(\omega_\alpha\tau) + 2\cos(\omega_\beta\tau)$$
$$- \cos[(\omega_\alpha - \omega_\beta)\tau] - \cos[(\omega_\alpha + \omega_\beta)\tau]\}, \qquad \text{[I-101]}$$

where $\omega_\alpha = \omega_a - \omega_b$, $\omega_\beta = \omega_c - \omega_d$. The matrix elements $|u|$ and $|v|$ that describe the extent to which the branching transitions are allowed or forbidden can be determined by applying transformations, which can be described as rotations of the electron and nuclear coordinate systems. By diagonalizing the electron Zeeman and electron-nuclear portions of a general Hamiltonian $\mathcal{H}_0$ in the basis of eigenvectors of the electron spin operator S_z,

the electron z axis is rotated along the direction of quantization of the electron spin. The nuclear spin coordinate system does not have to be the same as that for the electron spin. It can be defined through the basis of eigenvectors of the nuclear spin operator I_z, in which the nuclear Zeeman term is diagonal. A rotation of the nuclear xy axes about the nuclear z axis can be performed to eliminate the I_y term. One thus obtains the following two Hamiltonians, whose combination is equivalent to the Hamiltonian in Equation I-54,

$$\mathcal{H}_\alpha / \hbar = \omega_I I_z + 1/2\ A\ I_z + 1/2\ B\ I_x\ , \qquad \text{[I-102a]}$$

$$\mathcal{H}_\beta / \hbar = \omega_I I_z - 1/2\ A\ I_z - 1/2\ B\ I_x\ . \qquad \text{[I-102b]}$$

The eigenfrequencies of these Hamiltonians are

$$\omega_\alpha = [(\omega_I - A/2)^2 + (B/2)^2]^{1/2}\ , \qquad \text{[I-103a]}$$

$$\omega_\beta = [(\omega_I + A/2)^2 + (B/2)^2]^{1/2}\ , \qquad \text{[I-103b]}$$

and the corresponding eigenvectors determine the transition probabilities, or the elements of the transformation matrices $M = M_\alpha^{+} M_\beta$,

$$u = \sin[(\eta - \xi)/2], \qquad \text{[I-104a]}$$

$$v = \cos[(\eta - \xi)/2], \qquad \text{[I-104b]}$$

where η and ξ are defined by

$$\tan(\xi) = B / (A + 2\,\omega_I), \qquad \text{[I-105a]}$$

$$\tan(\eta) = B / (A - 2\,\omega_I). \qquad \text{[I-105b]}$$

The product $|v|^2|u|^2$ defines the modulation depth

$$k = 4\,|v|^2|u|^2 = \sin^2(\eta - \xi) = [\omega_I B/(\omega_\alpha \omega_\beta)]^2. \qquad \text{[I-106]}$$

After substituting u and v, Equation I-104, in Equation I-101 one obtains the final form of the two-pulse echo modulation function for a S = 1/2, I = 1/2 spin system, Equation I-57.

The Fourier[31] or parametric[38] analysis of the ESEEM time domain data reveals information on hyperfine interactions that is identical to that obtained in an ENDOR experiment. The two methods are often considered to be complementary to each other. Because of the constraints placed on ESEEM by the requirements of nuclear state mixing and microwave pulse bandwidth, the technique is generally more suitable for measuring weak hyperfine couplings of nuclei with small magnetic moments. The ENDOR experiments on such systems are typically difficult. Unlike in ENDOR, the amplitudes of the lines in an ESEEM spectrum can be used to quantitate the number of nuclei giving rise to an interaction once the coupling parameters have been determined.[39-41] However, the ESEEM data are more difficult to analyze and often require computer simulations to extract all of the information on magnetic couplings contained in the spectrum. Part of the reason for the greater complexity of the ESEEM data analysis is illustrated in Figure I-24.[24] Trace (a) shows the simulated powder ENDOR spectrum for an S = 1/2, I = 1/2 system with an axial hyperfine spectrum. In this case the tensor

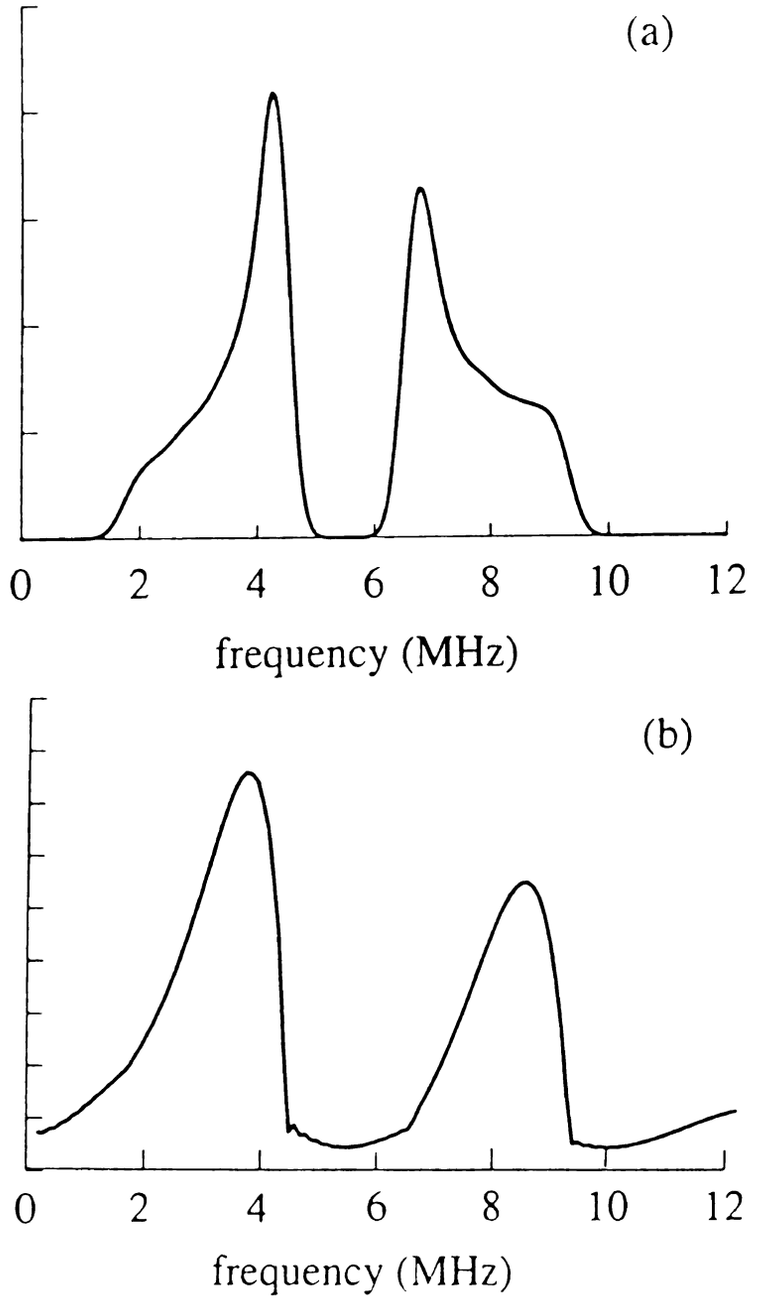

Figure I-24: Simulations of (a) powder ENDOR spectrum and (b) a three-pulse ESEEM spectrum for an S = 1/2, I = 1/2 spin system. Parameters: g = 2.004, g_n = 2.261 (^{31}P), $A_{||}$ = 7.0 MHz, $A_{\perp}$ = 2.4 MHz, B_0 = 3200 G; τ = 200 ns; dead-time, 240 ns. (From Ref. 24)

symmetry and principal values can be readily determined from the frequencies of the turning points and lineshape singularities.[42] The corresponding ESEEM spectrum displayed in trace (b) shows no lineshape features, because the intensity of the ESEEM is determined by the product of the orientation dependent coupling parameter (which gives rise to the classical lineshape seen in (a)) with the orientation dependent modulation depth parameter, k. k goes to zero at the canonical orientations (the turning points and lineshape singularities) because one of the EPR transition probability amplitudes, |u| or |v|, becomes zero.[43] Thus, the information on the hyperfine interactions is contained in the frequencies, amplitudes, and dumping characteristics of the modulations, which necessitates the use of computer simulations of the ESEEM data.

References

1. Zavoisky E. *J. Phys. U.S.S.R.* **1945**, *9*, 211.

2. Poole, C. P.; Farach, H. A., eds., *Handbook of Electron Spin Resonance, Data Sources, Computer Technology, Relaxation and ENDOR*, American Institute of Physics: New York, 1994.

3. Atherton, N. M. *Principles of Electron Spin Resonance*, Ellis-Harwood PTR Prentice Hall: New York, 1993.

4. Wertz, J. E.; Bolton, J. R. *Electron Spin Resonance, Elementary Theory and Practical Applications*, Chapman and Hall: New York, 1986.

5. Gordy, W. in *Techniques in Chemistry, Vol. XV: Theory and Applications of Electron Spin Resonance*; West, W., Ed.; Wiley: New York, 1980.

6. Carrington, A.; McLachlan, A. D. *Introduction to Magnetic Resonance with Applications to Chemistry and Chemical Physics*, Harper and Row: New York, 1967.

7. Pake, G. E.; Estle, T. L. *The Physical Principles of Electron Paramagnetic Resonance*, W. A. Benjamin, Inc.: Massachusetts, 1973.

8. Poole, C. P.; Farach, H. A. *The Theory of Magnetic Resonance*, Wiley-Interscience: New York, 1972.

9. Ayscough, P. B. *Electron Spin Resonance in Chemistry*, Methuen and Co. Ltd.: London, 1967.

10. Dorio, M. M.; Freed, J. H., eds., *Multiple Electron Resonance Spectroscopy*, Plenum Press: New York, 1979.

11. Kevan, L.; Kispert, L. D. *Electron Spin Double Resonance Spectroscopy*, Wiley-Interscience: New York, 1976.

12. Kurreck, H.; Kirste, B.; Lubitz, W. in *Methods in Stereochemical Analysis, Electron Nuclear Double Resonance Spectroscopy of Radicals in Solution, Application to Organic and Biological Chemistry*; Marchand, A. P., Ed.; VCH Publishers, Inc.: New York, 1988.

13. Kevan, L.; Bowman M. K., eds., *Modern Pulsed and Continuous-Wave Electron Spin Resonance*, Willey-Interscience: New York, 1990.

14. Keijzers, C. D.; Reijerse, E. J.; Schmidt, J. *Pulsed EPR: A New Field of Applications*, North Holland: Amsterdam, 1989.

15. Kevan, L.; Schwartz, R. N., eds., *Time Domain Electron Paramagnetic Resonance*, Wiley: New York, 1979.

16. Dikanov, S. A.; Tsvetkov, Yu. D. *Electron Spin Echo Envelope Modulation (ESEEM) Spectroscopy*, CRC Press: Boca Raton, 1992.

17. Adrian, F. J.; Cochran, E. L.; Bowers, V. A. *J. Chem. Phys.* **1965**, *43*, 462.

18. McConnell, H. M. *J. Chem. Phys.* **1956**, *24*, 632, 764.

19. Heller, C.; McConnell, H. M. *J. Chem. Phys.* **1960**, *32*, 1535.

20. Rehorek, D.; Hennig, H. *Z. Chem.* **1980**, *20*, 109.

21. Schweiger, A. in *Lecture Notes in Chemistry, Vol. 21, Electron Nuclear Double Resonance of Transition Metal Complexes with Organic Ligands*, Springer-Verlag: Berlin, 1982.

22. Feher, G. *Phys. Rev.* **1956**, *103*, 834.

23. Kwiram, A. L *J. Chem. Phys.* **1968**, *49*, 2860-2861.

24. McCracken, J. In *Handbook of Electron Spin Resonance*, Vol. II, Poole, C. P.; Farach, H. A., eds., in press.

25. Schweiger, A. *Angew Chem. Int. Ed. Engl.* **1991**, *30*, 265.

26. Ponti, A.; Schweiger, A. *Appl. Magn. Reson.* **1994**, *7*, 363.

27. Slichter, C. P. *Principles of Magnetic Resonance*, 3rd ed., Springer Verlag: Berlin, 1989.

28. Filep, G. *Ph. D. Dissertation*, Michigan State University, 1997.

29. Mims, W. B. *Phys. Rev.* **1972**, *B 5(7)*, 2409.

30. Mims, W. B. *Phys. Rev.* **1972**, *B 6(9)*, 3543.

31. Mims, W. B. *J. Magn. Reson.* **1984**, *59*, 291.

32. Mims, W. B. *Rev. Sci. Instr.* **1965**, *36*, 1472.

33. Mims, W. B.; Peisach, J. In *Advanced EPR: Applications in Biology and Biochemistry*, A. Hoff, Ed.; Elsevier: New York, 1988; Chapter 1.

34. Kevan, L., In *Time Domain Electron Paramagnetic Resonance*, Kevan, L.; Schwartz, R. N., eds., Wiley: New York, 1979, Chapter 8.

35. Schweiger, A. In *Modern Pulsed and Continuous-Wave Electron Spin Resonance*, Kevan, L.; Bowman M. K., eds., Willey-Interscience: New York, 1990; Chapter 2.

36. Feynman, R. P. *Statistical Mechanics: A set of Lecture Notes*, Benjamin: Reading, Mass., 1972.

37. Abragam, A. *The Principles of Nuclear Magnetism*, Oxford University Press, 1961.

38. DeBeer, R.; Van Ormondt, D.; Punappel, W. W. F.; van der Veen, J. W. C., *Is. J. Chem.* **1988**, *28*, 249.

39. Kevan, L.; Bowman M. K.; Narayana, P. A.; Boeckman, R. K. *J. Chem. Phys.* **1975**, *63*, 409.

40. Mims, W. B.; Peisach, J.; Davis, J. L. *J. Chem. Phys.* **1977**, *66*, 5536.

41. McCracken, J.; Pember, S.; Benkovic, S. J.; Villafranca, J. J.; Miller, R. J.; Peisach, J. *J. Am. Chem. Soc.* **1988**, *110*, 1069.

42. Blinder, S. M. *J. Chem. Phys.* **1960**, *33*, 748.

43. DeGroot, A.; Evelo, R.; Hoff, A. J. *J. Magn. Res.* **1986**, *66*, 331.

Chapter II

CW-EPR, ENDOR and ESEEM Studies of Pyruvate:Ferredoxin Oxidoreductase (PFOR) Reaction Intermediates

II.1. Introduction

Pyruvate:Ferredoxin Oxidoreductase (PFOR) belongs to the class of redox enzymes.[1,2] Such enzymes are defined as those that catalyze a reaction with an associated electron transfer event, wherein an external electron carrier is either reduced or oxidized. Enzymes that belong to this group are termed oxidoreductases, reductases, oxidases, or dehydrogenases, often for historical reasons. The main distinction between oxidoreductases and dehydrogenases lies in the nature of the electron carrier that the enzymes use. A characteristic of the oxidoreductases is the presence of metal-containing centers, which are typically iron-based. These centers can either function directly in substrate activation or, more typically, participate in the intra- and intermolecular transfer of electrons to or from an external electron donor. In contrast, the dehydrogenases are enzymes that make use of nicotinamide nucleotides as electron carriers. They usually do not contain a metal center that undergoes a redox reaction. Both dehydrogenases and oxidoreductases play role in the anaerobic fermentative metabolism.

In this Chapter an introduction to the 2-keto oxidoreductase enzymes is given, followed by a summary of the general, structural and functional properties of PFOR and the proposed reaction mechanism. The results of a CW-EPR, ENDOR, and ESEEM study

of the PFOR reaction intermediates are presented and discussed with an aim of elucidating some aspects of the reaction mechanism.

II.1.1. 2-Keto oxidoreductases

Common substrates in the anaerobic catabolism are the 2-keto carboxylic acids. Enzymes known as 2-keto oxidoreductases catalyze the oxidative decarboxylation of 2-keto acids with the transfer of the acyl moiety to coenzyme A (CoASH) as shown in Equation II-1.[2)]

$$RCOCOOH + CoASH \rightarrow RCOSCoA + CO_2 + 2H^+ + 2e^- \qquad [II\text{-}1].$$

The electrons from this reaction are transferred to low-potential redox-proteins such as ferredoxin or flavodoxin to be either disposed as H_2 or included in an organic compound.

Four types of 2-keto acid oxidoreductases have been characterized and studied in hyperthermophilic (i. e., microorganisms that grow at or above 90° C) and mezophilic microorganisms.[2)] They are classified and named according to the substrate used in their purification: POR (pyruvate substrate),[3,4)] IOR (indole pyruvate substrate),[5)] VOR (2-ketoisovalerate substrate),[6)] KGOR (2-ketoglutarate substrate).[7)] All 2-keto acid oxidoreductases appear to be composed of two "catalytic units" of $M_r \sim 120{,}000$. In enzymes from different sources a catalytic unit either exists as a single large subunit or consists of two or four subunits.[2)] For example, a single large subunit, denoted as subunit *A*, constitutes a catalytic unit of mesophilic bacterial and eucaryotic enzymes. Mesophilic archaeon *Hm. halobium* and hyperthermophilic IOR's have catalytic units consisting of

two subunits, *ab*. The catalytic unit in all other hyperthermophilic enzymes exists as a set of $\alpha\beta\gamma\delta$ subunits. There exists homology between *a* and α subunits and between *b* and β or γ subunits. The single subunit of the mesophilic enzymes also resembles the composite subunit in the other enzymes in that it contains $\alpha\beta\gamma\delta$ domains. All of the 2-keto acid oxidoreductases contain iron-sulfur clusters and thiamin pyrophosphate (TPP), although in different amounts. Typical TPP content is less than 1 mol per 120 kDa unit. The iron content varies from 3.5 to 12 atoms per 120 kDa unit. The iron content has been found to decrease upon exposure of the enzyme to oxygen due of the damage to the iron-sulfur clusters by O_2. Analyses of the 2-keto acid oxidoreductases by EPR spectroscopy have indicated that the enzymes contain two or more $[Fe_4S_4]$ clusters of the type found in 4Fe ferredoxins.[2] Thus, POR enzymes contain one iron-sulfur cluster per 120 kDa unit. Since the 2-keto acid oxidoreductases have the same fundamental structure and cofactor content (as shown by sequence analyses), they are expected to differ only in substrate specificity but not in the fundamental mechanism of catalysis.

Studies of the mechanism of 2-keto acid oxidation by oxidoreductase enzymes are based on the pioneering investigation of Oesterhelt and co-workers (1980) with the POR from *Hm. halobium* (*Halobacterium salinarium*).[8-11] They have detected a stable free radical by EPR spectroscopy in pure preparations of the enzyme, Figure II-1. The intensity of the radical signal has been found to increase upon addition of pyruvate, and to disappear with the addition of coenzyme A.[8,9] It has been shown that the reaction with pyruvate has lead to the reduction of a $[Fe_4S_4]$ cluster as well as radical formation, and to the tight binding of the decarboxylated substrate to the enzyme. The observation of spin coupling between the radical and the cluster has indicated that they must be in

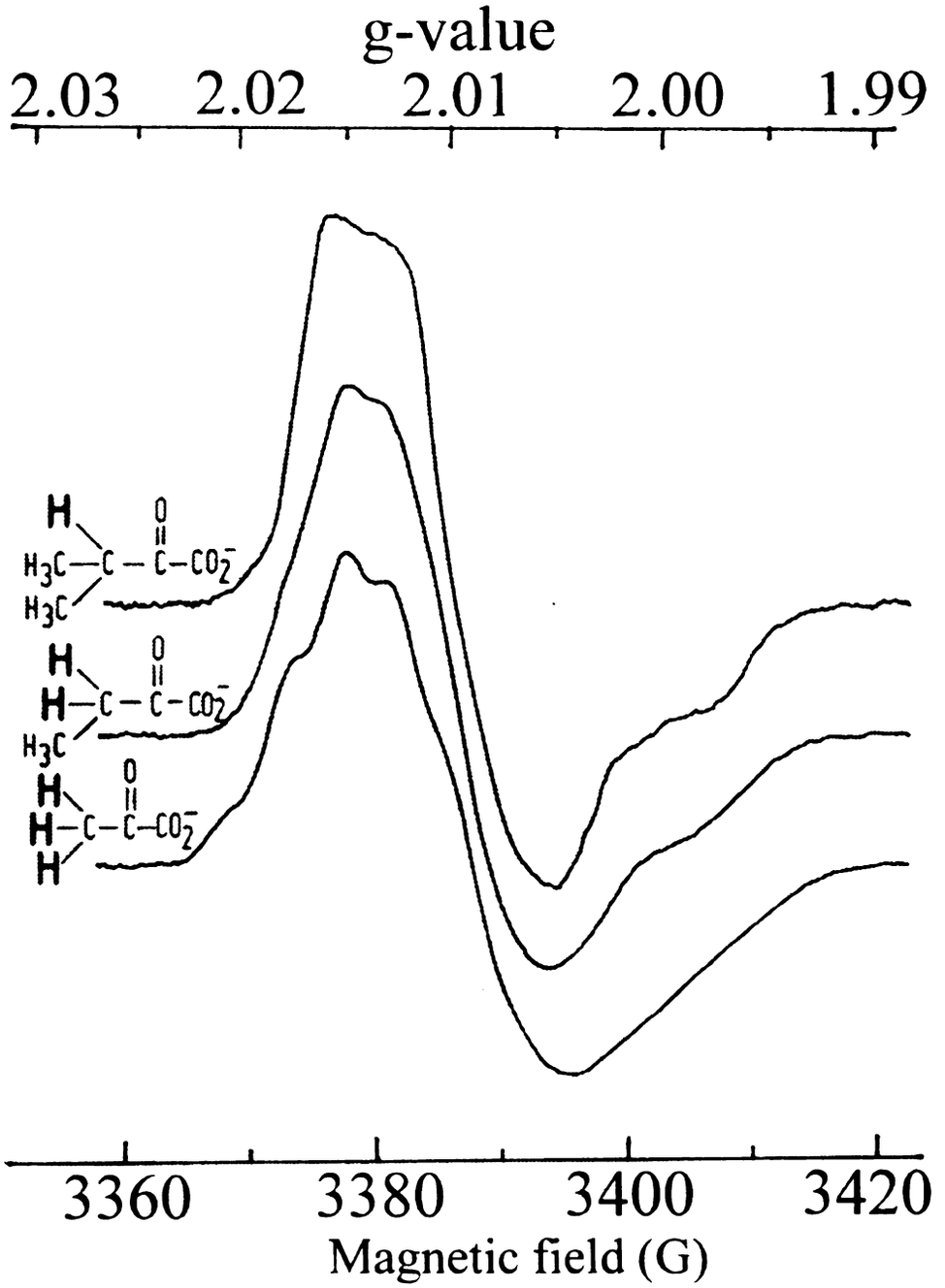

Figure II-1: First-derivative EPR spectra of PFOR from *Hm. Halobium*. (From Ref. 11)

close proximity (≤10 Å). The authors have therefore proposed that in the first step of catalysis pyruvate is bound covalently by its C-2 atom to the C-2 atom of TPP generating hydroxyethyl-TPP (HE-TPP), while the C-1 carboxyl group is released as CO_2.[10] The (oxidized) $[Fe_4S_4]^{2+}$ cluster then oxidizes HE-TPP to form a stable TPP=C-O·-R radical intermediate and the reduced cluster. Latter studies have shown that the addition of the 2-keto acid substrate to the oxidized form also leads to the detection of a stable, organic radical in POR,[4] IOR,[5] VOR,[6] and KGOR[7] from different sources. On the other hand, no stable radical has been observed on pyruvate addition to the POR from some sources,[4,12] while with VOR[6] and KGOR,[7] the formation of stable radical has been found to be dependent on the addition of TPP as well as the substrate and accompanied by the appearance of an EPR signal from a reduced $[Fe_4S_4]$ cluster. The TPP addition dependency suggests that these results may be due to loss of TPP during enzyme purification.

The current model for the structure of the 2-keto acid oxidoreductases and the proposed pathway of electron flow during catalysis is shown in Figure II-2.[2] The two sets of heterotetramers, α, β, γ, and δ, that constitute the holoenzymes are assumed to be catalytically independent. A 2-keto acid reducible $[Fe_4S_4]$ cluster is located in the β subunit, whereas two other $[Fe_4S_4]$ clusters are assigned to the δ subunit. In the absence of exogenous electron acceptor and in the presence of excess coenzyme A (CoA) and 2-keto acid, acyl-CoA is produced and the two $[Fe_4S_4]$ centers in the δ subunit become reduced, presumably one electron at a time via the β subunit $[Fe_4S_4]$ center. A second molecule of the 2-keto acid reacts to generate TPP-based radical and a reduced β subunit

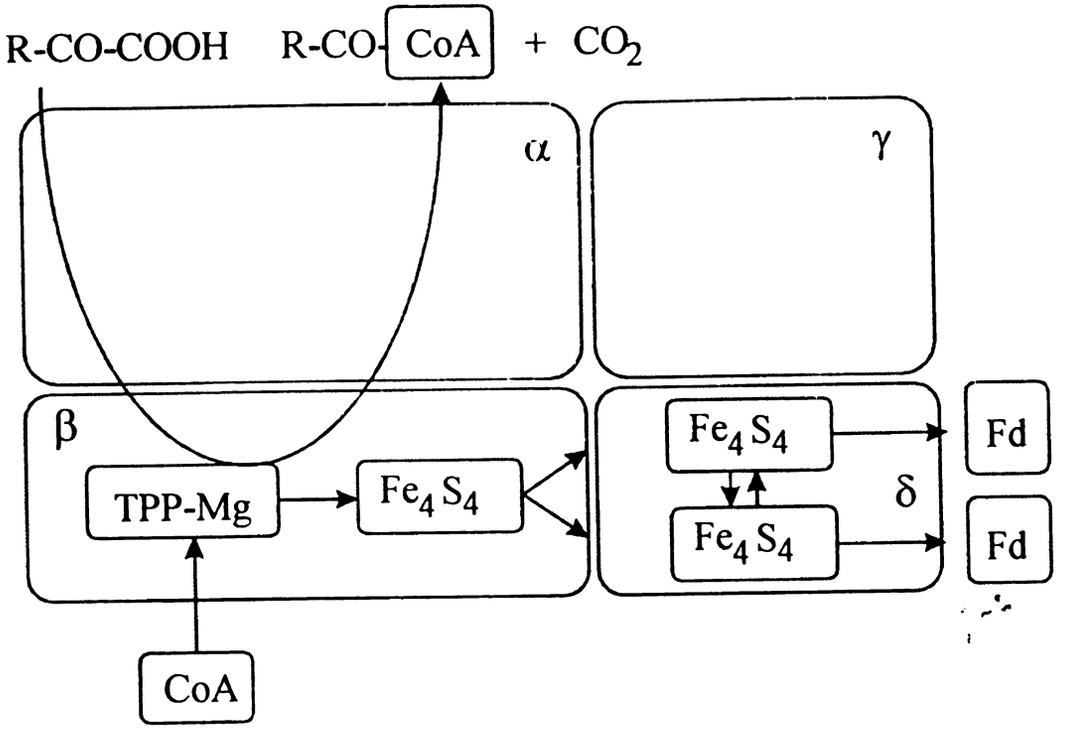

Figure II-2: Four subunit catalytic model of 2-keto acid oxidoreductases. (From Ref. 2)

$[Fe_4S_4]$ center. This form of the enzyme contains four unpaired electrons per heterotetramer. The enzymes that lack the δ subunit, e. g., *Hm. Halobium* POR reduce ferredoxin via the β subunit/domain.

Rationalizing the mechanism of the 2-keto acid oxidoreductase reaction lacks proper understanding of how these enzymes catalyze the reaction between two nucleophiles, hydroxyacyl-TPP and coenzyme A. In the well-characterized pyruvate dehydrogenase (PDH) complex found in aerobic organisms, the reaction between the PDH

TPP and coenzyme A is mediated by lipoic acid. (The PDH complex is similar to POR in that it catalyzes the same reaction - the oxidative decarboxylation of pyruvate to acetyl-CoA; however it differs from oxidoreductases in that it lacks iron-sulfur clusters, contains flavin and lipoic acids, and uses nicotinamid dinucleotide (NAD) as an electron carrier.)[13] The mechanism of pyruvate oxidation by PDH involves formation of an intermediate hydroxyethyl-TPP anion instead of a HE-TPP radical. The anion reacts with the oxidized form of lipoic acid to form acetyllipoic acid, which then reacts with coenzyme A to generate acetyl-CoA. With the mezophilic oxidoreductases, which have been shown to exhibit the TPP radical signal (e. g., *Hm. halobium*), two types of mechanisms have been proposed for the reaction of coenzyme A with the hydroxyacyl-TPP radical and the reduced $[Fe_4S_4]$ clusters. According to the mechanism given by Kerscher and Oesterhelt,[9] the processes of decarboxylation, radical formation, and reaction with coenzyme A to yield acyl-CoA all take place at the same enzyme site. The $[Fe_4S_4]$ cluster is first oxidized by the external electron acceptor. Coenzyme A then reacts with hydroxyacyl-TPP, causing transfer of an electron to the oxidized $[Fe_4S_4]$ cluster, while the coenzyme A accepts the acyl group. Docampo et al. (1987) have proposed an alternative mechanism based on their observation of a second intermediate radical.[14] This species has been assigned to a thiyl derivative of coenzyme A, CoAS·, generated by a direct reaction of coenzyme A with an oxidized $[Fe_4S_4]$ cluster. The thyil radical then reacts with the hydroxyacyl-TPP radical to form acyl-CoA and TPP.

Whether actual differences in the catalytic mechanism of 2-keto acid oxidoreductases exist or the reported variations reflect different methods of enzyme purification and/or sample preparation, is yet to be determined.

II.1.2. Mechanism of the oxidative decarboxylation of pyruvate by PFOR

Pyruvate:Ferredoxin Oxidoreductase (PFOR) is a member of the 2-keto acid oxidoreductase family, which plays a role in the anaerobic fermentative metabolism.[15] In its function, it is similar to enzymes such as pyruvate dehydrogenase (PDH), pyruvate decarboxylase (PDC), pyruvate oxidase, and pyruvate:formate lyase. All these enzymes can initiate pyruvate catabolism. For example, PDH and PFOR both catalyze the oxidative decarboxylation of pyruvate to acetyl-CoA and CO_2. However, unlike PDH, PFOR lacks lipoamide and is able to reduce a number of electron carriers such as ferredoxin (Fd), flavodoxin, and viologens, but not pyridine nucleotides.

The oxidative decarboxylation of pyruvate by PFOR occurs according to the following half-reaction:[16]

$$CH_3COCOO^- + CoASH \xrightleftharpoons{E_0=-540mV} CH_3COSCoA + CO_2 + H^+ + 2e^- \qquad \text{[II-2]}$$

In anaerobic acetogenic bacteria such as *Clostridium thermoaceticum*, CO_2 is reduced to CO by a bifunctional enzyme, CO dehydrogenase/acetyl-CoA synthase (CODH/ACS). CO generated *in situ* combines with the acetyl-CoA synthase active site to form a paramagnetic adduct, called the NiFeC species, which, in turn, is condensed with a bound methyl group and coenzyme A to generate acetyl-CoA. The acetyl-CoA is used both as a carbon and energy source by acetogenic bacteria.[17,18]

However, the cofactor content and the mechanism of PFOR remain controversial. Although the number of $[Fe_4S_4]$ clusters may vary in the different PFORs, apparently only two prosthetic groups are required for decarboxylation: TPP, Figure II-3, and $[Fe_4S_4]$ clusters.[19] Recently, Menon and Ragsdale[16] have used a combination of rapid freeze-quench EPR and stopped-flow spectroscopy to elucidate and quantify the elementary steps in the reaction mechanism of *Clostridium thermoaceticum* PFOR. Their kinetic data reveal the intermediacy of a radical, which has been identified as the hydroxyethyl thiamin pyrophosphate radical (HE-TPP), and proposed as a common transient intermediate in the catalytic reaction of PFORs from different sources. The

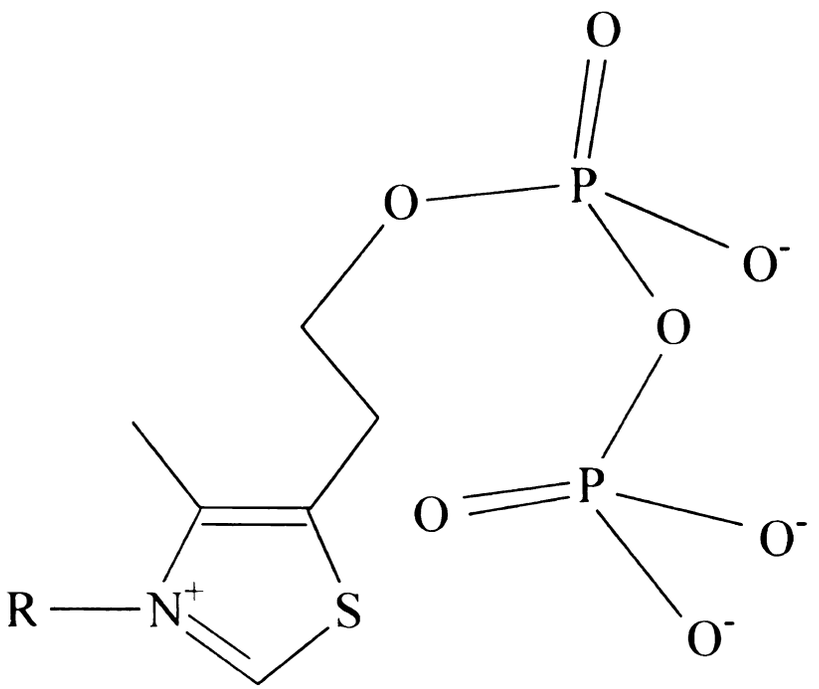

Figure II-3: Thiamin pyrophosphate prostetic group of PFOR.

mechanism for the oxidation of pyruvate by PFOR is illustrated in Figure II-4 and is similar to that of *Hm. halobium* PFOR proposed by Oesterhelt and co-workers. Thus, it complies with the idea that PFORs with different subunit composition and different cluster compositions should have essentially the same catalytic mechanism.[19] The first two steps in the reaction mechanism are common for PFOR, PDH, PDC, and thiamine pyrophosphate (TPP) in solution. The enzyme reacts with pyruvate to form a pyruvoil-TPP adduct (step 1) which decarboxylates to yield hydroxyethylidine-TPP intermediate (step 2). At step 3, one electron is transferred from hydroxyethylidine-TPP to one of the two $[Fe_4S_4]$ clusters generating a pyruvate-derived radical, the hydroxyethyl-TPP (HE-TPP) radical. Steps 4 and 5 involve transfer of one electron from the HE-TPP radical to another $[Fe_4S_4]$ cluster leaving an acetyl-TPP intermediate that undergoes cleavage by coenzyme A to form acetyl-CoA. These steps leave the enzyme in the two-electron reduced state, with both $[Fe_4S_4]$ clusters reduced. Completion of the catalytic cycle (step 6) requires two-electron oxidation of PFOR by external electron acceptors, such as ferredoxin (Fd) or flavodoxin, CODH/ACS, or even protons when electron acceptors are limiting. The intermediacy of the HE-TPP radical has been assumed on the basis of the fact that an EPR signal arises at $g = 2.008$ after the TPP-dependent decarboxylation of pyruvate, but before coenzyme A takes part in the reaction. However, no direct spectroscopic evidence for the presence of the TPP in the spin system has been found. There is controversy surrounding even the existence of this radical since it has not been detected with all PFORs.

The EPR spectra of frozen PFOR intermediates lack resolution, even when low modulation amplitude is used, because of the inhomogeneous line broadening (cf.

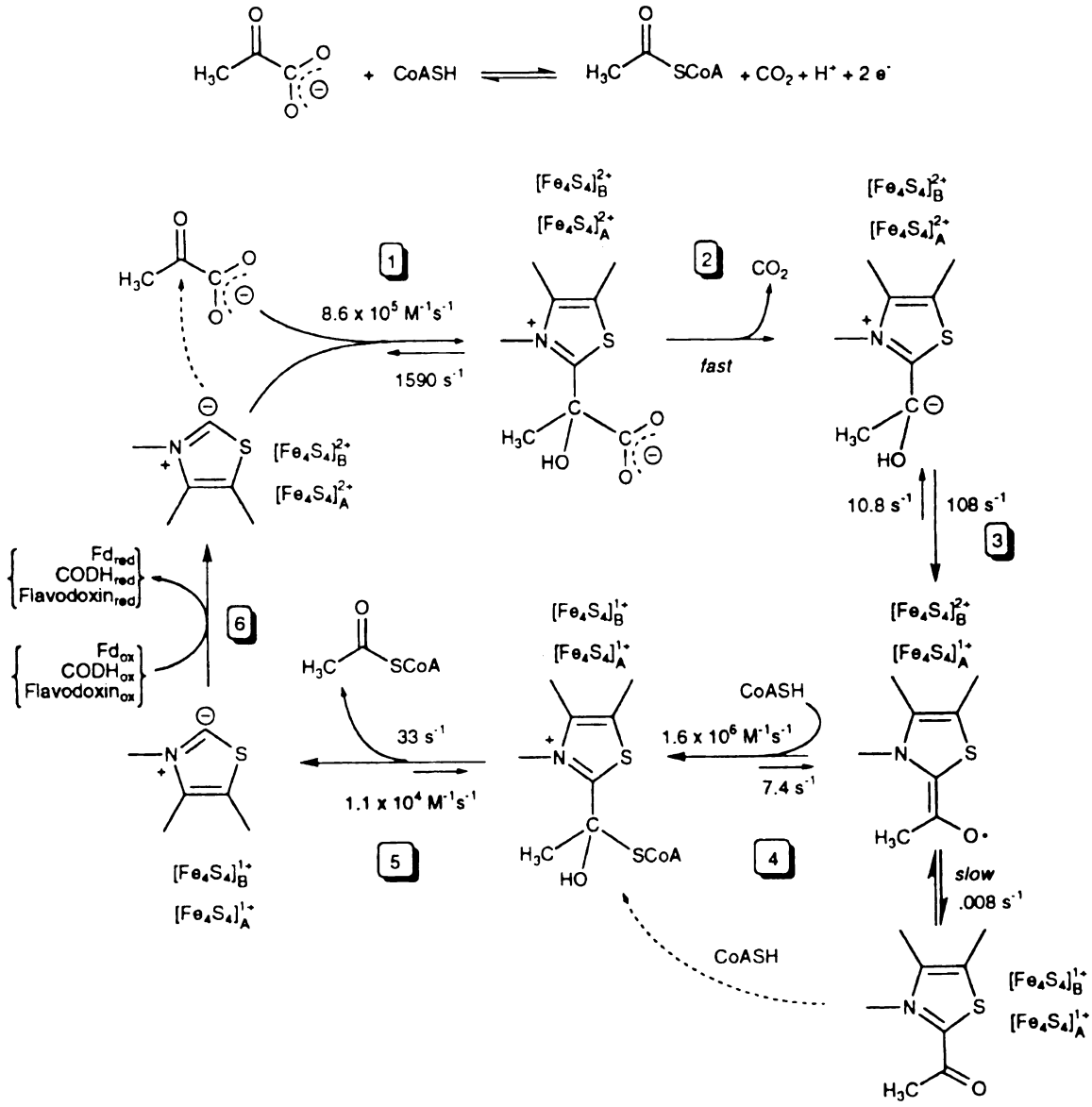

Figure II-4: Mechanism of the PFOR catalyzed reaction. Steps: (1) pyruvate binding; (2) formation of hydroxyethylidene-TPP intermediate; (3) formation of HE-TPP radical and reduction of cluster A; (4) CoA binding and reduction of cluster B; (5) formation of acetyl-CoA and regeneration of TPP anion; (6) reduction of external electron acceptors. (From Ref. 16)

Chapters I). The inhomogeneous spectral broadening masks the details of the EPR spectrum and reduces the certainty in the determination of magnetic properties for identification and characterization of the paramagnetic species in question. Figure II-5

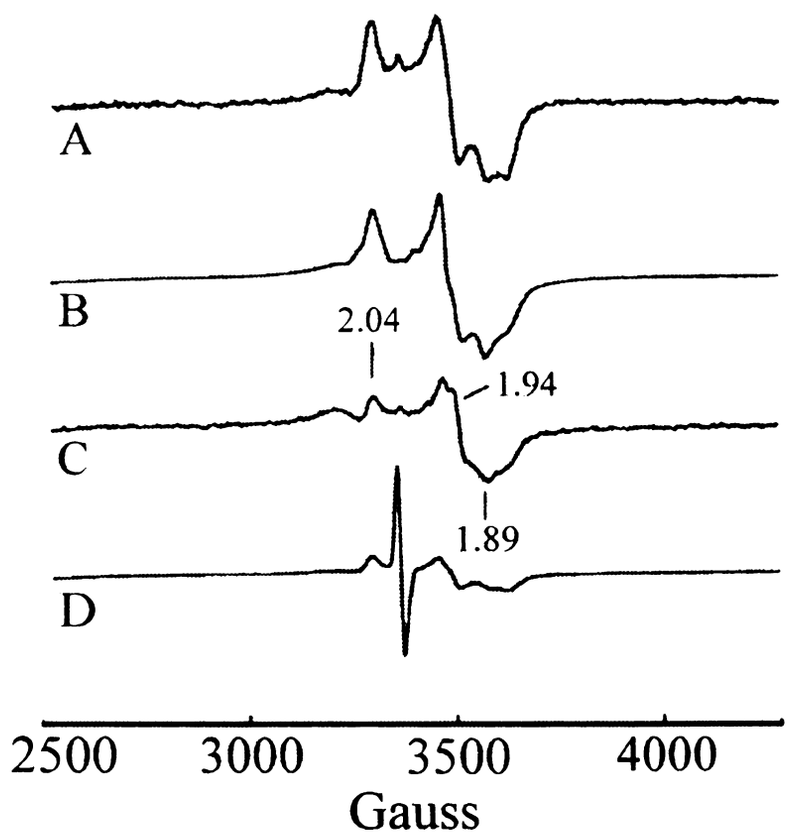

Figure II-5: First-derivative EPR spectra of *Clostridium Thermoaceticum* PFOR incubated with (A) sodium dithionite, (B) pyruvate and CoA, (C) CoA, or (D) pyruvate. EPR parameters: spectral width, 2000 G; field center, 3400 G; modulation frequency, 100 kHz; modulation amplitude, 10 G; temperature, 10 K; microwave power, 2 mW; microwave frequency, 9.447 GHz. (From Ref. 16)

shows the EPR spectra reported in Ref. 16, which are obtained from PFOR under different conditions. PFOR as isolated is EPR silent. When reduced by dithionite at pH 9.0, a complex EPR spectrum has been recorded, Figure II-5 (A). The observed spectrum, which cannot be explained by simple rhombic signals has been attributed to electron spin coupled $[Fe_4S_4]$ clusters that are within approximately 10 Å of each other (i. e., arising from a through-space dipolar magnetic interaction). The double integral of the spectrum has indicated that the $[Fe_4S_4]$ clusters are fully reduced. A similar spectrum has been obtained after reacting the enzyme with pyruvate and coenzyme A, Figure II-5 (B). Reaction of PFOR with coenzyme A alone has yielded the EPR spectrum shown in Figure II-5 (C), with g values at 2.04, 1.94 and 1.89. The signal intensity has indicated that half of the $[Fe_4S_4]$ centers have been reduced. An EPR spectrum which consists of an isotropic radical signal centered at 2.008 and a rhombic signal similar to that in the previous case has been recorded upon reacting PFOR with pyruvate alone, Figure II-5 (D). The signal intensity corresponds to two spins per monomeric unit of the enzyme. It has therefore been concluded that half of the spins reside in an $[Fe_4S_4]$ cluster and half in the radical. The complex EPR lineshape for the cluster has indicated that the reduced $[Fe_4S_4]$ cluster and the radical are close enough to experience magnetic dipolar interactions. The radical signal has disappeared after addition of coenzyme A, which has been interpreted as an indirect evidence that the radical is substrate-derived.

The EPR spectrum of the radical scanned at low modulation amplitudes, in a narrow field range around g = 2.0, has demonstrated some hyperfine structure, Figure II-6.[16] The predominant splittings observed in the pyruvate reacted enzyme have been altered when the three protons on carbon 3 of pyruvate have been substituted with

deuterons, implying that the radical signal is substrate-derived. A comparison of the two EPR spectra in Figure II-6 shows that the EPR line for the sample with deuterated substrate is narrower and contains less features than the one for the unlabeled sample. Spectral features that appear to remain after the isotopic substitution are assumed to arise from interaction of the unpaired electron with other nuclear spins (such as the thiazole nitrogen).[16]

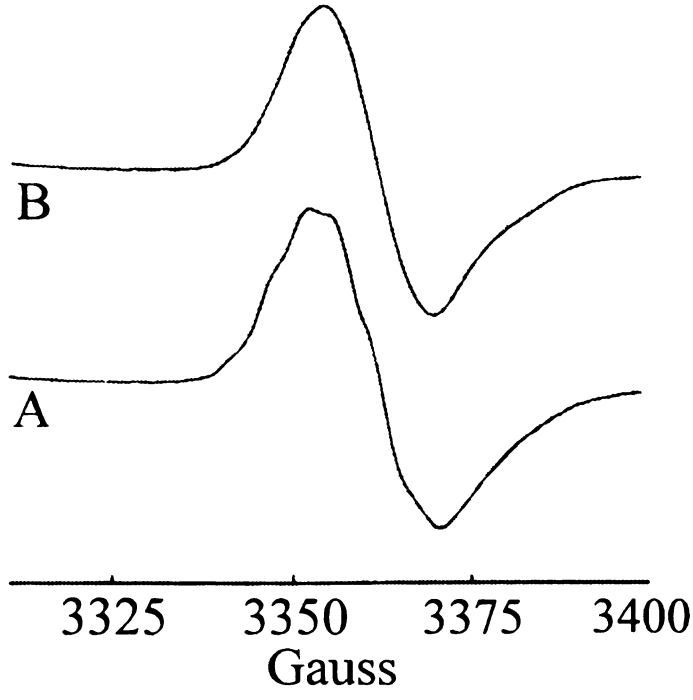

Figure II-6: First-derivative EPR spectra of *Clostridium Thermoaceticum* PFOR incubated with (A) pyruvate, and (B) CD_3-labeled pyruvate. EPR parameters: spectral width, 100 G; field center, 3360 G; modulation frequency, 100 kHz; modulation amplitude, 0.5 G; temperature, 10 K; microwave power, 2 mW; microwave frequency, 9.446 GHz. (From Ref. 16)

A dependency of the EPR signal of the radical intermediate on the number of protons at the C-3 position of the 2-oxoacid substrate has been observed by Kersher and Oesterhelt[11] in their study of *Hm. halobium* PFOR, Figure II-1. Apparently, the radical EPR signal becomes narrower and gradually loses hyperfine structure upon decreasing the number of the substrate C- 3 bonded protons. The hyperfine pattern has therefore been attributed to interactions between the unpaired electron and the three protons on carbon 3 of pyruvate. However, neither of the studies reports on values of electron-nuclearcoupling constants for the emerging radical species. Since the hyperfine structure of the radical EPR signal is not resolved it is of little use in determining the hyperfine coupling parameters. Hence, no reliable conclusions about the substrate nature of the enzyme can be drawn. The application of advanced EPR methods such as ENDOR and ESEEM, which can provide high resolution in detecting weak electron-nuclear magnetic interaction in samples of randomly oriented paramagnetic species, seems to be appropriate to the study of paramagnetic PFOR reaction intermediates. The present study was aimed at determining the magnetic and structural properties of the reaction intermediates in the PFOR enzyme, which would allow elucidating some aspects of the reaction mechanism.

II.2. Application of Advanced EPR Methods to the Study of *Clostridium thermoaceticum* PFOR Reaction Intermediates

II.2.1. Experimental

Samples of *Clostridium thermoaceticum* PFOR with different substrates have been provided by Dr. S. Ragsdale from the University of Nebraska. They have been prepared according to the procedure described in Ref. 16. The samples represent freeze quenched reactions between the enzyme and substrates in aqueous buffer solutions. As indicated in Ref. 16, the data of the metal, sulfide, and protein analysis of the *Clostridium thermoaceticum* PFOR have shown that it is a dimeric protein containing two $[Fe_4S_4]$ clusters per monomer. The 2-keto acid substrates used in the preparation of the samples include pyruvate, ^{13}C-2 (carbonyl) labeled pyruvate, ^{13}C-3 (methyl) labeled pyruvate, $^{2}H_3C$-pyruvate in deuterated ($^{2}H_2O$) buffer, 3-methyl-2-oxobutyrate, and 2-oxobutyrate. Each of the substrates has been reacted with PFOR and the reaction has been stopped by freezing the samples in liquid nitrogen.

The EPR and ENDOR spectra were recorded on a Bruker ESP300E spectrometer, equipped with a Bruker ESP 360 DICE ENDOR assembly, Oxford ESR-900 cryostat with an Oxford ITC 502 temperature controller, Bruker ER035M NMR Gaussmeter, and EIP 25 B frequency counter. The radio frequency (rf) in the ENDOR measurements was amplified by an ENI A-300 amplifier. ENDOR spectra were collected by sweeping the rf field in the range 0.5 MHz to 35 MHz. The ESEEM measurements were performed on a homebuilt pulsed EPR spectrometer described in Ref. 20. The microwave cavity system used for ESEEM measurements employed a slotted-tube resonator[21] combined with a

Gordon coupler arrangement.[22] Both two-pulse ($\pi/2 - \tau - \pi$) and (predominantly) three-pulse ($\pi/2 - \tau - \pi/2 - T - \pi/2$) microwave pulse sequences were employed to generate the ESEEM data.

II. 2.2. Results

The EPR spectra of the samples at 4 K, Figure II-7, are similar to those described in Ref. 16. An intense line at g = 2.0056, attributed to a reaction radical intermediate,[16] is present in all of them. This signal is superimposed on the broad, complex EPR lineshape with extrema at g = 2.046, g = 1.948, and g = 1.861 This complex signal, which is only observed at temperatures below ca. 20 K, is due to $[Fe_4S_4]$ clusters in the protein structure. The deviation of the spectral morphology of the signal from a rhombic lineshape has been attributed to dipolar through-space electron spin-spin interaction which involves the unpaired electrons of the $[Fe_4S_4]$ clusters and, possibly, the radical.[16]

Figure II-8 gives a detailed view of the EPR line at g = 2.0056. A hyperfine structure similar to that described in Ref. 16 is observed. Because this EPR signal is easily saturated at low temperatires, the spectra appear to demonstrate an enhancement in resolution at T = 60 K in comparison to that at T = 9.1 K. The peak-to-peak linewidth of the signal is ca. 20 gauss but the line extends over a range of about 70 gauss.

The EPR spectra of PFOR reacted with ^{13}C-2 and ^{13}C-3 labeled pyruvate at 9.0 K are shown in Figure II-9. They are similar to the EPR spectrum of PFOR with unlabeled substrate, Figure II-9 (a). However, different features are observed in the g = 2.00 region, Figure II-10. The spectrum of PFOR/^{13}C-2 pyruvate, shown in Figure II-10 (b),

Figure II-7: First-derivative EPR spectra of PFOR with pyruvate, (a), $^{2}H_{3}C$-pyruvate, (b), 3-methyl-2-oxobutyrate, (c), and 2-oxobutyrate, (d). Experimental parameters: field center, 3376 G; field sweep width, 1000 G; modulation frequency, 100 kHz; modulation amplitude, 5.0 G; time constant, 10 ms; microwave power, 0.1 mW; microwave frequency, 9.468 GHz; temperature, 4 K.

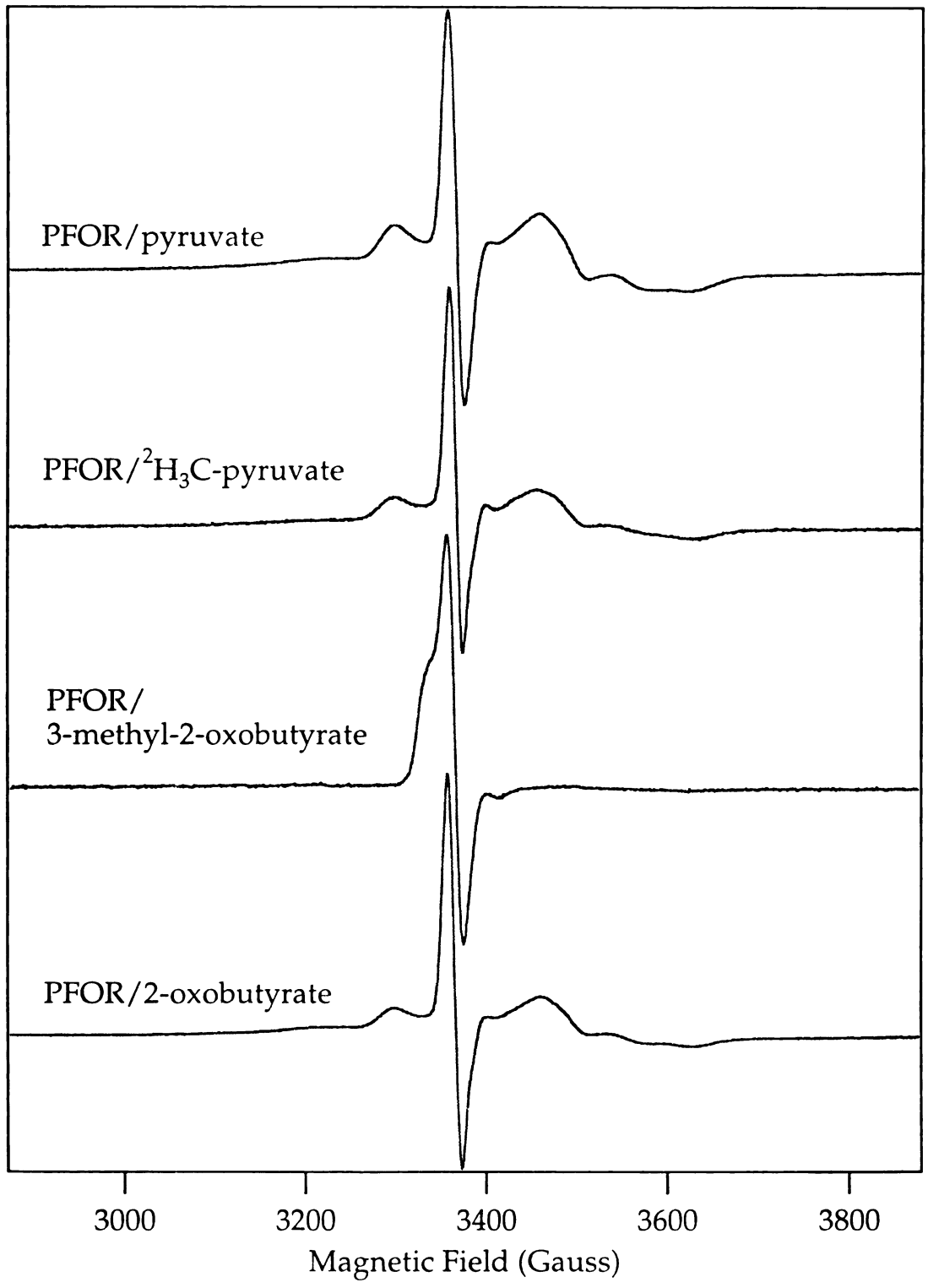
PFOR/pyruvate
PFOR/^2H_3C-pyruvate
PFOR/
3-methyl-2-oxobutyrate
PFOR/2-oxobutyrate
3000
3200
3400
3600
3800
Magnetic Field (Gauss)

Figure II-7

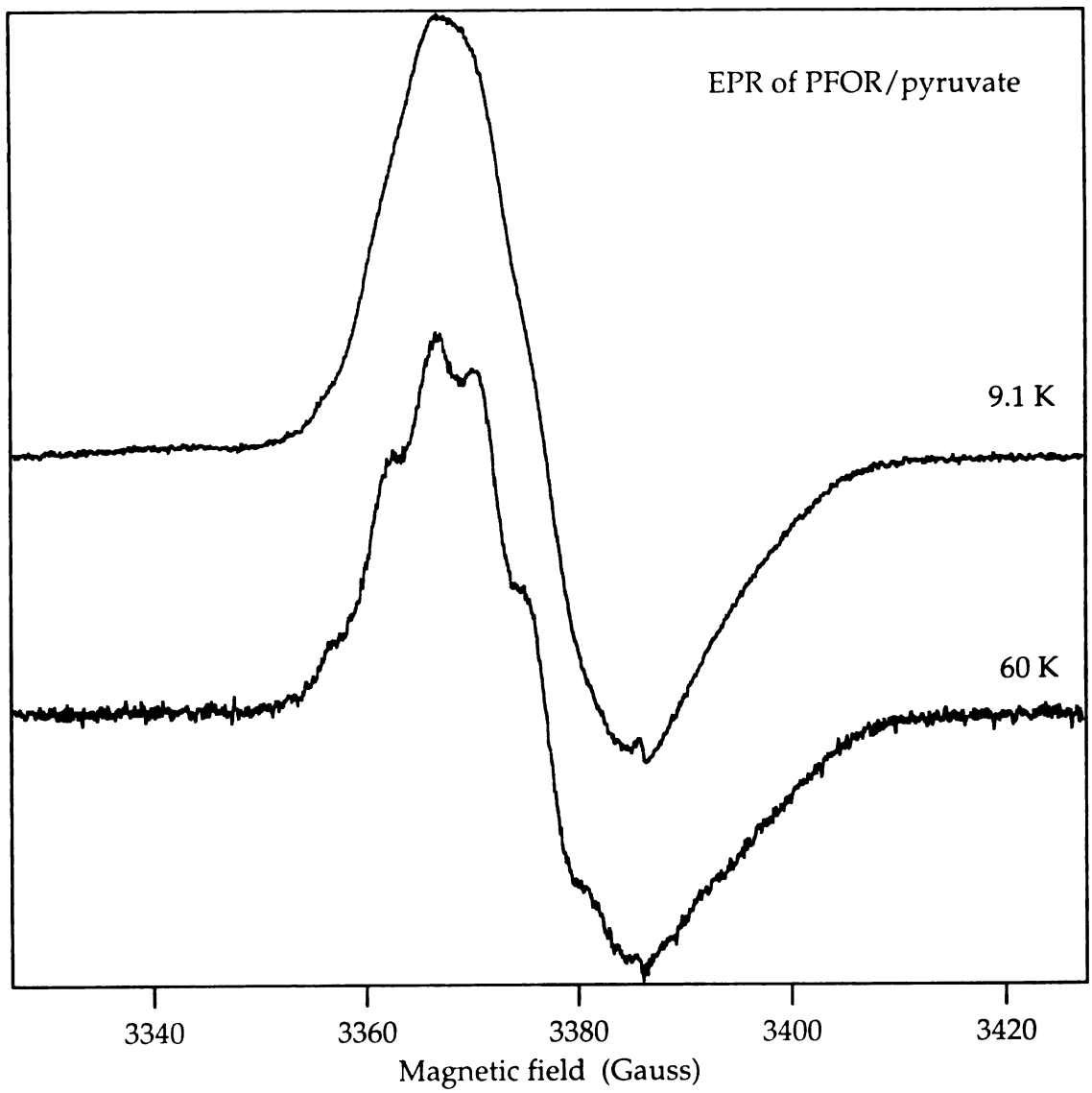

Figure II-8: First-derivative EPR spectra of PFOR reacted with pyruvate. Experimental parameters: field center , 3377.2 G; field sweep width, 100 G; modulation frequency, 100 kHz; modulation amplitude, 1.0 G; time constant, 10 ms; microwave power, 0.05 mW; microwave frequency, 9.482 GHz; temperature: 9.1 K, (a), and 60 K, (b).

Figure II-9: First-derivative EPR spectra of PFOR reacted with pyruvate, (a), ^{13}C-2 labeled pyruvate, (b), and ^{13}C-3 labeled pyruvate, (c). Experimental parameters: field center, 3377 G; field sweep width, 1000 G; modulation frequency, 100 kHz; modulation amplitude, 10.0 G; time constant, 10 ms; microwave power, 0.05 mW; microwave frequency, 9.481 GHz; temperature, 9.0 K.

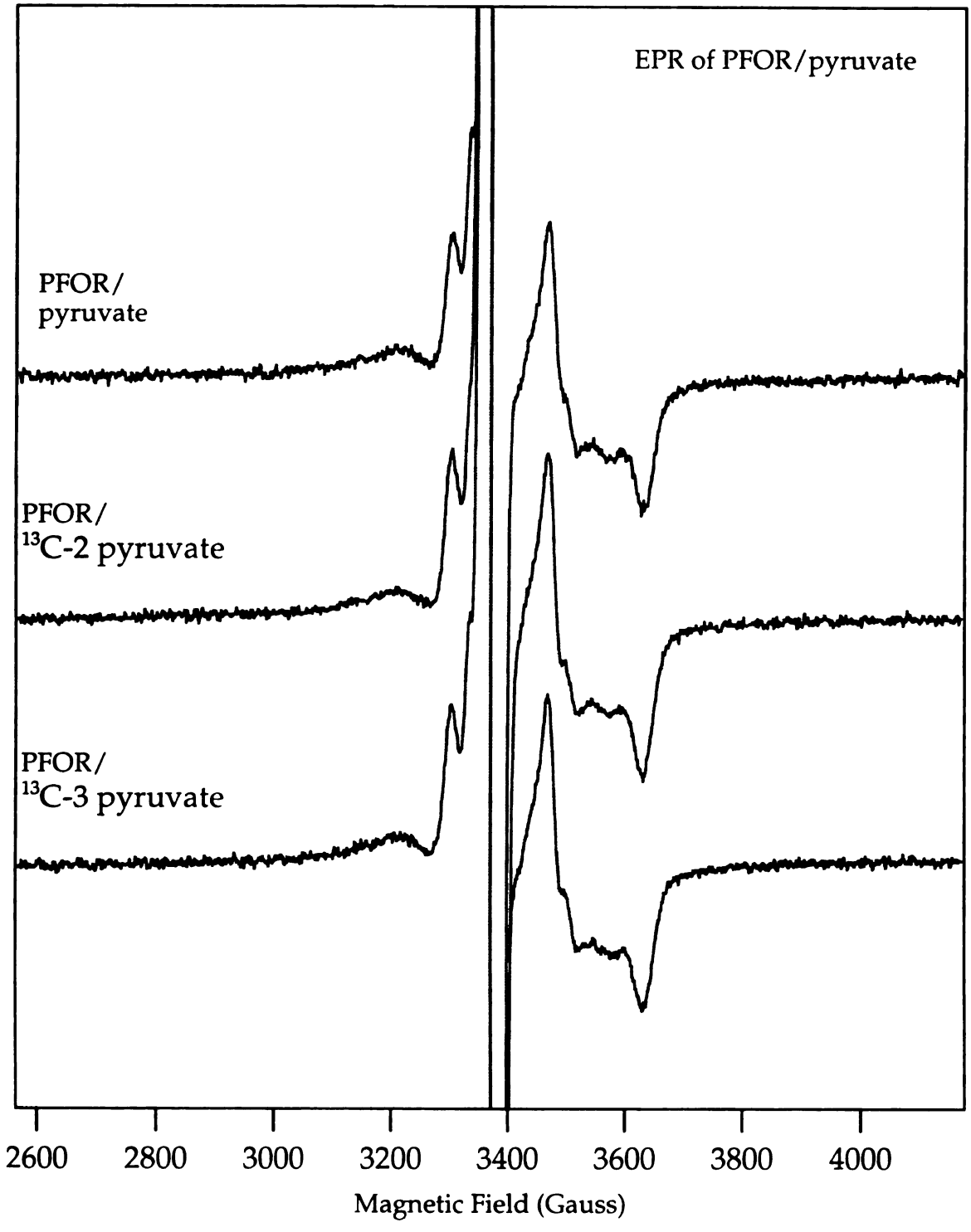
EPR of PFOR/pyruvate
PFOR/
pyruvate
PFOR/
^{13}C-2 pyruvate
PFOR/
^{13}C-3 pyruvate
2600
2800
3000
3200
3400
3600
3800
4000
Magnetic Field (Gauss)

Figure II-9

exhibits an intense, narrow (0.5 G peak to peak linewidth) EPR line at g = 2.0025 superimposed on the line at g = 2.0056. Two distinct narrow (~0.5 G peak to peak linewidth) EPR lines at g = 2.0025 and g = 2.0008 are observed in the spectrum of ^{13}C-3 pyruvate reacted enzyme. These additional features in the spectra of PFOR with ^{13}C labeled substrates are clearly due to hyperfine interactions of carbon-13. It is worth noting that besides the sharp lines due to ^{13}C hyperfine coupling, the hyperfine structure of the line at 2.0056 is different for all of the three spectra in Figure II-10. The hyperfine pattern is most pronounced for PFOR reacted with ^{13}C-3 pyruvate. The difference in the hyperfine patterns indicates that there exist more ^{13}C hyperfine components that overlap with the EPR line at g = 2.0056. This conclusion is supported by the fact that the linewidth of the g = 2.0056 EPR signal is larger in the case of ^{13}C labeled samples relative to the linewidth for the unlabeled sample.

ENDOR spectra of the samples were collected at temperatures, ranging from 4K to 200K, with the maximum ENDOR response being found at 60 K. To distinguish the contributions of the radical species from those of the paramagnetic iron-sulfur center, experiments were performed at different magnetic field strengths corresponding to different g values. An ENDOR spectrum of PFOR with added pyruvate, which was recorded at g = 2.0056 (the maximum EPR resonance effect for the radical), is shown in Figure II-11. A broad line due to matrix protons appears at ca. 14.2 MHz. A pair of intense lines is resolved at 5.48 MHz and 5.99 MHz. These frequencies are in the close proximity of the Larmor precession frequency of ^{31}P (5.77 MHz at 3349 G). They are, therefore, attributed to a long range hyperfine interaction of the radical unpaired electron with the HE-TPP phosphorus nuclei. The almost symmetrical lineshape of both signals

Figure II-10: First-derivative EPR spectra of PFOR reacted with pyruvate, (a), ^{13}C-2 labeled pyruvate, (b), and ^{13}C-3 labeled pyruvate, (c). Experimental parameters: field center, 3377.2 G; field sweep width, 100 G; modulation frequency, 100 kHz; modulation amplitude, 1.0 G; time constant, 10 ms; microwave power, 0.05 mW; microwave frequency, 9.481 GHz; temperature, 60.0 K.

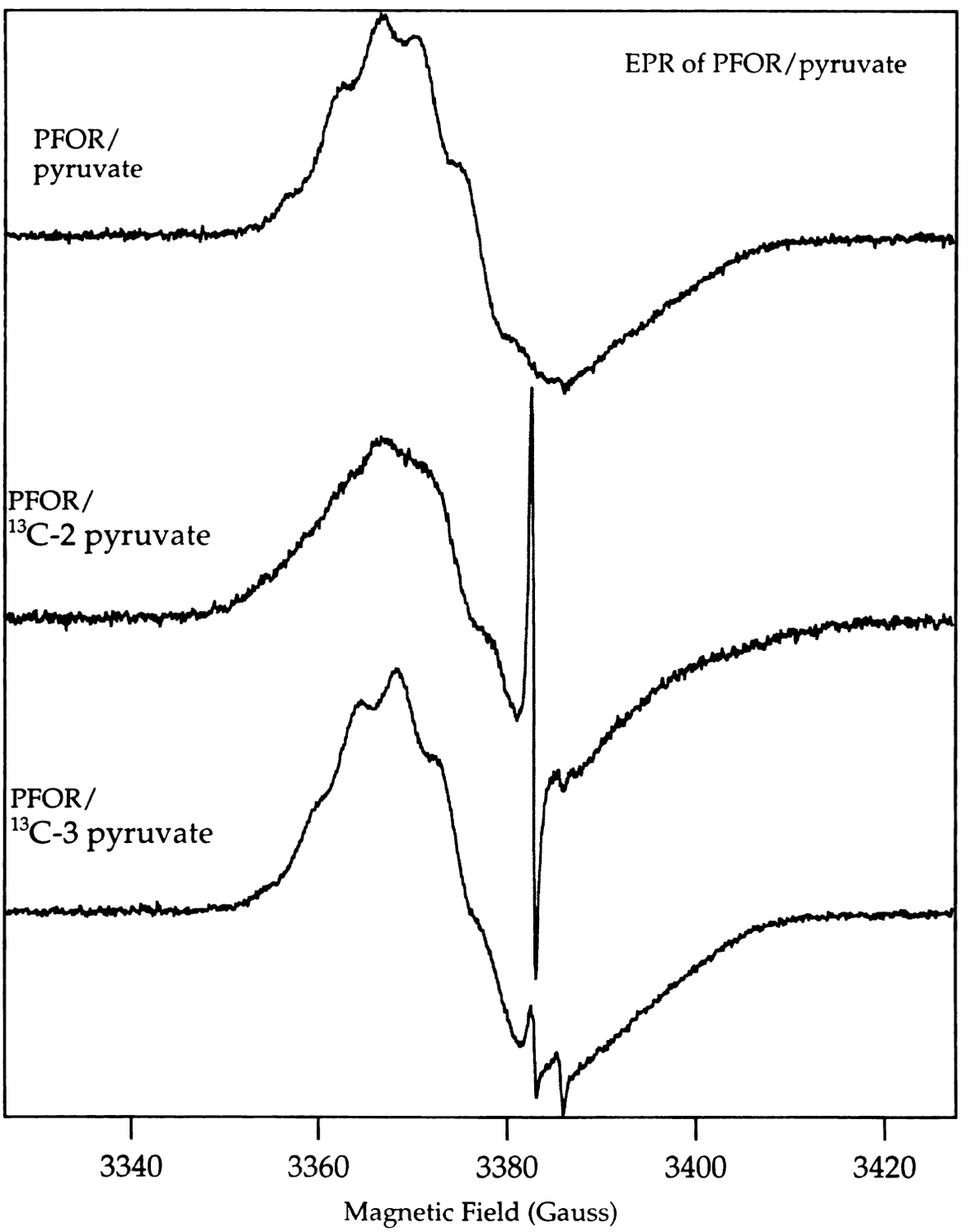
EPR of PFOR/pyruvate
PFOR/
pyruvate
PFOR/
^{13}C-2 pyruvate
PFOR/
^{13}C-3 pyruvate
3340
3360
3380
3400
3420
Magnetic Field (Gauss)

Figure II-10

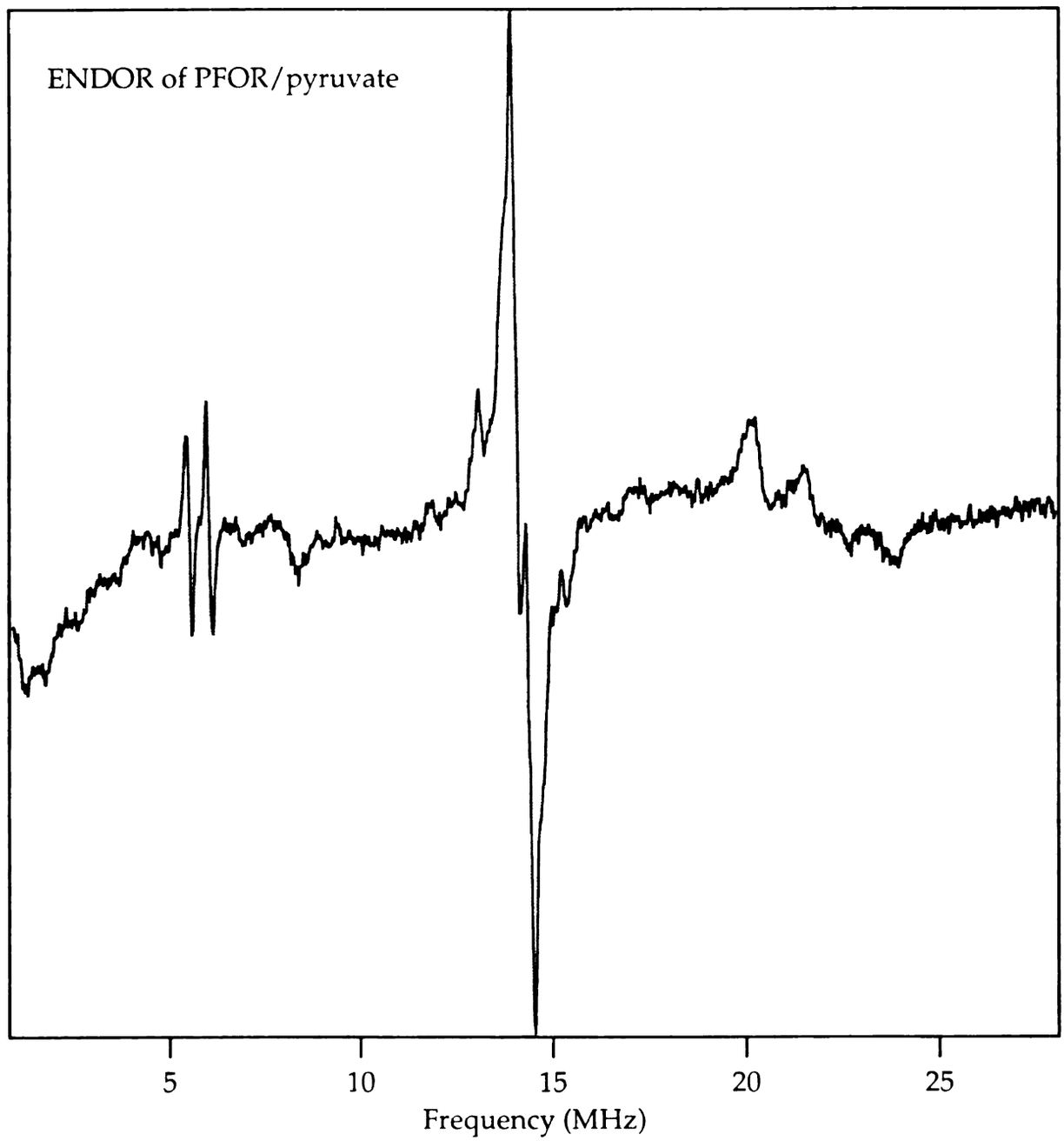

Figure II-11: ENDOR spectrum of PFOR/pyruvate. Experimental parameters: static magnetic field, 3349 G; microwave frequency, 9.400 GHz; microwave power, 10 mW; rf sweep width, 5.5 MHz; rf fm modulation depth, 100 kHz; rf power, 220 W; time constant, 10 ms; temperature, 60 K.

indicates that the hyperfine coupling is mainly isotropic with A_{iso} = 0.51 MHz. Figure II-12 shows the ENDOR spectrum obtained by averaging a large number (> 300) of scans in a narrow frequency range around the Larmor frequency of ^{31}P. However, the lineshapes still do not reveal distinct anisotropic components. This result is surprising since the TPP pyrophosphate fragment is σ-bonded via an ethylene bridge to the thiazole ring, and the only interaction between the radical unpaired electron and ^{31}P would be via a dipolar, through-space mechanism. The high-frequency region of the spectrum in Figure II-11 shows two overlapping proton powder type ENDOR patterns. The lineshape of these patterns is characteristic of axial hyperfine interaction of two sets of protons. The peaks in the patterns are positioned at 20.23 and 22.64 (set 1), and 21.50 and 23.85 MHz (set 2). The corresponding low-frequency signals are distorted because of their overlap with the ^{31}P lines at 5.48 MHz and 5.99 MHz. Low-intensity peaks at 16.50 MHz, and 11.84 MHz, are also resolved. From the proton ENDOR components, the magnitudes of proton hyperfine couplings were obtained. The results are summarized in Table II-1.

Table II-1: Hyperfine coupling constants from ^{1}H ENDOR of *Clostridium Thermoaceticum* PFOR reaction intermediates.

H set	A_{iso}, MHz	$B_{\|}$, MHz	$B_{\perp}$, MHz
1	13.75	3.60	-1.80
2	16.33	3.33	-1.67
3	4.66	-	-

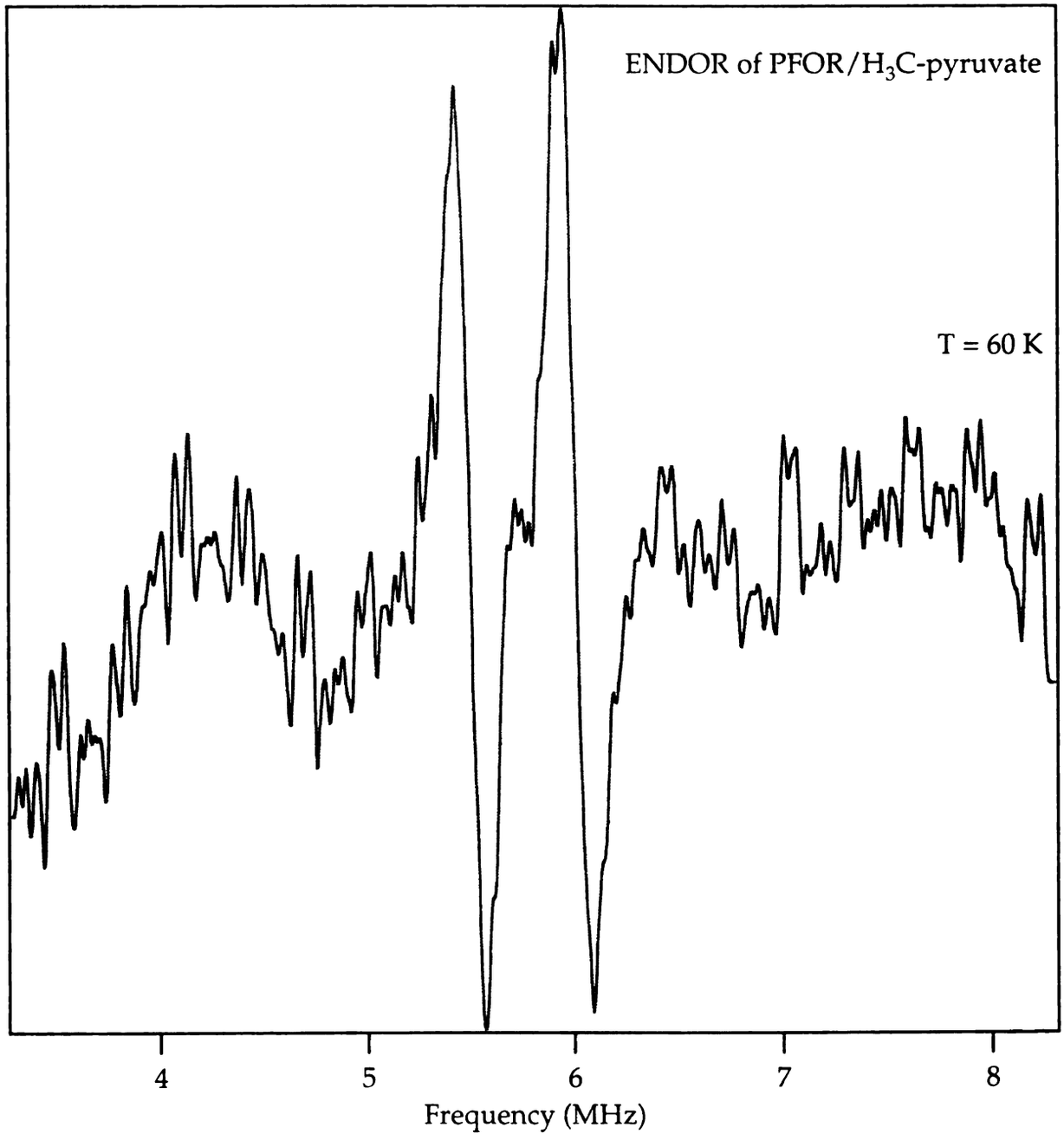

Figure II-12: ENDOR spectrum of PFOR/pyruvate. Experimental parameters: static magnetic field, 3349 G; microwave frequency, 9.400 GHz; microwave power, 10 mW; rf sweep width, 5 MHz; rf fm modulation depth, 100 kHz; rf power, 220 W; time constant, 10 ms; temperature, 60 K. 300 scans were averaged.

No significant changes in the observed spectral pattern and the lineshapes of the signals occurred as the temperature was varied between 4K and 200K (Figure II-13).

To check for contributions from the $[Fe_4S_4]$ clusters, ENDOR experiments were attempted at g = 2.0218, g = 1.9871 and g = 1.9293. At 60K no ENDOR signal was detected with those g values. Upon lowering the temperature to 4 K, a broad line corresponding to matrix protons emerged, Figure II-14; however, the rest of the ENDOR signals observed at g = 2.0056 (cf. Figure II-11) were not detected.

The ENDOR spectrum of PFOR reacted with $^{2}H_3C$-pyruvate at 60 K, Figure II-15, shows the proton matrix line at ~14.2 MHz and the two ^{31}P peaks at 5.48 MHz and 5.99 MHz, whereas the powder proton lines are strongly suppressed. An additional feature is resolved at 3.34 MHz and is assigned to the high-frequency deuteron hyperfine component. Figure II-16 shows an ENDOR spectrum collected in a narrow frequency range around the deuterium signal. This ENDOR signal has a characteristic lineshape due to the combined effect of nuclear quadrupole and electron-nuclear dipolar interactions. The detection of the corresponding low-frequency hyperfine component is obscured by baseline artifacts present in the 1 MHz region. This line is partially resolved at ~ 1 MHz.

Figure II-17 (a) shows the ENDOR spectrum of PFOR reacted with ^{13}C-3 pyruvate at g = 2.0048. ENDOR signals at 9.0 MHz and 9.5 MHz, not observed in the case of unlabeled substrate, Figure II-11, are detected. However, no matching signal components are found either symmetrically situated relative to the ^{13}C nuclear Larmor frequency ($\nu_I(^{13}C)$ = 3.58 MHz at 3349 G), or offset by $\pm 2\nu_I(^{13}C)$. No additional features are observed in the ENDOR spectrum of PFOR reacted with ^{13}C-2 pyruvate, Figure II-17 (b), when compared with the spectrum of PFOR/pyruvate, Figure II-11. The

Figure II-13: ENDOR spectrum of PFOR/pyruvate. Experimental parameters: static magnetic field, 3349 G; microwave frequency, 9.400 GHz; microwave power, 20 mW; rf sweep width, 27 MHz; rf fm modulation depth, 280 kHz; rf power, 220 W; time constant, 10 ms; temperature: 4K, (a), 77K, (b), 200K, (c).

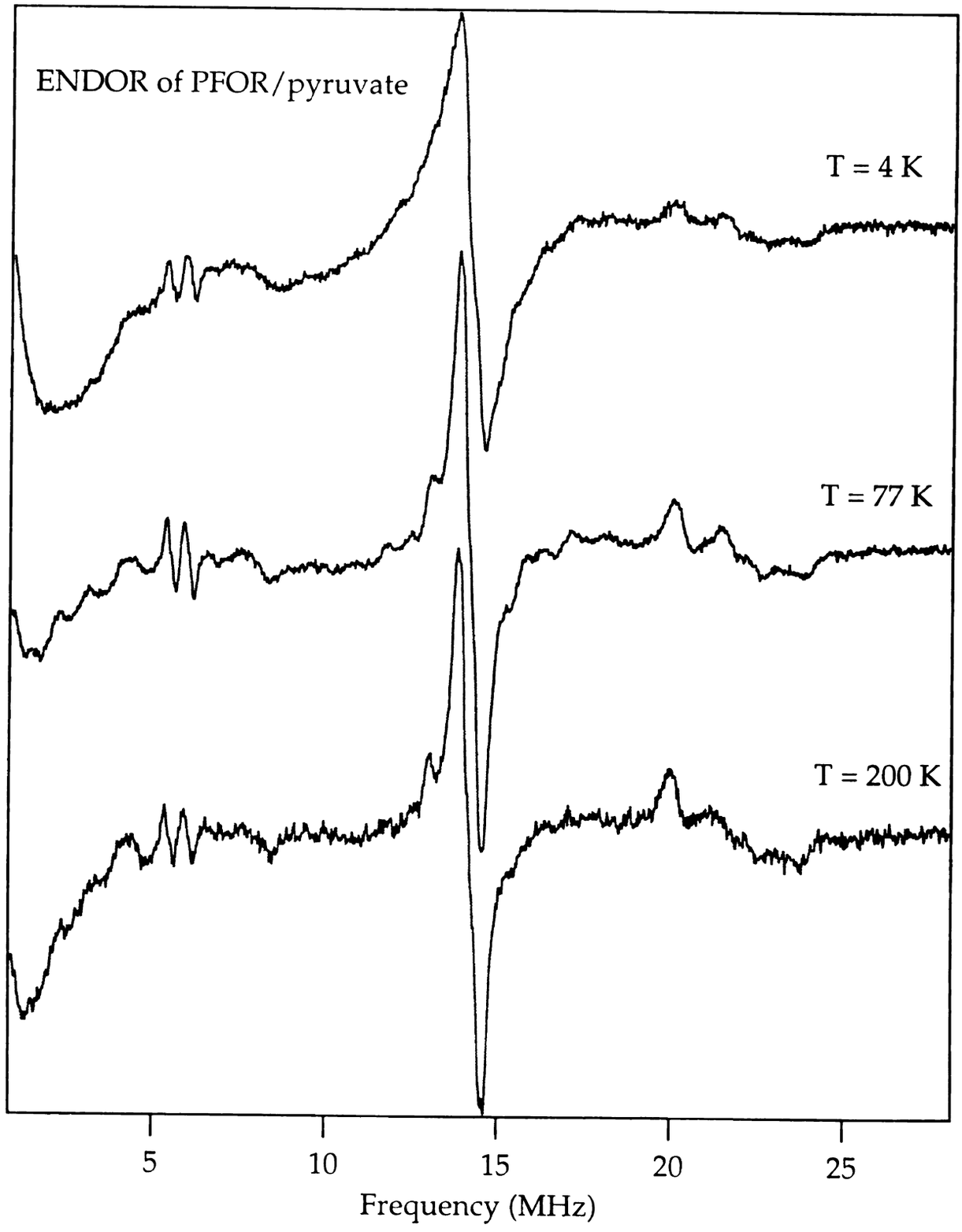
ENDOR of PFOR/pyruvate
T = 4 K
T = 77 K
T = 200 K
5
10
15
20
25
Frequency (MHz)

Figure II-13

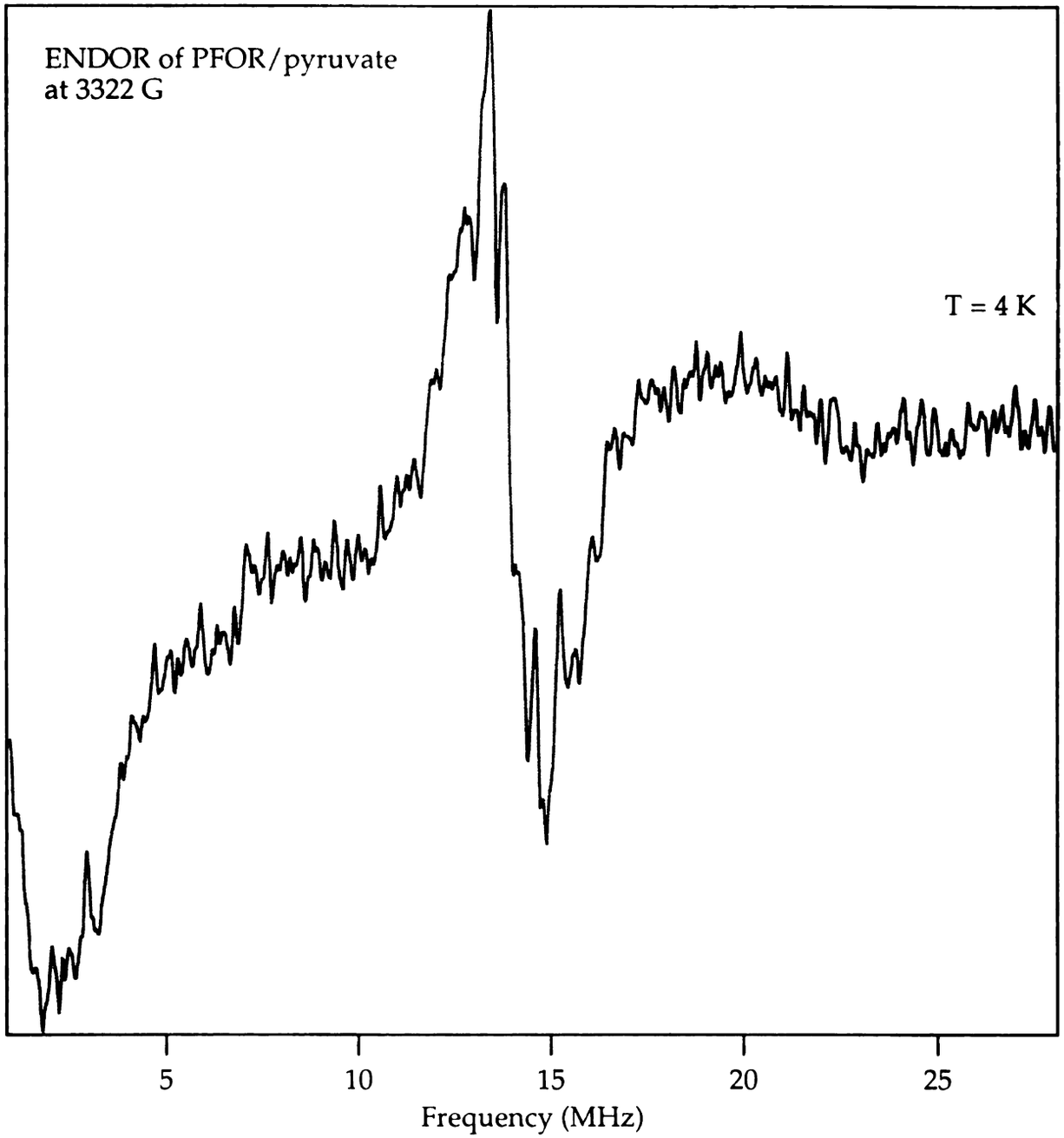

Figure II-14: ENDOR spectrum of PFOR/pyruvate. Experimental parameters: static magnetic field, 3322 G;microwave frequency, 9.400 GHz; microwave power, 1 mW; rf sweep width, 27 MHz; rf fm modulation depth, 280 kHz; rf power, 220 W; time constant, 10 ms; temperature: 4K.

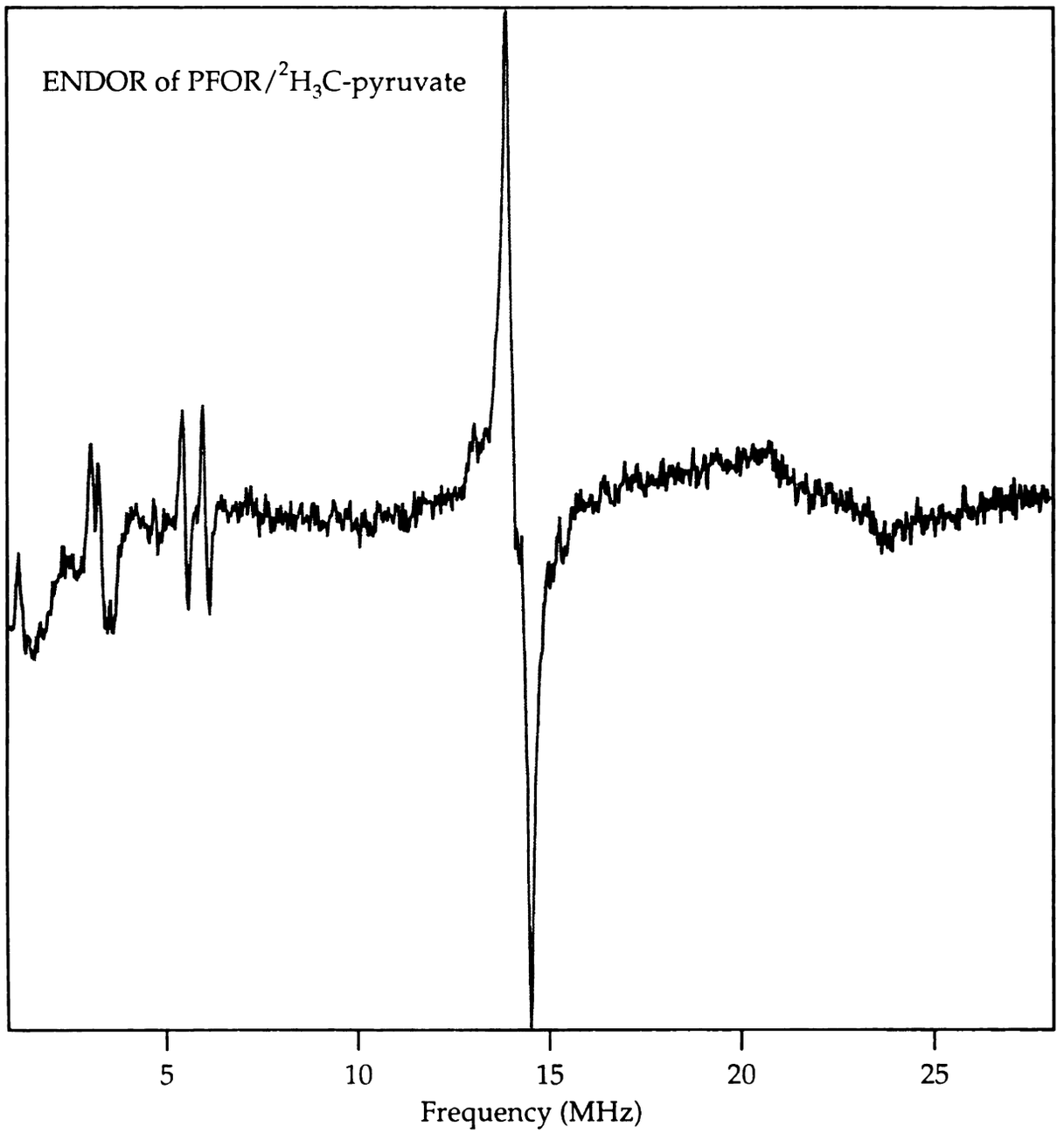

Figure II-15: ENDOR spectrum of PFOR/^2H_3C-pyruvate. Experimental parameters: static magnetic field, 3349 G; microwave frequency, 9.400 GHz; microwave power, 5 mW; rf sweep width, 27 MHz; rf fm modulation depth, 100 kHz; rf power, 220 W; time constant, 10 ms; temperature, 60 K.

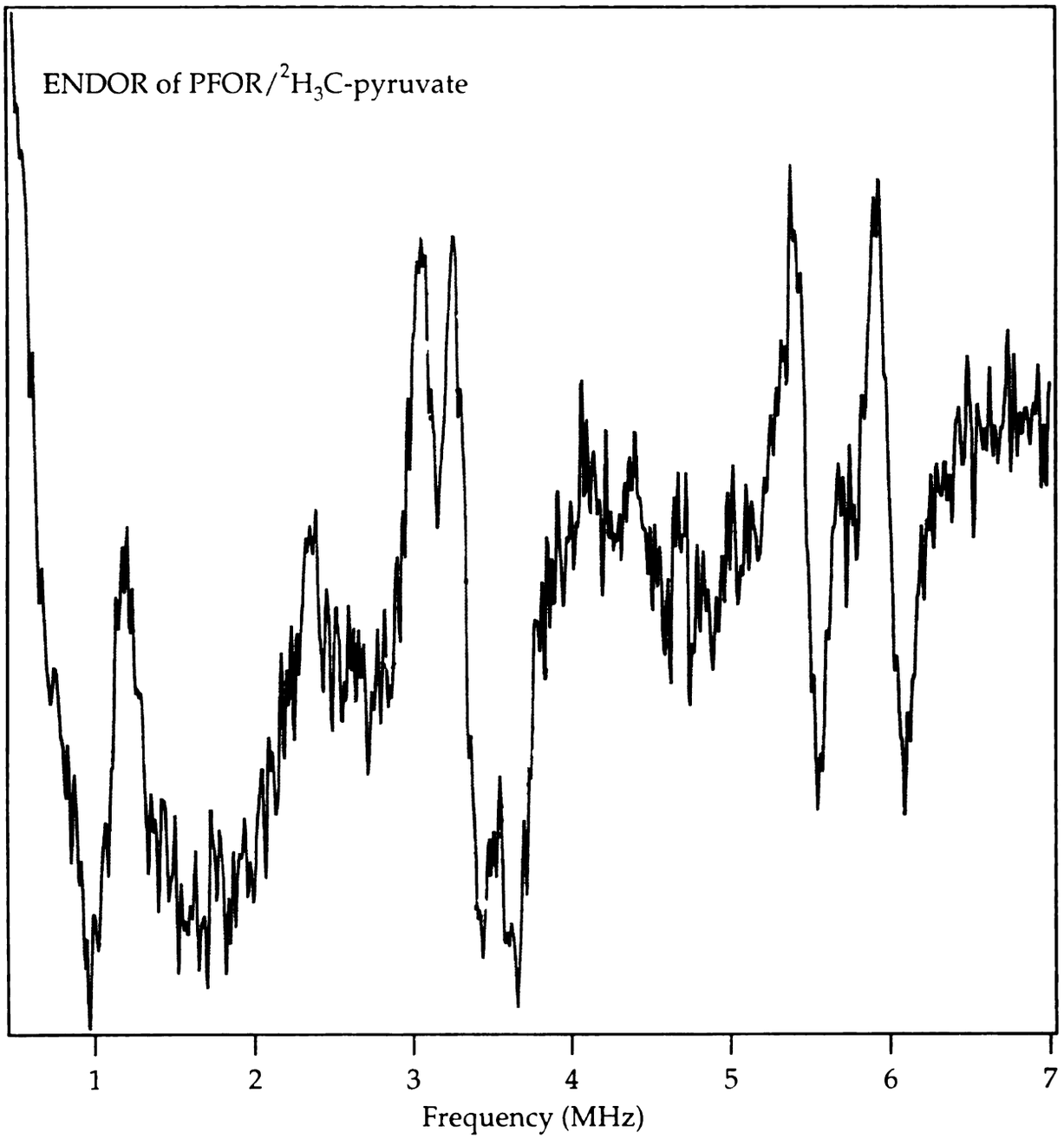

Figure II-16: ENDOR spectrum of PFOR/^2H_3C-pyruvate. Experimental parameters: static magnetic field, 3349 G; microwave frequency, 9.400 GHz; microwave power, 5 mW; rf sweep width, 6 MHz; rf fm modulation depth, 100 kHz; rf power, 220 W; time constant, 10 ms; temperature, 60 K.

Figure II-17: ENDOR spectrum of PFOR reacted with ^{13}C-3 labeled pyruvate, (a), and ^{13}C-2 labeled pyruvate, (b). Experimental parameters: static magnetic field, 3348.5 G; microwave frequency, 9.396 GHz; microwave power, 1 mW; rf sweep width, 35 MHz; rf fm modulation depth, 158.5 kHz; rf power, 220 W; time constant, 41 ms; temperature, 60 K.

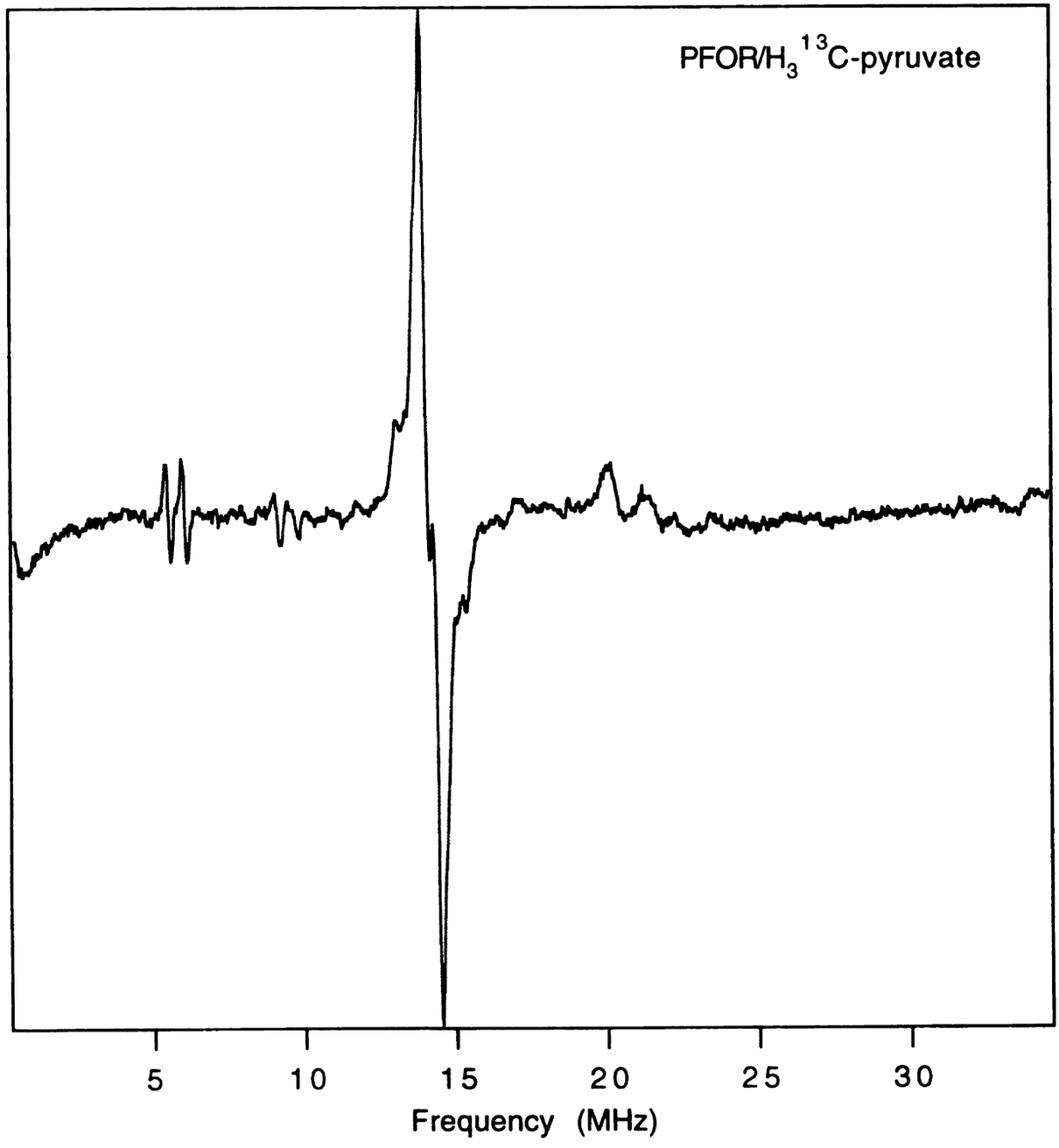

Figure II-17 (a)

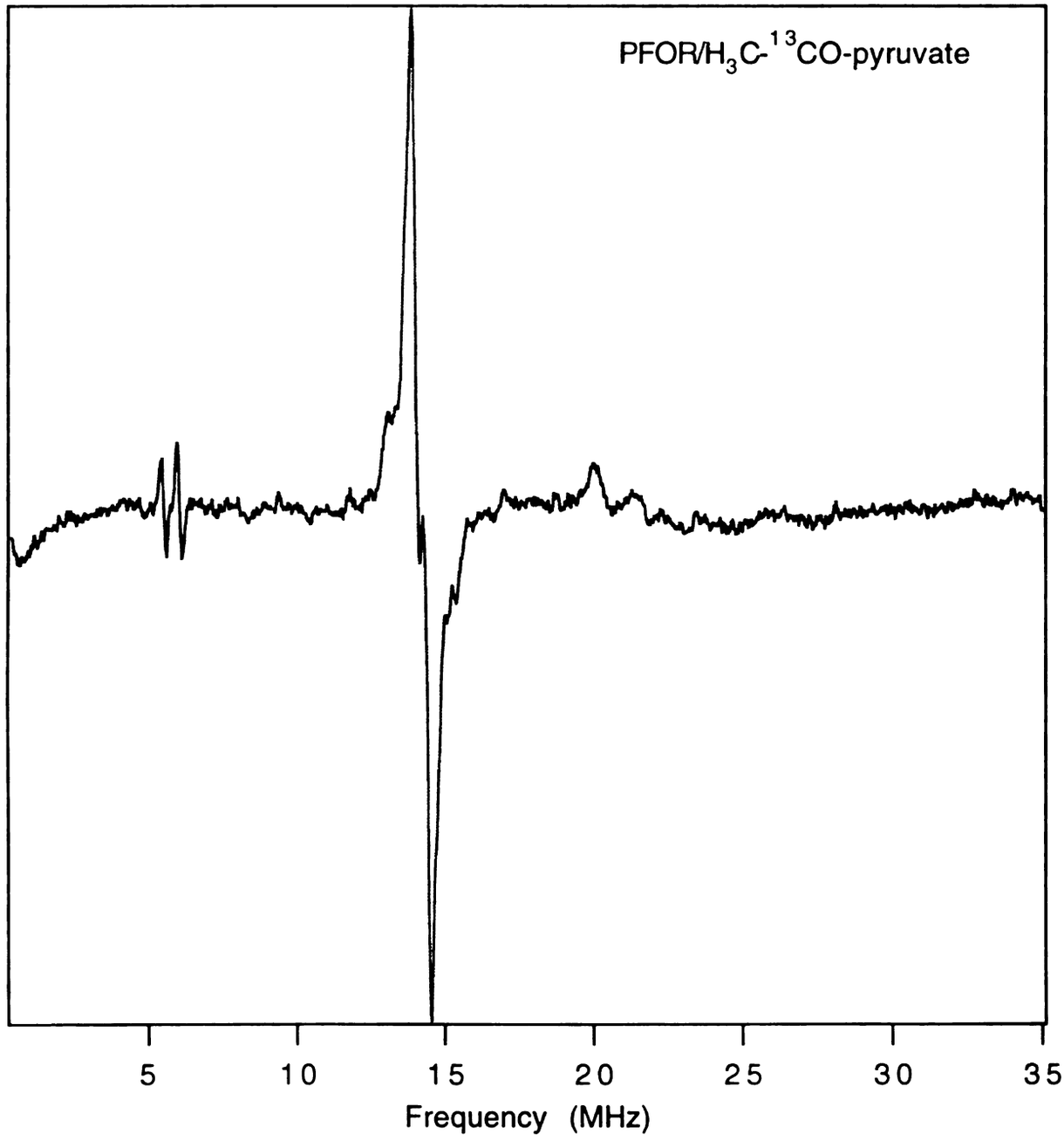

Figure II-17 (b)

reason for the lack of ^{13}C characteristic features is most probably in that the values of the ^{13}C hyperfine couplings extend beyond the employed rf scan range of 35 MHz (12.5 G).

ENDOR spectra of PFOR/3-methyl-2-oxobutyrate and PFOR/2-oxobutyrate at 60K are given in Figure II-18. ^{1}H ENDOR features analogous to those listed in Table II-1 are not observed for either of the substrate analogs.

ESEEM data were collected using a three-pulse ($\pi/2$ - τ - $\pi/2$ - T - $\pi/2$ - τ) microwave pulse sequence. τ-values were varied between 180 and 500 ns, so that the τ-suppression effect on the resolved modulation frequency components could be established.[23] Frequency spectra were obtained from the time domain by Fourier transformation, using the dead time reconstruction algorithm described by Mims.[24] Since the spin-lattice relaxation time of the radical species is longer than that of the $[Fe_4S_4]$ clusters, pulse sequence repetition rates of 40 Hz or less were employed in order to maximize contributions from the radical species to the echo amplitude. Figure II-19 represents three-pulse ESE-derived EPR spectra of PFOR reacted with pyruvate, which illustrate this dependency. The ratio between the maxima of the radical species peak at g = 2.0056 and the $[Fe_4S_4]$ cluster-derived peak at g = 1.931 changes insignificantly, from 1.06 at pulse sequence repetition rate 1 Hz to 0.97 at repetition rate 40 Hz. This implies the proximity of the $[Fe_4S_4]$ cluster to the radical, which agrees with the conclusion of Oesterhelt et al. that the radical and the cluster are in close proximity ($\leq$10 Å).

Figure II-20 (a) shows the time domain stimulated ESEEM data collected for PFOR/pyruvate at g = 2.0003. Shallow modulations, indicative of weak hyperfine interactions are observed. Examination of the frequency domain data, Figure II-20 (b), shows that the spectrum is dominated by the proton modulation line at 14.6 MHz.

Figure II-18: ENDOR spectrum of PFOR/3-methyl-2-oxobutyrate, (a). Experimental parameters: static magnetic field, 3349 G; microwave frequency, 9.410 GHz; microwave power, 2 mW; rf sweep width, 27 MHz; rf fm modulation depth, 100 kHz; rf power, 220 W; time constant, 10 ms; temperature, 60 K. ENDOR spectrum of PFOR/2-oxobutyrate, (b). Experimental parameters: static magnetic field, 3349 G; microwave frequency, 9.410 GHz; microwave power, 2 mW; rf sweep width, 27 MHz; rf fm modulation depth, 100 kHz; rf power, 220 W; time constant, 10 ms; temperature, 60 K.

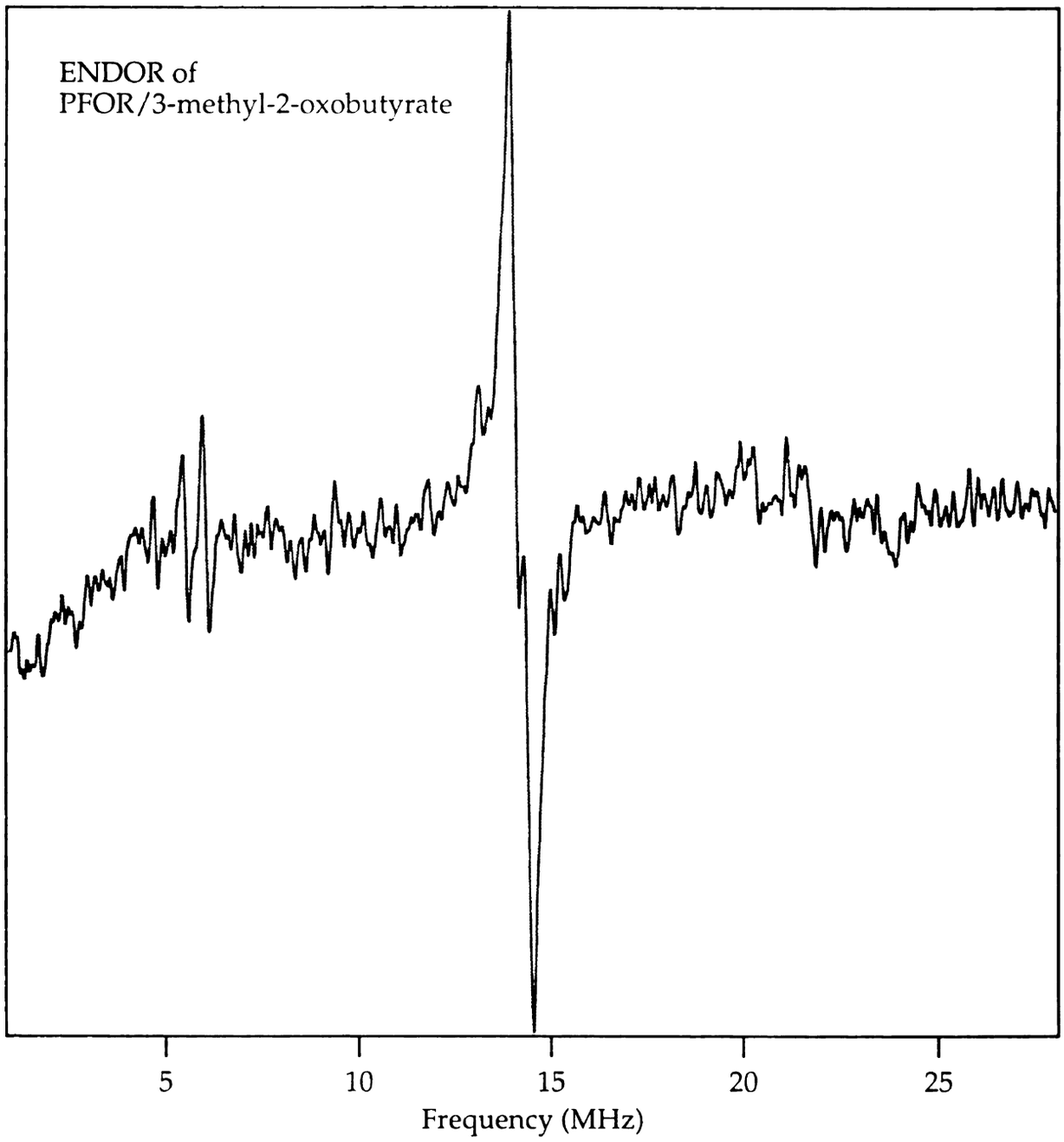

Figure II-18 (a)

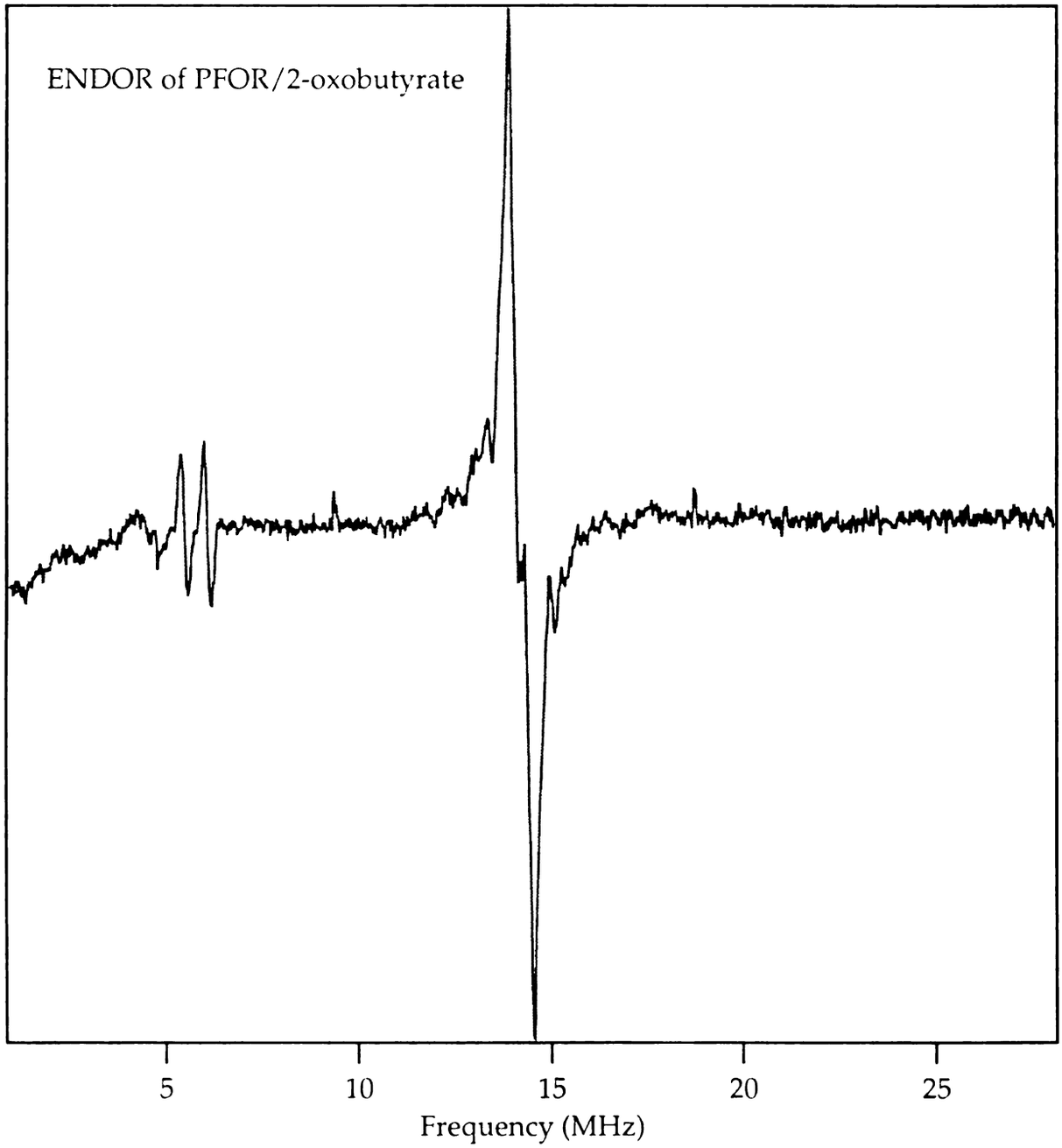

Figure II-18 (b)

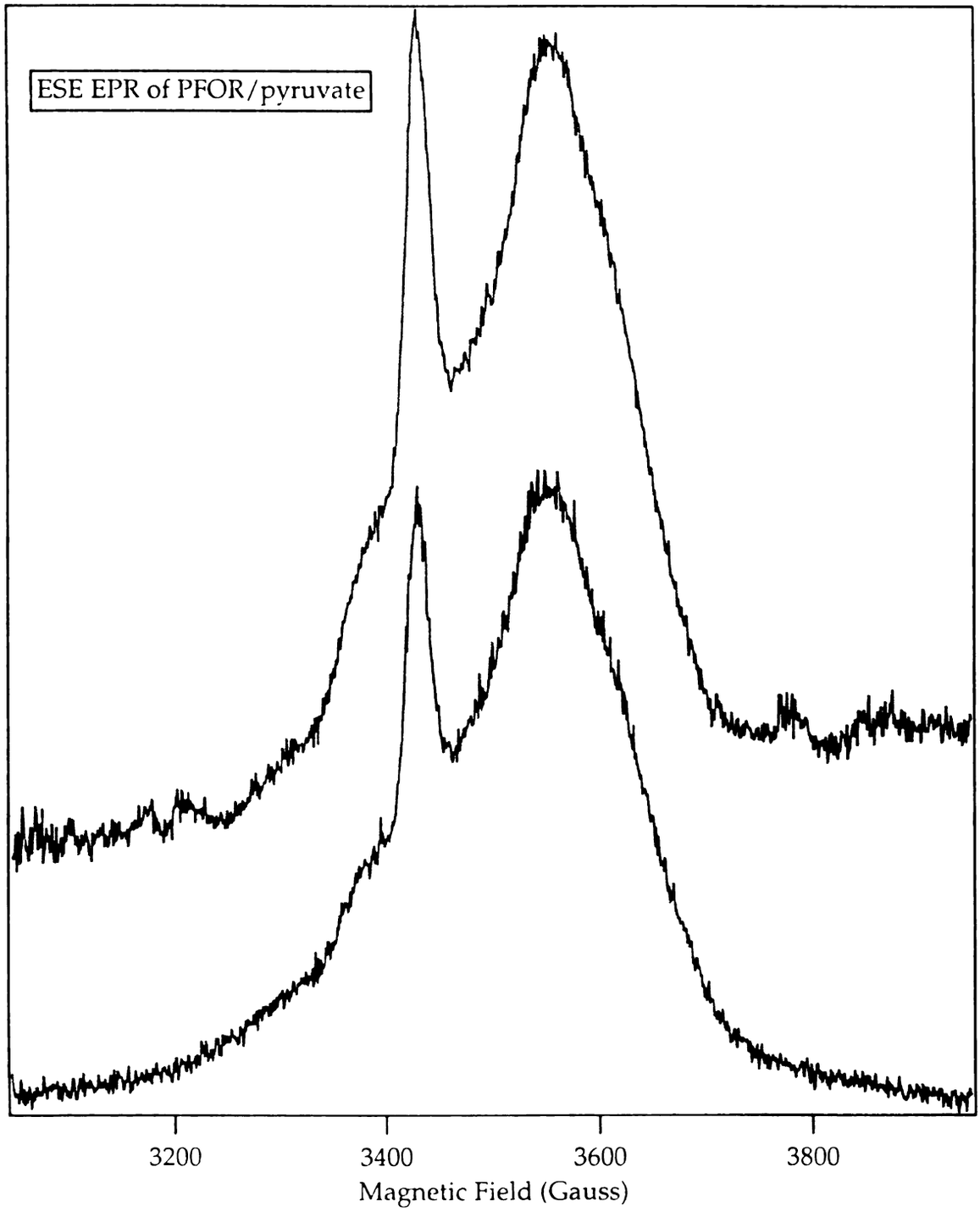

Figure II-19: ESE-EPR spectra of PFOR/pyruvate. Experimental parameters: magnetic field sweep width, 900 G; microwave frequency, 9.600 GHz; pulse duration, 17 ns; τ value, 205 ns; T value, 600 ns; temperature, 4.2 K; pulse sequence repetition rate: 1 Hz, (a), and 40 Hz, (b).

Figure II-20: Stimulated time domain ESEEM data for PFOR/pyruvate, (a). Experimental parameters: magnetic field strength, 3429 G; microwave frequency, 9.600 GHz; pulse duration, 17 ns; pulse sequence repetition rate, 10 Hz; τ value, 205 ns; initial T value, 100 ns; sample temperature, 4.2 K; number of data points, 1024; number of events averaged for each data point, 14; number of scans, 2. Corresponding frequency domain spectrum obtained by Fourier transformation of the time domain data, (b).

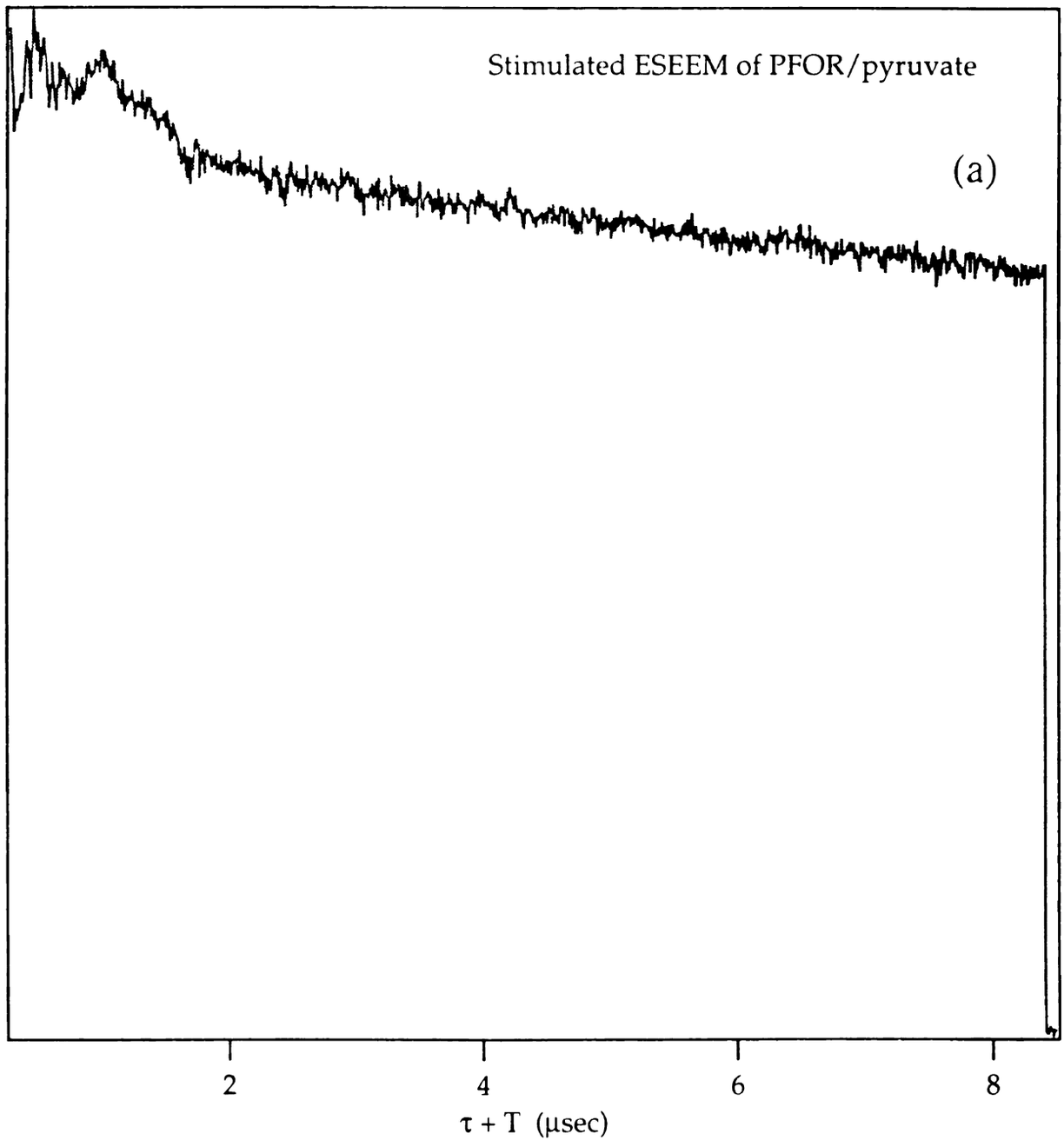

Figure II-20 (a)

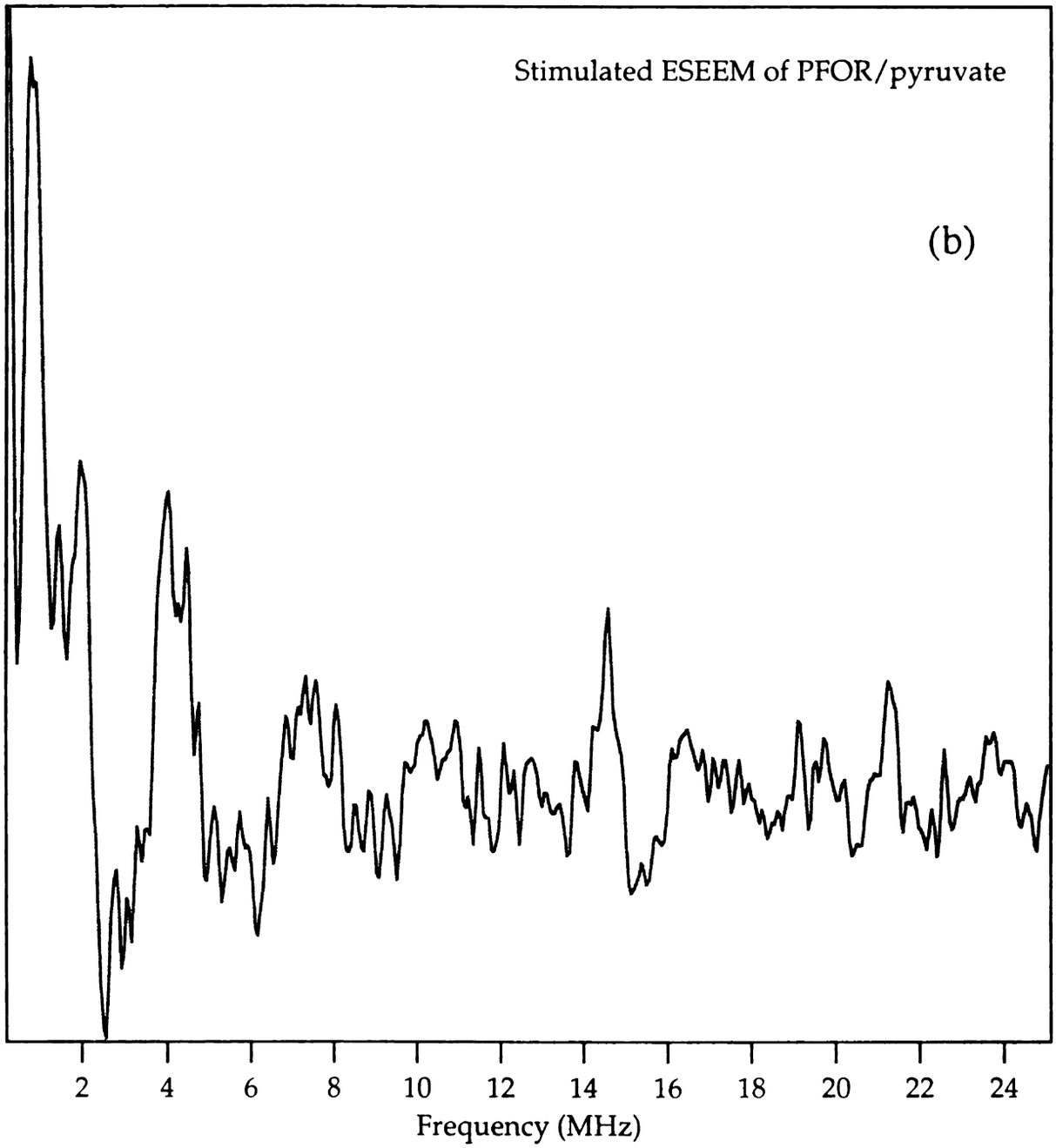

Figure II-20 (b)

However, there are low-frequency peaks at 0.8, 1.9, 3.1, 3.9, and 4.4 MHz, due to ^{14}N modulations. It is apparent that the relative intensity of the different frequency components changes with the τ value (Figure II-21) the component at 1.9 MHz becoming the most intense amongst the low-frequency lines at τ = 275 ns. τ values of 205 ns and 275 ns correspond to proton modulation suppression condition, while τ = 240 ns maximizes the amplitude of the proton modulations. Comparison of these spectra with a set of stimulated ESEEM data collected for PFOR/pyruvate at g = 1.931, Figure II-22, reveals the similarity of the corresponding pairs of spectra under similar experimental conditions. Absent from the spectra in Figure II-22 is the frequency component at 0.8 MHz. In addition, lines in these spectra are less intense and not well resolved.

The effect of the pulse sequence repetition rate on the three-pulse ESEEM at g = 2.00 is illustrated in Figure II-23. Lowering the repetition rate is expected to raise the relative intensity of the modulation frequencies associated with the nuclei in the structure of the radical due to the slower electron spin relaxation. Such effect could not be observed with certainty in the range from 40 Hz to 1 Hz, due to the low echo modulation amplitude (low intensity of the observed peaks) as well as the electron spin coupling between the radical and nearby $[Fe_4S_4]$ center, which increases the spin-lattice relaxation rate for the radical.

Typical stimulated ESEEM data for PFOR reacted with $^{2}H_3C$-pyruvate is given in Figure II-24. Pronounced deuterium modulations are present, inasmuch as the τ value selected, 205 ns, is significantly different from the deuterium suppression τ value of 445 ns determined by the inverse of the ^{2}H Larmor frequency (2.24 MHz at 3429 G). To single out the contribution from deuterium modulations the approach described in

Figure II-21: Stimulated ESEEM spectra of PFOR/pyruvate. Experimental parameters: magnetic field strength, 3429 G; microwave frequency, 9.600 GHz; pulse duration, 17 ns; pulse sequence repetition rate, 40 Hz; initial T value, 100 ns; sample temperature, 4.2 K; number of data points, 1024; number of events averaged for each data point, 34; number of scans, 2; τ value: 205 ns, (a); 240 ns, (b); 275 ns, (c); 340 ns, (d); 480 ns, (e).

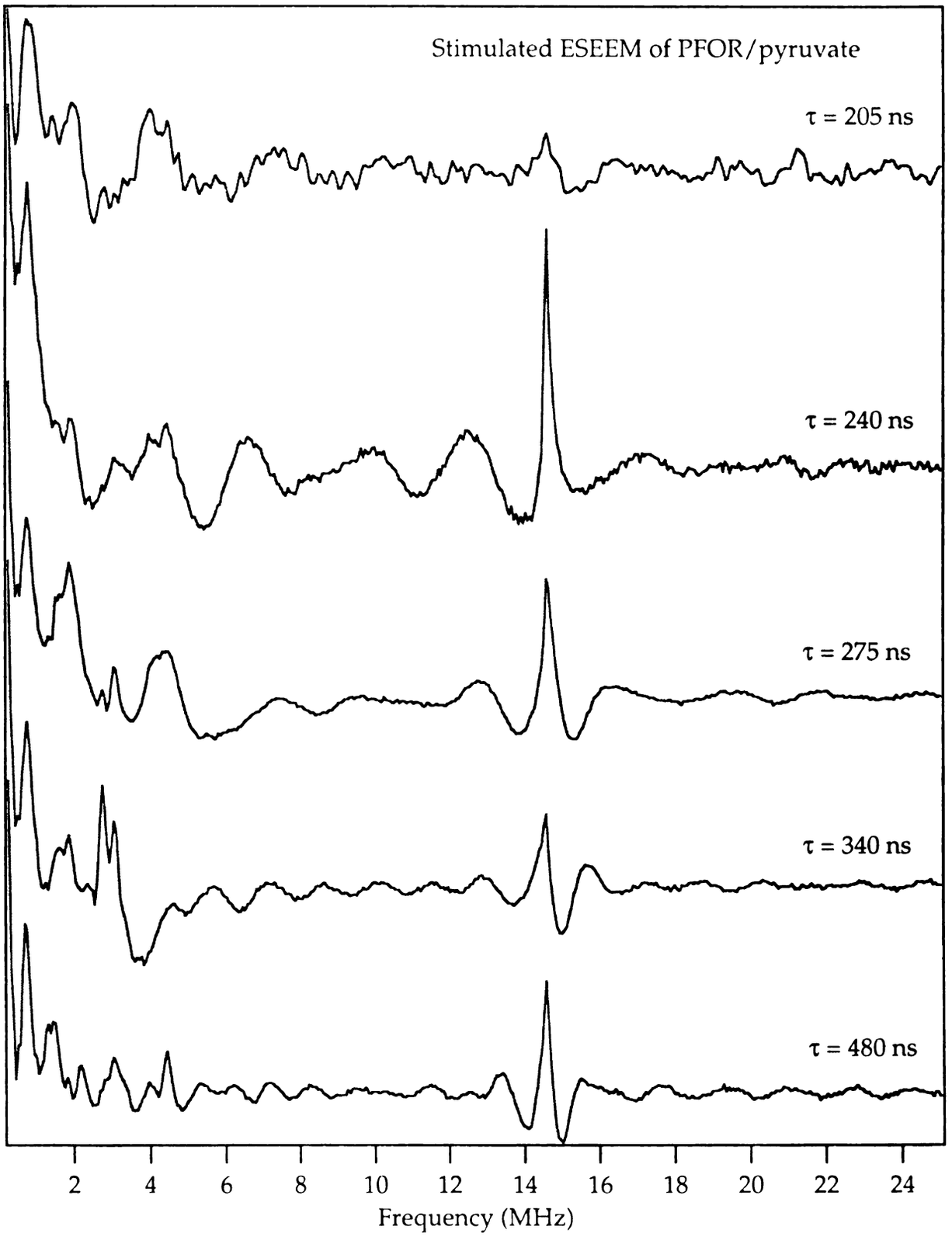
Stimulated ESEEM of PFOR/pyruvate
τ = 205 ns
τ = 240 ns
τ = 275 ns
τ = 340 ns
τ = 480 ns
2
4
6
8
10
12
14
16
18
20
22
24
Frequency (MHz)

Figure II-21

Figure II-22: Stimulated ESEEM spectra of PFOR/pyruvate. Experimental parameters: magnetic field strength, 3553 G; microwave frequency, 9.600 GHz; pulse duration, 17 ns; pulse sequence repetition rate, 40 Hz; initial T value, 100 ns; sample temperature, 4.2 K; number of data points, 1024; number of events averaged for each data point, 12; number of scans, 2; τ value: 203 ns, (a); 240 ns, (b); 340 ns, (c); 480 ns, (d).

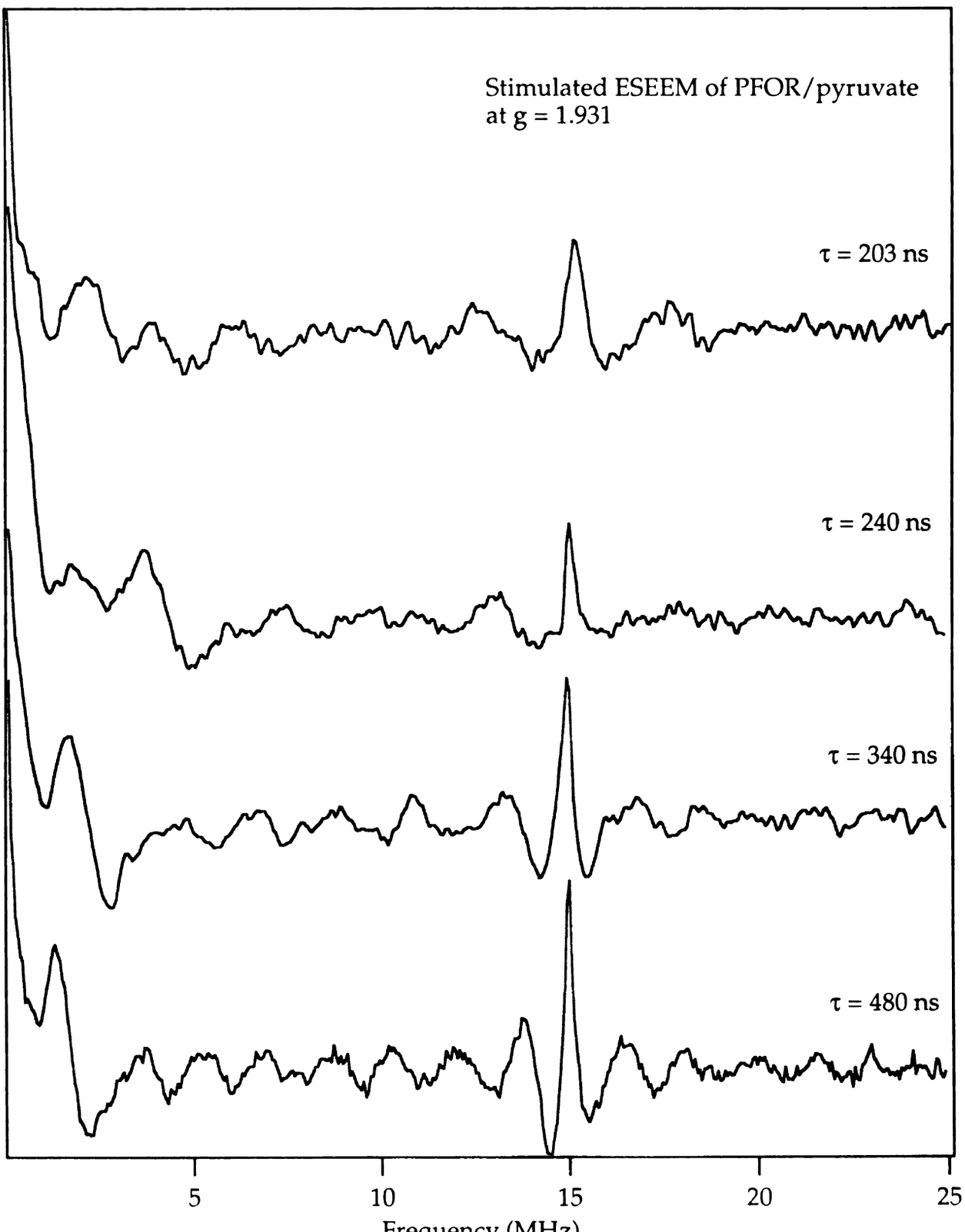
Stimulated ESEEM of PFOR/pyruvate
at g = 1.931
τ = 203 ns
τ = 240 ns
τ = 340 ns
τ = 480 ns
5
10
15
20
25
Frequency (MHz)

Figure II-22

Figure II-23: Stimulated ESEEM spectra of PFOR/pyruvate. Experimental parameters: magnetic field strength, 3429 G; microwave frequency, 9.600 GHz; pulse duration, 17 ns; initial T value, 100 ns; τ value, 203 ns; sample temperature, 4.2 K; number of data points, 1024; number of events averaged for each data point, 12; pulse sequence repetition rate: 1 Hz, (a), and 40 Hz, (b).

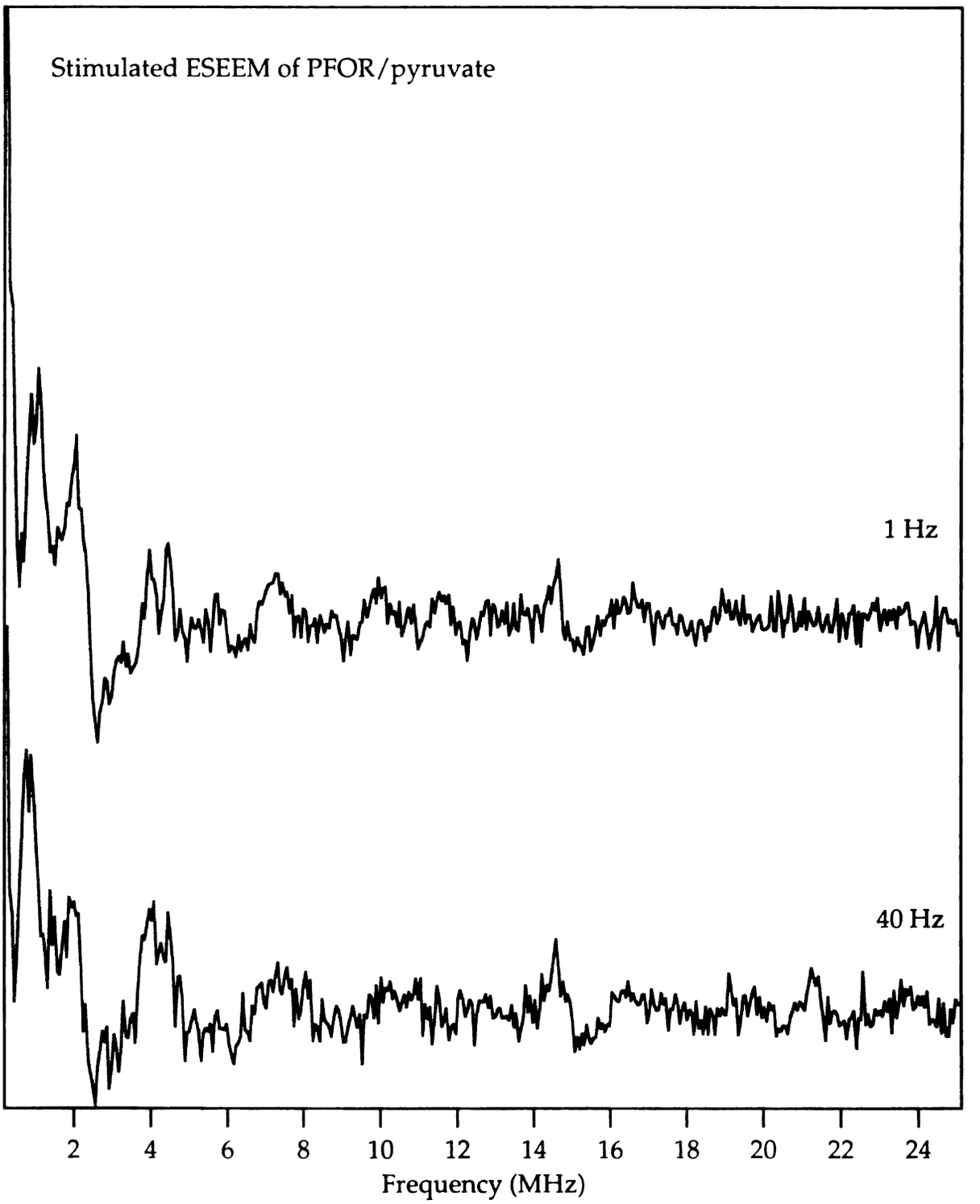
Stimulated ESEEM of PFOR/pyruvate
1 Hz
40 Hz
2
4
6
8
10
12
14
16
18
20
22
24
Frequency (MHz)

Figure II-23

Figure II-24: Stimulated ESEEM data for PFOR/$^{2}H_3C$-pyruvate. (a) Time-domain data; (b) The corresponding frequency-domain data obtained by Fourier transformation of trace (a). Experimental parameters: magnetic field strength, 3429 G; microwave frequency, 9.600 GHz; pulse duration, 17 ns; initial T value, 100 ns; pulse sequence repetition rate, 10 Hz; sample temperature, 4.2 K; number of data points, 1024; number of events averaged for each data point, 14; number of scans averaged, 2; τ value, 203 ns, (b), and 444 ns, (c).

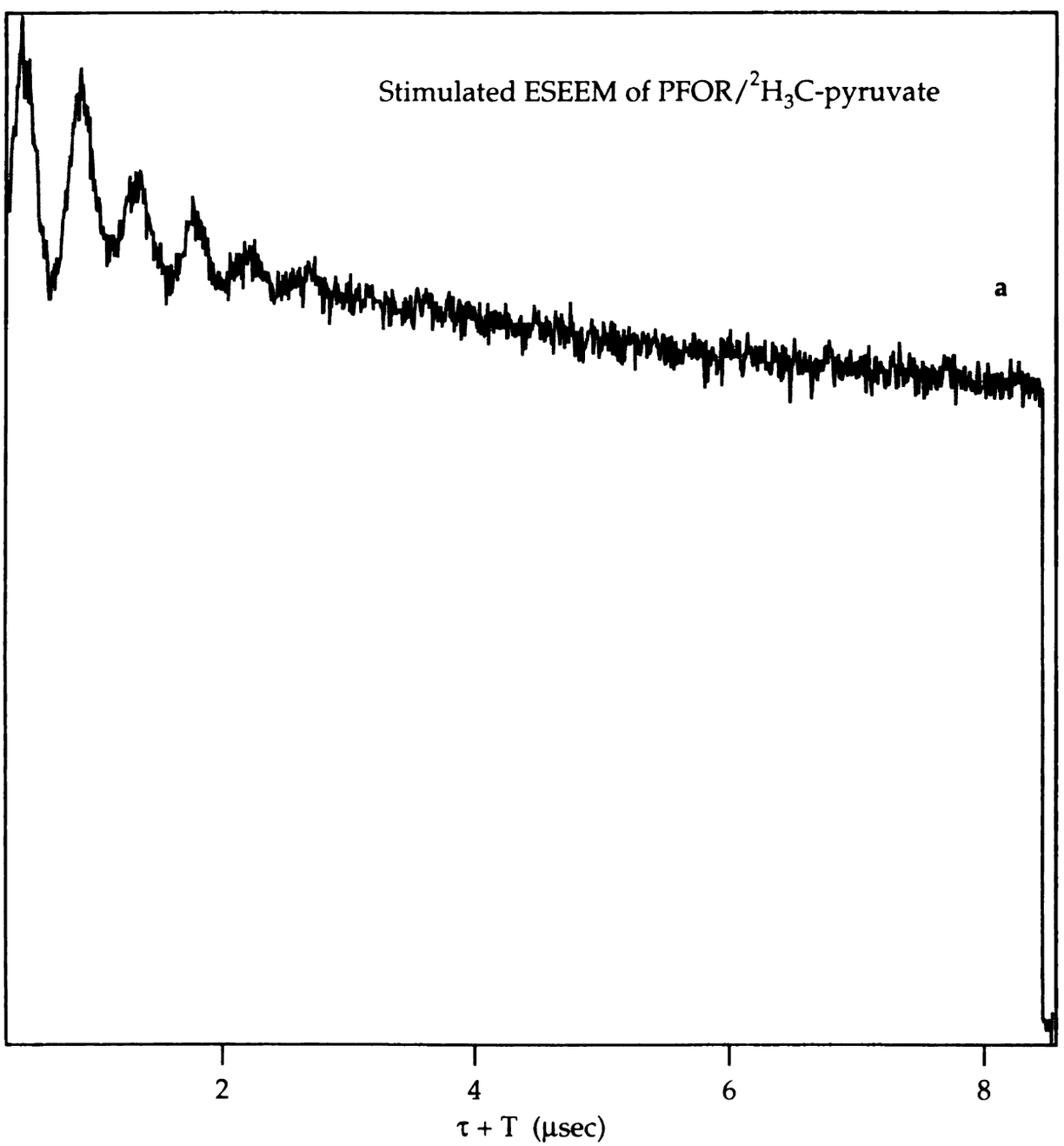

Figure II-24 (a)

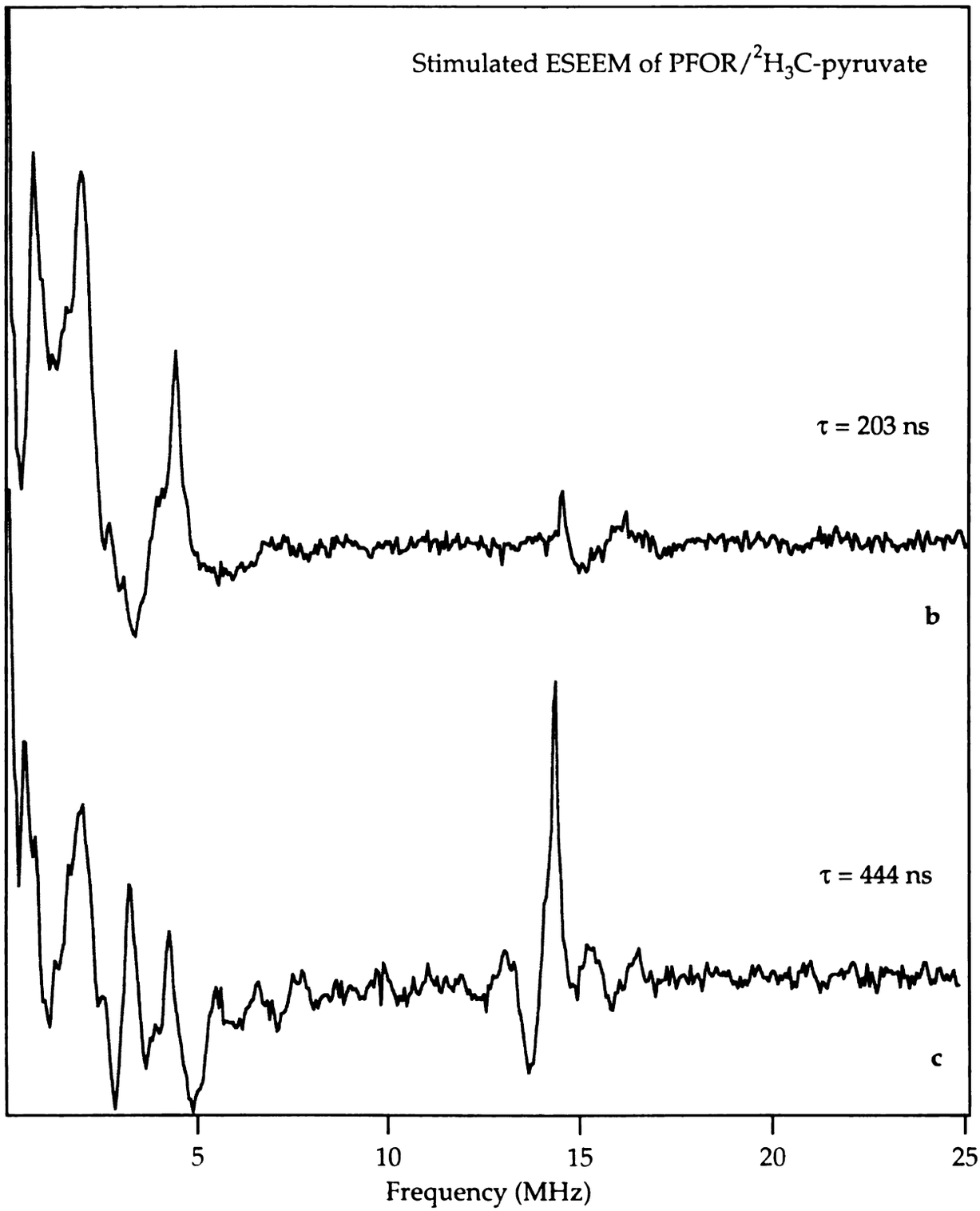

Figure II-24 (b, c)

Chapter I was used. The ESEEM time-domain data set for PFOR/^2H_3C-pyruvate sample (Figure II-24) is divided by the data set collected for PFOR/pyruvate (Figure II-20) under similar experimental conditions. The Fourier transformation of the resulting data set is shown in Figure II-25. It is evident from the figure that, except for the deuterium modulation at 2.3 MHz, the contribution from all of the other modulations is almost completely canceled.

Fourier transformations of the three pulse ESEEM data for PFOR reacted with 3-methyl-2-oxobutyrate and 2-oxobutyrate are represented in Figure II-26, respectively. They do not demonstrate any significant difference from the data for PFOR with added pyruvate. This is to be expected since the three samples differ essentially in the number of substrate protons, which does not affects the ESEEM spectrum below the proton Larmor frequency.

II.2.3. Discussion

The application of advanced EPR techniques capable of resolving weak electron-nuclear hyperfine couplings in disordered systems allows characterization of the magnetic and structural properties of the PFOR paramagnetic intermediates.

The ENDOR data presented here clearly show that the narrow EPR signal at g = 2.0056 corresponds to a substrate-derived catalytic intermediate. The presence of proton hyperfine transitions with coupling constants $A_{||}^{(1)}$= 17.35 MHz, $A_{\perp}^{(1)}$ = 11.95 MHz, $A_{||}^{(2)}$ = 19.66 MHz, and $A_{\perp}^{(2)}$ = 14.66 MHz, in the spectrum of PFOR/pyruvate, and their sensitivity to deuterium substitution, confirms the conclusion that the proton signals are due to the substrate hydrogens. In support of this conclusion is the appearance of

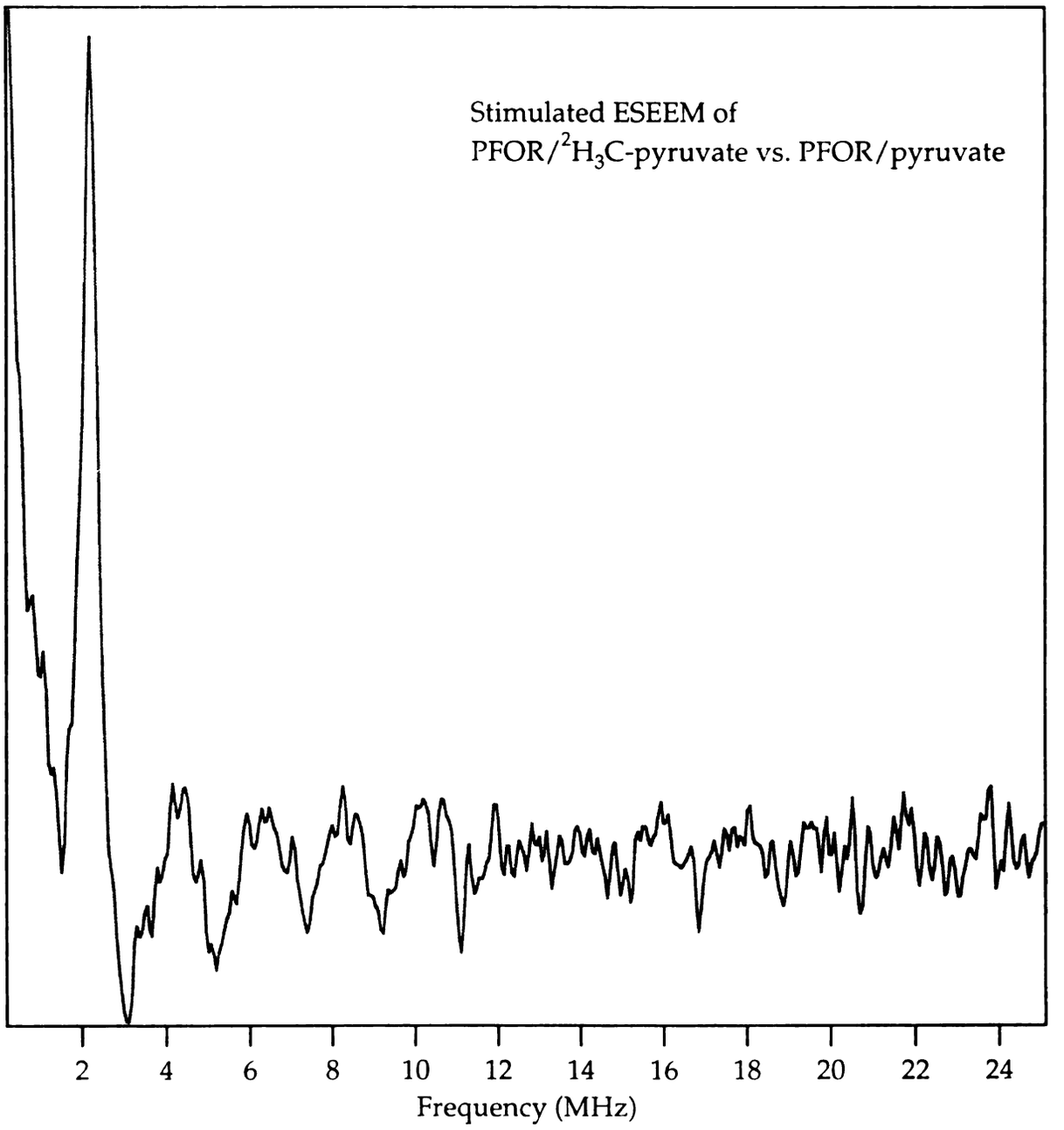

Figure II-25: Fourier transform of the time-domain ratio of the two data sets shown in Figure I-20 and Figure I-24 (a).

Figure II-26: Stimulated ESEEM spectrum of PFOR/3-methyl-2-oxobutyrate, (a). Experimental parameters: magnetic field strength, 3429 G; microwave frequency, 9.600 GHz; pulse duration, 17 ns; initial T value, 100 ns; τ value, 205 ns; pulse sequence repetition rate, 40 Hz; sample temperature, 4.2 K; number of data points, 1024; number of events averaged for each data point, 34; number of scans averaged, 4. Stimulated ESEEM spectrum of PFOR/2-oxobutyrate, (b). Experimental parameters: magnetic field strength, 3429 G; microwave frequency, 9.600 GHz; pulse duration, 17 ns; initial T value, 100 ns; τ value, 205 ns; pulse sequence repetition rate, 10 Hz; sample temperature, 4.2 K; number of data points, 1024; number of events averaged for each data point, 34; number of scans averaged, 4.

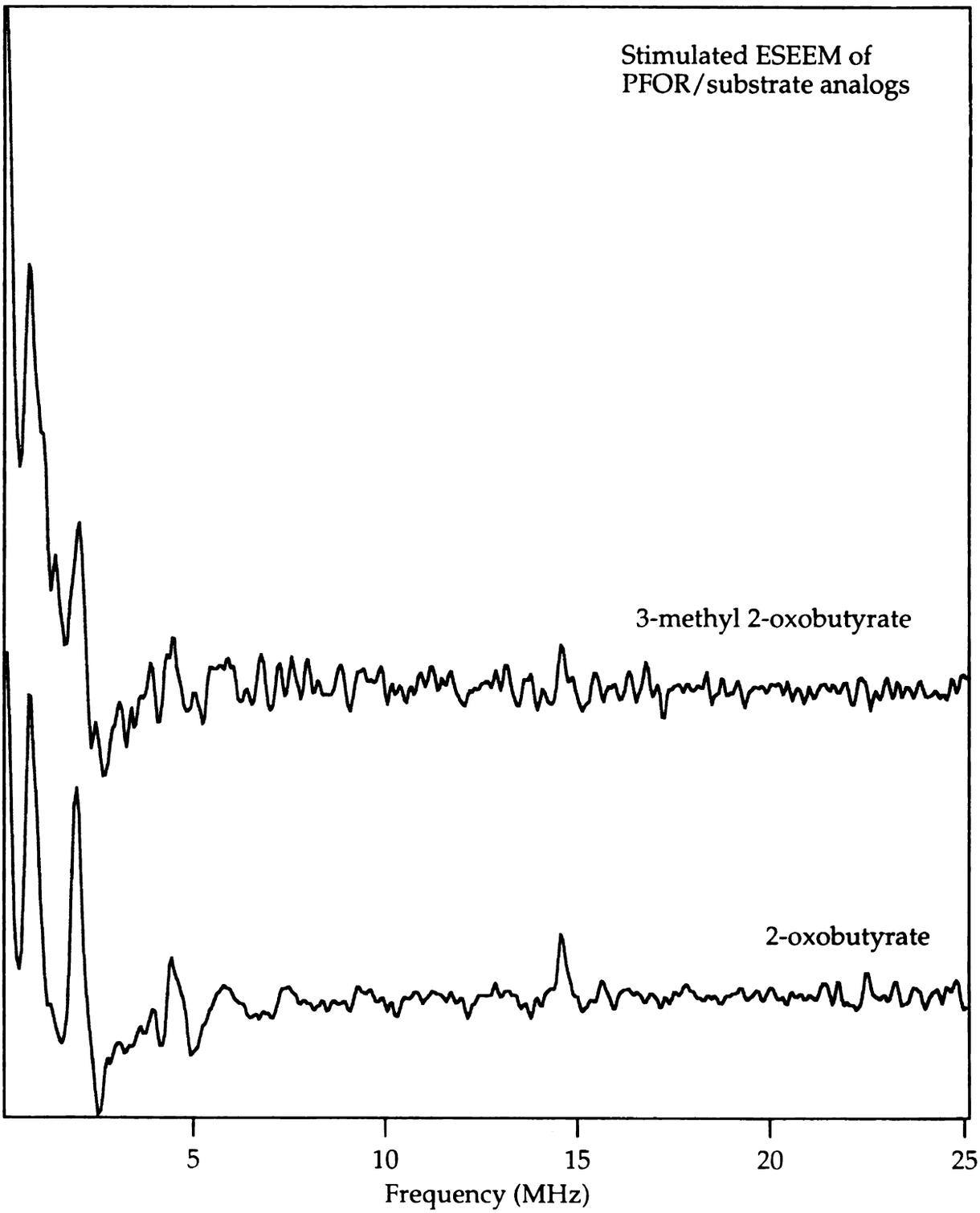
Stimulated ESEEM of
PFOR/substrate analogs
3-methyl 2-oxobutyrate
2-oxobutyrate
5
10
15
20
25
Frequency (MHz)

Figure II-26

corresponding deuteron ENDOR lines upon the isotopic substitution of the methyl protons of pyruvate. In addition, the ESEEM data on Figure II-25 shows the net contribution of the deuterium modulations arising from the substrate deuterons in the isotopically substituted pyruvate. The substrate origin of the EPR signal at g = 2.0056 is also indicated by the observed broadening of the signal upon a ^{13}C labeling of the substrate.

To justify the hypothesis that the detected ^{1}H ENDOR transitions are due to two sets of substrate protons, numerical simulations aimed at reproducing the experimental peak frequencies and lineshapes have been performed using the MATLAB scripting language[35] program "H12.m" .[35,54] One or two sets of proton spin Hamiltonian parameters have been used as input. Frequency histograms have been computed by diagonalizing the spin Hamiltonian and finding the $\Delta M_I = 1$ transitions for both electron spin manifolds. No weightings for nuclear state mixing have been included in the calculation. The amplitudes of the computed superhyperfine frequencies have been given a $\sin(\theta)$ weighting, where θ is the angle between the principal axis of the electron-nucleus hyperfine coupling tensor and the laboratory magnetic field. The integration over all possible orientations of the laboratory field, with respect to the hyperfine tensor principal axes has been done in angle increments of either 1.1° or 2.2°. Each "stick" corresponding to a particular orientation has been convoluted with a Gaussian line function having a full width at half-height between 0.3 MHz and 0.4 MHz to obtain smooth powder-type lineshapes. The powder patterns for each proton set have been differentiated numerically and added together to yield the simulated spectrum. A polynomial fit of experimental baseline points has been introduced to account for the baseline distortion that might possibly affect the appearance of the ENDOR peaks. Five equally spaced experimental

baseline points have been picked on either side of the ^{1}H ENDOR signals, and along with two additional intermediate experimental points have been fit with a fourth-degree polynomial. The polynomial function has been added as a correction factor to the derivative function representing the simulated spectrum. The above procedure has also been applied to simulate ^{2}H and ^{31}P ENDOR spectra, as described later in this Section. It should be underlined that these simulations concern only the frequencies and the lineshapes but not the intensities of the ENDOR lines. The ^{1}H ENDOR experimental and simulated spectra are shown in Figure II-27.

In all cases, the frequencies of the corresponding peaks agree within $\pm$ 0.2 MHz. However, the correspondence between the experimental (solid lines) and simulated (dotted lines) spectra with respect to the lineshapes is definitely closer for traces (a) and (b), where two sets of axially symmetric coupling parameters have been assumed. Trace (c), which has been obtained considering only one set of protons with a hyperfine tensor of rhombic symmetry shows poorer agreement with the experimental lineshape. On the other hand, the results of the simulations give little indication on whether the two sets of protons have very similar (trace (a)) or very different (trace (b)) anisotropic hyperfine interactions. In both cases, the values of the proton simulation parameters correspond closely to the ones measured directly from the experimental data set. The consideration of two sets of protons with very similar anisotropic couplings will be adopted tentatively as a working hypothesis for reasons outlined later on in this discussion.

The two hyperfine tensors extracted from the ENDOR data, Table II-1, are thus associated with two sets of substrate methyl protons. The anisotropic dipolar coupling

Figure II-27: Simulated ^{1}H ENDOR spectra for PFOR paramagnetic reaction intermediate. Each simulation data set is plotted using dotted lines and shown in comparison with the experimental spectrum (solid line). Simulation parameters: g = 5.5856012, B = 3349 G; (a) $A_{xx}^{(1)} = A_{yy}^{(1)} = 11.95$ MHz, $A_{zz}^{(1)} = 16.90$ MHz, $A_{xx}^{(2)} = A_{yy}^{(2)} = 14.66$ MHz, $A_{zz}^{(2)} = 19.10$ MHz, number of θ increments in the range 0° - 90°, 80, Gaussian linewidth, 0.40 MHz; (b) $A_{xx}^{(1)} = A_{yy}^{(1)} = 11.95$ MHz, $A_{zz}^{(1)} = 19.10$ MHz, $A_{xx}^{(2)} = A_{yy}^{(2)} = 14.66$ MHz, $A_{zz}^{(2)} = 16.90$ MHz, number of θ increments in the range 0° - 90°, 80, Gaussian linewidth, 0.40 MHz; (c) A_{xx} = 11.65 MHz, A_{yy} = 15.50 MHz, A_{zz} = 19.10 MHz, number of θ increments in the range 0° - 90°, 40, number of φ increments in the range 0° - 90°, 40, Gaussian linewidth, 0.30 MHz.

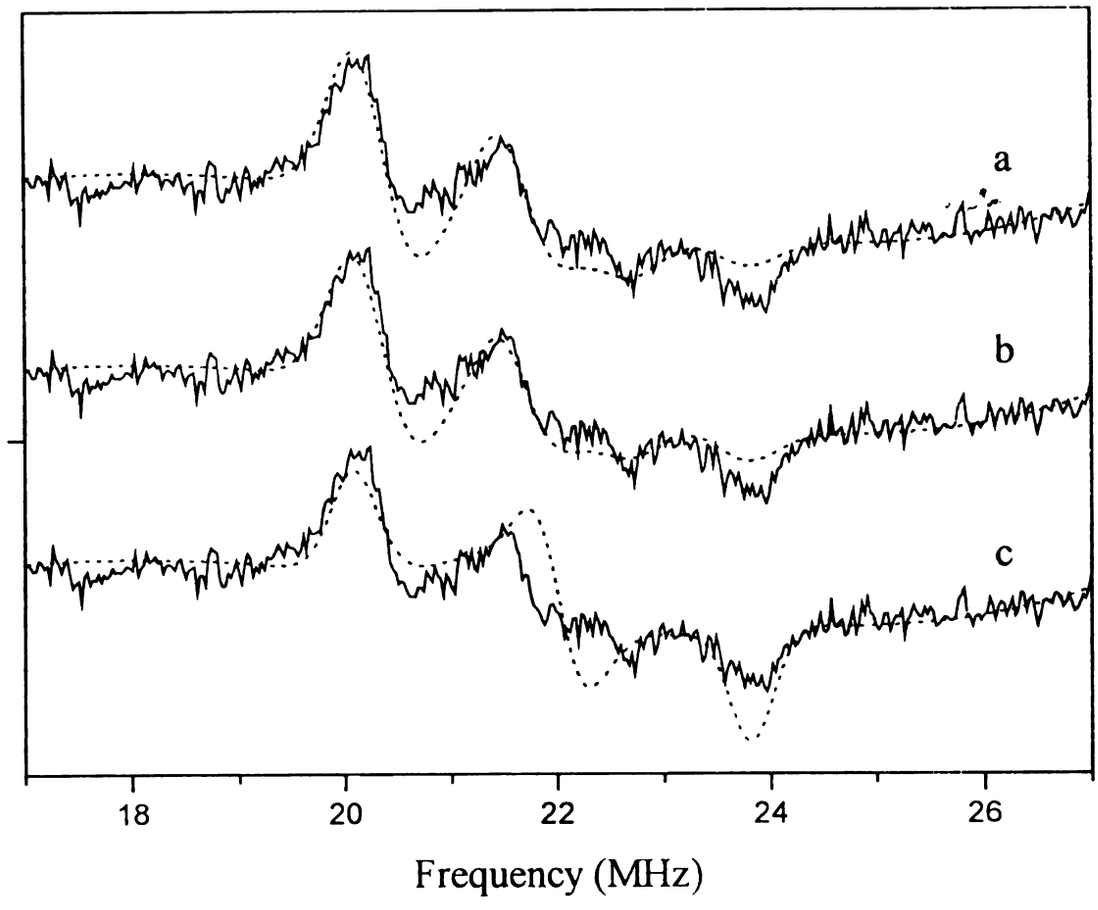

Figure II-27

constants are only small fractions of the respective isotropic constants. Such a hyperfine pattern is characteristic of the interaction of a unpaired electron with β-protons (cf. Chapter I). The small difference between the values of the hyperfine isotropic couplings indicate that the corresponding sets of β-protons are nearly equivalent. β-couplings of three methyl protons to an unpaired electron would hypothetically give rise to eight lines in the EPR spectrum and three line pairs in the ENDOR spectrum, provided that the three protons were non-equivalent. Such spectra would be expected at sufficiently low temperatures, at which the *rotation of the methyl group* is frozen. However, if the internal rotation of the methyl group about the C_α-C_β bond is fast enough, so that the frequency of rotation is high in comparison with the hyperfine precession frequency of the protons, the proton couplings will be equalized.[25] The EPR spectrum of the methyl group will then consist of a 1:3:3:1 quartet, while the corresponding ENDOR spectrum will be a single pair of lines with small anisotropy characteristic of β protons. This situation is encountered in solutions and even in solids at sufficiently high temperatures. It is well known that significant rotation of the CH_3-group is present even at temperatures as low as 4.2 K.[26-31] For instance, the methyl group in the $CH_3C^{\cdot}(COOH)_2$ radical, which can be observed in a methylmalonic acid crystal, undergoes almost free internal rotation at 4.2 K.[26] In addition, at low temperatures (e. g., below 77 K) the methyl group may execute restricted rotation through a quantum mechanical barrier-tunneling process that exchanges the methyl protons.[28-31] The tunneling rotational motion of the methyl group affects the energies of the spin states and leads to an additional term in the spin Hamiltonian, which introduces a so called tunneling splitting. The tunneling frequency of a methyl group varies

greatly from radical to radical. For the $CH_3C^{\cdot}(COOH)_2$ radical in methylmalonic acid at 4.2 K a methyl tunneling frequency of 192 MHz has been found.[30]

The detection of only two pairs of proton hyperfine lines in the ENDOR spectrum of PFOR reacted with pyruvate cannot be accounted for by the hyperfine effects of a frozen, stationary methyl group (which would give rise to three ENDOR pairs). On the other hand, raising the temperature would lower the potential barrier to the internal rotation and the ENDOR lines for the non-equivalent, frozen protons would collapse into a single pair. However, such effects were not observed in this study. The invariance of the methyl proton ENDOR lineshapes with respect to the temperature (cf. Figure II-13) indicates that the pyruvate methyl group must be rapidly rotating in a broad temperature range, even at temperatures as low as 4.2 K. The two pairs of β-proton ENDOR signals that correspond to two sets of almost equivalent methyl protons then should originate from two types of radical species that differ slightly in their structure, most likely in their conformation. The reason for having two radical species most probably lies in the sample preparation procedure, which includes quenching the reaction by rapidly freezing the sample in liquid nitrogen.

The third proton coupling constant listed in Table II-1, A_{iso} = 4.66 MHz, characterizes a more distant proton hyperfine interaction. It is known that more distant protons exhibit a nearly pure dipolar coupling, in which the maximum anisotropy is small.[28] Therefore, this coupling can be assigned to γ-proton hyperfine interaction in the radical intermediate. As mentioned in Chapter I the typical coupling constants for γ-protons are in the range of a few MHz.[25,32,33] For example, the acetoxyl radical ($CH_3COO\cdot$) whose structure resembles the hydroxyethyl fragment of the proposed HE-

TPP radical intermediate, has γ-proton isotropic hyperfine coupling of 1.7 ± 0.2 G, i. e., about 4.8 MHz.[34], which is in very good agreement with the one for the PFOR intermediate.

The isotopic replacement of the pyruvate methyl hydrogens by deuterium causes the observed ENDOR hyperfine lines to appear in a different spectral region - around the deuteron Larmor precession frequency (2.19 MHz at 3349 G). On account of the gyromagnetic ratios for protons and deuterons the isotropic hyperfine constant for the methyl protons is reduced by a factor $g_n(^1H)/g_n(^2H) = 6.51$ upon the isotopic substitution. Thus the isotropic constants for the three sets of protons listed in Table IV-1 ($A_{iso}^{(1)} = 13.75$ MHz, $A_{iso}^{(2)} = 16.33$, and $A_{iso}^{(3)} = 4.66$ MHz) are expected to be scaled down to 2.11, 2.50, and 0.72 MHz, respectively. However, the values for the deuteron hyperfine couplings are expected to be modified by the nuclear quadrupole interaction. Using the MATLAB scripting language program "D12.m",[54] numerical simulations have been performed to reproduce the frequencies and lineshapes of the experimentally observed ^2H ENDOR lines. The simulation procedure outlined above for the case of ^1H ENDOR has been followed to yield the simulated spectra shown in Figure II-28.

The values of the hyperfine coupling parameters used in the ^1H ENDOR simulations, Figure II-27(a-c), have been scaled down by a factor of approximately 6.5 and used as input data to yield the corresponding ^2H ENDOR simulated traces (a-c) in Figure II-28 (dotted lines). These hyperfine parameters have been combined with a nuclear quadrupole coupling constant, e^2qQ/h, with values in the range 40 kHz to 50

Figure II-28: Simulated ^2H ENDOR spectra for PFOR paramagnetic reaction intermediate. Each simulation data set is plotted using dotted lines and shown in comparison with the experimental spectrum (solid line). Simulation parameters: g = 0.85739, B = 3349 G; (**a**) $A_{xx}^{(1)} = A_{yy}^{(1)} = 1.80$ MHz, $A_{zz}^{(1)} = 2.60$ MHz, $e^2qQ^{(1)} = 0.05$ MHz, $A_{xx}^{(2)} = A_{yy}^{(2)} = 2.2$ MHz, $A_{zz}^{(2)} = 2.965$ MHz, $e^2qQ^{(2)} = 0.04$ MHz, $\eta^{(1)} = \eta^{(2)} = 0.1$, number of θ increments in the range 0° - 90°, 40, number of φ increments in the range 0° - 90°, 40, Gaussian linewidth, 0.092 MHz; (**b**) $A_{xx}^{(1)} = A_{yy}^{(1)} = 1.83$ MHz, $A_{zz}^{(1)} = 2.93$ MHz, $A_{xx}^{(2)} = A_{yy}^{(2)} = 2.25$ MHz, $A_{zz}^{(2)} = 2.47$ MHz, $e^2qQ^{(1)} = e^2qQ^{(2)} = 0.05$ MHz, $\eta^{(1)} = \eta^{(2)} = 0.1$, number of θ increments in the range 0° - 90°, 40, number of φ increments in the range 0° - 90°, 40, Gaussian linewidth, 0.0925 MHz; (**c**) $A_{xx} = 1.74$ MHz, $A_{yy} = 2.30$ MHz, $A_{zz} = 2.934$ MHz, $e^2qQ = 0.05$, $\eta = 0.1$, number of θ increments in the range 0° - 90°, 40, number of φ increments in the range 0° - 90°, 40, Gaussian linewidth, 0.085 MHz.

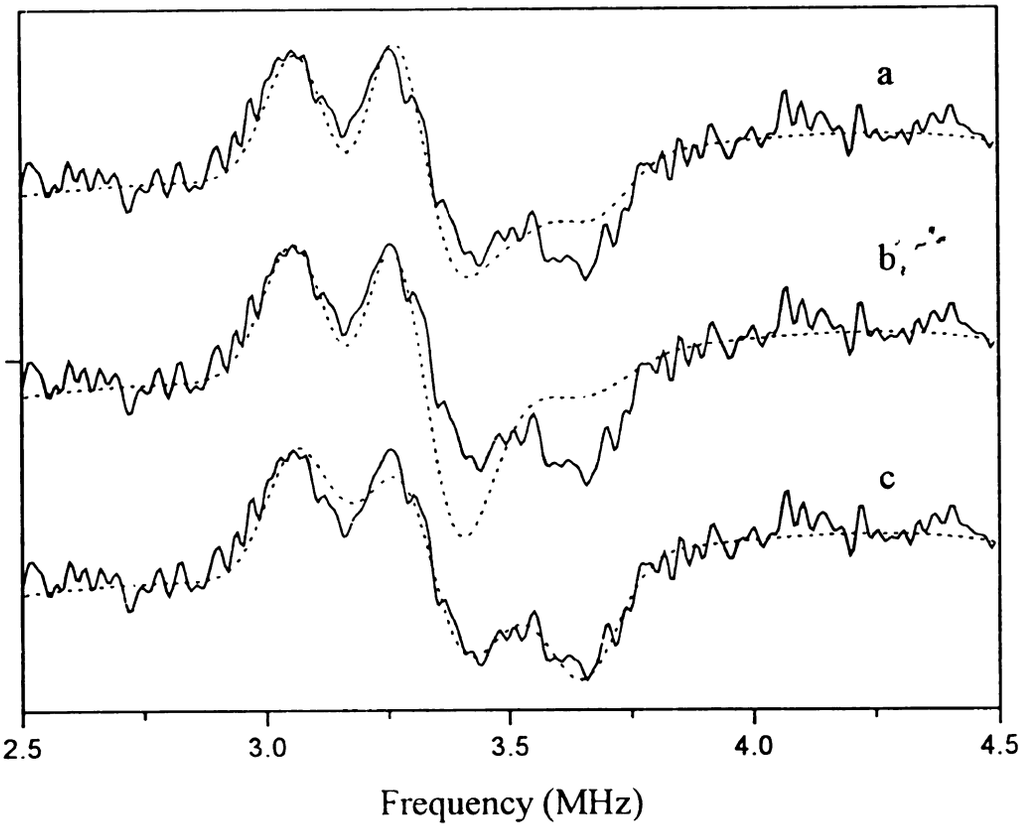

Figure II-28

kHz, and a small assymetry parameter, $\eta \sim 0.1$. (Due to the small value of e^2qQ for deuterons, the asymmetry parameter has been found to not influence the results significantly.) The values for the quadrupole coupling constant are within the range of reported magnitudes for the quadrupole interaction in organic compounds with covalently bonded deuterons.[32,36-38] In all of the three cases, the frequencies of the corresponding experimental and simulated peaks agree within $\pm$ 0.1 MHz, while it is difficult to assess the degree of agreement between the experimental and simulated lineshapes. It appears that traces (a) and (c) correspond better to the experimental spectrum with respect to the lineshape. However, only the simulated spectrum in Figure II-28(a) has a corresponding ^{1}H ENDOR simulated spectrum that is in satisfactory agreement with the experiment, Figure II-27(a). This observation is supportive of the assumption that the complex ^{1}H ENDOR lineshape is due to hyperfine interactions of two sets of protons with similar hyperfine parameters.

Surprisingly, no corresponding deuterium modulation peaks are observed in the ESEEM experiment, Figure II-24. This is most probably due to the fact that the ESEEM spectrum is dominated by a strong deuterium Larmor line at 2.24 MHz arising from matrix deuterons.

The hyperfine parameters for the β-proton hyperfine interaction in the PFOR reaction intermediate are very similar to the corresponding parameters found for the protons in polycrystalline acetyl radical ($CH_3\dot{C}=O$).[39] The acetyl radical is relevant to the PFOR catalyzed reaction as it can potentially emerge as a product of the pyruvate decarboxylation. The principal values of the proton hyperfine coupling tensor reported by Bennet and Mile[39] from their carbon-13 and proton EPR studies of polycrystalline acetyl

radical are $A_{\perp}$ = 13.0 MHz and $A_{\parallel}$ = 16.9 MHz, overall error being estimated at ±4 MHz. Thus, the isotropic component is A_{iso} = 14.3 MHz, and the purely anisotropic components are $B_{\parallel}$ = 2.6 MHz, $B_{\perp}$ = -1.3 MHz, where the symmetry axis lies close to the C_{α}-C_{β} bond direction. The authors have concluded that the acetyl radical is a σ-type radical (cf. Chapter I) with a valence angle C_{β}-C_{α}=O equal to approximately 130°. Their analysis shows that the unpaired electron is located primarily in a sp-hybrid orbital on the carbonyl carbon atom, but that there is also an appreciable spin density on the adjacent carbon and on the oxygen atom. The unpaired spin density on the two carbons has been calculated by using the obtained values for the principal elements of the ^{13}C axially symmetric hyperfine tensors and the theoretical values of the hyperfine coupling constants for the fully occupied 2s- and 2p-orbitals to find the corresponding fractions of the unpaired spin density in the 2s- and 2p-orbitals, which then have been summed. The reported total unpaired spin densities are as follows: 0.27 for the methyl carbon and 0.52 for the carbonyl carbon atom. The similarity of the total spin density on the methyl carbon atom to that on the hydrogen atom in H·CO[40] has suggested that there is a participation of the excited state, [H_3C·:C=O], in the overall electronic structure of acetyl radical comparable to that proposed for the formyl radical (cf. Chapter I). Supporting evidence for the participation of this resonance structure has been found in the low C-C bond strength in the acetyl radical (50 kJ/mol).[39] As pointed out by Bennet and Mile,[39] however, it is not necessary to postulate such delocalization of the unpaired electron since the observed isotropic methyl coupling constant (14.3 MHz) can arise from hyperconjugation (cf. Chapter I). Hyperconjugation results in a positive isotropic hyperfine coupling constant. In the acetyl radical, the delocalization of the unpaired

electron on the methyl carbon will produce a *negative* contribution to the hyperfine coupling and thus will reduce that caused by hyperconjugation which is positive. In addition, the orbital overlap due to hyperconjugation is less because of the elongated (as concluded from the bond energy) C-C bond. These two factors account for the observation that A_{iso} for the methyl protons in acetyl is much smaller than the isotropic hyperfine couplings measured for methyl protons in other σ- and π-radicals (45-80 MHz).[25,32,41] The smaller magnitudes of the anisotropic hyperfine components for acetyl radical compared to those observed for a freely rotating methyl group in π-radicals ($B_{\|}$ = 6 MHz, $B_{\perp}$ = -3 MHz)[41] has been attributed to differences in the spatial configuration and also the lower spin density (0.52) on the carbonyl carbon atom.

Applying a reasoning similar to the one given by Bennet and Mile[39] for the acetyl radical, towards the PFOR radical intermediate would lead to the conclusion that there is a pyruvate derived acetyl radical that may be bound to the TPP by a weak, non-covalent bond. This conclusion is supported by the fact that the nitrogen modulations observed in ESEEM at g = 2.003 are weak indicating a small unpaired electron spin density on the nitrogen atom. (If the radical intermediate was the HE-TPP radical, in which the hydroxyethyl fragment is covalently bound to TPP and the unpaired electron occupies the C_{α} $2p_{\pi}$ orbital, more significant spin density on the TPP nitrogen would be expected because of the effect of π delocalization over the thiazole ring). Within the frame of such a model, the small isotropic ^{31}P coupling observed in ENDOR can be explained by the proximity of the loosely bound radical and a phosphorus nucleus from the pyrophosphate fragment.

On the other hand, the results of the ENDOR and ESEEM experiments can also be explained within the frame of a π-type radical model with a rapidly rotating methyl group. The typical values for isotropic β- coupling of methyl protons in π-type radicals with a rapidly rotating methyl group are between 65 MHz and 80 MHz.[25,32,41-49] However, in the present study no ENDOR frequencies were detected beyond 23 MHz with the magnetic field being set at different values that correspond to different resonance positions in the inhomogeneously broaden radical EPR line. The deviation of the measured hyperfine couplings from the typical values for β couplings reported in the literature for alkyl and acyl radicals can be accounted for by a possible unpaired electron delocalization, which leads to a distribution of the unpaired electron spin density over the π-orbital system of the intermediate. The proposed PFOR intermediate, the HE-TPP radical (Figure II-29), is a conjugated system in which a significant electron delocalization may exist. Figure II-30 shows three of the possible resonance structures for the HE-TPP radical, the superposition of which can explain the observed β- and γ-proton hyperfine couplings.

γ -proton couplings are more likely to arise from the magnetic interaction of the methyl protons with the unpaired spin density on the TPP carbon (resonance structure I) than from their interaction with the unpaired electron centered on the hydroxyethyl oxygen since alkoxy-radicals, in which the unpaired spin is mainly concentrated on the oxygen atom, usually do not show hyperfine interaction with the alkyl protons.[50] Additional resonant structures which give rise to nitrogen hyperfine couplings are also relevant to the HE-TPP structure. This idea is in agreement with the conclusion of Menon and Ragsdale[16] that the HE-TPP radical is not purely oxygen centered, but that there

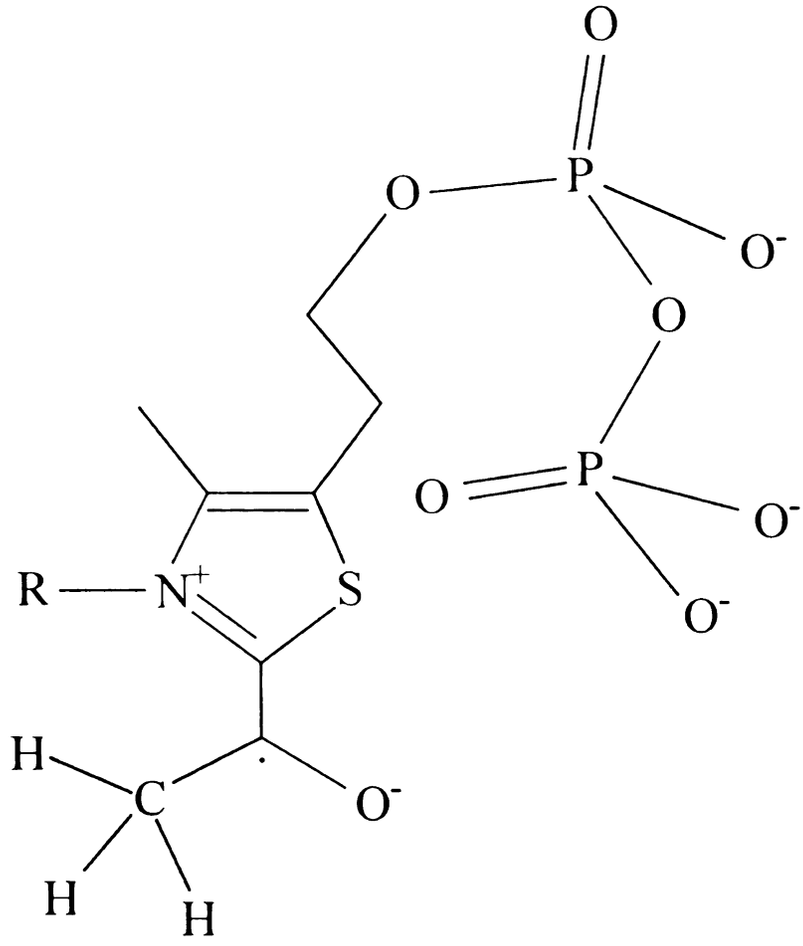

Figure II-29: Hydroxyethyl thiaminpyrophosphate radical (HE-TPP).

must be significant spin density among a number of atoms in the radical. The presence of some electron spin density on the TPP nitrogen, as indicated by the weak nitrogen ESEEM modulations at g = 2.003, can thus be related to the delocalization of the unpaired electron over the thiazole ring system. The unpaired electron delocalization may also be responsible for the remote ^{31}P hyperfine interaction observed in the ENDOR spectra of the intermediate radical.

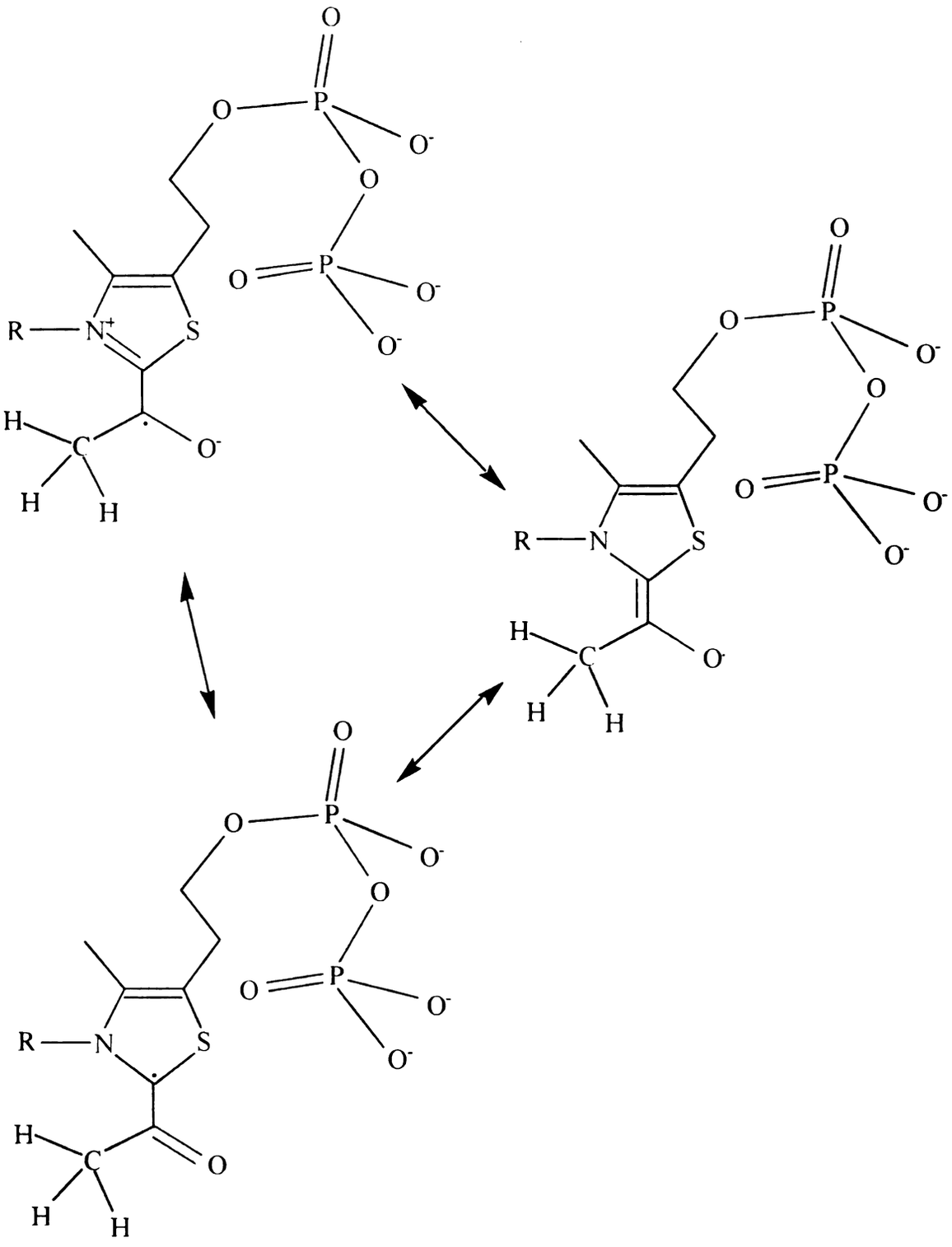

Figure II-30: Resonance structures for the HE-TPP radical.

With the assumption of a π type radical with a rapidly rotating methyl group, the unpaired electron density at the α carbon atom, $\rho_\pi^{C\alpha}$, can be obtained using the well known relationship (cf. Chapter I)

$$A_{iso}^{\beta,rot} = \rho_\pi^{C\alpha} Q_\beta \langle\cos^2\theta\rangle , \qquad [II\text{-}3]$$

where θ is the dihedral angle between the plane of the unpaired electron $2p_\pi$ orbital and the projection of a C-H bond, $\langle\cos^2\theta\rangle = 0.5$ for a rotating methyl group, and $Q_\beta = 164$ MHz.[25] The calculated $\rho_\pi^{C\alpha}$ is 0.168 for species 1 and 0.199 for species 2. This result indicates that most of the spin density (approximately 0.8) is concentrated not on the carbonyl carbon atom but that it is distributed over the rest of the atoms in the conjugated system. There is little spin density on the TPP nitrogen and the hydroxyethyl oxygen most probably carries the largest fraction of the unpaired electron population. However, a considerable spin density may also be present at the thiazole carbon atom, to which the pyruvate acyl fragment is bound by a covalent bond, as well as at the thiazole sulfur. The question of the unpaired electron distribution over the atoms in the HE-TPP intermediate can be elucidated by carrying out an experiment with an ^{17}O-labeled pyruvate, which would allow unambiguous determination of the unpaired spin density at the carbonyl oxygen atom. By using the calculated unpaired electron populations on the α-carbon atom and the dipolar field value obtained from $A_{\|}$ and $A_{\perp}$ (cf. Chapter I), the distance between the H_β nuclear dipole and the C_α electron dipole has been calculated. For species 1, the dipolar distance is 1.95 Å, while for species 2 it is 2.11 Å. These values are in good correspondence (within 10 %) with the molecular geometry average distance (2.150 Å)

between the methyl hydrogens and the carboxyl carbon in H_3CCOOH.[51] The agreement shows that the π-radical model is self-consistent.

The EPR spectrum of PFOR reacted with ^{13}C labeled substrates shows that there is significant spin density on the carbonyl carbon so as to perturb the lineshape of the radical EPR signal. The EPR spectra lack sufficient resolution to allow determination of ^{13}C hyperfine couplings. Since the hyperfine patterns of the g = 2.0056 EPR signal in the spectra of PFOR/puruvate, PFOR/^{13}C-2 pyruvate and PFOR/^{13}C-3 pyruvate are different (Figure II-10), it may be concluded that ^{13}C hyperfine components are present within the range of the EPR powder lineshape at g = 2.0056 but masked by the inhomogeneous line broadening. The presence of narrow EPR lines at the g value for the free electron (2.0023) can be associated with a dynamic averaging of hyperfine couplings and evidences the presence of a less bound, freely moving paramagnetic species. The absence of ^{13}C ENDOR signals in the spectrum of PFOR/^{13}C-2 pyruvate indicates that, most probably, the ^{13}C ENDOR spectrum occurs above the radiofrequency upper bound (35 MHz). If a free acetyl-like σ-type radical is assumed, the total unpaired spin density on the isotopically substituted C_α atom would be close to 0.52,[39] which would give rise to hyperfine splittings on the order of 300 to 450 MHz (approximately 100 to 160 gauss). Such splittings exceed the full width of the inhomogeneously broadened EPR line at g = 2.0056. However, in the present study, no distinct EPR lines extending beyond the field range of the EPR powder line at g = 2.0056 were detected at 60 K. This indicates that the value of the $^{13}C_\alpha$ hyperfine coupling has an upper bound of approximately 70 gauss (ca. 200 MHz) and that the unpaired spin density on $^{13}C_\alpha$ is less than 0.52.

The derivative-like ENDOR lineshapes at 9.0 MHz and 9.5 MHz observed in the ENDOR spectrum of PFOR/^{13}C-3 pyruvate can be assigned to the perpendicular edges of two anisotropic powder-type hyperfine lines that are associated with two sets of almost equivalent $^{13}C_{\beta}$ nuclei. It is well known that ^{13}C hyperfine interactions usually exhibit large anisotropy.[25,32,39] It is therefore possible that a single ^{13}C anisotropic hyperfine powder line covers a frequency range that is equal to or larger than the scanned range (i. e., $3T \geq 35$ MHz). Thus, in the study of Bennet and Mile,[39] T = -21 MHz for the methyl $^{13}C_{\beta}$ hyperfine interaction. High-frequency ENDOR studies of ^{13}C hyperfine interactions in PFOR with ^{13}C labeled substrates are necessary to allow an independent determination of the unpaired spin density on C_{α} and C_{β} carbons of pyruvate and an unambiguous assignment of a structure to the radical intermediate.

The observed ESEEM frequencies in the range 0.7 MHz - 5 MHz are due to ^{14}N modulations that arise from nuclear hyperfine and quadrupole interactions. These modulations are present in the ESEEM experiments at different conditions, which indicates that their origin is not solely the thiamin nitrogen. [Fe_4S_4] clusters that are encased in the protein structure show ^{14}N modulations due to [N-H S]-type hydrogen bonding between the protein amino groups and the [Fe_4S_4] cluster sulfur. Comparison of the ESEEM spectra obtained at different g values, Figure II-21 and Figure II-22, shows that the modulation frequency component at 0.8 MHz with g = 2.003 is characteristic of the TPP nitrogen. To extract information on the nitrogen magnetic coupling contained in the stimulated ESEEM data computer simulations with the FORTRAN program "sepac1" have been performed. A simulated frequency-domain ESEEM spectrum is shown in Figure II-31. The correspondence between the experimentally obtained and calculated ESEEM

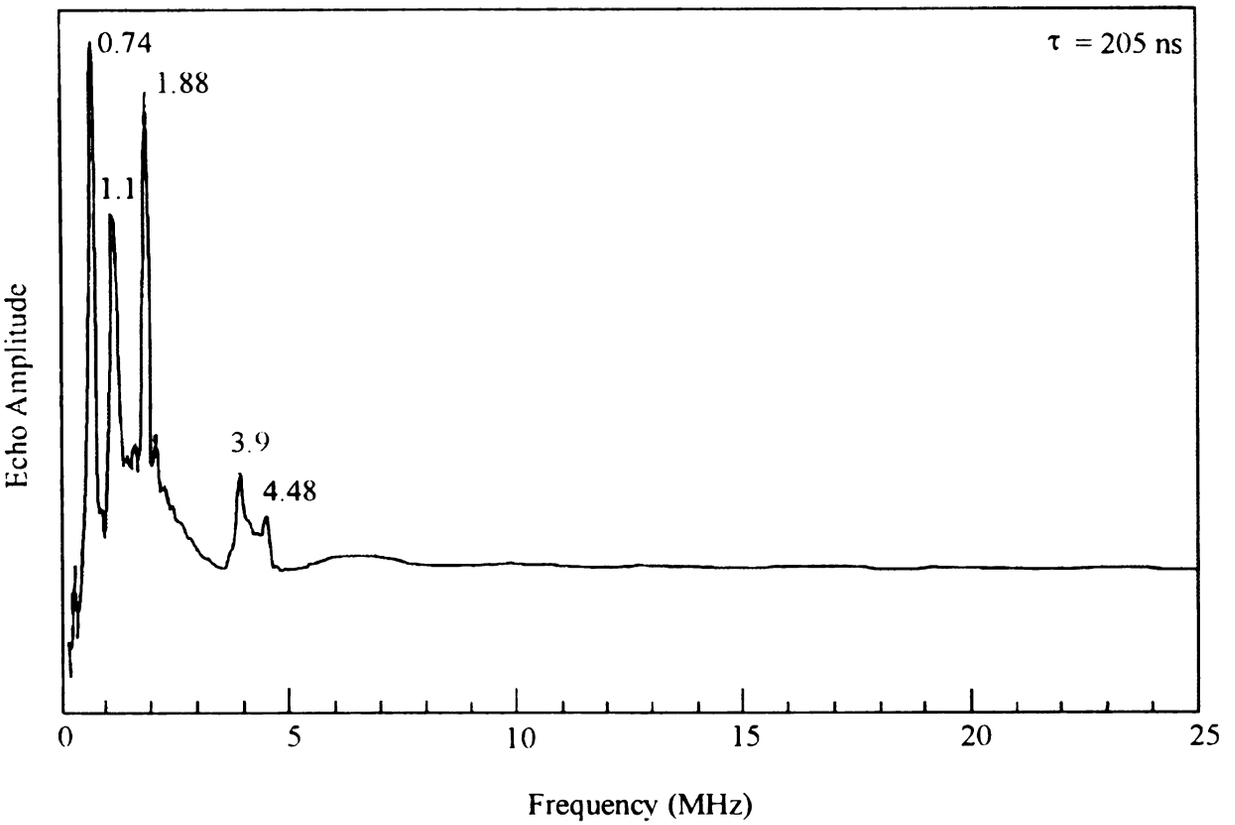

Figure II-31: Simulated ^{14}N ESEEM frequency domain spectrum. Simulation parameters: nuclear Larmor frequency, ν_I = 1.05 MHz; $A_\perp$ = 1.36 MHz, $A_{||}$ = 2.36 MHz; e^2qQ = 1.9 MHz, η = 0.74; number of θ increments in the range 0-90°, 60, number of φ increments in the range 0-90°, 40; τ = 205 ns.

frequencies is satisfactory (±0.1 MHz). However, there is some discrepancy in the intensities of the low-frequency peaks indicating that the Hamiltonian parameters used in the simulation are not optimal. The ^{14}N spin Hamiltonian parameters used for the simulation of Figure II-31 were $A_\perp$ = 1.36 MHz and $A_{||}$ = 2.36 MHz, e^2qQ = 1.9 MHz, and η = 0.74, indicating that the superhyperfine couplings are dominated by ^{14}N nuclear

quadrupole interactions. The hyperfine and nuclear quadrupole parameters are comparable to the ones reported for nitrogen couplings in heterocyclic systems.[32,38,52] The large value of the asymmetry parameter reflects an uneven electronic charge distribution around the nitrogen nucleus due to a more localized (C=N) double bonding in the thiazole ring and the low local molecular symmetry. The parameters estimated via the simulation illustrate one of the reasons for not observing nitrogen hyperfine transitions in the ENDOR experiments. The small values of the hyperfine coupling constants combined with the exceptionally low gyromagnetic ratio of ^{14}N relative to the one for ^{1}H ($g_n(^{1}H)/g_n(^{14}N) = 13.85$) cause the ^{14}N ENDOR lines to appear in the ~1 MHz region, where the detection is impeded for instrumental reasons.

An interesting feature in the ENDOR spectra of the radical intermediate in the PFOR catalyzed reaction are the ^{31}P signals. The lineshapes of these signals are characteristic of a predominantly isotropic hyperfine interaction of ^{31}P nucleus with the unpaired electron in the radical, which implies proximity of the phosphorus and the unpaired electron. This is supported by the ^{31}P ENDOR simulation results shown in Figure II-32. [54]

The simulation procedure described for ^{1}H ENDOR has been followed, with the assumption of an axially symmetric anisotropic hyperfine interaction. No baseline correction has been attempted. The best agreement with the experimental spectrum is obtained for the cases of either a purely isotropic hyperfine interaction, Figure II-32(a), or a predominantly isotropic hyperfine interaction, $A_{iso} >> T$, where T denotes the dipolar part of the axially symmetric hyperfine tensor, Figure II-32(d). It is not clear how such an isotropic interaction can arise since the pyrophosphate phosphorus nuclei and the substrate

remainder that carries the unpaired electron are separated by a number of bonds. There is little possibility for delocalization of the unpaired electron as the pyrophosphate group is bonded to the thiazole ring via an ethylene bridge. The most probable cause for the observed weak (~0.5 MHz) ^{31}P hyperfine interaction is the hydrogen bonding between the carbonyl oxygen in the decarboxylated pyruvate and the pyrophosphate part of the molecule, with the participation of solvent molecules (H_2O).

However, there exist possibility that the ^{31}P ENDOR signals are primarily due to remote, through-space dipolar electron-nuclear magnetic interactions. Trace (b) in Figure II-32 represents the simulated ^{31}P ENDOR spectrum for the case of a purely anisotropic hyperfine interaction. Similar lineshapes are obtained when the dipolar coupling is combined with a smaller isotropic component. Apparently, the correspondence between the experimental and simulated lineshapes is less satisfactory in this case relative to the case of a dominating isotropic hyperfine interaction.

A third interpretation can be considered, assuming that the observed ^{31}P ENDOR signals represent the perpendicular edges of two broad ^{31}P hyperfine powder patterns whose low-intensity parallel edges either span beyond the scanned frequency region, or overlap with the proton matrix line. This assumption results in trace (c) of Figure II-32. Multiple simulated spectra of type (c) can be obtained with various combinations of A_{iso} and T. For example, the combination of A_{iso} = 10.53 MHz and T = 10.00 MHz which ensures the appearance of the parallel edges outside the region 1 MHz – 30 MHz, leads to a simulated spectrum that is very similar to that shown in Figure II-32(c). As in the case of A_{iso} = 0, simulated lineshapes do not agree well with the experimental ones. Moreover, larger values of A_{iso} and T are even more difficult to be accounted for, taking

Figure II-32: Simulated ^{31}P ENDOR spectra for PFOR paramagnetic reaction intermediate. Each simulation data set is plotted using dotted lines and shown in comparison with the experimental spectrum (solid line). Simulation parameters: g = 2.2633, B = 3345 G; (**a**) A_{iso} = 0.53 MHz, T = 0 MHz, number of θ increments in the range 0° - 90°, 80, Gaussian linewidth, 0.09 MHz; (**b**) A_{iso} = 0 MHz, T = 0.59 MHz, number of θ increments in the range 0° - 90°, 80, Gaussian linewidth, 0.08 MHz; (**c**) A_{iso} = 6.15 MHz, T = 5.725 MHz, number of θ increments in the range 0° - 90°, 160, Gaussian linewidth, 0.09 MHz; (**d**) A_{iso} = 0.53 MHz, T = 0.12 MHz, number of θ increments in the range 0° - 90°, 80, Gaussian linewidth, 0.07 MHz.

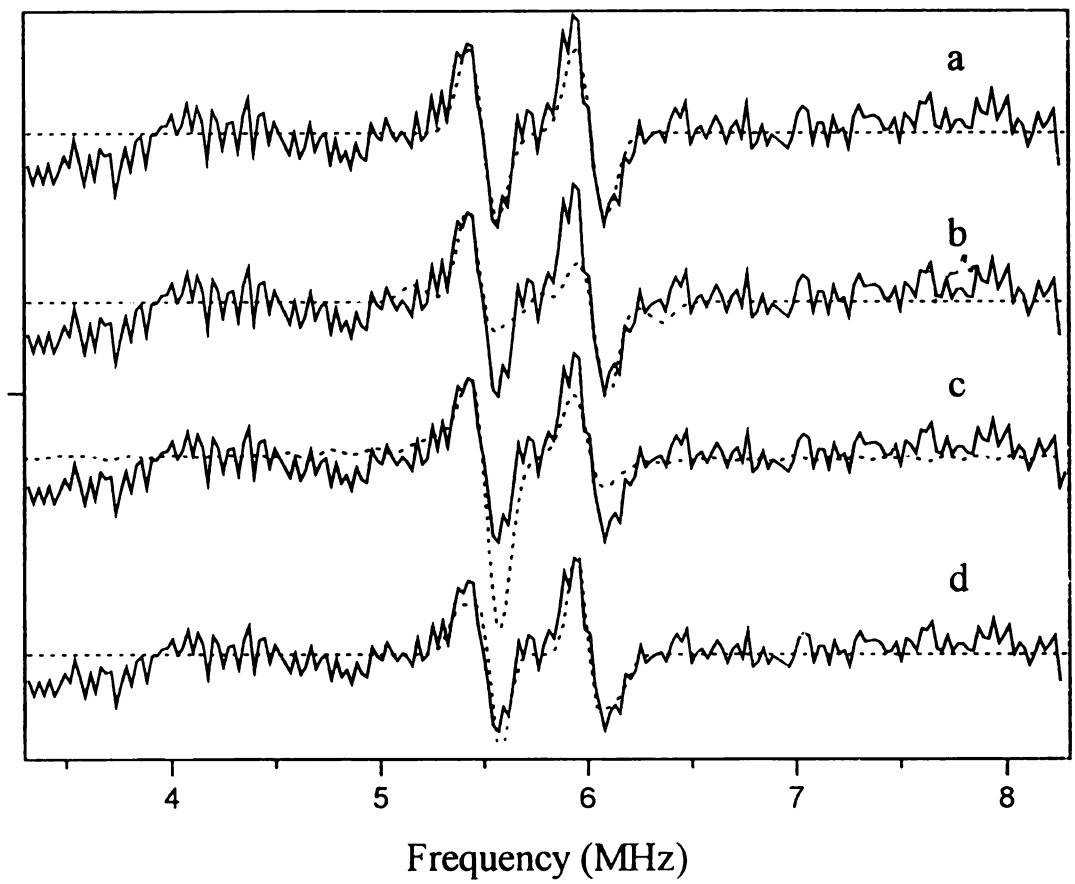

Figure II-32

into consideration the remoteness of the phosphorus nucleus relative to the paramagnetic center.

Molecular mechanics computations have been carried out to estimate a reasonable distance between the phosphorus (labeled as P^2) in the structure of HE-TPP radical and the hydroxyethyl oxygen atom carrying most of the unpaired electron density. Spartan 4.0 with the Sibyl force field has been used to perform the computations.[54] The molecular geometry has been first optimized to find a minimum on the potential energy surface. The resulting conformation has a planar thiamine ring and an unfolded pyrophosphate chain, with both phosphorus atoms being in the opposite end with respect to the hydroxyethyl oxygen. The optimized molecular conformation has been used as a starting geometry for the next computations. All bond lengths and bond angles have been constrained to their optimized values. The ring system has also been constrained to remain flat by fixing the relevant dihedral angles. A force constant (SIGMA) equal to 100 for each of the constrained parameters has been used. Several partial optimizations of the constrained system have been performed at fixed distances between the hydroxyethyl oxygen and P^2. The resulting conformations have been visually monitored for unrealistic distortions and some of the values for the interatomic distances (e. g., between oxygens of the pyrophosphate remainder and the thiamine sulfur) have been examined for consistency. 2.5 Å has been found to be a reasonable estimate for the smallest P^2-O distance at which no significant distortions of the rest of the molecule occur (Figure II-33). Such a distance is not unrealistic, considering that the TPP is contained within the protein structure which may place constraints on the TPP conformations. Clearly, a distance in the range 2.5 - 3 Å is sufficient for an efficient, through-space electron-nuclear magnetic interaction to take

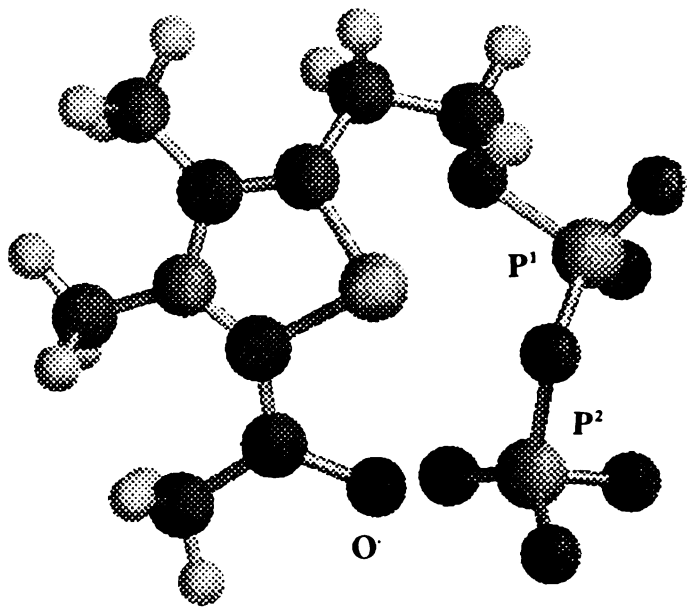

Figure II-33: A constrained conformation of the HE-TPP radical. All valence bond lengths and valence angles are set to their equilibrium values in the optimal conformation. P^2 - O distance is fixed at 2.5 Å. Optimization of the molecular geometry has been performed by adjusting dihedral angles.

place. If a purely dipolar electron-nuclear hyperfine interaction is assumed ($A_{iso} = 0$), so that the two ^{31}P ENDOR components overlap as shown in Figure I-12 (a), the unpaired spin density on the pyruvate oxygen, ρ^O, can be estimated. With $A_\perp = 2T = 0.5$ MHz and $T = \rho^O (g\, g_n\, \mu_B\, \mu_{B,n} / r^3)$, the calculated unpaired electron density on the pyruvate oxygen is $\rho^O = 0.2$ at an electron dipole-nuclear dipole distance $r(O\text{-}P^2) = 3.0$ Å. On the other hand, if ρ^O is assumed to be $\rho^O \sim 0.8$, a limiting value in accordance with the model

of a π-radical, the corresponding dipolar distance is $r(O\text{-}P^2) = 4.7$ Å. With T = 0.12 MHz, i. e., the dipolar coupling from the simulated spectrum that most adequately reproduces the experimental lineshape (Figure II-32(d)), the 2p-unpaired electron density on the pyruvate oxygen is found to be $\rho^O = 0.1$ at $r(O\text{-}P^2) = 3.0$ Å, while the dipolar distance turns out to be $r(O\text{-}P^2) = 5.98$ Å for $\rho^O \sim 0.8$. It can be concluded that the estimated range of electron nuclear dipolar distances, 3.0-6.0 Å, correlates well with the expected range of unpaired spin densities on the pyruvate oxygen.

II.2.4. Conclusion

The study of PFOR paramagnetic intermediates by EPR, ENDOR and ESEEM has brought some insight into the nature and magnetic properties of the reaction intermediates. It has been shown unambiguously that the EPR signal detected at g = 2.00 is due to a substrate-derived radical. A number of hyperfine couplings have been determined from the spectra. The results can be explained equally well within the frame of two models. The σ-type radical model postulates a pyruvate-derived acetyl radical which is not covalently bound to TPP, but is in proximity of (or weakly bound to) both the thiazole nitrogen and the pyrophosphate, i. e., it forms an adduct with TPP. The π -type radical model adopts the proposed HE-TPP radical as the reaction intermediate. The results show that the reaction intermediate is related to the enzyme TPP prosthetic group.

References

1. Stryer, L. *Biochemistry*, Freeman: New York, 1995.

2. Adams, M. W. W.; Kletzin, A. *Adv. Protein Chem.* **1996**, *48*, 101-180.

3. Blamey, J. M.; Adams, M. W. W. *Biochim. Biophys. Acta* **1993**, *1161*, 19-27.

4. Smith, E. T.; Blamey, J. M.; Adams, M. W. W. *Biochemistry* **1994**, *33*, 1008-1016.

5. Mai, X.; Adams, M. W. W. *J. Biol. Chem.* **1994**, *269*, 16726-16732.

6. Heider, J.; Mai, X.; Adams, M. W. W. *J. Bacteriol.* **1996**, *178*, 780-787.

7. Mai, X.; Kletzin, A.; Heider, H.; Ma, K.; Verhagen, M. F. J. M.; Adams, M. W. W. *J. Inorg. Biochem.* **1995**, *59*, 541.

8. Cammack, R.; Kerscher, L.; Oesterhelt, D. *FEBS Lett.* **1980**, *118*, 271-273.

9. Kerscher, L.; Oesterhelt, D. *Eur. J. Biochem.* **1981**, *116*, 587-594.

10. Kerscher, L.; Oesterhelt, D. *Eur. J. Biochem.* **1981**, *116*, 595-600.

11. Kerscher, L.; Oesterhelt, D. *Trends Biochem. Sci.* **1982**, *7*, 371-374.

12. Wahl, R. C.; Orme-Johnson, W. H. *J. Biol. Chem.* **1987**, *262*, 10489-10496.

13. Wieland, O. H. *Rev. Biochem. Physiol. Pharmacol.* **1983**, *96*, 123-170.

14. Docampo, R.; Moreno, S. N. J.; Mason, R. P. *J. Biol. Chem.* **1987**, *262*, 12417-12420.

15. Hrdy, I.; Müller M. *J. Mol. Evol.* **1995**, *41*, 388-396.

16. Mennon S.; Ragsdale S. W. *Biochemistry* **1997**, *36*, 8484-8494.

17. Drake, H. L.; Hu, S.-I.; Wood, H. G. *J. Biol. Chem.* **1981**, *256*, 11137-11144.

18. Mennon S.; Ragsdale S. W. *Biochemistry* **1996**, *35*, 12119-12125.

19. Zhang, Q; Iwasaki, T.; Wakagi, T.; Oshima, T. *J. Biochem. (Tokyo)* **1996**, *120*, 587-599.

20. McCracken, J.; Peisach, J.; Dooley, D. M. *J. Am. Chem. Soc.* **1987**, *109*, 4064-4072.

21. Schneider H. J.; Dullenkopf P. *Rev. Sci. Instrum.* **1977**, *48*, 68.

22. Gordon J. P. *Rev. Sci. Instrum.* **1961**, *32(6)*, 658-661.

23. Mims, W. B. *Phys. Rev. B: Solid State* **1972**, *5*, 2409-2419.

24. Mims, W. B. *J. Magn. Reson.* **1984**, *59*, 291-306.

25. Gordy, W. in *Techniques in Chemistry, Vol. XV: Theory and Applications of Electron Spin Resonance*; West, W., Ed.; Wiley: New York, 1980.

26. Heller, C. J. *Chem. Phys.*, **1962**, *36*, 175.

27. Horsfield, A.; Morton, J. R.; Whiffen, D. H. *Molec. Phys.* **1961**, *4*, 425.

28. Kevan, L.; Kispert, L. D. In *Electron Spin Double Resonance Spectroscopy*, Wiley-Interscience: New York, 1976, pp. 199-204.

29. Clough, S.; Poldy, F. *J. Chem. Phys.* **1969**, *51*, 2076-2084.

30. Clough, S.; Hill, J.; Poldy, F. *J. Phys. C: Solid State Phys.* **1972**, *5*, 518.

31. Clough, S.; Poldy, F. *J. Phys. C: Solid State Phys.*, **1973**, *6*, 2357.

32. Poole, C. P.; Farach, H. A., eds., *Handbook of Electron Spin Resonance, Data Sources, Computer Technology, Relaxation and ENDOR*, American Institute of Physics: New York, 1994.

33. Ayscough, P.B. In *Electron Spin Resonance in Chemistry*, Methuen: London, 1967, pp. 288-290.

34. Rehorek, D.; Hennig, H. *Z. Chem.* **1980**, *20*, 109-110.

35. The MathWorks, Inc. MATLAB. [Online] Available http://www.mathworks.com/index.html, August 20, 1998.

36. Bonera, G.; Rigamonti, A. *J. Chem. Phys.*, **1965**, *42*, 175-180.

37. Glasel, J. A. *J. Am. Chem. Soc.* **1969**, *91*, 4569-4571.

38. Lucken, E. A. C. *Nuclear Quadrupole Coupling Constants*, Academic Press: New York, 1969.

39. Bennet, J. E.; Mile, B. *Trans. Faraday Soc.*, **1971**, *67*, 1587-1597.

40. Cochran, E. L.; Adrian, F. J.; Bowers, V. A. *J. Chem. Phys.* **1966**, *44*, 4626.

41. Ayscough, P.B. In *Electron Spin Resonance in Chemistry*, Methuen: London, 1967.

42. Read, S. F. J.; Whiffen, D. H. *Mol. Phys.*, **1967**, *12*, 159-164.

43. Morton, J. R.; Horsfield, A. *J. Chem. Phys.* **1961**, *35*, 1142-1143.

44. Morton, J. R., *Chem. Rev.* **1964**, *64*, 453.

45. Wells, J. W.; Box, H. C. *J. Chem. Phys.* **1966**, *35*, 2935-2938.

46. Kwiram, A. *J. Chem. Phys.* **1968**, *49*, 2860-2861.

47. Box, H. C.; Budzinski, E. E.; Lilga, K. T. *J. Chem. Phys.* **1972**, *57*, 4295-4298.

48. Brustolon, M.; Cassol, T.; Micheletti, L.; Serge, U. *Mol. Phys.*, **1986**, *57*, 1005-1014.

49. Atherton, N. M.; Oliver, C. E. *J. Chem. Soc. Faraday Trans. 1*, **1988**, *84*, 3257-3262.

50. Ayscough, P.B. In *Electron Spin Resonance in Chemistry*, Methuen: London, 1967, pp. 347-348.

51. Tabor. W. J. *J. Chem. Phys.* **1957**, *26*, 974-975.

52. Warncke, K.; Brooks, H. B.; Lee, H.-I.; Davidson, V. L.; Babcock, G. T.; McCracken, J. *J. Am. Chem. Soc.* **1995**, *117*, 10063-10075.

53. Wavefunction, Inc. Spartan. [Online] Available http://www.wavefun.com/index.html, August 6, 1998.

54. Simulations of ENDOR Frequencies for PFOR Reaction Intermediates. [Online] Available http://www.cem.msu.edu/~bouchev/simulations/ENDOR/ENDORSimulations.html, April 25, 1999.

Chapter III

Hyperfine Sublevel Correlation Spectroscopy (HYSCORE) of S = 1/2, I = 1 Spin Systems

III.1. Introduction

Two-dimensional (2D) ESEEM techniques have proved to be useful for disentangling complicated ESEEM spectra by correlating pairs of transitions between hyperfine levels, determining the relative sign of different hyperfine couplings, and separating ESEEM lines belonging to different paramagnetic species. The first 2D Fourier transform (FT) ESEEM experiment proposed by Merks and de Beer[1] is based on the three-pulse sequence. It is essentially a three-pulse ESEEM experiment in which the time-domain data points are systematically collected in both τ- and T-dimensions to aid in spectral assignment. A single 2D Fourier transform thus contains the precise information that is available from a large number of 1D three-pulse ESEEM spectra. For an S=1/2, I=1/2 spin system the 2D spectrum is symmetrical relative to the diagonal ($\omega_1 = \omega_2$) and consists of peaks (ω_1, ω_2) at (0, 0), (ω_α, 0), (0, ω_α), (ω_β, 0), (0, ω_β), (ω_α, ω_β), (ω_β, ω_α).[1,2] In the absolute value Fourier transform spectrum, the amplitude of all peaks (except that of the peak at (0, 0)) is the same and no suppression effect typical of the 1D stimulated ESEEM is observed. However, the use of the three pulse sequence for 2D ESEEM is limited by the fact that the decay of the electron spin echo is governed by different relaxation times in both τ- and T- time dimensions. Since the time of the primary

echo decay is much shorter than that of the stimulated echo, the resolution along the different frequency axes may differ by orders of magnitude. An alternative method that overcomes the disadvantages of the three-pulse 2D ESEEM is the HYSCORE (hyperfine sublevel correlation spectroscopy) technique proposed by Höfer et al.[3)]

The simplest pulse scheme for HYSCORE utilizes a four-pulse sequence ($\pi/2$ - τ - $\pi/2$ - t_1 - π - t_2 - $\pi/2$) to generate a stimulated echo at time τ after the third $\pi/2$ microwave pulse, Figure III-1. The additional π pulse inserted in the three pulse sequence that is normally used in the 1D stimulated ESEEM experiment, mixes, or correlates, hyperfine frequencies that arise from the same coupling. The amplitude of the echo at fixed τ is measured as a function of the two time periods, t_1 and t_2, which are systematically varied to build up a two-dimensional data set, Figure III-2 (a). The linewidth in both dimensions is determined by the electron spin-lattice relaxation time, T_{1e}. The subsequent 2D

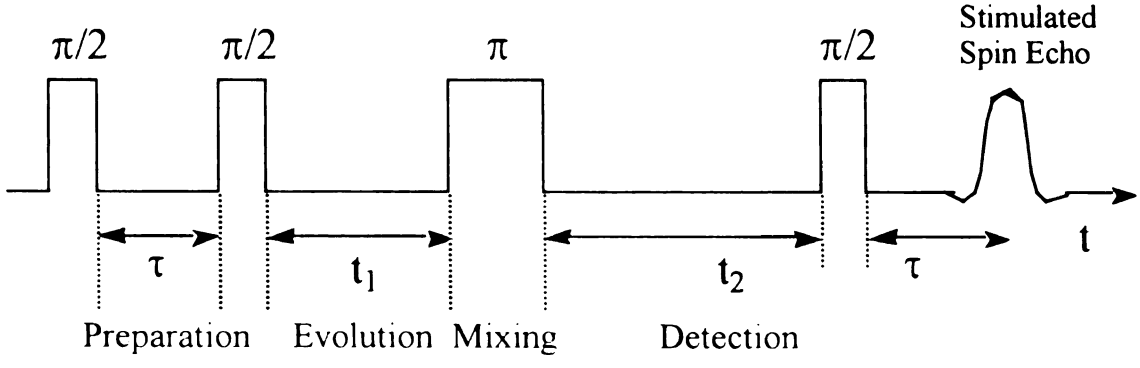

Figure III-1: Sequence of events during a four-pulse ESEEM experiment. The amplitude of the four-pulse echo is measured as a function of t_1 and t_2.

Figure

128 t_1-

magnitu

data ma

plot of t

Figure III-2: (a) An exemplary 2D time-domain data matrix, with only 33 of all the 128 t_1-slices shown. (b) 3D representation of the HYSCORE frequency-domain magnitude spectrum obtained by 2D Fast Fourier Transformation of the time-domain data matrix and taking the absolute value of the resulting complex matrix. (c) Contour plot of the above spectrum. $\nu_1 = \omega_1/2\pi$, $\nu_2 = \omega_2/2\pi$. (After Ref. 21)

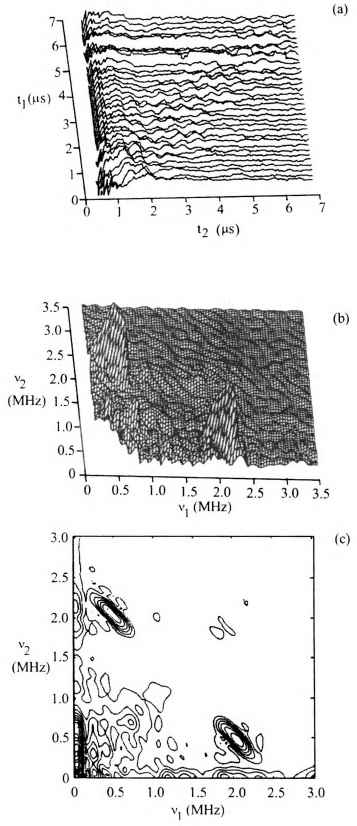

Figure III-2

Fourier transformation yields the HYSCORE spectrum in frequency-domain, Figure III-2 (b), which is more conveniently represented as a contour plot, Figure III-2 (c). In a HYSCORE experiment each data set is collected with a fixed value of τ, which is to be adjusted according to the spectral properties and the desired information (cf. Section III-3).

HYSCORE is a relatively new technique with a limited number of applications reported in the literature. However, it is becoming increasingly popular as the experimental data demonstrate its advantages. The resolution and information enhancement that can be gained via the correlation of nuclear spin transitions[1,3] or by correlating the electron spin transitions with the nuclear spin transitions[4,5] has been demonstrated in a number of single-crystal applications. Pöppl and coworkers have used HYSCORE to analyze the homogeneous and inhomogeneous line broadening effects of proton ESEEM signals in single crystals.[6] The potential of HYSCORE applied to disordered systems has been explored in studies on a oxovanadium complex with nitrogen-containing ligands.[7,8] Dikanov and coworkers have analyzed the HYSCORE contour lineshapes in an experiment on imidazole and histidine complexes of VO^{2+}.[9] HYSCORE has been utilized to separate the ESEEM contributions of weakly coupled nitrogens from those of strongly coupled ones in a bacterial photosynthetic reaction center.[10] Another application of HYSCORE to the study of systems of biological interest includes correlating pairs of ESEEM frequencies belonging to certain ^{14}N couplings in a Fe-S protein.[11] Höfer has illustrated the suppression effect and the interpretation of HYSCORE powder patterns of $S = 1/2$, $I = 1/2$ systems and proposed a 3D version of ESEEM to completely eliminate the suppression effect.[12] Other developments of the

correlation spectroscopy includes a six-pulse 2D ESEEM technique proposed by Pilbrow and coworkers,[13] which offers enhancement of the intensity of the cross peaks relative to that of the diagonal peaks due to the increased modulation depth[14]

In this Chapter, some aspects of the analysis of HYSCORE data will be discussed. First, the theoretical background and computational aspects of the HYSCORE experiment will be considered, followed by the derivation of the four pulse echo envelope modulation function for a S = 1/2, I = 1 system. Finally, an application of the derived formula to the analysis of HYSCORE spectra of randomly oriented 3,5-^{2}H labeled tyrosyl radical species will be presented.

III.2. Principles of HYSCORE

Gemperle et al.[15] have derived a HYSCORE modulation formula for the S=1/2, I=1/2 spin system, with the assumption of non-selective, ideal $\pi/2$ and π pulses. The spin system is described in the high field approximation by the Hamiltonian given by Equation I-54. The amplitude of the four-pulse echo has been obtained by using the density matrix approach described in Chapter I. The result is given by the following formula:

$$\begin{aligned} S(t_1,t_2) = 1 - \frac{k}{4}\{ & C_0 + C_\alpha\left[\cos(\omega_\alpha t_1 + \omega_\alpha \tau/2) + \cos(\omega_\alpha t_2 + \omega_\alpha \tau/2)\right] \\ & + C_\beta\left[\cos(\omega_\beta t_1 + \omega_\beta \tau/2) + \cos(\omega_\beta t_2 + \omega_\beta \tau/2)\right] \\ & + C_c\left[c^2\cos(\omega_\alpha t_1 + \omega_\beta t_2 + \omega_+ \tau/2) + c^2\cos(\omega_\beta t_1 + \omega_\alpha t_2 + \omega_+ \tau/2)\right. \\ & \left. + s^2\cos(\omega_\alpha t_1 - \omega_\beta t_2 + \omega_- \tau/2) + s^2\cos(\omega_\beta t_1 - \omega_\alpha t_2 + \omega_- \tau/2)\right]\} \end{aligned}$$

[III-1a]

with the amplitudes

$$C_0 = 3 - \cos(\omega_\beta \tau) - \cos(\omega_\alpha \tau) - s^2 \cos(\omega_+ \tau) - c^2 \cos(\omega_- \tau) \qquad \text{[III-1b]}$$

$$C_\alpha = c^2 \cos(\omega_\beta \tau - \omega_\alpha \tau/2) + s^2 \cos(\omega_\beta \tau + \omega_\alpha \tau/2) - \cos(\omega_\alpha \tau/2) \qquad \text{[III-1c]}$$

$$C_\beta = c^2 \cos(\omega_\alpha \tau - \omega_\beta \tau/2) + s^2 \cos(\omega_\alpha \tau + \omega_\beta \tau/2) - \cos(\omega_\beta \tau/2) \qquad \text{[III-1d]}$$

$$C_0 = -2\sin(\omega_\alpha \tau/2)\sin(\omega_\beta \tau/2), \qquad \text{[III-1e]}$$

the sum and difference frequencies $\omega_+ = \omega_\alpha + \omega_\beta$ and $\omega_- = \omega_\alpha - \omega_\beta$, $s^2 = \sin^2(\delta/2)$, $c^2 = \cos^2(\delta/2)$, and the modulation depth parameter $k = 4 \sin^2(\delta/2) \cos^2(\delta/2)$. δ corresponds to the angle between the two effective magnetic fields at the nucleus with $M_S = 1/2$ and $M_S = -1/2$, and is defined by

$$\sin^2(\delta/2) = \frac{\left|\omega_I^2 - [(\omega_\alpha + \omega_\beta)^2/4]\right|}{\omega_\alpha \omega_\beta} \qquad \text{[III-2a]}$$

$$\cos^2(\delta/2) = \frac{\left|\omega_I^2 - [(\omega_\alpha - \omega_\beta)^2/4]\right|}{\omega_\alpha \omega_\beta} \qquad \text{[III-2b]}$$

C_0 in Equation III-1 is a constant term that depends on τ only and does not contribute to the echo modulation. The second and third terms in Equation III-1 proportional to C_α and C_β contain the modulation frequencies ω_α and ω_β in either of the t_1 or t_2 time domains. In the frequency domain this gives rise to peaks at $(0, \omega_\alpha)$, $(\omega_\alpha, 0)$, $(0, \omega_\beta)$, $(\omega_\beta, 0)$. The last term with coefficient C_c (Equation III-1a) contains cosine functions with both time variables simultaneously in the argument. It yields cross peaks in the 2D spectrum at $(\omega_\alpha, \omega_\beta)$ and $(\omega_\beta, \omega_\alpha)$. Thus, for a S=1/2, I=1/2 spin system, a 2D FT ESEEM spectrum,

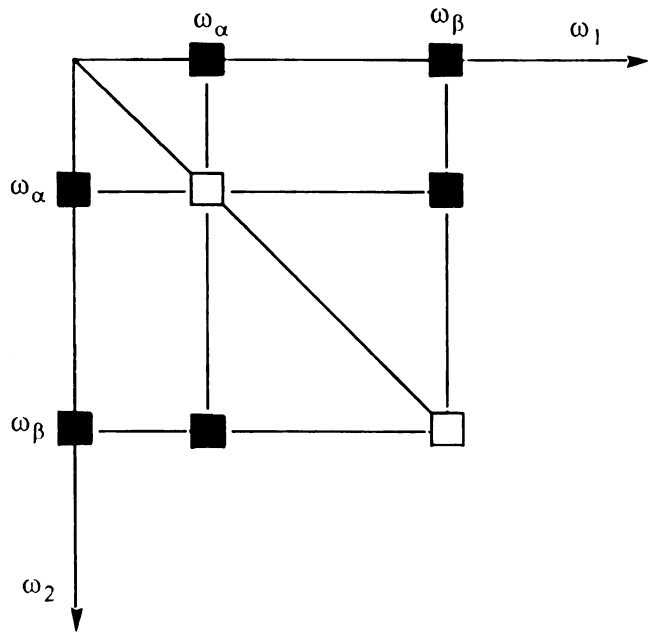

Figure III-3: Schematic HYSCORE 2D spectrum for an S = 1/2, I = 1/2 spin system. Solid squares: peaks observed for ideal pulses. Open squares: diagonal peaks that are observed only for non-ideal pulses that cause partial excitation. (After Ref. 15)

$S(\omega_1, \omega_2)$, will consist of six peaks as shown schematically in Figure III-3 by the solid squares. Two pairs of axial peaks with frequencies ω_α and ω_β appear along the axes $\omega_1 = 0$ and $\omega_2 = 0$, forming two identical 1D spectra. The two cross peaks $(\omega_\alpha, \omega_\beta)$ and $(\omega_\beta, \omega_\alpha)$ are related by reflection symmetry with respect to the diagonal $\omega_1 = \omega_2$. Since ideal pulses are assumed, no diagonal peaks occur. However, in reality the pulses have finite bandwidth and diagonal peaks do occur (Figure III-3). Equation III-1a shows that the peaks appear as a mixture of absorption and dispersion type signals[16] with a variable phase shift that depends on τ. Since phasing is not normally possible, magnitude (absolute value) spectra are to be plotted. The peak amplitudes in a magnitude spectrum are

$$A(\omega_\alpha,0) = A(0,\omega_\alpha) = \frac{k}{4}\left|c^2\cos(\omega_\beta\tau - \omega_\alpha\tau/2) + s^2\cos(\omega_\beta\tau + \omega_\alpha\tau/2) - \cos(\omega_\alpha\tau/2)\right| \qquad \text{[III-3a]}$$

$$A(\omega_\beta,0) = A(0,\omega_\beta) = \frac{k}{4}\left|c^2\cos(\omega_\alpha\tau - \omega_\beta\tau/2) + s^2\cos(\omega_\alpha\tau + \omega_\beta\tau/2) - \cos(\omega_\beta\tau/2)\right| \qquad \text{[III-3b]}$$

$$A(\omega_\alpha,\omega_\beta) = \frac{k}{4}\left|\sin(\omega_\alpha\tau/2)\sin(\omega_\beta\tau/2)\right|(2c^4 + 2s^4)^{1/2} \qquad \text{[III-3c]}$$

Depending on the actual values of ω_α, ω_β, τ, s^2 and c^2, blind spots may occur, at which the intensity of pairs of peaks drops to zero. If the microwave field strength of the pulses,

B_1, is not sufficient to fulfill the condition of complete excitation (i. e., $\mathcal{H}_1 >> \mathcal{H}_0$, or, equivalently $\omega_1 >> \omega_\alpha, \omega_\beta$, where $\omega_1 = g\,\mu_B\,B_1/\hbar$), the two allowed and two forbidden transitions are no longer equally excited. Consequently, the Hamiltonian of Equation I-54 cannot be neglected during the pulses[17,18] and the problem must be solved numerically. A non-ideal mixing π-pulse also causes an incomplete coherence exchange between the two nuclear transitions ω_α and ω_β, which results in the appearance of two diagonal peaks at $(\omega_\alpha, \omega_\alpha)$ and $(\omega_\beta, \omega_\beta)$. In this case the above formulae for the peak intensities the modulation depth parameter, k, are not valid anymore. Another difficulty arising from a non-ideal excitation is formation of all possible two-, three- and four-pulse echoes, which necessitates the elimination of the unwanted echoes by phase-cycling.

As already pointed out, the properties of a HYSCORE spectrum, $S(\omega_\alpha, \omega_\beta)$, can be inferred from the 2D Fourier transform (FT) of the time-domain data, $S(t_1, t_2)$. A 2D Fourier transform is performed by consecutively transforming $S(t_1, t_2)$ with respect to each of the independent time variables. A real or complex Fourier transformation of the data set with respect to a particular time variable can be carried out, which leads to different spectral representations as well as different spectral densities.[2] Höfer has analyzed the cases of amplitude modulation and phase modulation of 2D ESEEM signals.[19]

In a 2D experiment, both the phase and the amplitude of a signal observed during a time t_2 can be modulated as a function of a previous time interval t_1.[19] In the ESEEM experiments non-quadrature detection is normally utilized and the detected signal contains

both absorption and dispersion components. Consider a simplified, exemplary 2D time domain signal described as

$$S(t_1, t_2) = \cos(\omega_a t_1) \cos(\omega_b t_1 + \omega_c t_2). \qquad \text{[III-4]}$$

(The above expression is oversimplified in that the relaxation and amplitude factors have been neglected and the constant phase shifts arising from the spectrometer dead time have been omitted.) The frequency ω_c in $S(t_1, t_2)$ is detected during the time t_2. The signal $S(t_1, t_2)$ as a function of t_1 is modulated by the two frequencies ω_a and ω_b, where ω_a affects the amplitude and ω_b the phase of the signal $S(t_1)$. A complex Fourier transformation performed in the t_2 time domain will generate a real- and imaginary part spectrum $F(\omega_2) = A(\omega_2) + i\, D(\omega_2)$, containing the absorption (A) and dispersion (D) lineshape, respectively. For a phase modulated signal, such decomposition of F into two parts is only valid for $t_1 = 0$ (i. e., for the first slice in the t_1 time domain). After the Fourier transformation with respect to t_2, the signal $S(t_1, \omega_2)$ can be written as

$$\begin{aligned} S(t_1, \omega_2) &= \cos(\omega_a t_1) \exp(i\, \omega_b t_1)\, F(\omega_2 = \omega_c) \\ &= (1/2)\, F(\omega_2 = \omega_c) \{\exp[i\, (\omega_a + \omega_b) t_1] + \exp[i\, (\omega_b - \omega_a) t_1]\}. \end{aligned} \qquad \text{[III-5]}$$

If the signal S as a function of time t_2 is only modulated in amplitude ($\omega_b = 0$), no information about the sign of the modulation frequency is present. A complex FT in the t_1 domain will then produce a pair of lines at the positions (ω_a, ω_c) and $(-\omega_a, \omega_c)$. Since only

the real part signal in t_2 domain is recorded, the complex FT with respect to t_2 also generates two lines at ω_c and $-\omega_c$ and the calculation of the 2D Fourier transform results in four lines containing equivalent information. Thus, for an amplitude modulated real part signal only the frequency range $\omega_1 > 0$, $\omega_2 > 0$ has to be considered. If the signal is only phase-modulated ($\omega_a = 0$), the complex FT with respect to t_1 will preserve the sign of the modulation frequency, which results in a single line at (ω_b, ω_c). In the most general case, when both amplitude and phase of $S(t_1, t_2)$ are modulated, the FT in the t_1 domain results in a pair of lines at positions ($\omega_a + \omega_b$, ω_c) and ($\omega_b - \omega_a$, ω_c), similar to the case of exclusive amplitude modulation. However, both positive and negative frequencies have to be considered in the ω_1 domain, while it suffices to deal only with the positive ω_2 frequencies. Since the lineshapes obtained after a 2D Fourier transformation are normally a mixture of absorption and dispersion lines,[16] the absolute value (modulus, or magnitude) spectrum defined by

$$S(t_1, t_2) = [Re^2(\omega_1, \omega_2) + Im^2(\omega_1, \omega_2)]^{1/2} \qquad \text{[III-6]}$$

is usually used in practice.

The term of most interest in the HYSCORE modulation function for a S = 1/2, I = 1/2 spin system, Equation III-1, is the one that yields cross peaks after the Fourier transformation.

$$S(t_1, t_2) = \frac{k}{4} C_c [c^2 \cos(\omega_\alpha t_1 + \omega_\beta t_2 + \varphi_+) + c^2 \cos(\omega_\beta t_1 + \omega_\alpha t_2 + \varphi_+) + s^2 \cos(\omega_\alpha t_1 - \omega_\beta t_2 + \varphi_-) + s^2 \cos(\omega_\beta t_1 - \omega_\alpha t_2 + \varphi_-)] \quad \text{[III-7]}$$

The amplitude factor C_c and the phase constants φ_+ and φ_- depend only on the time separation τ between the first and the second pulses. The t_1 dependence influences only the phase of the signal detected in t_2. Therefore, if the time domain data are processed by taking a cosine Fourier transform in the t_2 dimension followed by a complex Fourier transform in the t_1 dimension, the cross peaks will separate into two different frequency quadrants according to the sign of the dominant phase of $S(t_1, t_2)$. For weak anisotropic hyperfine interactions the nuclear transition frequencies can be approximated by

$$\omega_\alpha = |\omega_I - A/2| \quad \text{[III-8a]}$$

$$\omega_\beta = |\omega_I + A/2|, \quad \text{[III-8b]}$$

where A denotes the hyperfine coupling constant for a particular orientation and ω_I is the nuclear Larmor precession frequency. With the above expressions the factors c^2 and s^2 are

$$c^2 = |\omega_I^2 - (A/2)^2|/(\omega_\alpha \omega_\beta) \quad \text{[III-9a]}$$

$$s^2 = 0 \quad \text{[III-9b]}$$

for $\omega_I > A/2$, and

$$c^2 = 0 \qquad \text{[III-10a]}$$

$$s^2 = |\omega_I^2 - (A/2)^2|/(\omega_\alpha \omega_\beta) \qquad \text{[III-10b]}$$

for $\omega_I < A/2$.

The Fourier transform of Equation III-7 in the t_2 time dimension results in

$$S(t_1, \omega_2) = \exp(i \omega_\alpha t_1) F(\omega_2 = \omega_\beta) + \exp(i \omega_\beta t_1) F(\omega_2 = \omega_\alpha) \qquad \text{[III-11]}$$

for $\omega_I > A/2$, and

$$S(t_1, \omega_2) = \exp(-i \omega_\alpha t_1) F(\omega_2 = \omega_\beta) + \exp(-i \omega_\beta t_1) F(\omega_2 = \omega_\alpha) \qquad \text{[III-12]}$$

for $\omega_I < A/2$. (The contribution from the time independent phase shift in Equation III-7 to $S(t_1, \omega_2)$ has not been taken into account). The sign of the phase modulation in t_1 depends on the relation of the hyperfine coupling to the nuclear Larmor frequency. The absolute value spectrum calculated after carrying out the Fourier transformation in the second dimension contains a pair of cross peaks at $(\omega_\alpha, \omega_\beta)$ and $(\omega_\beta, \omega_\alpha)$ provided that $\omega_I > A/2$. In the case of $\omega_I < A/2$, the cross peaks are in the negative ω_1 region, at $(-\omega_\alpha, \omega_\beta)$ and $(-\omega_\beta, \omega_\alpha)$. This is verified by the experimental examples in Figure III-4,[19] showing both $(+\omega_1, +\omega_2)$ and $(-\omega_1, +\omega_2)$ regions of the HYSCORE spectra of radicals prepared from succinic and malonic acids. In each example there are two pairs of dominant peaks which originate from different crystal sites. In the succinic acid radical, Figure III-4 (a),

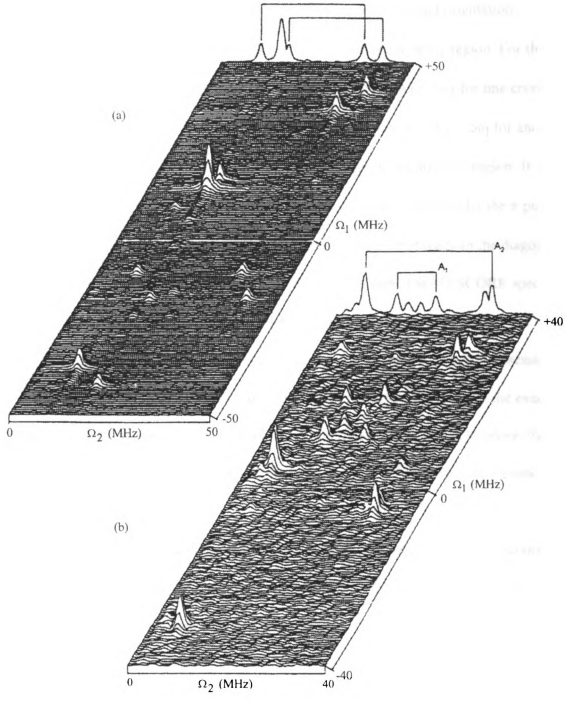

Figure III-4: HYSCORE absolute value spectrum of irradiated (a) succinic acid and (b) malonic acid after Fourier transformation with respect to t_1 and t_2. $\Omega_1 = \omega_1/2\pi$, $\Omega_2 = \omega_2/2\pi$. (From Ref. 19)

both hyperfine couplings are greater than $2\omega_I$ (at the particular crystal orientation selected). The corresponding pairs of peaks are thus in the negative ω_1 region. For the malonic acid radical, Figure III-4 (b), the hyperfine coupling is $A_1 < 2\omega_I$ for one crystal orientation, which leads to cross peaks in the $+\omega_1$ region, while it is $A_2 > 2\omega_I$ for another crystal orientation leading to appearance of cross peaks in the negative ω_1 region. It is interesting to note that the diagonal peaks due to an incomplete inversion by the π pulse are mainly confined to the positive ω_1 region. The modulation that leads to the diagonal peaks is therefore a phase modulation in t_1 with a positive sign. The HYSCORE spectrum of malonic acid radical shows residuals of the diagonal peaks and cross peaks in the corresponding other side of the ω_2 region, accounted for by the fact that the expressions for the nuclear transition frequencies, Equations III-8, are approximate. With the exact expressions for the nuclear frequencies, s^2 and c^2 will not drop to zero. Therefore, there will also be a contribution from a positive phase modulation for every negative phase modulation in t_1, and vice versa.

The optimization of the HYSCORE experiment includes adjusting two parameters, the duration of the time period τ and the width and amplitude of the mixing π pulse.[12,15] The value of τ should be selected so that the suppression effect of the cross peaks is minimized. Höfer has proposed a procedure of finding the optimum τ value by recording a series of three-pulse ESEEM spectra with increasing τ, Fourier-transforming it with respect to T and calculating the absolute value spectrum. The HYSCORE optimum τ is selected to be that value of τ in the three-pulse experiment at which the least suppression occurs in the frequency region of interest. Since single crystal spectra are characterized by

a limited number of lines there may exist several τ values that satisfy this condition. In disordered systems, however, the smallest τ at which all lines are present has to be chosen to minimize line-shape distortions.[12] The typical τ values used in practice range from 120 to 200 ns.

Another aspect of the optimization procedure is to improve the amplitude ratio of the cross peaks to the disturbing diagonal peaks. The appearance of diagonal peaks is due to an incomplete mixing by the inverting π pulse.[15] Ideally, this pulse should be much shorter than the $\pi/2$ pulses for a complete mixing to occur. This condition cannot always be fulfilled, e. g., in the case of relatively high frequency proton lines, because of the limited microwave power available. The degree of inversion obtained for certain pulse widths and amplitudes can be estimated from the appearance of the HYSCORE echo. With the ability to generate pulses of different amplitudes, one can use a π pulse with a width between 10 ns and 20 ns to achieve almost complete inversion of the spectral region excited by the $\pi/2$ pulses, thus efficiently suppressing the diagonal peaks.

The systematic analysis of HYSCORE data allows recovering the hyperfine tensor principal values and tensor orientation with respect to other magnetic tensors associated with a paramagnetic center. This information is contained in contour plots of the cross peaks. This is visualized in Figure III-5 by considering first-order hyperfine interactions in a S = 1/2, I = 1/2 spin system with axial symmetry under the (a) strong- and (b) weak-coupling limits.[20] For the weak coupling condition, $A_{||} < 2\omega_I$, the first- order powder ENDOR spectrum consists of a pair of peaks whose lineshape characteristics, singularities, and turning points are symmetric about the nuclear Larmor frequency. Cross peaks corresponding to these idealized powder patterns can be constructed by connecting

Figure III-5: Schematic HYSCORE contour plots of cross peaks arising from an S = 1/2, I = 1/2 spin system considered at the level of first-order perturbation theory. (a) $\omega_I > A_{||}/2$; (b) $\omega_I < A_{\perp}/2$. $f_1 = \omega_1/2\pi$, $f_2 = \omega_2/2\pi$. (From Ref. 20)

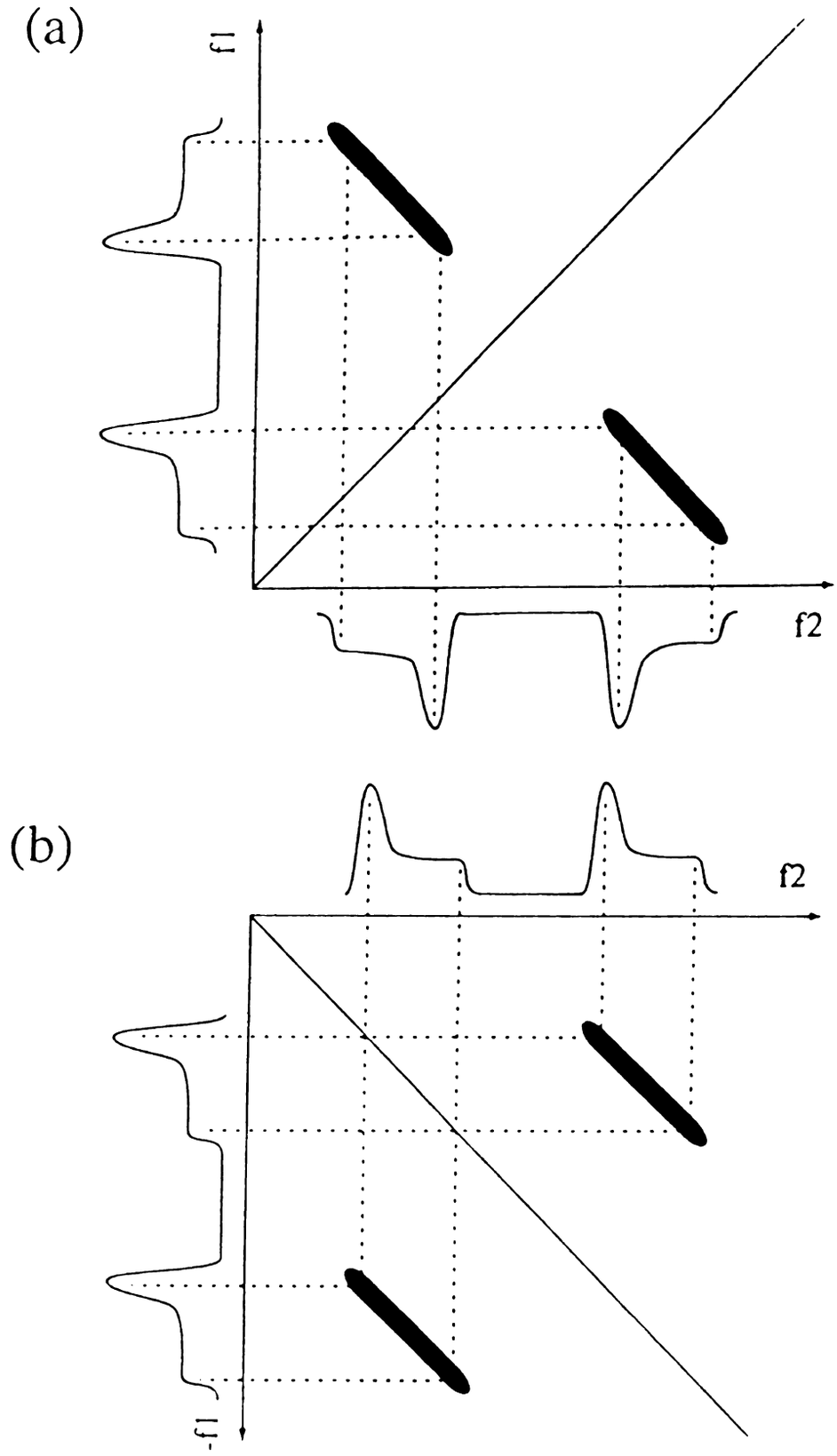

Figure III-5

the corresponding lineshape features of the ν_α peak along the ν_2 axis with the ν_β peak along the ν_1 axis and vice versa. The cross peaks thus form "ridges" (shaded area in Figure III-5) perpendicular to the frequency diagonal. The extremes of these ridges provide a measure of the parallel and perpendicular components of the hyperfine coupling. For the strong coupling condition, $A_{||} > 2\omega_I$, the powder ENDOR spectra are no longer symmetrically positioned about a center frequency, with respect to their parallel turning points and perpendicular singularities. Similarly to the case of weak coupling, the contour lines for the cross peaks define ridges that are now parallel to the frequency diagonal.[7] When second order effects are included in the hyperfine interactions or the anisotropy is increased (i. e., greater $T = (g\, g_n\, \mu_B\, \mu_{B,n})/r^3$), the ridges develop a curvature, as shown in Figure III-6.[12,21]

Recently, Dikanov and Bowman have developed simple analytical expressions for cross-peak contours predicted for disordered S=1/2, I=1/2 systems.[22] They have presented a simple graphical method for determining the principal elements of the hyperfine tensor. Plotting of the cross peaks on an axis system where the frequencies ω_1 and ω_2 are squared results in "straight-line" where tensor elements can be derived from the slope and the intercept. The authors have also addressed the case of rhombic hyperfine couplings, where the arc-shaped contours found for the axial case change to wedge-shaped (horn-shaped) cross peaks, Figure III-7. The analysis of these more complex shapes can still be performed by plotting the contours in an ω_1^2 vs. ω_2^2 coordinate system and analyzing the triangular shapes to extract the principal elements of the hyperfine tensor.

Figure III-6: Simulated HYSCORE contour plots arising from an S = 1/2, I = 1/2 spin system with an axially symmetric hyperfine tensor. Parameters: ν_I = 3 MHz; (a) $A_{||}$ = 3.6 MHz, $A_{\perp}$ = 1.2 MHz; (b) $A_{||}$ = 5.2 MHz, $A_{\perp}$ = 0.4 MHz. $f_1 = \omega_1/2\pi$, $f_2 = \omega_2/2\pi$. (From Ref. 21)

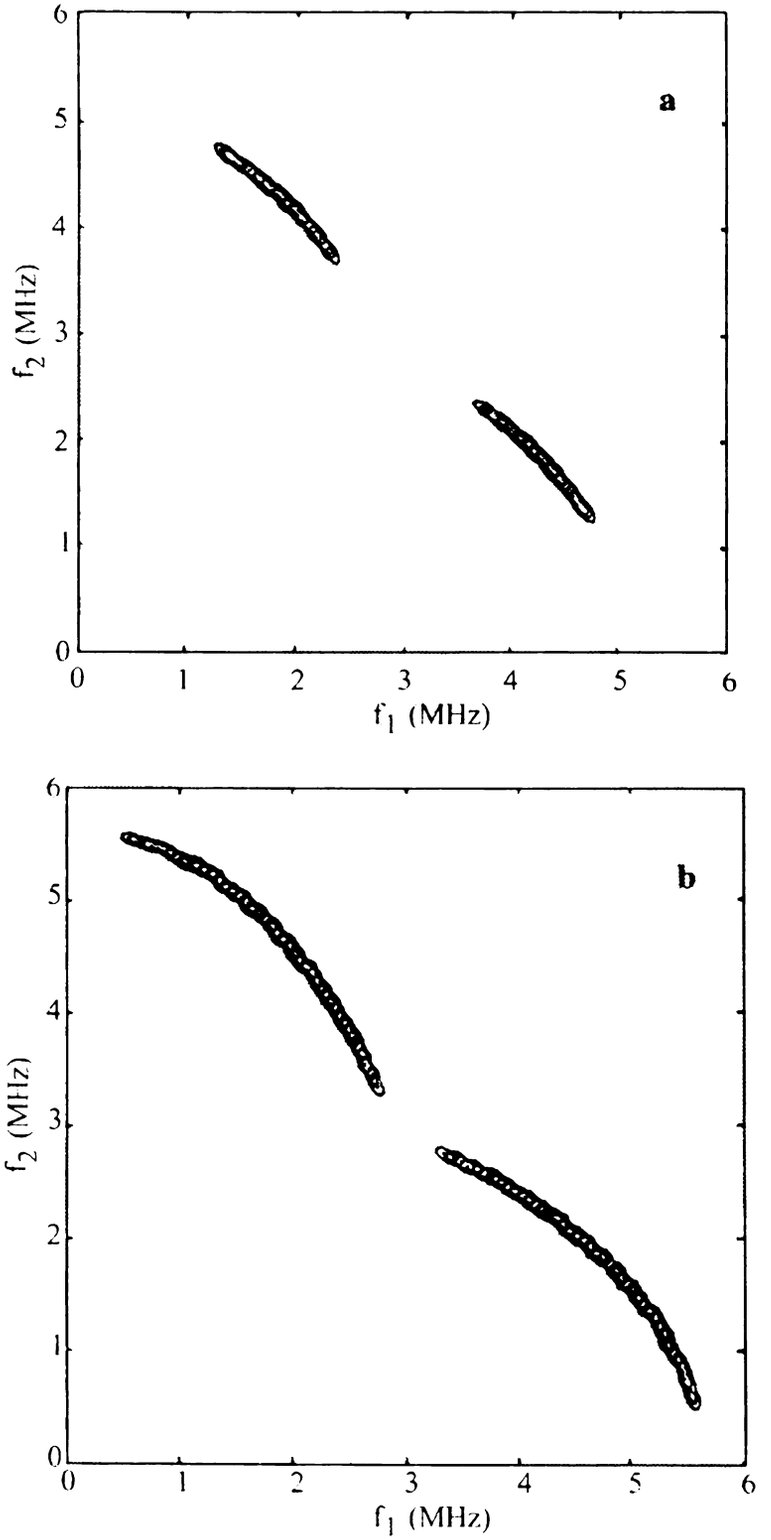

Figure III-6

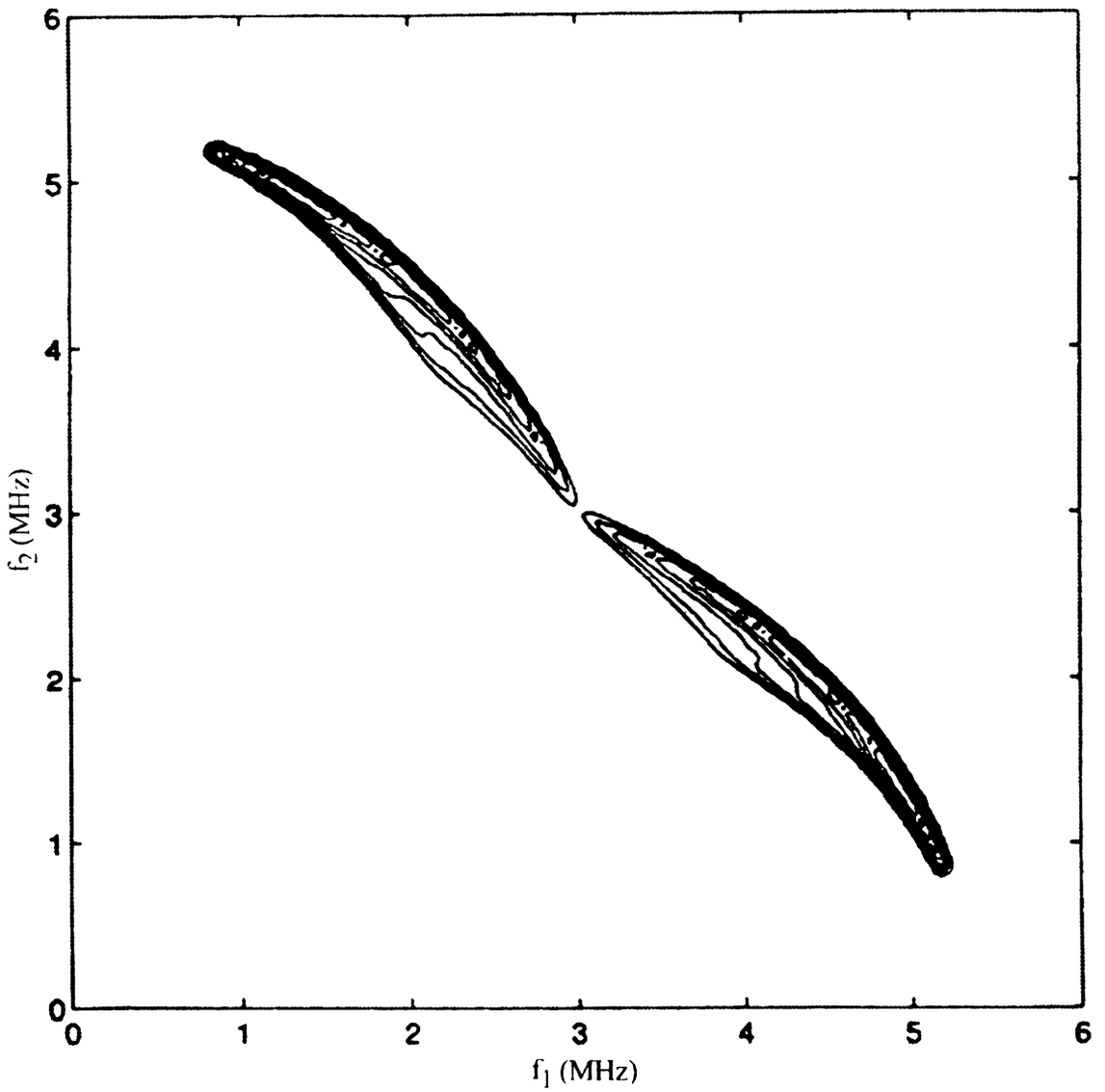

Figure III-7: Simulated HYSCORE contour plots arising from an S = 1/2, I = 1/2 spin system with a rhombic hyperfine tensor. Parameters: ν_I = 3 MHz, A_{xx} = - 0.04 MHz, A_{yy} = 1.64 MHz, A_{zz} = 4.40 MHz. $f_1 = \omega_1/2\pi$, $f_2 = \omega_2/2\pi$. (From Ref. 21)

III.3. HYSCORE Modulation Function for an S = 1/2, I = 1 Spin System

While the proton ENDOR is an established technique that achieves high hyperfine resolution, the ENDOR spectroscopy of nuclei with low gyromagnetic ratios (γ_N) and higher nuclear spin is associated with a number of difficulties, especially when nuclei other than protons exhibit small hyperfine constants.[23] Although nuclei with small magnetic moments are not inherently less sensitive than protons (nuclear transitions are detected indirectly via the EPR signal), optimum ENDOR signals for these nuclei are usually more difficult to achieve than for protons. Moreover, the ENDOR resolution for nuclei with small gyromagnetic ratios is lower than that for the corresponding isotopes with higher nuclear magnetic moments. For example, the lower gyromagnetic ratios for ^2H and ^{14}N relative to ^1H and ^{15}N, respectively, results in smaller hyperfine constants and lower Larmor frequencies for the former. On the other hand, a large anisotropy in a spin I = 1/2 nucleus, e. g., a strong α-proton hyperfine interactions, causes a broad spectral extent, which may also place the transitions in regions of weak ENDOR enhancement and poor instrument sensitivity. When ENDOR experiments are carried out on biological samples, detection difficulties are combined with the typically low paramagnet concentrations.

In contrast, the sensitivity of the ESEEM technique is inherently high for nuclei with low gyromagnetic ratio (γ) and increases with nuclear spin I as $2I(I + 1)$.[24,25] ESEEM has been applied extensively to the study of weak hyperfine interactions of nuclei such as ^2H or ^{14}N. ^2H ESEEM offers a number of advantages over the proton ESEEM. Thus, strong ^2H hyperfine contributions to ESEEM overwhelmingly dominate contributions from ^1H when coupling to both nuclei is present. The low γ of ^2H leads to a

concentration of anisotropically broadened hyperfine transitions in a relatively narrow spectral band and assures complete excitation[26] of the EPR transitions that connect the ^{2}H nuclear hyperfine sublevels. The narrow ^{2}H linewidths curtail undesired lineshape distortion arising from the spectrometer dead time.[27]

HYSCORE experimental data for S = 1/2, I = 1 spin systems have also appeared in the literature. However, no 2D ESEEM function describing precisely and adequately the HYSCORE data for such systems has been reported so far. In this Section, the derivation of an analytical expression for the echo modulation amplitude in four-pulse echo experiments (e. g., HYSCORE) for ideal non-selective $\pi/2$ and π pulses will be presented. The density matrix formalism from Chapter III will be utilized, following Mims.[24] The resultant formula will be used in Section III.4 to simulate the HYSCORE data for a tyrosyl radical.

The formula for the HYSCORE modulation effect will be derived under the assumptions and with the approximations described in Chapter I for the case of a two-pulse ESEEM experiment. The spin system under consideration consists of one electron spin with S = 1/2 and one nuclear spin I = 1 in an external laboratory magnetic field $\mathbf{B}_0$, and is described by the Hamiltonian

$$\mathcal{H}_0 / \hbar = \omega_S S_z - \omega_I I_z + \mathbf{I}\cdot\mathbf{A}\cdot\mathbf{S} + \mathbf{I}\cdot\mathbf{Q}\cdot\mathbf{I}, \qquad \text{[III-13]}$$

with the electron and nuclear Zeeman frequencies $\omega_S = (g\,\mu_B\,B_0)/\hbar$ (isotropic **g** tensor) and $\omega_I = (g_n\,\mu_{B,n}\,B_0)/\hbar$, respectively, the anisotropic hyperfine tensor **A**, and the nuclear

quadrupole tensor **Q**. The nuclear quadrupole interaction is assumed to be small enough to be ignored when calculating the unitary matrix M (cf. Chapter I) which determines the modulation amplitudes. Thus, the applicability of the resulting algebraic expression is expected to be limited to spin I = 1 nuclei that possess small quadrupole moments (e. g., ^2H or ^{14}N). The relevant energy-level diagram is displayed in Figure I-22 with the $|\alpha>$ states labeled a, b, c and the $|\beta>$ states d, e, f. Neglecting the nuclear quadrupole term, $\mathbf{I}\cdot\mathbf{Q}\cdot\mathbf{I}$, one can obtain the two eigenfrequencies of $\mathcal{H}_0/\hbar$, ω_α and ω_β, which are associated with the electronic spin states $M_S = 1/2$ and $M_S = -1/2$, respectively. In the high-field approximation where the S_x and S_y terms are neglected, the nuclear transition frequencies with no quadrupolar effects are given by

$$\omega_\alpha = \mathbf{n}^t\cdot(\omega_I \boldsymbol{I} + \mathbf{A}/2)\cdot\mathbf{n}, \qquad \text{[III-14a]}$$

$$\omega_\beta = \mathbf{n}^t\cdot(\omega_I \boldsymbol{I} - \mathbf{A}/2)\cdot\mathbf{n}, \qquad \text{[III-14b]}$$

where **n** is a direction vector aligned with the external magnetic field $\mathbf{B}_0$ and $\boldsymbol{I}$ is a 3×3 unit matrix. The corresponding eigenvectors define the elements of the 3×3 unitary transformation matrices M_α, M_β, and $M = M_\alpha^+ M_\beta$. The calculated matrix M thus is[24)]

$$M = \begin{bmatrix} \frac{1}{2}[1+\cos(\eta-\xi)] & -\frac{1}{\sqrt{2}}\sin(\eta-\xi) & \frac{1}{2}[1-\cos(\eta-\xi)] \\ \frac{1}{\sqrt{2}}\sin(\eta-\xi) & \cos(\eta-\xi) & -\frac{1}{\sqrt{2}}\sin(\eta-\xi) \\ \frac{1}{2}[1-\cos(\eta-\xi)] & \frac{1}{\sqrt{2}}\sin(\eta-\xi) & \frac{1}{2}[1+\cos(\eta-\xi)] \end{bmatrix} \qquad \text{[III-15]}$$

The difference, $\delta = (\eta - \xi)$, determines the angle between the two effective magnetic fields at the nucleus with $M_S = 1/2$ and $M_S = -1/2$ and is defined as in Chapter I and Section III.2, by[15,24]

$$\sin^2(\delta/2) = \frac{\left|\omega_I^2 - [(\omega_\alpha + \omega_\beta)^2/4]\right|}{\omega_\alpha \omega_\beta} \qquad \text{[III-16a]}$$

$$\cos^2(\delta/2) = \frac{\left|\omega_I^2 - [(\omega_\alpha - \omega_\beta)^2/4]\right|}{\omega_\alpha \omega_\beta}. \qquad \text{[III-16b]}$$

The eigenfrequencies are next adjusted to take account of quadrupolar interactions. This approach of including the quadrupole interactions (a perturbation) only for calculating the frequencies but not the modulation amplitudes is justified by the fact that small frequency differences are experimentally easier to detect than to make a precise experimental measurement of the modulation amplitudes.[24] Quadrupolar corrections to ω_α and ω_β are obtained by diagonalizing the nuclear quadrupole term in the Hamiltonian in Equation III-13. Since the eigenfrequencies of $\mathbf{I}\cdot\mathbf{Q}\cdot\mathbf{I}$ are (cf. Chapter I) $E_\pm = -\kappa(1 \pm \eta)$, $E_0 = 2\kappa$, the corrected nuclear transition frequencies are

$$\omega_{ab} = \omega_\alpha - \Delta_1 - \Delta_3 \qquad \text{[III-17a]}$$

$$\omega_{bc} = \omega_\alpha + \Delta_2 + \Delta_3 \qquad \text{[III-17b]}$$

$$\omega_{ac} = 2\,\omega_\alpha - \Delta_1 + \Delta_2 \qquad \text{[III-17c]}$$

$$\omega_{de} = \omega_\beta - \Delta_1 - \Delta_3 \qquad \text{[III-17d]}$$

$$\omega_{ef} = \omega_\beta + \Delta_2 + \Delta_3 \qquad \text{[III-17e]}$$

$$\omega_{df} = \omega_\beta - \Delta_1 + \Delta_2 \qquad \text{[III-17f]}$$

with $\Delta_1 = K\,(3 - \eta)$, $\Delta_2 = K\,(3 + \eta)$, $\Delta_3 = 2\,K\,\eta$, where $K = e^2qQ/4$.

Introducing a resonance microwave field interaction $\mathcal{H}_1$ of the form

$$\mathcal{H}_1 = \frac{\hbar\,\omega_N}{2}\begin{bmatrix} 0 & M \\ M^* & 0 \end{bmatrix} \qquad \text{[III-18]}$$

one can obtain the appropriate rotation operators which determine the evolution of the density matrix during the pulses and the free precession periods. The rotation operators for the nutation period p (of duration $t_{N,p}$) and the free precession period l (of duration t_l) are expressed according to Equations I-80 and I-81, respectively, as

$$R_{N,p} = \exp[i\,(\mathcal{H}_0 + \mathcal{H}_1)\,t_{N,p}/\hbar], \qquad \text{[III-19]}$$

$$R_{t,l} = \exp[i\,\mathcal{H}_0\,t_l/\hbar]. \qquad \text{[III-20]}$$

The evolution of the density matrix is then written out as

$$\rho_E = R^+\,\rho_0\,R, \qquad \text{[III-21]}$$

where the rotation operator R for the four-pulse sequence shown in Figure I-23 (c) is

$$R = R_{N,I}\, R_{\tau}\, R_{N,II}\, R_{t_1}\, R_{N,III}\, R_{t_2}\, R_{N,IV}\, R_{\tau+t} \,. \qquad \text{[III-22]}$$

The initial density matrix, ρ_0, and the rotation operators $R_{t,I}$ and $R_{N,p}$ are represented in terms of submatrices $\rho_\alpha{}^0$, $\rho_\beta{}^0$, $P_{t,I}$, $Q_{t,I}$, $T_{N,p}$, $U_{N,p}$, $V_{N,p}$, and $W_{N,p}$, respectively, according to Equations I-84, I-85, and I-86.

The amplitude of the (unnormalized) stimulated echo in a four pulse experiment, $E = Tr\{\rho_E S_Y\}$, is obtained using ρ_E, given by Equation III-21, and S_Y represented by means of submatrices M and M^+, according to Equation I-91. The matrix multiplication in symbolic form is conveniently performed by the algebraic computer program Mathematica.[28] The result consists of a sum of a large number of matrix product terms. After enforcing the phase factor cancellation constraint (cf. Chapter I, Section I.4) only sixteen terms are retained in the sum:

$$\begin{aligned}
Tr\{\rho_E S_Y\} = i/2\, Tr\{ & \\
& Q_{\tau+t}{}^{+} U_{IV}{}^{+} P_{t_2}{}^{+} T_{III}{}^{+} P_{t_1}{}^{+} T_{II}{}^{+} P_{\tau}{}^{+} T_I{}^{+} \rho_\alpha{}^0 U_I Q_\tau V_{II} P_{t_1} T_{III} P_{t_2} T_{IV} P_{\tau+t} M \\
& - P_{\tau+t}{}^{+} T_{IV}{}^{+} P_{t_2}{}^{+} T_{III}{}^{+} P_{t_1}{}^{+} V_{II}{}^{+} Q_\tau{}^{+} U_I{}^{+} \rho_\alpha{}^0 T_I P_\tau T_{II} P_{t_1} T_{III} P_{t_2} U_{IV} Q_{\tau+t} M^+ \\
& + Q_{\tau+t}{}^{+} W_{IV}{}^{+} Q_{t_2}{}^{+} U_{III}{}^{+} P_{t_1}{}^{+} T_{II}{}^{+} P_{\tau}{}^{+} T_I{}^{+} \rho_\alpha{}^0 U_I Q_\tau V_{II} P_{t_1} U_{III} Q_{t_2} V_{IV} P_{\tau+t} M \\
& - P_{\tau+t}{}^{+} V_{IV}{}^{+} Q_{t_2}{}^{+} U_{III}{}^{+} P_{t_1}{}^{+} V_{II}{}^{+} Q_\tau{}^{+} U_I{}^{+} \rho_\alpha{}^0 T_I P_\tau T_{II} P_{t_1} U_{III} Q_{t_2} W_{IV} Q_{\tau+t} M^+ \\
& + Q_{\tau+t}{}^{+} U_{IV}{}^{+} P_{t_2}{}^{+} V_{III}{}^{+} Q_{t_1}{}^{+} U_{II}{}^{+} P_{\tau}{}^{+} T_I{}^{+} \rho_\alpha{}^0 U_I Q_\tau W_{II} Q_{t_1} V_{III} P_{t_2} T_{IV} P_{\tau+t} M \\
& - P_{\tau+t}{}^{+} T_{IV}{}^{+} P_{t_2}{}^{+} V_{III}{}^{+} Q_{t_1}{}^{+} W_{II}{}^{+} Q_\tau{}^{+} U_I{}^{+} \rho_\alpha{}^0 T_I P_\tau U_{II} Q_{t_1} V_{III} P_{t_2} U_{IV} Q_{\tau+t} M^+ \\
& + Q_{\tau+t}{}^{+} W_{IV}{}^{+} Q_{t_2}{}^{+} W_{III}{}^{+} Q_{t_1}{}^{+} U_{II}{}^{+} P_{\tau}{}^{+} T_I{}^{+} \rho_\alpha{}^0 U_I Q_\tau W_{II} Q_{t_1} W_{III} Q_{t_2} V_{IV} P_{\tau+t} M \\
& - P_{\tau+t}{}^{+} V_{IV}{}^{+} Q_{t_2}{}^{+} W_{III}{}^{+} Q_{t_1}{}^{+} W_{II}{}^{+} Q_\tau{}^{+} U_I{}^{+} \rho_\alpha{}^0 T_I P_\tau U_{II} Q_{t_1} W_{III} Q_{t_2} W_{IV} Q_{\tau+t} M^+
\end{aligned}$$

$$+ Q_{\tau+t}{}^{+}W_{IV}{}^{+}Q_{t_2}{}^{+}W_{III}{}^{+}Q_{t_1}{}^{+}U_{II}{}^{+}P_{\tau}{}^{+}V_{I}{}^{+}\rho_{\beta}{}^{0}W_{I}Q_{\tau}W_{II}Q_{t_1}W_{III}Q_{t_2}V_{IV}P_{\tau+t}M$$

$$- P_{\tau+t}{}^{+}V_{IV}{}^{+}Q_{t_2}{}^{+}W_{III}{}^{+}Q_{t_1}{}^{+}W_{II}{}^{+}Q_{\tau}{}^{+}W_{I}{}^{+}\rho_{\beta}{}^{0}V_{I}P_{\tau}U_{II}Q_{t_1}W_{III}Q_{t_2}W_{IV}Q_{\tau+t}M^{+}$$

$$+ Q_{\tau+t}{}^{+}U_{IV}{}^{+}P_{t_2}{}^{+}V_{III}{}^{+}Q_{t_1}{}^{+}U_{II}{}^{+}P_{\tau}{}^{+}V_{I}{}^{+}\rho_{\beta}{}^{0}W_{I}Q_{\tau}W_{II}Q_{t_1}V_{III}P_{t_2}T_{IV}P_{\tau+t}M$$

$$- P_{\tau+t}{}^{+}T_{IV}{}^{+}P_{t_2}{}^{+}V_{III}{}^{+}Q_{t_1}{}^{+}W_{II}{}^{+}Q_{\tau}{}^{+}W_{I}{}^{+}\rho_{\beta}{}^{0}V_{I}P_{\tau}U_{II}Q_{t_1}V_{III}P_{t_2}U_{IV}Q_{\tau+t}M^{+}$$

$$+ Q_{\tau+t}{}^{+}W_{IV}{}^{+}Q_{t_2}{}^{+}U_{III}{}^{+}P_{t_1}{}^{+}T_{II}{}^{+}P_{\tau}{}^{+}V_{I}{}^{+}\rho_{\beta}{}^{0}W_{I}Q_{\tau}V_{II}P_{t_1}U_{III}Q_{t_2}V_{IV}P_{\tau+t}M$$

$$- P_{\tau+t}{}^{+}V_{IV}{}^{+}Q_{t_2}{}^{+}U_{III}{}^{+}P_{t_1}{}^{+}V_{II}{}^{+}Q_{\tau}{}^{+}W_{I}{}^{+}\rho_{\beta}{}^{0}V_{I}P_{\tau}T_{II}P_{t_1}U_{III}Q_{t_2}W_{IV}Q_{\tau+t}M^{+}$$

$$+ Q_{\tau+t}{}^{+}U_{IV}{}^{+}P_{t_2}{}^{+}T_{III}{}^{+}P_{t_1}{}^{+}T_{II}{}^{+}P_{\tau}{}^{+}V_{I}{}^{+}\rho_{\beta}{}^{0}W_{I}Q_{\tau}V_{II}P_{t_1}T_{III}P_{t_2}T_{IV}P_{\tau+t}M$$

$$- P_{\tau+t}{}^{+}T_{IV}{}^{+}P_{t_2}{}^{+}T_{III}{}^{+}P_{t_1}{}^{+}V_{II}{}^{+}Q_{\tau}{}^{+}W_{I}{}^{+}\rho_{\beta}{}^{0}V_{I}P_{\tau}T_{II}P_{t_1}T_{III}P_{t_2}U_{IV}Q_{\tau+t}M^{+}$$

$$\} \qquad \text{[III - 23]}$$

The above equation represents the general expression for envelope modulation with four-pulse echoes. The initial Boltzmann populations of all nuclear sublevels belonging to a particular electron spin manifold can be considered equal to a good approximation, i. e., $\rho_{\alpha}{}^{0} \cong aI$, $\rho_{\beta}{}^{0} \cong bI$, where I is a 3×3 unit matrix, and a and b are proportionality constants.

With the assumption of complete excitation ($\mathcal{H}_1 >> \mathcal{H}_0$) the rotation operator for nutation, Equation III-19, can be expanded as in Equation I-92 to yield the submatrices T, U, V, and W in the form of Equations I-93. After substitution of the submatrices for the initial density and the nutation with the corresponding expressions the unnormalized four-pulse echo modulation function becomes

$$E = (1/16)\sin(\omega_N t_{pI})\sin(\omega_N t_{pII})\sin(\omega_N t_{pIV})(a - b) \times$$

$$\mathrm{Tr}\{\sin^2[(\omega_N t_{pIII})/2]\,[Q_{\tau+t}{}^{+}Q_{t_2}{}^{+}M^{+}P_{t_1}{}^{+}P_{\tau}{}^{+}MQ_{\tau}M^{+}P_{t_1}MQ_{t_2}M^{+}P_{\tau+t}M$$

$$+ P_{\tau+t}{}^{+}MQ_{t_2}{}^{+}M^{+}P_{t_1}{}^{+}MQ_{\tau}{}^{+}M^{+}P_{\tau}P_{t_1}MQ_{t_2}Q_{\tau+t}M^{+}$$

$$+ Q_{\tau+t}{}^{+}M^{+}P_{t_2}{}^{+}MQ_{t_1}{}^{+}M^{+}P_{\tau}{}^{+}MQ_{\tau}Q_{t_1}M^{+}P_{t_2}P_{\tau+t}M$$

$$+ P_{\tau+t}{}^{+}P_{t_2}{}^{+}MQ_{t_1}{}^{+}Q_{\tau}{}^{+}M^{+}P_{\tau}MQ_{t_1}M^{+}P_{t_2}MQ_{\tau+t}M^{+}]$$

$$- \cos^2[(\omega_N t_{pIII})/2]\,[Q_{\tau+t}{}^{+}M^{+}P_{t_2}{}^{+}P_{t_1}{}^{+}P_{\tau}{}^{+}MQ_{\tau}M^{+}P_{t_1}P_{t_2}P_{\tau+t}M$$

$$+ P_{\tau+t}{}^{+}P_{t_2}{}^{+}P_{t_1}{}^{+}MQ_{\tau}{}^{+}M^{+}P_{\tau}P_{t_1}P_{t_2}MQ_{\tau+t}M^{+}$$

$$+ Q_{\tau+t}{}^{+}Q_{t_2}{}^{+}Q_{t_1}{}^{+}M^{+}P_{\tau}{}^{+}MQ_{\tau}Q_{t_1}Q_{t_2}M^{+}P_{\tau+t}M$$

$$+ P_{\tau+t}{}^{+}MQ_{t_2}{}^{+}Q_{t_1}{}^{+}Q_{\tau}{}^{+}M^{+}P_{\tau}MQ_{t_1}Q_{t_2}Q_{\tau+t}M^{+}]\,\}$$

[III-24]

The normalization factor for the envelope modulation function is given by the echo amplitude when all times are set to zero, $\tau \rightarrow 0$, $t_1 \rightarrow 0$, $t_2 \rightarrow 0$, while the free precession matrices P and Q are set to I. It is equal to

$$- (1/4)\sin(\omega_N t_{pI})\sin(\omega_N t_{pII})\sin(\omega_N t_{pIV})(a - b)\cos(\omega_N t_{pIII})\,\mathrm{Tr}\{I\}.$$

[III-25]

The normalized echo modulation envelope function is then given by

$$E(\tau, t_1, t_2) = (1/12)\,\mathrm{Tr}\{$$

$$- \sin^2[(\omega_N t_{pIII})/2]/\cos(\omega_N t_{pIII}) \times$$

$$[Q_{\tau+t}{}^{+}Q_{t_2}{}^{+}M^{+}P_{t_1}{}^{+}P_{\tau}{}^{+}MQ_{\tau}M^{+}P_{t_1}MQ_{t_2}M^{+}P_{\tau+t}M$$

$$+ P_{\tau+t}{}^{+}MQ_{t_2}{}^{+}M^{+}P_{t_1}{}^{+}MQ_{\tau}{}^{+}M^{+}P_{\tau}P_{t_1}MQ_{t_2}Q_{\tau+t}M^{+}$$

$$+ Q_{\tau+t}{}^{+}M^{+}P_{t_2}{}^{+}MQ_{t_1}{}^{+}M^{+}P_{\tau}{}^{+}MQ_{\tau}Q_{t_1}M^{+}P_{t_2}P_{\tau+t}M$$

$$+ P_{\tau+t}{}^{+}P_{t_2}{}^{+}MQ_{t_1}{}^{+}Q_{\tau}{}^{+}M^{+}P_{\tau}MQ_{t_1}M^{+}P_{t_2}MQ_{\tau+t}M^{+}]$$

$$+ \cos^2[(\omega_N t_{pIII})/2]/\cos(\omega_N t_{pIII}) \times$$

$$[Q_{\tau+t}{}^{+}M^{+}P_{t_2}{}^{+}P_{t_1}{}^{+}P_{\tau}{}^{+}MQ_{\tau}M^{+}P_{t_1}P_{t_2}P_{\tau+t}M$$

$$+ P_{\tau+t}{}^{+}P_{t_2}{}^{+}P_{t_1}{}^{+}MQ_{\tau}{}^{+}M^{+}P_{\tau}P_{t_1}P_{t_2}MQ_{\tau+t}M^{+}$$

$$+ Q_{\tau+t}{}^{+}Q_{t_2}{}^{+}Q_{t_1}{}^{+}M^{+}P_{\tau}{}^{+}MQ_{\tau}Q_{t_1}Q_{t_2}M^{+}P_{\tau+t}M$$

$$+ P_{\tau+t}{}^{+}MQ_{t_2}{}^{+}Q_{t_1}{}^{+}Q_{\tau}{}^{+}M^{+}P_{\tau}MQ_{t_1}Q_{t_2}Q_{\tau+t}M^{+}]$$

$$\}. \qquad \text{[III-26]}$$

In a HYSCORE pulse sequence the turning angle for the third pulse is chosen to be $\omega_N t_{pIII} = \pi$. With this selection of the turning angle,

$$\cos(\omega_N t_{pIII}) = -1,$$

$$\cos^2[(\omega_N t_{pIII})/2] = 0,$$

$$\sin^2[(\omega_N t_{pIII})/2] = 1,$$

and

$$E(\tau, t_1, t_2) = (1/12)\,\mathrm{Tr}\{Q_{\tau+t}{}^{+}Q_{t_2}{}^{+}M^{+}P_{t_1}{}^{+}P_{\tau}{}^{+}MQ_{\tau}M^{+}P_{t_1}MQ_{t_2}M^{+}P_{\tau+t}M$$

$$+ P_{\tau+t}{}^{+}MQ_{t_2}{}^{+}M^{+}P_{t_1}{}^{+}MQ_{\tau}{}^{+}M^{+}P_{\tau}P_{t_1}MQ_{t_2}Q_{\tau+t}M^{+}$$

$$+ Q_{\tau+t}{}^{+}M^{+}P_{t_2}{}^{+}MQ_{t_1}{}^{+}M^{+}P_{\tau}{}^{+}MQ_{\tau}Q_{t_1}M^{+}P_{t_2}P_{\tau+t}M$$

$$+ P_{\tau+t}{}^{+}P_{t_2}{}^{+}MQ_{t_1}{}^{+}Q_{\tau}{}^{+}M^{+}P_{\tau}MQ_{t_1}M^{+}P_{t_2}MQ_{\tau+t}M^{+}\}.$$

[III-27]

Note that since the sum contains both product terms and their Hermitian conjugates, the corresponding terms can be combined to simplify the expression: In addition, the variable time, t, must be set to zero to ensure exact cancellation of the phase factors associated with inhomogeneous broadening. Equation III-27 can thus be rewritten in the form

$$E(\tau, t_1, t_2) = (1/6)\,\mathrm{Tr}\{\, Q_\tau^{+} Q_{t_2}^{+} M^{+} P_{t_1}^{+} P_\tau^{+} M Q_\tau M^{+} P_{t_1} M Q_{t_2} M^{+} P_\tau M$$
$$+ Q_\tau^{+} M^{+} P_{t_2}^{+} M Q_{t_1}^{+} M^{+} P_\tau^{+} M Q_\tau Q_{t_1} M^{+} P_{t_2} P_\tau M \,\}. \qquad \text{[III-28]}$$

For an S = 1/2, I = 1 spin system, the 3×3 diagonal matrices P and Q for the free precession period I have non-zero elements

$$(P_{jj})_{t,I} = \exp(i\,\omega_{\alpha j}\, t_I), \qquad \text{[III-29a]}$$

$$(Q_{jj})_{t,I} = \exp(i\,\omega_{\beta j}\, t_I), \qquad \text{[III-29b]}$$

where α_i and β_j refer to the nuclear spin states |a>, |b>, |c>, and |d>, |e>, |f>, respectively. Evaluation of Equation III-28 (carried out by the algebraic computer program Mathematica) with definitions of P and Q according to Equation III-29, and M according to Equation III-15 leads to an explicit form of the HYSCORE echo modulation formula for S = 1/2, I = 1 spin system. The expression is given in Appendix B and consists of a lengthy sum of cosine terms, each multiplied by a modulation depth related factor. Examination of the expression shows that it includes (a) constant terms that do not contribute to the echo modulation (numeric constants or cosine terms that depend only on

τ), (b) terms containing the modulation frequencies ω_{ab}, ω_{bc}, ω_{ac}, ω_{de}, ω_{ef}, ω_{df} in either t_1 or t_2 time domain, which produce peaks along either ω_1 or ω_2 axes in the frequency domain, and (c) terms that contain cosine functions with both time variables simultaneously in the argument giving rise to cross peaks. Unfortunately, due to the size of the expression, simplification of the formula is not feasible by symbolic manipulations even when utilizing heavy computing resources. However, the derived echo modulation function can be readily encoded as a C or FORTRAN function and used for numerical simulations of experimental HYSCORE spectra.

III.4. Application of HYSCORE to the Study of a Tyrosyl Radical Model System

III.4.1. Introduction

Tyrosyl radicals belong to the class of amino acid radicals, which are known as essential participants in the reactions of a variety of enzymes.[29,30] The first catalytically important amino acid radical, the tyrosyl radical in the Ribonucleotide Reductase (RNR) from E. coli , was only discovered in the 1970s.[31] Tyrosyl radicals have been found in other enzymes such as RNR,[32] Photosystem II (PS II),[33] Prostaglandin H Synthase (PGHS),[34] Galactose Oxidase (GOase),[35] and in amine oxidases.[36] Of the twenty biologically essential aminoacids, tyrosine is the easiest to oxidize. In aqueous solution at pH 7 it has a redox potential of +930 mV relative to normal hydrogen electrode.[37] This fact may account for its widespread occurrence in enzyme catalysis.

Radical enzymes[29] generally contain metal centers such as Fe, Cu, Co or Mn,[38] or a redox active cofactors such as S-adenosyl methionine whose function is similar to that

of the metal. The metal center acts to generate the amino-acid radical, which in turn initiate catalysis by abstracting a hydrogen atom from the substrate. This general functional scheme is related to a general structural frame of the metalo-radical enzymes. The metal, the redox-active side chain and the substrate-binding channel are all physically close in the enzyme structure. The aminoacid radicals typically occur as transient species during the enzyme catalytic cycle. There are exceptions, such as the Y122 in RNR or YD in PS II, both of which are stable radicals.

The transient nature of the radicals necessitates the use of more sophisticated spectroscopic and trapping methods to detect and characterize them, which accounts for the delayed discovery of the metalo-enzyme aminoacid radicals.

III.4.2. EPR spectroscopic studies of tyrosyl radicals

Determination of the electronic and nuclear structures of tyrosyl radicals is necessary to gain insight into the molecular mechanisms of participation of protein-attached tyrosine-based radicals in enzyme catalyses[39-41]. EPR has proven to be the most informative spectroscopy to study the tyrosyl radicals in both biological and model systems. However, since the radical is effectively immobilized in the protein structure at random orientations, powder EPR spectra are generated. These spectra lack resolution due to inhomogeneous EPR line broadening. To obtain information on various hyperfine couplings, ENDOR and pulsed EPR spectroscopies have been utilized in combination with specific isotopic labeling. β-CH_2 proton, Figure III-8, is characterized by an axial hyperfine tensor, which reports on the unpaired electron spin density on Carbon-1 as well

as on the dihedral angle of the C_β-H bonds with respect to the $2p_z$ orbital of Carbon-1, in accordance with the relation (cf. Chapter I),

$$A_{iso} = [Q^{\beta}_0 + Q^{\beta}_2 \cos^2(\theta)]\rho_\pi^{C\alpha}, \qquad [III\text{-}30]$$

where A_{iso} is the isotropic hyperfine coupling for the β-proton, $\rho_\pi^{C\alpha}$ is the unpaired electron density at Carbon-1, $Q^{\beta}_0 \cong 8$ MHz, $Q^{\beta}_2 = 164$ MHz, θ is the dihedral angle of the C-H bond of the β-proton relative to the $2p_z$ orbital of Carbon-1 (cf. Chapters I, II).[42] β-^{2}HC- labeled tyrosyl radicals have been found to exhibit unexpected ^{2}H -ESEEM lineshapes as well as anomalous EPR and ENDOR linewidths.[43-45] This phenomenon has

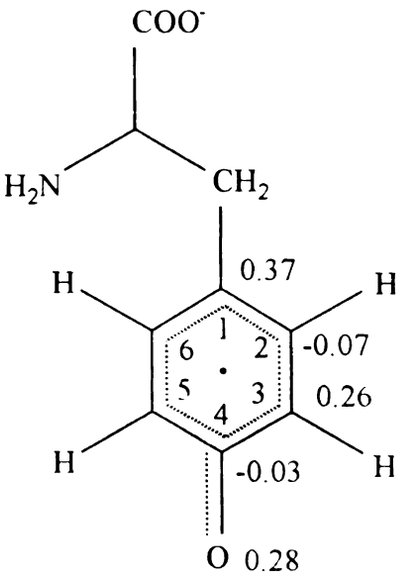

Figure III-8: Spin-density distribution in the tyrosine neutral radical.

been attributed to the rotation mobility of the phenol head group about the C_1-C_β bond. As the rotation barrier decreases, the heterogeneity in the dihedral angles increases, leading to increased dispersion of the magnitude of the isotropic coupling, A_{iso}. Analysis of ^{2}H-ESEEM spectra has yielded values of the rotational barrier and relative populations of the rotamers.[44,46]

The α-protons at the 2,6 and 3,5 ring positions, Figure III-8, are characterized by rhombic hyperfine tensors. In general, the coupling to the 2,6 protons is relatively weak, reflecting low unpaired spin density at these positions. The 3,5 as well as the methylene protons are more strongly coupled. The hyperfine tensors for tyrosyl radicals in various enzymes and in two model systems are summarized in Table III-1.[21] The results of various studies lead to the same basic spin density pattern displayed in Figure III-8, which appears to be common for all tyrosyl radicals studied so far. ENDOR and high-field EPR experiments[45,47,48] have led to the conclusion that possible hydrogen bonding interactions perturb the basic spin-density pattern only slightly and that the striking variation of lineshapes observed in the CW-EPR spectra of tyrosyl radical enzymes and models is due to variations in the dihedral angles of the β-CH_2 bonds, rather than variations in the spin-density distribution.

In the present study, the hyperfine coupling of 3,5-proton nuclei in tyrosyl neutral radical in frozen, aqueous NaOH glass is addressed to illustrate the applicability of the HYSCORE analysis with the 2D ESEEM modulation function derived in the previous section, and to determine the corresponding nuclear quadrupole and anisotropic hyperfine parameters. The 3,5-proton hyperfine tensor components have been estimated indirectly from simulation of EPR spectra,[39] and the 3,5-^{1}H coupling in tyrosyl radical in

Table III-1: Hyperfine tensors of tyrosyl radicals. Values are in MHz. (From Ref. 21)

	Radical Source					
Atom/ Position	RNR	GO	Y_D (PS-II)	Y_Z (PS-II)	PGHS	Aqueous Glass
H 3,5 x	-26.7		-26.4	-26.8	-25.7	-25.4
H 3,5 y	-8.4	-8.4	-7.9	-8.4		-7.2
H 3,5 z	-19.6	-21.6	-19.5	-19.5	-19.5	-19.5
H 2,6 x	5.0	4.8	4.2	5.0	4.9	
H 2,6 y	7.6	6.8	7.1	7.5	7.1	6.5
H 2,6 z	2.1	2.4		1.3		
H CH_2 $\parallel$	61.2	43.4	31.5	35.4	69	3.0
H CH_2 $\perp$	53.7	39.8	27.2	29	58.2	2.3
H CH_2 $\parallel$	2.1	11.4	9.8	7.9		
H CH_2 $\perp$	-4.5		4.4	1.4		
H bond $\parallel$	N. A.					
H bond $\perp$	N. A.	3.1	3.0			
O $\parallel$ (z)	-125					-111
Ref.	47,55	56	39,43,57, 58	45	a)	44,46,49, 55

a) Shi, W.; Hoganson, C. W.; Espe, M.;Bender, C. J.; Babcock, G. T.; Kulmacz, R. J.; Palmer, G.; Tsai, A.-L. unpublished results.

ribonucleotide reductase has been determined at liquid helium temperatures under near-optimum conditions for ENDOR.[47] These studies indicate that the hydrogen nuclei at ring positions 3 and 5 are essentially magnetically equivalent. Utilizing the advantages of the ^{2}H ESEEM over ^{1}H-ESEEM Warncke and McCracken have characterized the coupling of the 3,5 α-protons, using tyrosine specifically ^{2}H labeled at these positions.[49] Their ^{2}H ESEEM results have demonstrated that, by rational manipulation of the microwave pulse time interval, τ, in the stimulated echo ESEEM experiment, the magnitude of the principal components of the rhombic hyperfine tensor and the relative sign of the isotropic coupling can be determined.

III.4.3. HYSCORE of 3, 5 ^{2}H-labeled tyrosyl radical model system

Recently, Filep[21] has carried out HYSCORE experiments a 3, 5 ^{2}H-labeled tyrosyl radical model system. The neutral tyrosyl radical (Figure III-8) has been generated by UV irradiation of 5 mM specifically labeled tyrosine in frozen, aqueous NaOH glass containing 5 mM Gd^{3+} ions and approximately 12 M LiCl. The metal salts have been added to form a glass matrix as well as to enhance the relaxation of tyrosyl radical at liquid helium temperatures. Without increasing the relaxation rate of the tyrosyl radical, low sampling rates (below 10 Hz) in the pulsed EPR experiments would have to be used, which would make impractical collecting experimental data points in two time dimensions. An HYSCORE time-domain data set (128×128 data points) and a contour plot of the corresponding frequency-domain spectrum are shown in Figure III-9. The contour pattern is clearly different from the one generated by an axial hyperfine interaction (cf. Section III.2.). As rhombic hyperfine tensors are expected to give rise to horn-shaped contour

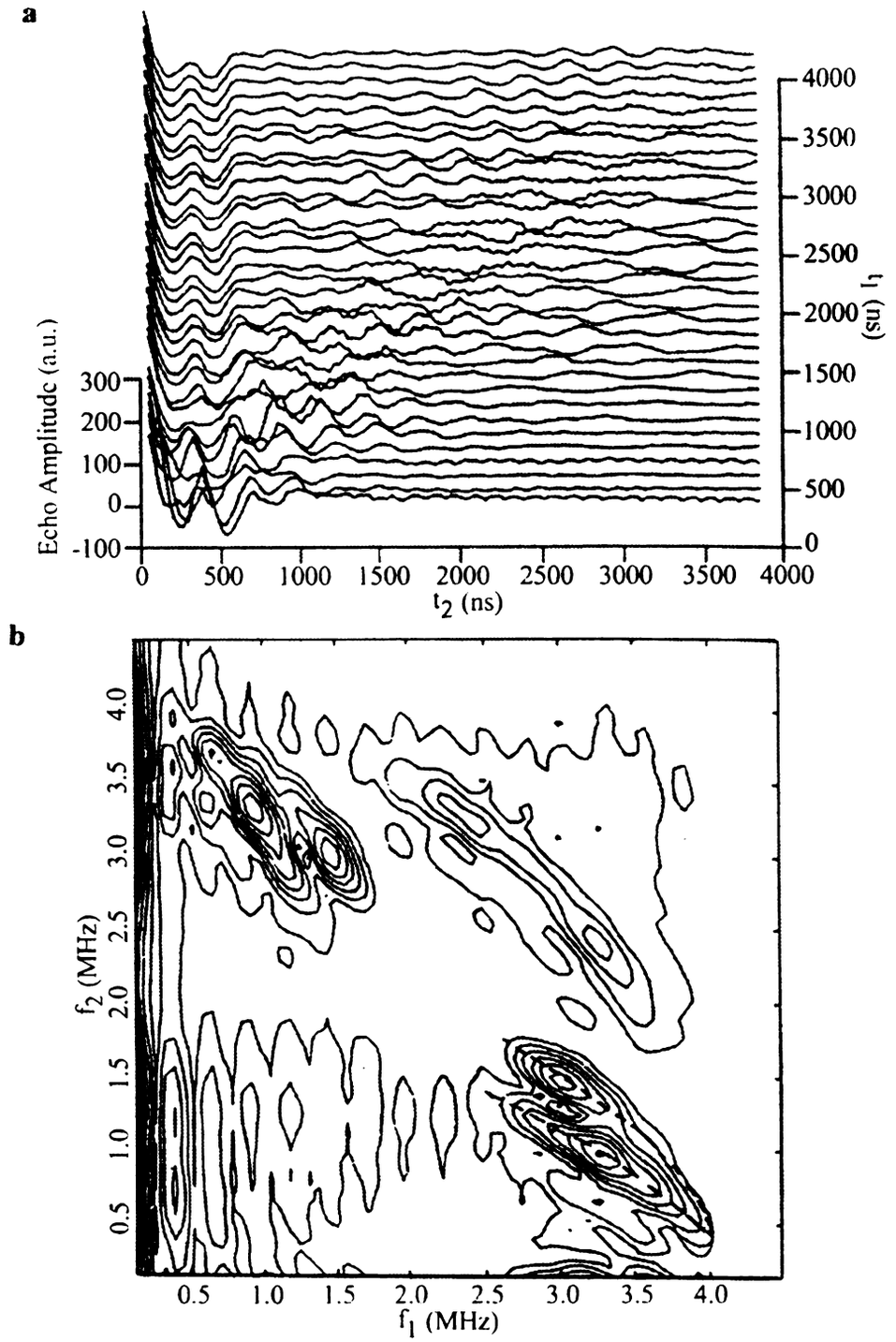

Figure III-9: (a) Time-domain HYSCORE data (128×128 data points) from 3,5 ^{2}H-tyrosyl, with τ = 200 ns; (b) the corresponding HYSCORE frequency-domain contour plot. B_0 = 3129 G, ν = 8.910 GHz. $f_1 = \omega_1/2\pi$, $f_2 = \omega_2/2\pi$. (From Ref. 21)

lines, the two clearly resolved arcs (designated by 1 and 2) are identified as the two limiting arcs, which form the boundary of the horn. They correspond to $\varphi = 0°$ and $\varphi = 90°$, where φ is the azimuthal angle specifying the position of $\mathbf{B}_0$ in the principal axis system of the hyperfine tensor (Figure III-10). In a randomly oriented sample $\mathbf{B}_0$ spans with equal probability all possible positions determined by pairs of values of φ and θ between 0° and 90°. At a particular value of φ, sweeping $\mathbf{B}_0$ from $\theta = 0°$ to $\theta = 90°$ results in a pair of

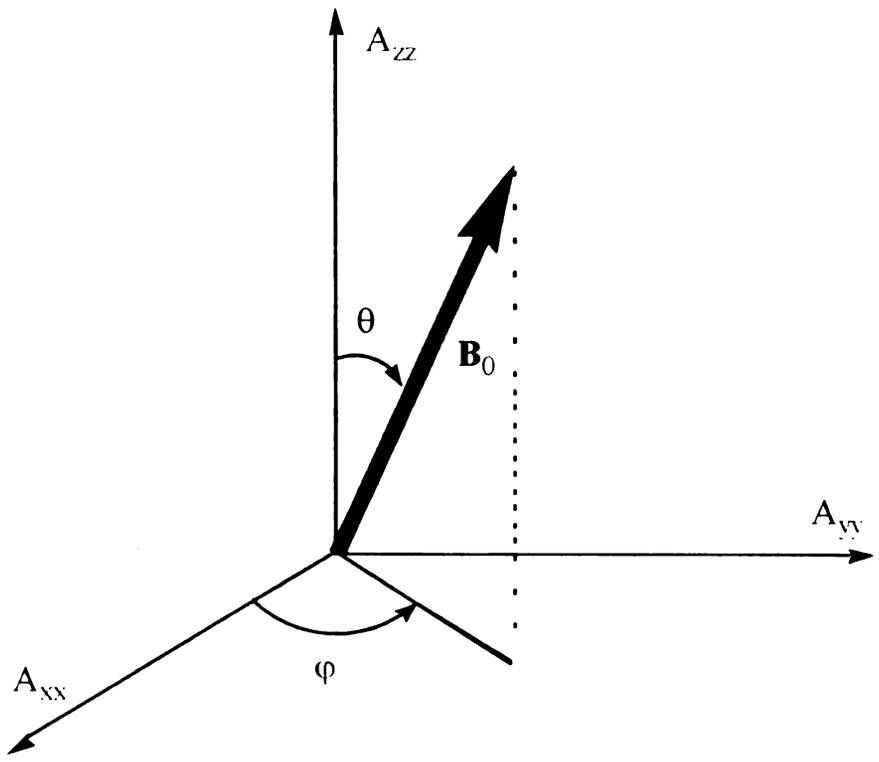

Figure III-10: Definition of the position of the external magnetic field vector, $\mathbf{B}_0$, in the principal axis system of a hyperfine tensor with rhombic symmetry.

arcs as for an axial hyperfine tensor. There is one such pair for each φ and the ensemble of these arcs creates the horn. When φ = 0°, the two principal values of the hyperfine tensor are $A_{\perp} = A_{xx}$ and $A_{\parallel} = A_{zz}$. When φ = 90° the hyperfine parameters are $A_{\perp} = A_{yy}$ and $A_{\parallel} = A_{zz}$. The evaluation of these boundary arcs can, in principle, yield all three principal values of the rhombic hyperfine tensor. (One should be cautious, however, since the observed arcs might not represent the actual boundary arcs because the modulation depth at the turning points and the singularity points becomes zero. In addition, it is not clear how the τ suppression comes into effect for an S = 1/2, I = 1 spin system.)

The hyperfine tensor components can be obtained by analyzing the boundary arcs 1 and 2, following the method of Dikanov and Bowman[22] and combining the two resultant axial hyperfine matrices into a rhombic one.[21] The principal values for the 3,5 ^{2}H hyperfine tensor obtained through this analysis are A_{xx} = -0.8 MHz, A_{yy} = -3.1 MHz, and A_{zz} = -3.6 MHz[21], while the values determined by Warncke and McCracken by theoretical simulations of stimulated ESEEM data for a tyrosyl model trapped in 40% NaOH glass matrix are A_{xx} = -3.0 MHz, A_{yy} = -3.9 MHz, and A_{zz} = -1.1 MHz, ±0.1 MHz.[49]

Numerical simulations of the HYSCORE contour map[21] have shown poor agreement with the experimental spectra, Figure III-11. The simulated spectrum in Figure III-11 (b) has been generated using hyperfine parameter values considerably different from those determined according to the method of Dikanov and Bowman.[22] There is also significant discrepancy in the intensities at certain parts of the contour lines (e. g., the tail of arc 1). This can be understood considering that the intensities have been calculated using the formulae of Gemperle et al.[15] derived for S=1/2, I=1/2 spin systems. While the

Figure III-11: (a) HYSCORE contour plot of 3,5 ^{2}H-tyrosyl (same as Figure III-9b); (b) the corresponding frequency-domain simulation using the following parameters: nuclear Larmor frequency, ν_I = 2.1 MHz; A_{xx} = - 3.82 MHz, A_{yy} = - 2.98 MHz, A_{zz} = -1.0 MHz; tau-value, τ = 200 ns. $f_1 = \omega_1/2\pi$, $f_2 = \omega_2/2\pi$. (From Ref. 21)

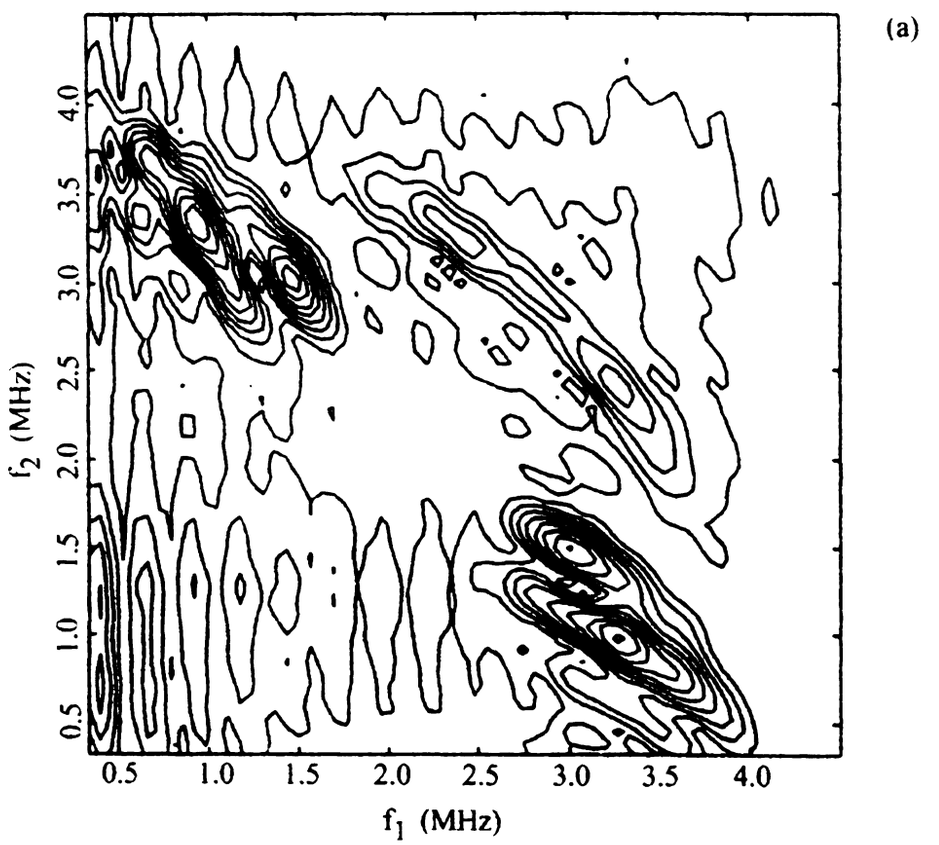

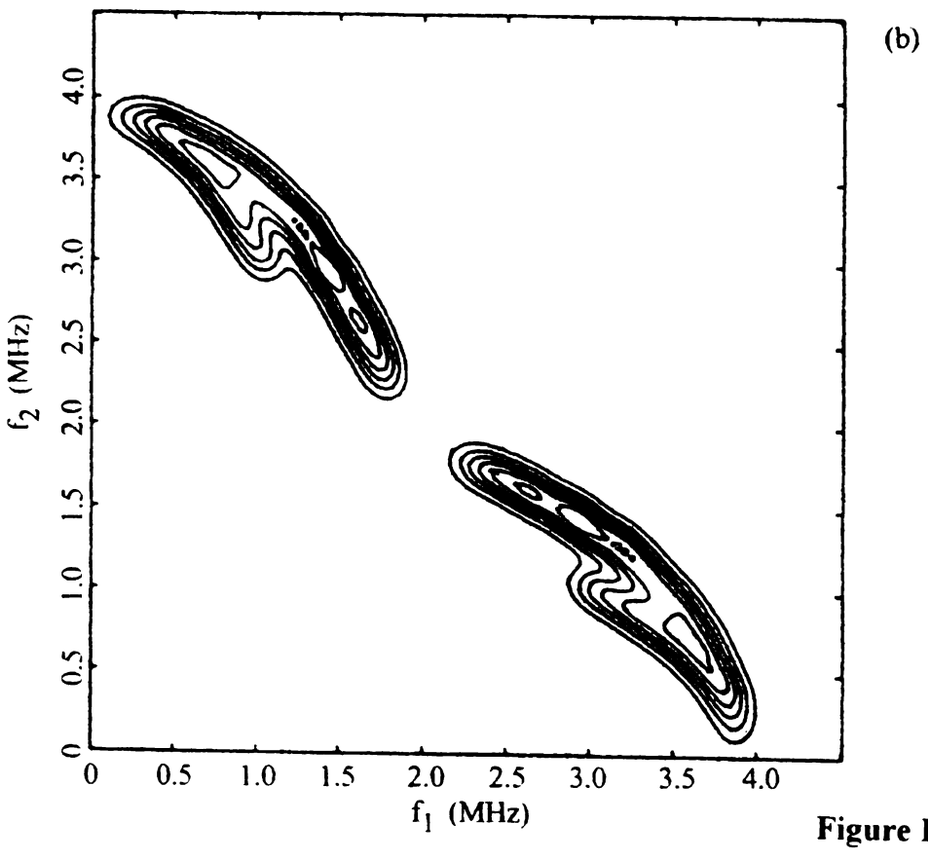

Figure III-11

frequencies can still be calculated with this formula to a good approximation (the small nuclear quadrupole interaction of deuterium does not alter the hyperfine frequencies substantially), the intensities of the cross peaks may be more significantly affected by the quadrupole interaction.[21] The observed hyperfine correlation pattern, Figure III-11 (a), is also strongly affected by the τ-suppression effect, which is not apparent from the presented simulation.

III.4.4. τ-suppression effect in HYSCORE

The τ-suppression effect in HYSCORE has been mentioned in Section III-2. There is cross peaks intensity dependence on the separation τ of the first two pulses superimposed on the amplitudes determined by the spin Hamiltonian. As a result, at certain τ-values the intensity of certain cross-peaks becomes zero (blind spots). In randomly oriented samples this leads to a distortion of the lineshape, which makes the lineshape analysis necessary in both 1D ESEEM and HYSCORE experiments. In HYSCORE of S = 1/2, I = 1/2 spin systems, partially suppressed contour lines may still provide sufficient information to deduce the hyperfine tensor parameters without spectral simulations.[22] As shown by Höfer,[12] in this case, the τ-suppression effect can be predicted and possibly avoided by experimentally adjusting the value of τ. For a limiting case of a weak hyperfine anisotropy, $A_{zz} < \omega_I$, where the modulation frequencies can be approximated by

$$\omega_{\alpha,\beta} = |\omega_I \pm A_{zz}/2|, \qquad \text{[III-31]}$$

the suppression effect can be calculated from the cross peak amplitude, Equation III-3c, as a function of A_{zz} and $\omega_I\tau$, as shown in Figure III-12 for $0 < A_{zz} < 6\omega_I$ and $0 < \omega_I\tau < 4\pi$. If one line of a pair is at zero frequency, the corresponding cross peaks cannot be observed. The frequency width of this blind spot decreases, however, with increasing τ. Line pairs arising from $A_{zz} < 2\omega_I$ fell within the frequency range $0 < \omega < 2\omega_I$. If τ is chosen according to $\omega_I\tau < \pi$, a bell-shaped amplitude function attenuates cross peaks at the wings of this spectral window $(0, 2\omega_I)$, but no extra suppression holes are generated inside the spectral window. At the expense of signal-to-noise, the frequency dependence of the amplitude function is reduced for decreasing $\omega_I\tau$. For $\pi < \omega_I\tau < 2\pi$, two suppression holes are generated which merge into one hole at $\omega = \omega_I$ when $\omega_I\tau = 2\pi$. A further increase of $\omega_I\tau$ produces an increasing number of suppression holes across the spectrum. By a proper choice of τ, a spectral window can be selected to minimize amplitude distortions for a given range of hyperfine coupling constants. It is clear that the summation of suppression-effect functions for an infinite number of τ values will result in a frequency-independent amplitude function with two blind spots, at $\omega = 0$ and $\omega = 2\omega_I$. For $A_{zz} > 2\omega_I$, a general rule for the optimum $\omega_I\tau$ cannot be established other than an increase of A_{zz} should be compensated for by a decrease of τ to maintain a certain amplitude function.

If there is appreciable hyperfine anisotropy, the modulation frequencies, ω_α and ω_β, are described by

$$\omega_{\alpha,\beta} = [A_{xz}^2/4 + A_{yz}^2/4 + (\omega_I \pm A_{zz}/2)^2]^{1/2}. \qquad \text{[III-32]}$$

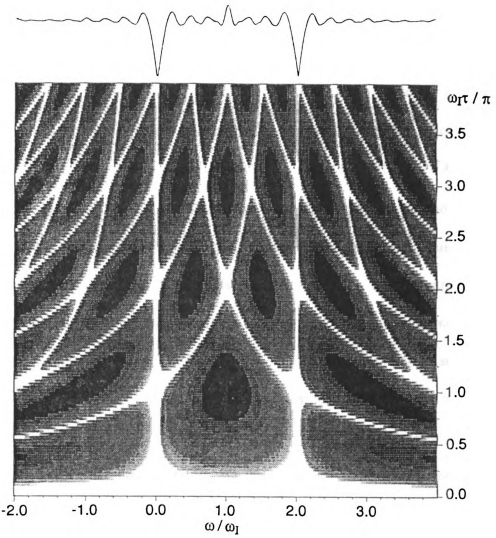

Figure III-12: Calculated suppression effect as a function of A_{ZZ} ($0 < A_{ZZ} < 6\omega_I$) and $\omega_I\tau$ assuming $\omega = |\omega_I \pm A_{ZZ}/2|$. Dark (light) shading corresponds to weak (strong) suppression effect. The sum of the suppression function over $\omega_I\tau$ results in an amplitude function with only two suppression holes at $\omega = 0$ and $\omega = 2\omega_I$ (top). (From Ref. 21)

The presence of A_{xz} and A_{yz} components in the expressions for ω_α and ω_β destroys the symmetry of the ESEEM lines with respect to ω_I (or $A_{zz}/2$), and the correlation ridges in a HYSCORE spectrum are no longer perpendicular (or parallel) to the frequency diagonal. However, for those paramagnetic species which have one of the hyperfine tensor principal axes parallel to the external magnetic field, the simple equation for ω_α and ω_β, Equation III-31, is valid. Therefore, the corresponding cross peaks will be located at (ω_I - $A_{ii}/2$, ω_I + $A_{ii}/2$) and (ω_I + $A_{ii}/2$, ω_I - $A_{ii}/2$) and the distance between the peaks, measured parallel to either one of the two axes of the 2D spectrum, gives directly the principal values of the hyperfine tensor. Although these cross peaks have zero intensity (k = 0), their expected location can still be found by following the ridges to the points where they intersect the line crossing the diagonal at (ω_I, ω_I). Höfer has shown that, in general, when no simple picture of the suppression effect can be developed, the amplitude distortions can be eliminated completely if 2D spectra are collected for a series of τ values and then added together, i. e., by a 3D experiment.[12] Obviously, improving the spectrum authenticity in this manner requires collection of a large amount of experimental data.

For an S = 1/2, I = 1 spin system, the analysis and prediction of the τ-suppression effect becomes more difficult because it is also influenced by the quadrupole coupling. The τ-dependence of the 1D ESEEM lineshape for the 3, 5 ^{2}H-labeled tyrosyl radical has been described in Ref. 49. Figure III-13 shows a series of experimental HYSCORE contour plots obtained with different τ-values[21]. Suppression of various parts of the lineshape depending on τ can be observed. These spectra demonstrate that the shortest τ-value (200 ns) yields the least suppressed features, in agreement with Höfer's analysis.[21]

Figure III-13: HYSCORE experimental contour plots of 3,5 ^{2}H-tyrosyl radical taken at various values of τ: (a) 200 ns; (b) 300 ns; (c) 400 ns; (d) 500 ns; (e) 600 ns. $f_1 = \omega_1/2\pi$, $f_2 = \omega_2/2\pi$. (From Ref. 21)

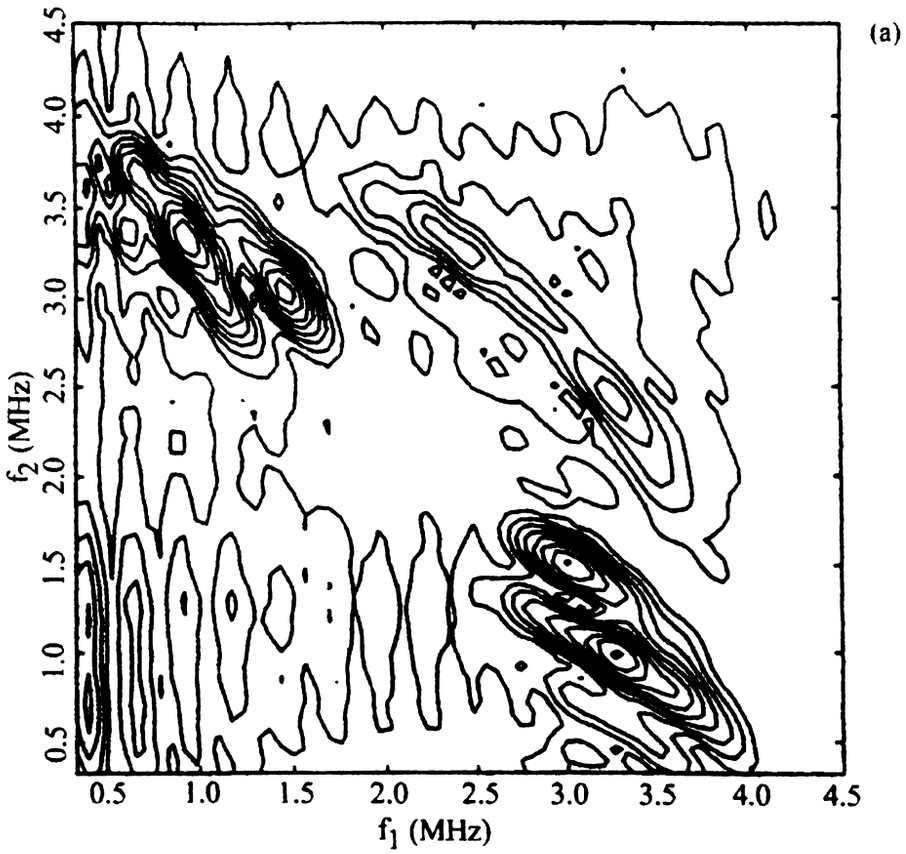

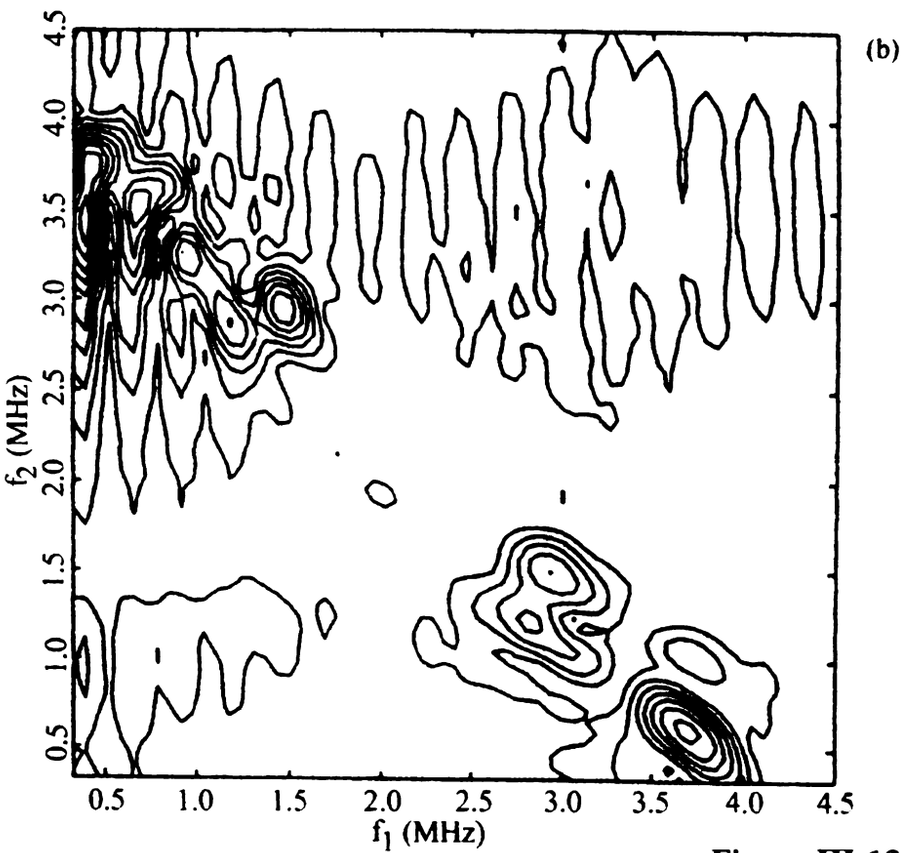

Figure III-13 (a, b)

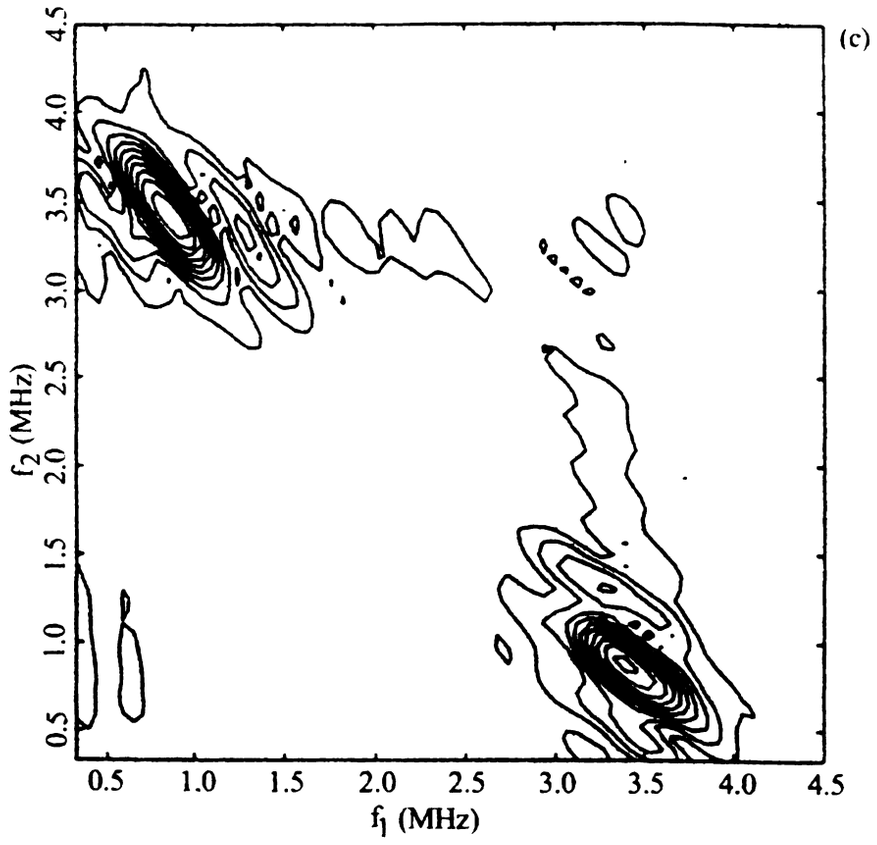

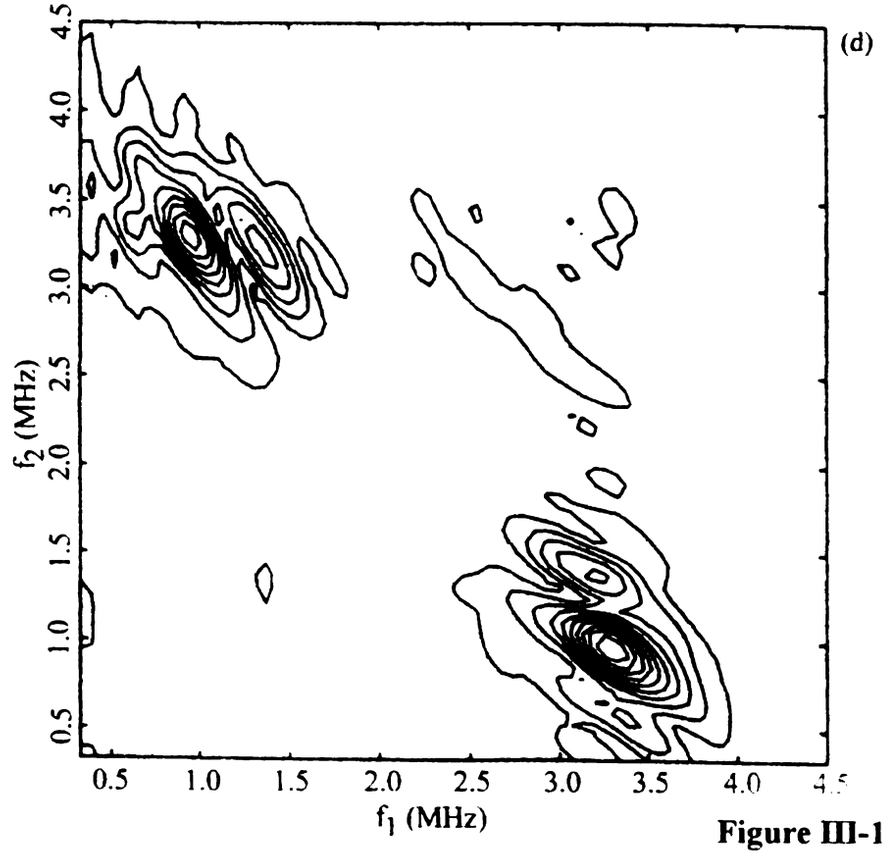

Figure III-13 (c, d)

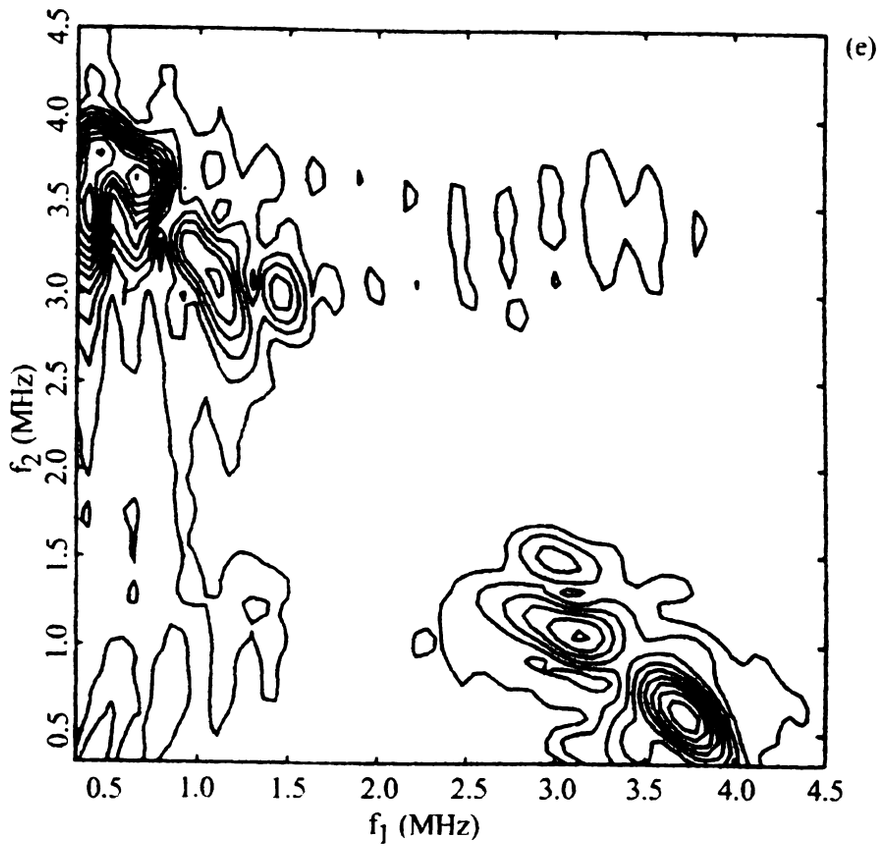

Figure III-13 (e)

III.4.5. Simulations of the HYSCORE experimental data for 3, 5 ^{2}H-labeled tyrosyl radical

The HYSCORE experimental spectra obtained for the 3, 5 ^{2}H-labeled tyrosyl radical from Ref. 21 have been simulated using the C-language program "mims4".[59] The program evaluates the HYSCORE modulation function, encoded as the module "EnvE4.c", for given spin Hamiltonian parameters and values of τ, t_1, and t_2. The modulation function is multiplied by an exponential dumping factor ($\exp[- \lambda(t_1 + t_2)]$, where λ is an adjustable parameter determining the linewidths in the frequency-domain spectrum) to simulate the decay of the echo envelope. By incrementing t_1 and t_2 the simulated two-dimensional spectrum is built for a particular orientation defined in terms of the angles θ and φ (Figure III-10). The orientation dependency is contained in the zero-order hyperfine frequencies, ω_α and ω_β, expressed as[49,50]

$$\omega_\alpha = [(\omega_I - A_{xx}/2)^2 \sin^2(\theta)\cos^2(\varphi) + (\omega_I - A_{yy}/2)^2 \sin^2(\theta)\sin^2(\varphi) + (\omega_I - A_{zz}/2)^2 \cos^2(\varphi)]^{1/2} \quad \text{[III-33a]}$$

$$\omega_\beta = [(\omega_I + A_{xx}/2)^2 \sin^2(\theta)\cos^2(\varphi) + (\omega_I + A_{yy}/2)^2 \sin^2(\theta)\sin^2(\varphi) + (\omega_I + A_{zz}/2)^2 \cos^2(\varphi)]^{1/2}. \quad \text{[III-33b]}$$

where $l_x = \sin(\theta)\cos(\varphi)$, $l_y = \sin(\theta)\sin(\varphi)$, and $l_z = \cos(\varphi)$ are the direction cosines for the direction of the laboratory field $\mathbf{B}_0$ in the hyperfine principal axis system. These frequencies are modified by the quadrupole corrections as in Equation III-17. Averaging of the 2D time domain data is performed over all orientations of the paramagnetic species.

$0 < \theta < 90^{\circ}$, $0 < \varphi < 90^{\circ}$, via Simpson numerical integration over θ and φ with the usual solid-angle probability distribution weighting for the random molecular orientations. A small ε region ($\varepsilon = |\sin(\alpha) - \alpha| < 10^{-4}$, where α denotes θ or φ) around the boundary values for the angles is excluded from the computation, as the modulation depth becomes zero or a very large number there. The final result is a HYSCORE time-domain data file for the disordered paramagnetic system. The time-domain data are then analyzed by 2D Fourier transformation in the same manner as the experimental HYSCORE data, using a set of MATLAB scripts. [51,59]

A 2D time-domain data set and its corresponding frequency-domain contour map are shown in Figure III-14. The agreement with the respective experimental HYSCORE contour plot, Figure III-11, is satisfactory. Each cross peaks appears split as a result of the τ-suppression effect. The major discrepancies are observed in the relative intensity of the two portions of a cross peak as well as the orientation of the peak lineshapes in the f_1f_2 coordinate system. A series of contour maps for different τ values is shown in Figure III-15. It is apparent that the τ-suppression effect creates blind spots in the spectra and modifies the appearance of the contributions of the hyperfine frequency components. The demonstrated τ-suppression effect is consistent with the experimental HYSCORE data in that larger τ values create more suppression holes. Although there is no complete correspondence between simulated (Figure III-15) and experimental (Figure III-13) contour maps for all values of τ, the simulated and experimental cross-peak patterns follow the same trend. Detailed simulations carried out upon incrementing τ by 20 ns have shown that there is a smooth development of cross-peaks lineshapes between the patterns of Figure III-15. The lack of complete agreement between the HYSCORE experimental

Figure III-14: Simulated HYSCORE spectra of 3,5 ^{2}H-tyrosyl radical. (a) A 3D plot of the time-domain simulated data (128×128 points). (b) The corresponding 3D frequency-domain magnitude spectrum obtained by 2D Fourier transformation of the time-domain data in (a). (c) Contour plot of the frequency spectrum. Parameters: nuclear Larmor frequency, ν_I = 2.1 MHz; A_{xx} = - 2.3 MHz, A_{yy} = - 3.1 MHz, A_{zz} = - 0.9 MHz; η = 0.1; e^2qQ = 0.22 MHz; λ = 0.7 μsec^{-1}; tau-value, τ = 200 ns; number of θ increments over the interval 0-90°, 30; maximum number of φ increments over the interval 0-90°, 30. $f_1 = \omega_1/2\pi$, $f_2 = \omega_2/2\pi$.

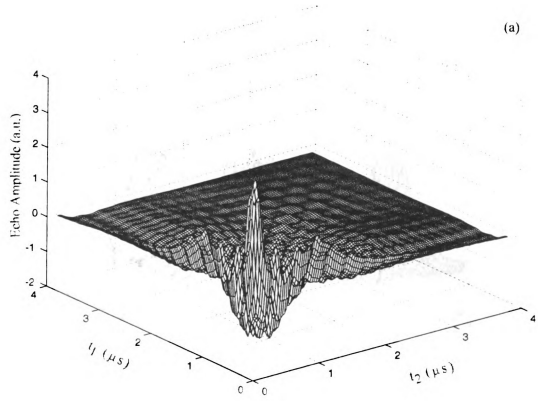

Figure III-14 (a)

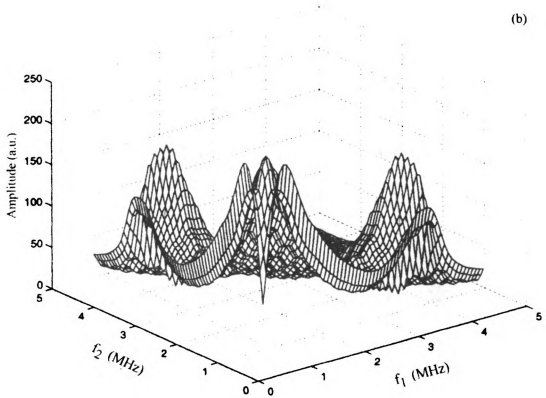

Figure III-14 (b)

(c)

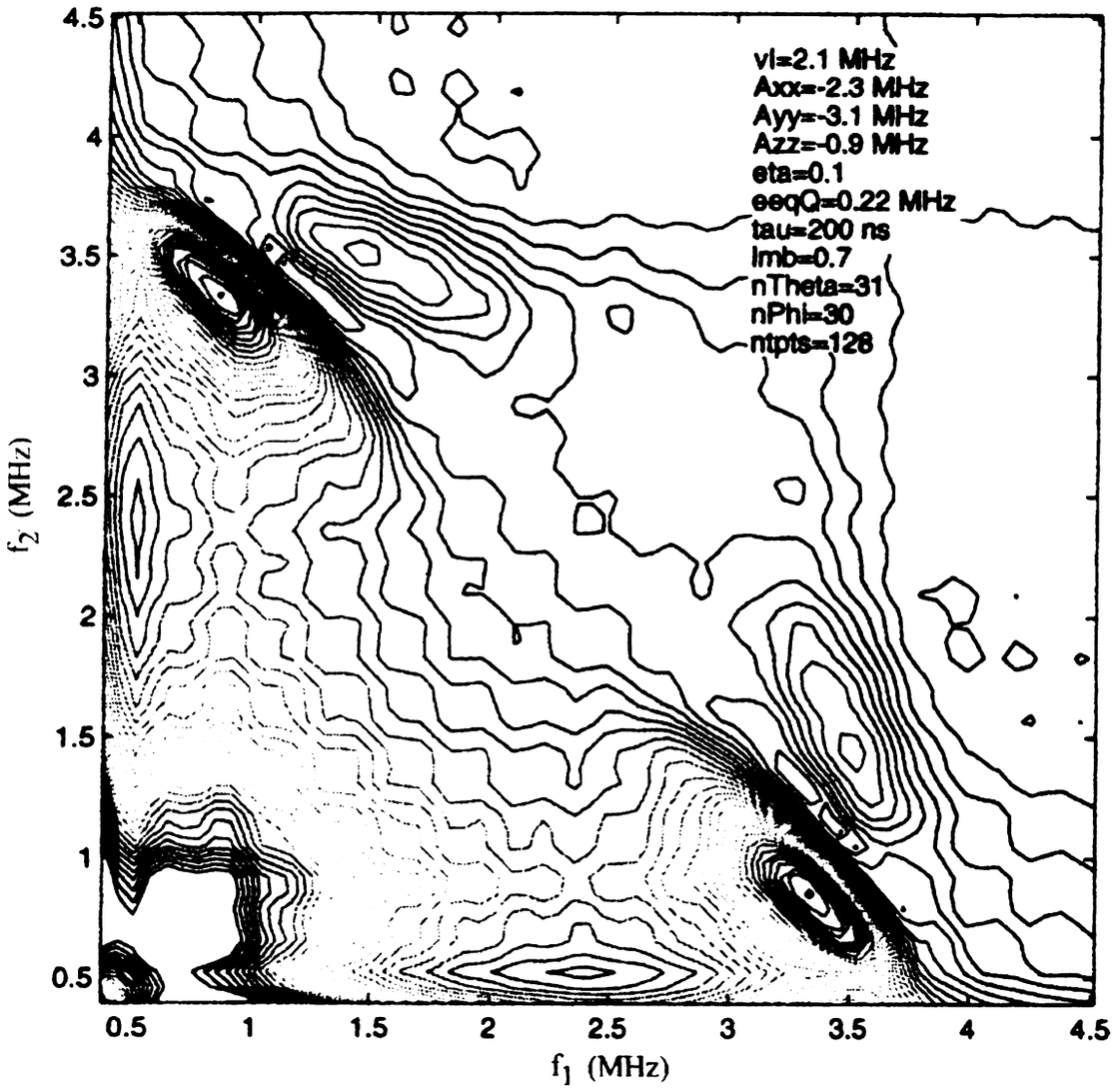

Figure III-14 (c)

and simulated spectra may be due, in part, to a possible offset between the τ values from the experiment relative to those from the simulations. Time offset of 30 ns can influence the cross-peak morphology substantially. Another reason for the observed discrepancies may, of course, come from lack of perfect adjustment of the spin Hamiltonian parameters used in the simulations.

Figure III-16 represents a HYSCORE contour map generated with no quadrupole coupling, (a), and with a relatively large value of the deuteron quadrupole coupling parameter, e^2qQ = 300 kHz, (b). It is evident that the quadrupole coupling does affect the lineshape of the cross peaks by modifying the τ-suppression effect. This is to be expected since the quadrupole coupling is included in the ω_{ij} (i, j = a, b, c, d, e, f) hyperfine frequencies, which appear in the HYSCORE modulation function as arguments of cosines of the type $\cos(\omega_{ij}\,\tau)$.

The values of the simulation parameters for the hyperfine and quadrupole interactions, A_{xx} = -2.3 MHz, A_{yy} = -3.1 MHz, A_{zz} = -0.9 MHz, e^2qQ/h = 220 kHz, asymmetry parameter η = 0.1, fall in the range of the 3,5 α-proton values (cf. Table III-1) after appropriate scaling by the factor of 6.51, and agree well with the range of ^2H quadrupole coupling constants for a wide variety of organic compounds[52-54], respectively. HYSCORE cannot provide direct information on the sign of the hyperfine coupling; however, it reports on the relative sign of the isotropic and the dipolar part of the hyperfine interaction. Furthermore, it is known that $A_{iso} < 0$ for α-protons, which is expressed in the negative value of the McConnell constant ($Q_\alpha(^2HC)$ = -10.7 MHz).[42]

The discrepancies in the exact hyperfine constant values can be attributed to the effect of the matrix. Gadolinium (III) salt has been added to the sample to enhance the

Figure III-15: Frequency-domain contour plots for the 3,5 ^{2}H-tyrosyl radical HYSCORE time-domain simulations performed with the C program "mims4" using the following parameters: nuclear Larmor frequency, ν_I = 2.1 MHz; A_{xx} = - 2.3 MHz, A_{yy} = - 3.1 MHz, A_{zz} = -0.9 MHz; η = 0.1; e^2qQ = 0.22 MHz; λ = 0.7 μsec^{-1}; number of time-domain data points, 128×128; number of θ increments over the interval 0-90°, 30; maximum number of φ increments over the interval 0-90°, 30; tau-value, τ = 150 ns (a), 200 ns (b), 300 ns (c), 400 ns (d), 500 ns (e), 600 ns (f). $f_1 = \omega_1/2\pi$, $f_2 = \omega_2/2\pi$.

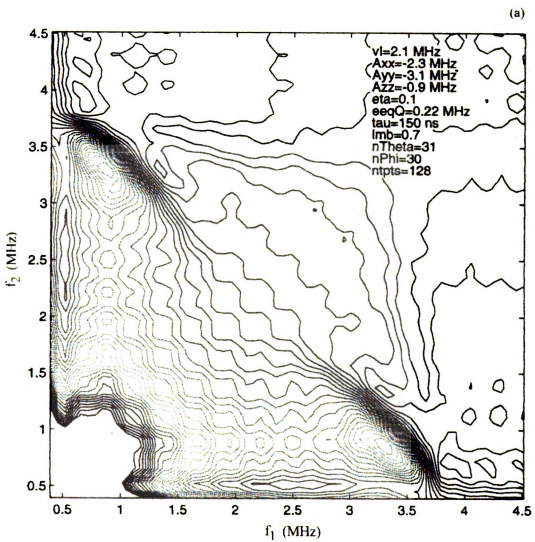

Figure III-15 (a)

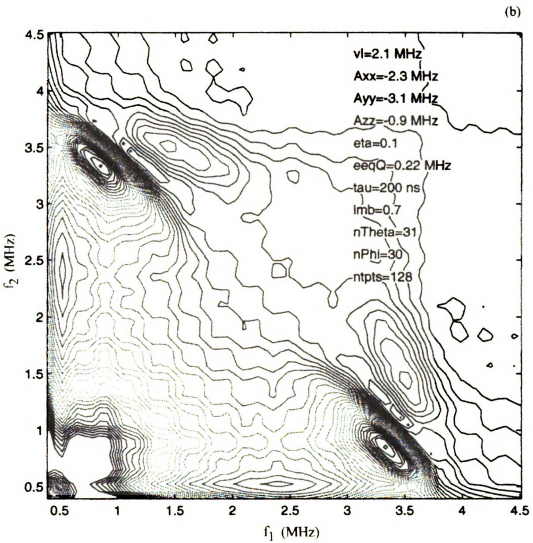

Figure III-15 (b)

(c)

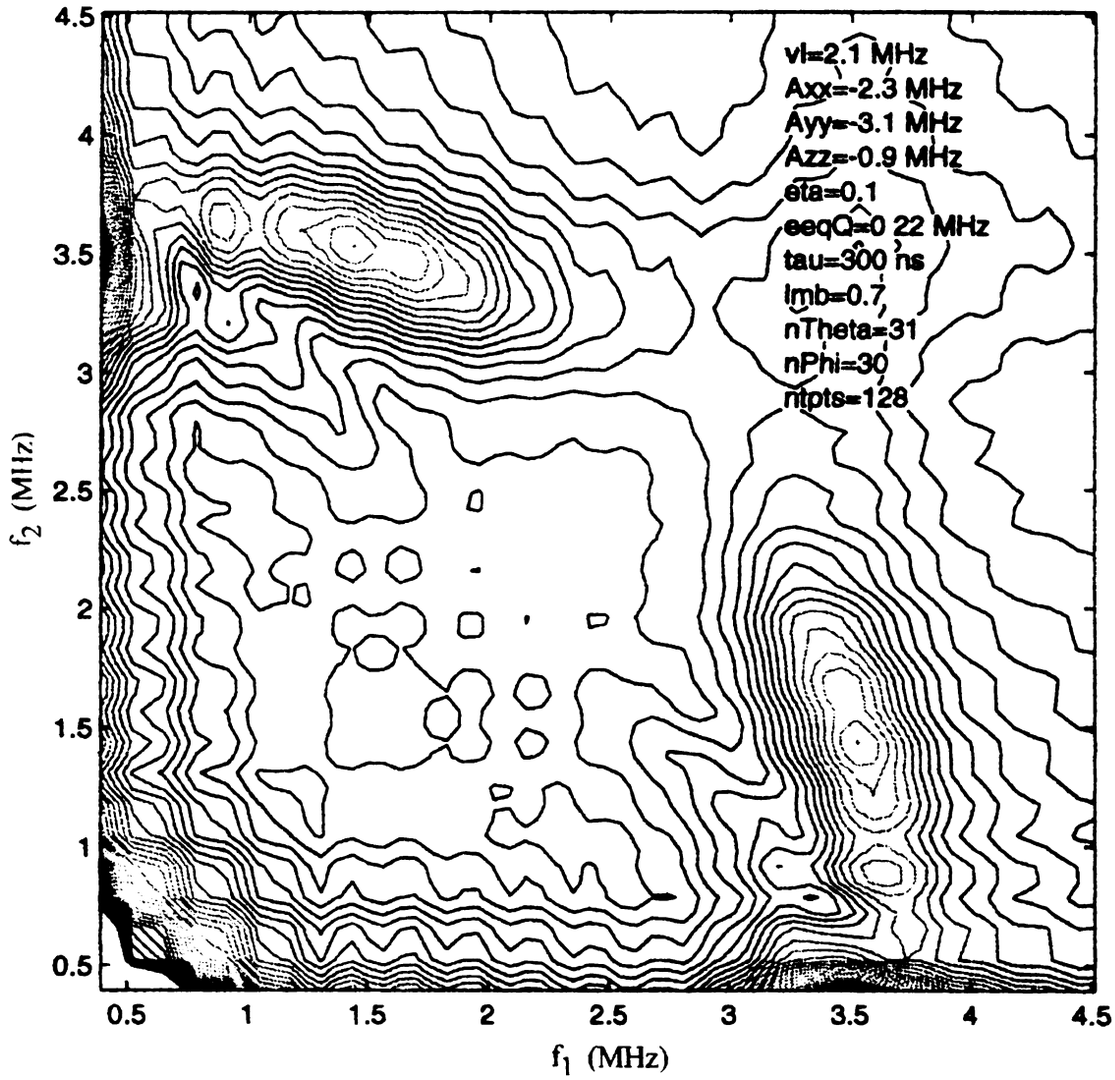

Figure III-15 (c)

(d)

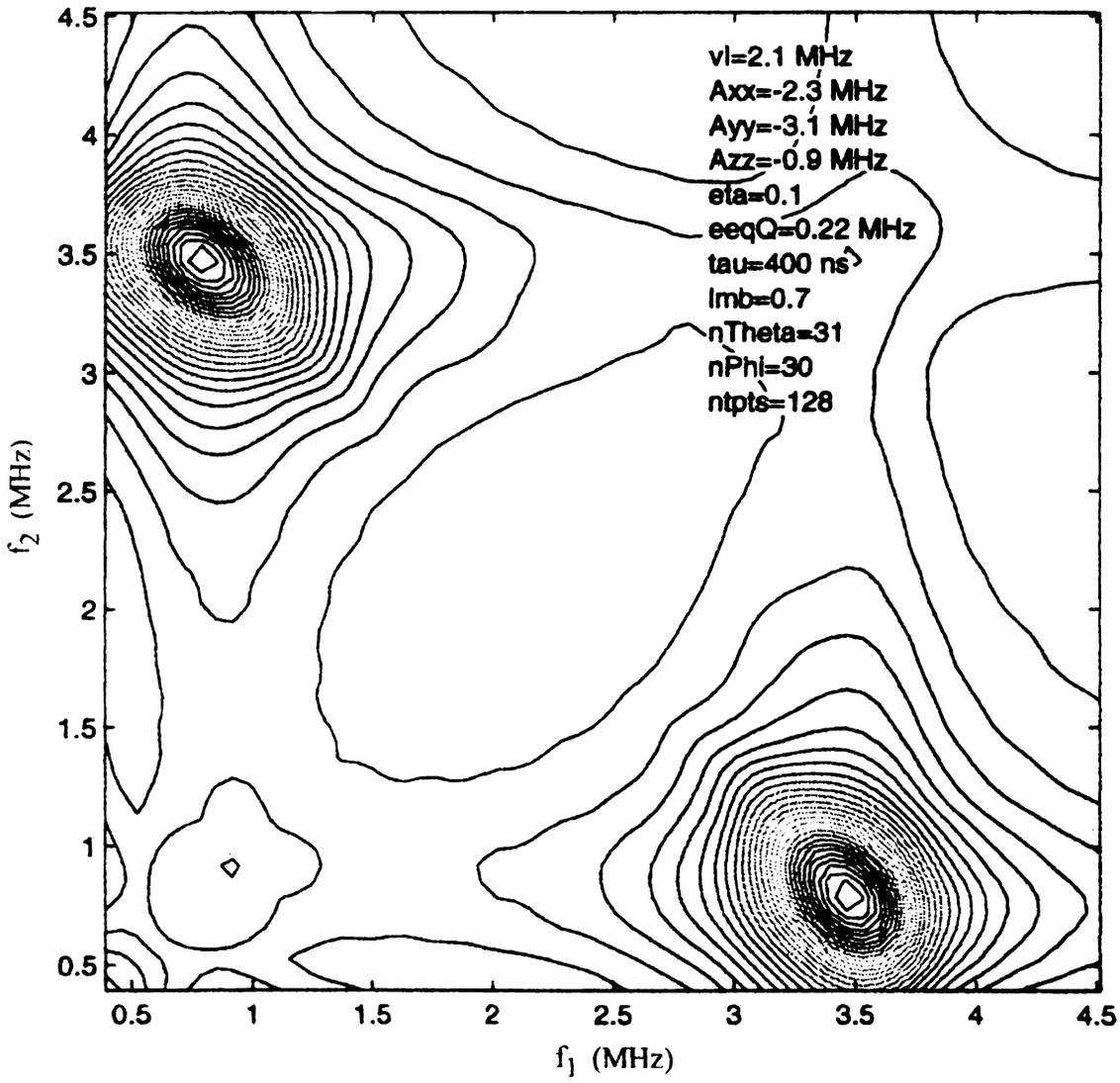

Figure III-15 (d)

(e)

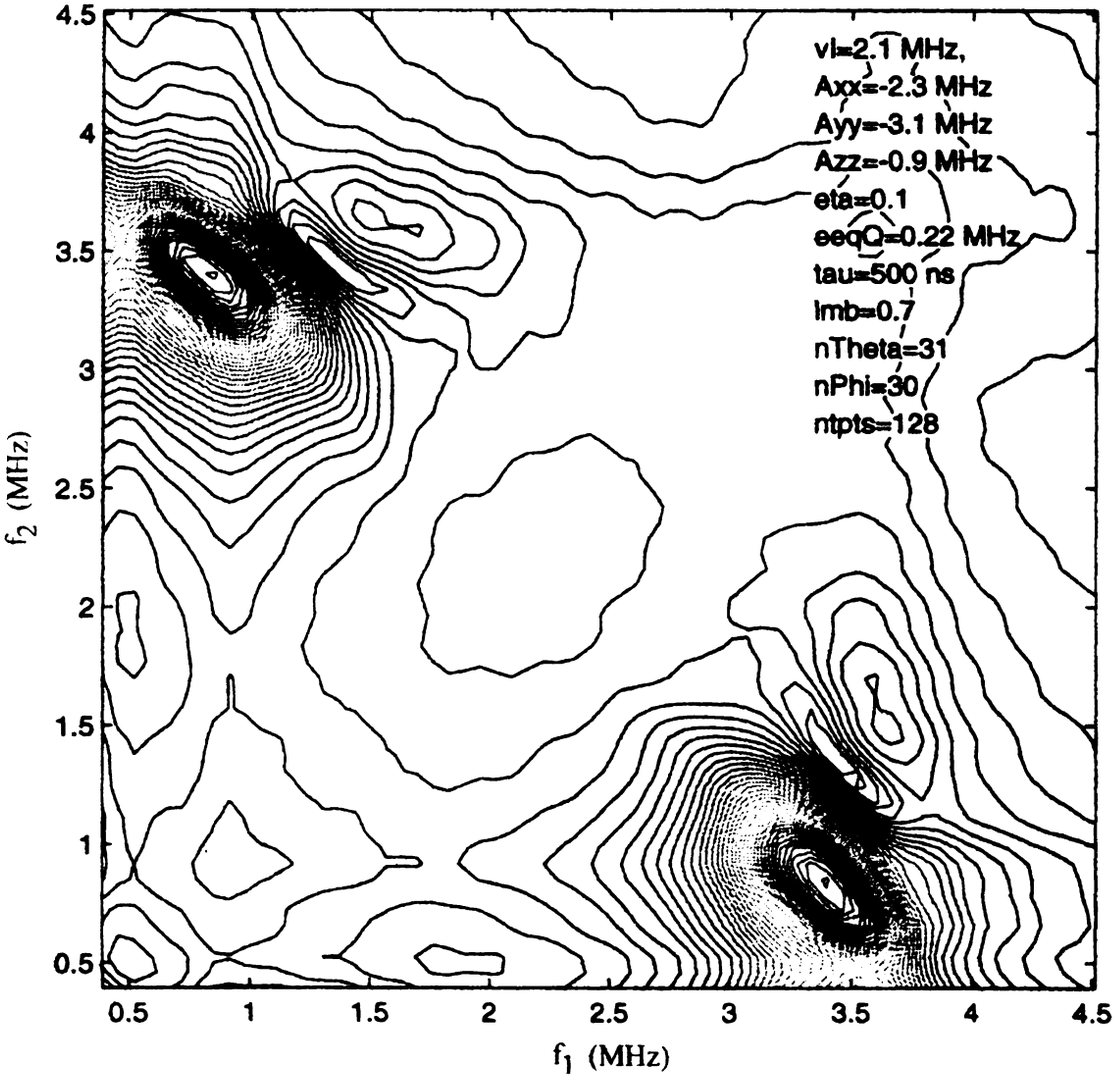

Figure III-15 (e)

(f)

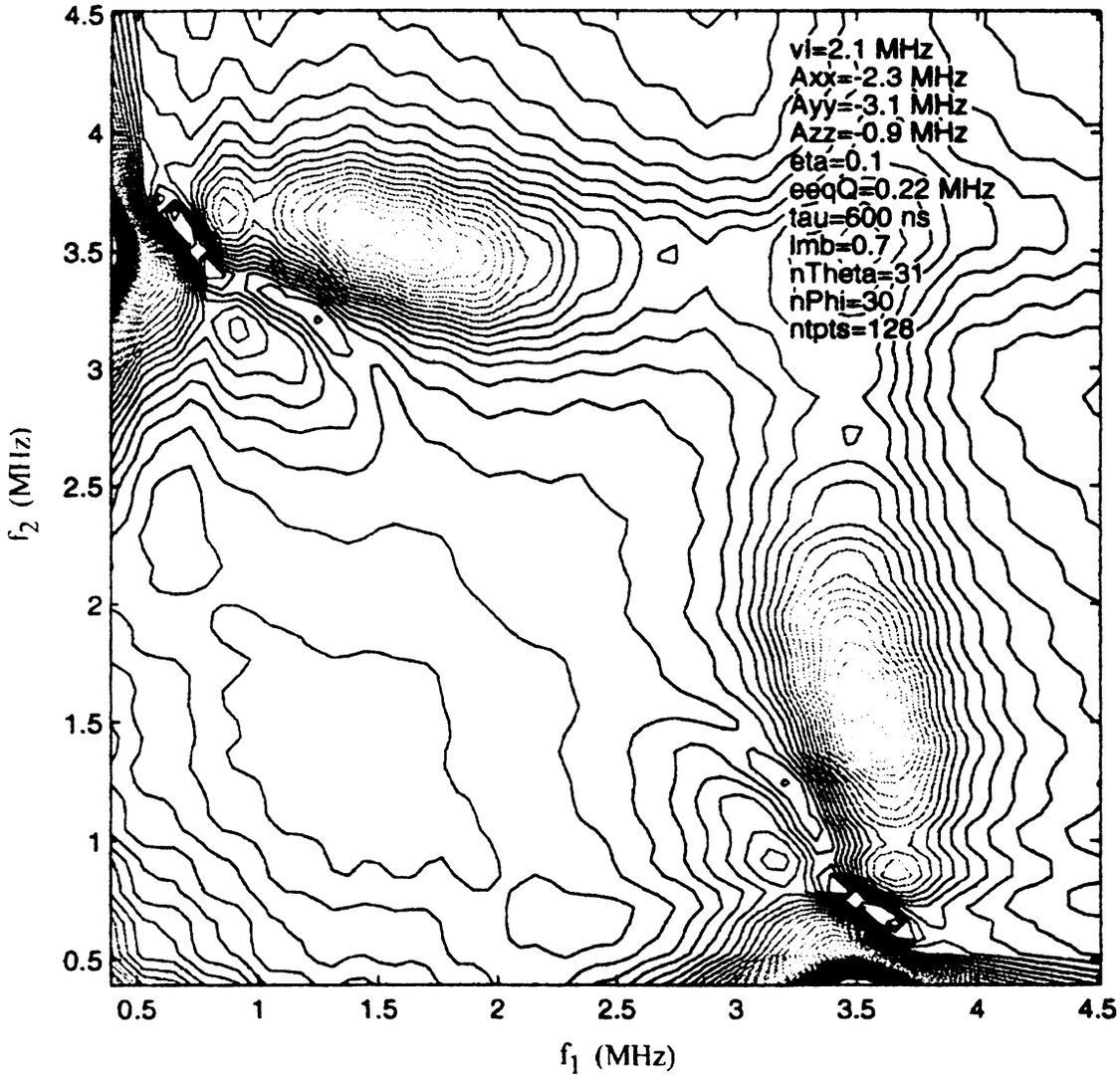

Figure III-15 (f)

Figure III-16: Frequency-domain contour plots for the 3,5 ^{2}H-tyrosyl radical HYSCORE time-domain simulations performed with the C program "mims4" using the following parameters: nuclear Larmor frequency, ν_I = 2.1 MHz; A_{xx} = -2.3 MHz, A_{yy} = - 3.1 MHz, A_{zz} = -0.9 MHz; number of time-domain data points, 128×128; number of θ increments over the interval 0-90°, 30; maximum number of φ increments over the interval 0-90°, 30; λ = 0.7 μsec^{-1}; tau-value, τ = 200 ns; η = 0.1; e^2qQ = 0, (a), e^2qQ = 0.3 MHz, (b). $f_1 = \omega_1/2\pi$, $f_2 = \omega_2/2\pi$.

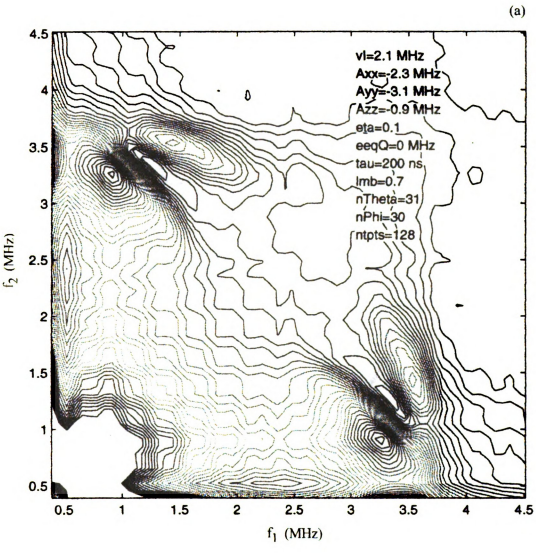

Figure III-16 (a)

(b)

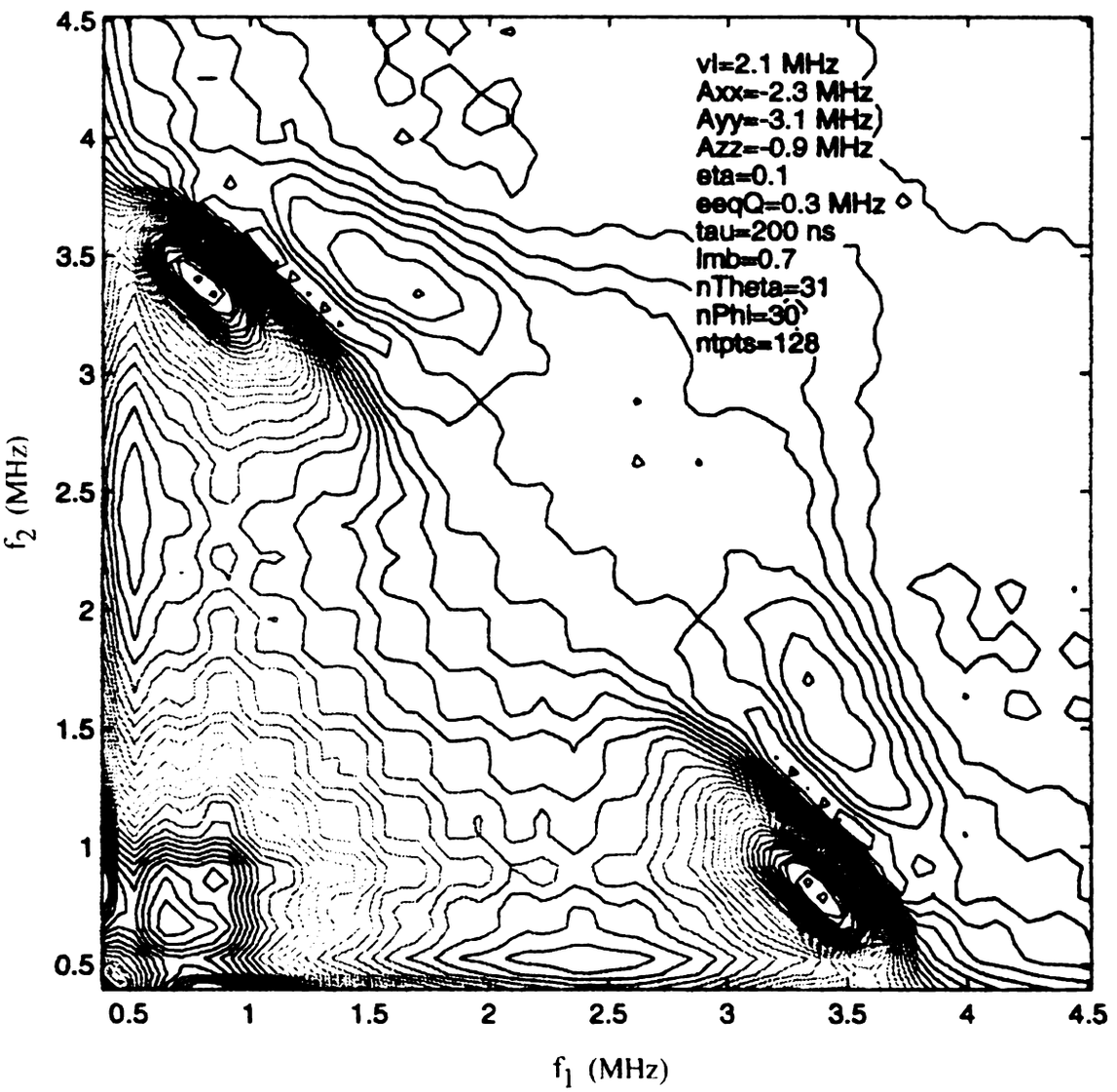

Figure III-16 (b)

very slow relaxation of tyrosyl radicals at low temperatures, thus making possible collection of a large number of 2D HYSCORE data points in a reasonable amount of time. Gd^{3+} is a strongly paramagnetic ion, containing seven unpaired electrons (S = 7/2). It gives rise to a very broad EPR signal, which is hardly observable in derivative EPR spectra. This signal is superimposed on the tyrosyl radical signal. As a consequence, the spin densities on Carbon 3 and Carbon 5 may be altered changing the values of the hyperfine coupling parameters.

III.5. Conclusion

^{2}H-ESEEM is an alternative method to proton ENDOR to obtain detailed structural information on organic radicals. The potential of HYSCORE technique has still not been exploited to its full extent. The HYSCORE echo modulation function for an S = 1/2, I = 1 spin system has been derived using the density matrix formalism. Its applicability to the interpretation of the HYSCORE data for ^{2}H-labeled tyrosyl radical has been demonstrated through simulations. The simulations show that the 2D ESEEM function adequately describes the experimental correlation patterns. In particular, it reproduces to a good approximation the τ-suppression-effect modulated lineshapes of the observed HYSCORE cross peaks.

References

1. Merks, R. P. J.; de Beer, R. *J. Phys. Chem.* **1979**, *83*, 3319.

2. Höfer, P. In *Electron Magnetic Resonance of Disordered Systems II*; Yordanov, N. D., Ed.; World Scientific: Singapore, 1991, pp. 1-15.

3. Höfer, P.; Grupp, A.; Nebenführ, H.; Mehring, M. *Chem. Phys. Lett.* **1986**, *132*, 279-282.

4. Isoya, J.; Bowman, M. K.; Norris, J. R.; Weil, J. A. *J. Chem. Phys.* **1983**, *78*, 1735.

5. Lee, S.; Patyal, B. R.; Freed, J. H. *J. Chem. Phys.* **1993**, *98*, 3665.

6. Pöppl, A.; Böttcher, R.; Völkel, G. *J. Magn. Reson.* **1996**, *Series A 120*, 214.

7. Shane, J. J.; Höfer, P.; Reijerse, E. J.; de Boer, E. J. *J. Magn. Reson.* **1992**, *99*, 596-604.

8. Reijerse, E. J.; Shane, J. J.; de Boer, E. J.; Höfer, P.; Collison, D. In *Electron Magnetic Resonance of Disordered Systems II*; Yordanov, N. D., Ed.; World Scientific: Singapore, 1991, p. 253.

9. Dikanov, S. A.; Samoilova, R. I.; Smieja, J. A.; Bowman, M. K. *J. Am. Chem. Soc.* **1995**, *117*, 10579.

10. Käss, H.; Rautter, J.; Bönigk, B.; Höfer, P.; Lubitz, W. *J. Phys. Chem.* **1995**, *99*, 436-448.

11. Shergill, J. K.; Joannou, C. L.; Mason, J. R.; Cammack, R. *Biochemistry* **1995**, *34(51)*, 16533-16542.

12. Höfer, P. *J. Magn. Reson.*, **1994**, *Series A 111*, 77-86.

12. Song, R.; Zhong, Y. C.; Noble, C. J.; Pilbrow, J. R.; Hutton, D. R. *Chem. Phys. Lett.* **1995**, *237*, 86-90.

14. Gemperle, C.; Schweiger, A.; Ernst, R. R. *Chem. Phys. Lett.* **1991**, *178*, 565.

15. Gemperle, C.; Aebli, G.; Schweiger, A.; Ernst, R. R. *J. Magn. Reson.* **1990**, *88*, 241-256.

16. Ernst, R. R.; Bodenhausen, G.; Wokaun, A. *Principles of Nuclear Magnetic Resonance in One and Two Dimensions*, Clarendon Press: Oxford, 1987, Chapter 8.

17. Barkhuijsen, H.; de Beer, R.; Pronk, B. J.; van Ormondt, D. *J. Magn. Reson.* **1985**, *61*, 284.

18. Astashkin, A. V.; Dikanov, S. A.; Kurshev, V. V.; Tsvetkov, Yu. D. *Chem. Phys. Lett.* **1987**, *136*, 335.

19. Höfer, P. *Bruker Report EPR* **1993**, *118*, 1-8.

19. McCracken, J. In *Handbook of Electron Spin Resonance*, Vol. II, Poole, C. P.; Farach, H. A., eds., in press.

21. Filep, G. *Ph. D. Dissertation*, Michigan State University, 1997.

22. Dikanov, S. A.; Bowman, M. K. *J. Magn. Reson.* **1995**, *Series A 116*, 125-128.

23. Kurreck, H.; Kirste, B.; Lubitz, W. in *Methods in Stereochemical Analysis, Electron Nuclear Double Resonance Spectroscopy of Radicals in Solution, Application to Organic and Biological Chemistry*; Marchand, A. P., Ed.; VCH Publishers, Inc.: New York, 1988.

24. Mims, W. B. *Phys. Rev.* **1972**, *B 5*, 2409-2419.

25. Mims, W. B. *Phys. Rev.* **1972**, *B 6*, 3543-3545.

26. Rowan, L. G.; Hahn, E. L.; Mims, W. B. *Phys. Rev.* **1965**, *137*, A61.

27. Astashkin, A. V.; Dikanov, S. A.; Tsvetkov, Yu. D. *Chem. Phys. Lett.* **1987**, *136*, 204.

28. Wolfram Research, Inc. Mathematica. [Online] Available http://www.wolfram.com/index.html, August 20, 1998.

29. Sigel, H.; Sigel, A., Eds. *Metal Ions in Biological Systems, Vol. 30*; Marcel Dekker: New York, 1994.

30. Fontecave, M.; Pierre, J.-L. *Bull. Soc. Chim. Fr.* **1996**, *133*, 653.

31. Reichard, P.; Ehrenberg, A. *Science* **1983**, *221*, 514.

32. Sjöberg, B.-M.; Gräslund, A. *Adv. Inorg. Biochem.* **1983**, *5*, 87.

33. Barry, B. A.; Babcock, G. T. *Proc. Natl. Acad. Sci. U.S.A.* **1987**, *84*, 7099.

34. Smith, W. L.; Eling, T. E.; Kulmacz, R. J.; Marnett, L. J.; Tsai, A. L. *Biochemistry* **1992**, *31*, 3.

35. Whittaker, M. M.; Whittaker, J. W. *J. Biol. Chem.* **1990**, *265*, 9610.

36. Jones, S. M.; Mu, D.; Wemmes, D.; Smith, A. J.; Kaus, S.; Maltby, D.; Burlingname, A. L.; Klinman, J. P. *Science* **1990**, *248*, 981.

37. DeFillipis, M. R.; Murthy, C. P.; Faraggi, M.; Klapper, M. H. *Biochemistry* **1989**, *28*, 4847.

38. Frey, P. A. *Chem. Rev.* **1990**, *90*, 1343.

39. Hoganson, C. W.; Babcock, G. T.; *Biochemistry* **1992**, *31*, 11874.

40. Stubbe, J. *Annu. Rev. Biochem.* **1989**, *58*, 257.

41. Davidson, V. L. In *Principles and Applications of Quinoproteins*, Davidson, V. L., Ed., Dekker: New York, 1992.

42. Gordy, W. in *Techniques in Chemistry, Vol. XV: Theory and Applications of Electron Spin Resonance*; West, W., Ed.; Wiley: New York, 1980.

43. Warncke, K.; McCracken, J.; Babcock, G. T. *J. Am. Chem. Soc.* **1994**, *114*, 7332.

44. Warncke, K.; McCracken, J. *J. Chem. Phys.* **1995**, *103*, 6829.

45. Tommos, C.; Tang, X.-S.; Warncke, K.; Hoganson, C. W.; Styring, S.; McCracken, J.; Diner, B. A.; Babcock, G. T. *J. Am. Chem. Soc.* **1995**, *117*, 10325.

46. Warncke, K.; Babcock, G. T. McCracken, J. *J. Phys. Chem.* **1996**, *100*, 4654.

47. Bender, C. J.; Sahlin, M.; Babcock, G. T.; Barry, B. A.; Chandrashekar, T. K.; Salowe, S. P.; Stubbe, J.; Lindström, B.; Petersson, L.; Ehrenberg, A.; Sjöberg, B.-M. *J. Am. Chem. Soc.* **1989**, *111*, 8076.

48. Un, S.; Atta, M.; Fontecave, M.; Rutherford, A. W. *J. Am. Chem. Soc.* **1995**, *117*, 10713.

49. Warncke, K.; McCracken, J. *J. Chem. Phys.* **1994**, *101*, 1832-1841.

50. Dalton, L. R.; Kwiram, A. L. *J. Chem. Phys.* **1972**, *57*, 1132-1145.

51. The MathWorks, Inc. Matlab. [Online] Available http://www.mathworks.com/index.html, August 20, 1998.

52. Lucken, E. A. C. *Nuclear Quadrupole Coupling Constants*, Academic Press: New York, 1969.

53. Bonera, G.; Rigamonti, A. *J. Chem. Phys.*, **1965**, *42*, 175-180.

54. Glasel, J. A. *J. Am. Chem. Soc.* **1969**, *91*, 4569-4571.

55. Hoganson, C. W.; Sahlin, M.; Sjöberg, B.-M.; Babcock, G. T. *J. Am. Chem. Soc.* **1996**, *118*, 4672.

56. Babcock, G. T.; El-Deeb, M. K.; Sandusky, P. O.; Whittaker, M. M.; Whittaker, J. W. *J. Am. Chem. Soc.* **1992**, *114*, 3727.

57. Rigby, S. E.; Nugent, J. H. A.; O'Malley, P. *J. Biochem.* **1994**, *33*, 1734.

57. Tommos, C.; Madsen, C.; Styring, S.; Vermaas, W. *Biochemistry* **1994**, *33*, 11805.

58. HYSCORE Simulations for S=1/2, I=1 Spin Systems. [Online] Available http://www.cem.msu.edu/~bouchev/simulations/HYSCORE/HYSCORESimulations.html, April 25, 1999.